Carbon Nanotube and Graphene Nanoelectromechanical Systems

by

Benjamín José Alemán

A dissertation submitted in partial satisfaction of the

requirements for the degree of

Doctor of Philosophy

in

Physics

in the

Graduate Division

of the

University of California, Berkeley

Committee in charge:

Professor Alex Zettl, Chair

Professor Carlos Bustamante

Professor Tsu Jae King Liu

Fall 2011

Carbon Nanotube and Graphene Nanoelectromechanical Systems

Abstract

Carbon Nanotube and Graphene Nanoelectromechanical Systems

by

Benjamín José Alemán

Doctor of Philosophy in Physics

University of California, Berkeley

Professor Alex Zettl, Chair

One-dimensional and two-dimensional forms of carbon are composed of sp^2-hybridized carbon atoms arranged in a regular hexagonal, honeycomb lattice. The two-dimensional form, called graphene, is a single atomic layer of hexagonally-bonded carbon atoms. The one-dimensional form, known as a carbon nanotube, can be conceptualized as a rectangular piece of graphene wrapped into a seamless, high-aspect-ratio cylinder or tube. This dissertation addresses the physics and applied physics of these one and two-dimensional carbon allotropes in nanoelectromechanical systems (NEMS).

First, we give a theoretical background on the electrodynamics and mechanics of carbon nanotube NEMS. We then describe basic experimental techniques, such as electron and scanning probe microscopy, that we then use to probe static and dynamic mechanical and electronic behavior of the carbon nanotube NEMS. For example, we observe and control non-linear beam bending and single-electron quantum tunneling effects in carbon nanotube resonators. We then describe parametric amplification, self-oscillation behavior, and dynamic, non-linear effects in carbon nanotube mechanical resonators. We also report a novel approach to fabricate carbon nanotube atomic force microscopy (AFM) probes, and show that they can lead to exceptional lateral resolution enhancement in AFM when imaging both hard and soft (biological) materials.

Finally, we describe novel fabrication techniques for large-area, suspended graphene membranes, and utilize these membranes as TEM-transparent, AFM-compatible, NEMS resonators. Laser-driven mechanical vibrations of the graphene resonators are detected by optical interferometry and several vibration harmonics are observed. A degeneracy splitting is observed in the vibrational modes of square-geometry resonators. We then attribute the observed degeneracy splitting to local mass inhomogeneities and membrane defects, and find good overall agreement with the developed theoretical model.

To Corina

Contents

List of Figures

Acknowledgments

To my family. Corina, for your advise, clarity, love, and inspiration; you have forever changed my life for the better. To my sons, Pablo and Plácido, the purity of your love has given me the deepest happiness. To my mother, for life, encouragement, and a true testament to the accomplishments of life-long, hard work; by the way, that *enano* got away again! To my brother, Tomás, and my sister, Chayo, for your love and support all of these years. Tomás, your friendship has made the long road possible. Chayo, thanks for teaching my about square-roots when my peers were still learning to add. To Blake and Marie, I can never thank you enough for your kindness and generosity; this would have been impossible without you.

To my advisor, Alex Zettl, for believing in me, and giving me the resources, space, and confidence to be creative in science. The spirit of independent thinking that you cultivate in your students is unmatched. Thank you! We have yet to climb a mountain together, ice-covered or not; I'm ready when you are.

To my dissertation committee members, Professor Carlos Bustamante and Professor Tsu Jae King Liu, for taking the time to read my dissertation and to serve on my qualification exam committee. To Professor Steven Louie for serving on my preliminary and qualification exam committees, and passing me both times!

To those behind close doors who've helped make Physics@Berkeley possible: Anne Takizawa, Donna Sakima, Claudia Trujillo, and G^2 Lang. Thank you for everything!

To my friends and colleagues. To Çaglar, for tennis when science should have been a priority, for so many good times, for advice, for having faith in me and bringing me to the next level; Berkeley would have been impossible without you! To Jeff Weldon, for many good lunches, advice about parenting, getting me back into electronics, and for putting up with me during collaborations. To Will Regan, for serious laughs and listening to and offering crazy ideas; your creativity will take you to great places. To Allen and Maria, for keeping up with my office antics; you've helped make Berkeley an enjoyable place to be. To Mike Rousseas, the philosopher and thinker, for caring kindness, and for skiing through serious pain; may light guide your path. To Kris Erickson, always willing to lend an ear and offer good advice; your good spirit will be welcome and lighten any room you walk into. To Will Gannett, for your voice of reason and a seemingly unlimited supply of membrane devices; follow your heart. To Willi Mickelson for listening to my crazy ideas and asking penetrating questions, you are like a brother to me. To Bibiana Onoa, for her scientific rigor and willingness to be critical of even the most solid of results. To Gabe Dour, for music, sanity, insanity, and friendship; Tipsoo 4Life. To the Compass Project Crew: Angie, Badr, Hal, Joel, Myles, and all the students; you helped make Berkeley a special time. To everyone at the Center of Integrated Nanomechanical Systems (COINS) for sharing your research and ideas; best of luck to all. To the rest of my research colleagues, Kwanpyo Kim, Nasim Alem, Seita Onishi, Aidin Fathalizadeh, Anna Zaniewski, Jian Hau Chen, Ashley Gibb, Jong Min Yuk, Brady Anderson, Matthias Loster, Kenneth

Jensen, David Okawa, Takashi Ikuno, Shaul Aloni, Brian Kessler, Gavi Begtrup, Toby Sainsbury, Yisheng Yang, Professor Claudio Rivetti, Dr. Marta Kopaczynska, Professor Carlos Bustamante, and Professor Feng Wang. Working alongside you has been a true pleasure and privilege.

I would also like to acknowledge contributions made to work appearing in the following: Chapter 1: Will Gannett; Chapter 2: Dr. Jeff Weldon; Chapter 3: Dr. Jeff Weldon, Allen Sussman, Dr. Willi Mickelson, and Will Gannett; Chapter 4: Dr. Jeff Weldon and Allen Sussman; Chapter 5: Dr. Willi Mickelson, Allen Sussman; Chapter 6: Dr. Jeff Weldon; Chapter 7: Will Regan, Dr. Shaul Aloni, Dr. Virginia Altoe, Dr. Nasim Alem, Dr. Çaglar Ö. Girit, Baisong Geng (F. Wang Group), Lorenzo Maserati (M. Crommie Group); Chapter 8: Will Regan and Yisheng Yang (F. Wang Group); Appendix A: Dr. Bibiana Onoa (C. Bustamante Group), Dr. Claudio Rivetti, Dr. Lacramioara Bintu (C. Bustamante Group) and Dr. Marta Kopaczynska (C. Bustamante Group). Appendix B: Will Regan and Jong Min Yuk.

Part I

Introduction to Carbon Nanotube and Graphene-Based Nanoelectromechanical Systems (NEMS)

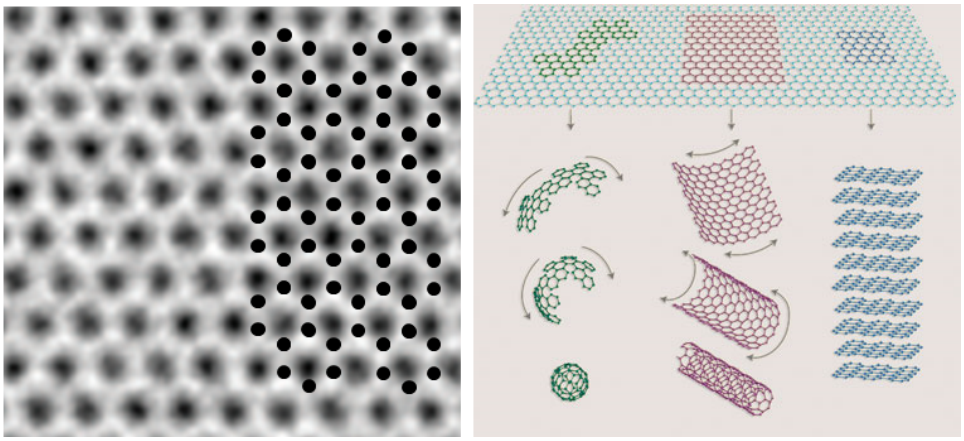

Figure 0.1: Transmission Electron Microscopy Image of Graphene and Schematic of Structural Hierarchy. Aberration-corrected transmission electron micrograph of graphene (left)[85]. Black dots have been added to the image to specify location of carbon atoms in the graphene lattice. Conceptual schematic (right) showing the relationship between graphene and other sp^2 allotropes of carbon (from [64])

The miniaturization of electromechanical systems–systems possessing electronic and mechanical functionality–toward nanometer (one-billionth of a meter) dimensions has led to technologies with unprecedented size[35], sensitivity[28, 52], and decreased power consumption [170]. Furthermore, this nanoscale miniaturization has unveiled a world where both quantum mechanics (the physics of atoms and molecules) and classical mechanics (the physics of cars and stars) govern the behavior of the system[169], which has led to the discovery of novel quantum-electromechanical phenomenon[18, 52]. Electromechanical systems with nanoscaled dimensions are commonly known by the abbreviation NEMS[92], or nanoelectromechanical systems, and are the scaled-down successor of MEMS, or microelectromechanical systems.

Allotropes of carbon with sp^2 bonding have proven important to the emerging field of NEMS and nanotechnology in general. Graphene, the one-atom-thick, two-dimensional form of sp^2 carbon (see Figure 0.1 (left)) can be viewed as the "mother" or basic building block of the other forms, such as graphite, carbon nanotubes and buckyballs, that is C_{60}, and graphite (see Figure 0.1 (right)). Since its discovery in 2004 [62], graphene has been in the spotlight of the nanoscience community, and has led to a multitude on scientific and technological discoveries. These discoveries have uncovered a list of remarkable material properties, some of which translate directly to the "daughter" materials, such as carbon nanotubes and C_{60}: strongest material ever measured [72]; highest electrical mobility; quasi-relativistic "massless" charge carriers [62]; largest thermal conductivity [93]; thinnest possible material; largest possible surface-to-volume ratio, to name a few.

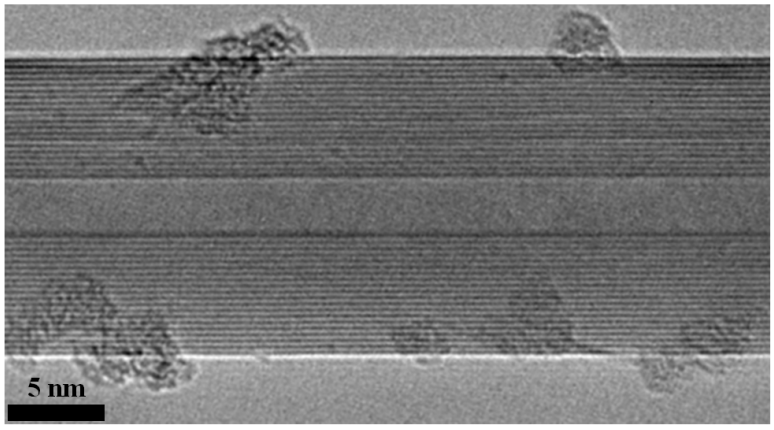

Figure 0.2: TEM Image of Multiwalled Carbon Nanotubue

Carbon nanotubes–nanometer diameter, cylindrical crystals of graphitic carbon–can be conceptualized as rolled-up, seamless cylinders of graphene (see Figure 0.1 (right)). Carbon nanotubes can have a single wall of graphene (single wall carbon nanotubes, or SWCNTs), or multiple walls (multiwall carbon nanotubes, or MWCNTs); a transmission electron micrograph of a MWCNT is shown in Figure 0.2; the dark horizontal lines correspond to cross-sections of individual graphene sheets. Carbon nanotubes have been an important material in the development of NEMS owing to their inherent nanoscale dimensions (length-to-diameter ratios as high as 132,000,000:1) and, as mentioned previously in relation to graphene, their extraordinary thermal (thermal conductivity, 3500 $W \cdot m^{-1} \cdot K^{-1}$)[154], 10 times that of copper), electronic (electrical current capacity, 4×10^9 $A \cdot cm^{-2}$[155], 1000 times that of copper or aluminum; Electron mobility of 10,000 $cm^2 \cdot V^{-1} \cdot s^{-1}$, which is better than that of silicon[156]), mechanical (strength, Young's Modulus $\sim$ TPa[139, 141], 100 times that of steel; tensile strength on the order of 10–100 GPa, which is 10–100 times that of high-grade stainless steel), and optical properties ("blackest" material known to man.) Furthermore, the electronic band structure of SWCNTs depends on the relative orientation of the principle axis of the nanotube to the underlying graphene lattice, and can be found by taking conical sections about the *Dirac* cone of graphene's electronic band structure [157]. Therefore, SWCNTs are observed to be metallic or semiconducting[51].

Advancements in the synthesis of carbon nanotubes and graphene allow them to be grown quite economically and with basic laboratory equipment, and thus facilitate their integration into NEMS. Carbon nanotubes can be produced in many ways including arc discharge[150], laser ablation[151], and chemical vapor deposition [152]. Graphene can be produced by mechanical exfoliation [62] or chemical vapor deposition [82]. For more detailed information on the synthesis, properties, and ap-

plications of carbon nanotubes and graphene, the reader is referred to Jorio *et al.* [51] and graphene reviews[64, 65, 158].

In many ways, carbon nanotubes and graphene are the ideal NEMS materials[92], which should be strong, have small mass, and have large surface area. To this end, carbon nanotubes and graphene represent the very extreme of potential NEMS materials, for they can have the smallest possible mass (SWNCTs), largest possible surface-to-volume ratio (graphene), and are the strongest materials known to man(Graphene and CNTs). For instance, graphene's large surface-to-volume ratio make it, in terms of mass-flux detection, the most sensitive inertial mass spectrometer known[171]. On the other extreme, SWCNT mechanical resonators can be readily prepared with linear mass densities equivalent to that of a graphene nanoribbon (GNR) of width $\pi \approx 3$ nm. Thus, since preparing suspended GNRs of these dimensions is currently quite challenging (if not impossible), carbon nanotubes can compose the lightest possible mechanical resonators and can achieve atomic-scale inertial mass[28] and single-electron [52] sensitivities. Furthermore, because graphene and carbon nanotubes are good conductors of electrons, one can easily couple the electronic and mechanical degrees of freedom of the system directly, as opposed to building in piezoresistive layers or using light reflection to facilitate this coupling, and so these systems have the capacity to be much more versatile and simple to integrate. Also, the large surface area together with the highly tunable electronic structure of SWCNTs and graphene opens up the possibility of surface states coupling strongly to the mechanical motion of the resonator. Additionally, because they are carbon-based, there is the added benefit of not relying on silicon or other expensive semiconductor materials for device fabrication. Thus, from the practical and theoretical standpoint, carbon nanotube and graphene-based NEMS have a bright future.

It is the goal of this dissertation to describe the fabrication, performance, and novel properties of carbon nanotube and graphene-based NEMS. Apart from the introductory remarks presented above, this dissertation is divided into four parts. Part II covers the fabrication of carbon nanotube NEMS, introductory electromechanical theory, basic experimental background and techniques, and related experimental work, including static and dynamic NEMS resonator behavior and field emission. Part III describes parametric amplification, self-oscillation behavior, and dynamic, non-linear effects in CNT mechanical resonators. Part IV covers fabrication and experimentation with graphene-based NEMS resonators. Finally, Part V is a collection of appendices with supplementary information on fabrication, special techniques, mathematical derivations, and related, yet important, work with carbon nanotube AFM probes.

Part II

Carbon Nanotube NEMS

Chapter 1

Background and Fabrication

In this chapter, we present the techniques utilized to fabricate suspended SWCNT and MWCNT devices. These techniques include *in situ* scanning electron microscopy (SEM) and transmission electron microscopy (TEM) mechanical assembly, and conventional nano/microfabrication with electron and optical lithography.

1.1 Fabrication I: Mechanical Assembly

The carbon nanotube resonator devices that we focus on in the bulk of this entire dissertation are singly clamped mechanical resonators–nanocantilevers. We'll exploit the free end of the resonator to monitor field emission current(see Chapter 3) which couples strongly with the mechanical motion of the nanotube (see Part III). Carbon nanotube mechanical resonators in a cantilevered geometry can be fabricated using "bottom-up" techniques to directly attach a nanotube to a sharp probe, usually a commercial atomic force microscopy (AFM) probe or sharpened metal wires such as tungsten scanning tunneling microscopy (STM) probes. Although this technique is not scalable (they are in fact made one at a time), it allows the prepared researcher to readily fabricate and test a device in less than 1 hour. Also, because the nanotube and its support electrode are free to move, these "bottom up" devices allow one to vary geometric parameters (such as relative electrode position and separation distance) in real time using the same nanopositioning system used to assemble them.

The first attempts at mechanical attachment were performed with the aid of optical microscopes [117], although the low spatial resolution of optical microscopes led to poor identification of single nanotubes and mostly produced nanotube-bundle devices. Mechanical attachment of *single* nanotubes was made possible through the use of sub-angstrom precision piezo-drive positioning stages operated in a high resolution scanning electron microscope (SEM) [124]. Alternative methods were also developed that retrieve vertically aligned nanotubes from a substrate using AFM [113], and that use deposition of catalyst particles on sharpened tips to grow the nanotube directly

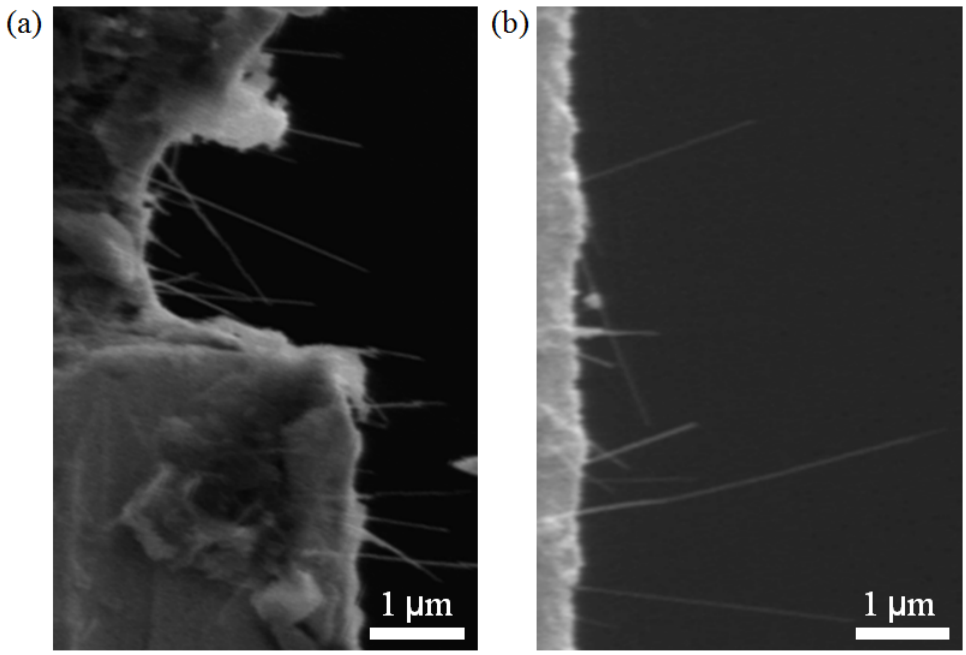

Figure 1.1: Carbon Nanotubes on the Edge (a) by razor blade electrophoretic alignment and (b) simple drop-casting

onto the tip [106, 107] via chemical vapor deposition (CVD).

We use piezo-driven nanopositioning systems operated in a SEM and a transmission electron microscope (TEM) to attach single carbon nanotubes to sharpened tips. The high electron kinetic energies used in TEM (100-200 keV) result in few-angstrom spatial resolution, which opens up the possibility of attaching single single-walled carbon nanotubes (SWCNTs) to sufficiently sharp tips. Details of *in situ* TEM fabrication and related work wherein nanotubes attached to AFM probes are utilized for high-resolution AFM are given in Appendix A.

The mechanical attachment described here requires that carbon nanotubes be prepared to protrude from the edge of a surface. It is relatively important that the edge be straight (and clean) so that individual nanotubes can be contacted without touching the substrate edge or other nanotubes. Nanotubes must also extend several micrometers from the edge of the substrate; longer nanotubes are more flexible and conform much more readily to the surface of the sharpened tip and, thus, facilitate nanotube attachment. Samples of such protruding nanotubes were prepared in several ways:

- **Electrophoretic Alignment** In this method, nanotubes are electrophoretically aligned off the edge of a metal foil. First, a nanotube solution is prepared by sonicating (10-15 minutes under medium power) a small quantity of

nanotubes (Arc-discharge MWCNT or SWCNT) in solvent such as isopropyl alcohol. The solution should be *light* grey in color; the higher concentration of dark grey colored solutions cause the nanotubes to form nest-like structures of bundles that make mechanical attachment arduous if not altogether impossible. Two sterile razor blade edges are clamped parallel to and within 500 μm of each other. A 40 V, 10 MHz sinusoid is applied across the razor blades using a signal generator, and drops of the freshly sonicated nanotube solutions are deposited over the two edges. The solution is allowed to dry and the two razor blades are carefully separated from each other and stored sharp-edge-side-up in a electrostatic discharge safe box for later use. Samples prepared in this way are shown in Figure 1.1 (a).

- **Deposition and Cleavage of Substrate** In this relatively simple method, nanotubes are deposited onto a crystalline substrate, and then the substrate is cleaved resulting in protruding nanotubes from the cleaved edge. First, a nanotube solution is prepared as in the above method. A degenerately doped or metallized (coated with a thin layer (100 nm) of a metal like gold or platinum) silicon or metallized silicon nitride (Si_3N_4) die is then cleaned and placed on a hot plate at 75° C. The surface in contact with the nanotube must be metallic to avoid charging in SEM or TEM, and to allow accessing the nanotube electronically for cutting and sharpening the nanotube [142]. With the die hot, freshly sonicated nanotube suspension is dropped onto the die and allowed to dry. It is also possible to forgo the use of a hotplate, and spin cast the solution onto the die which usually takes a bit longer and results in lower nanotube density. The die is then scribed near its edge to avoid the center, and cleaved into two pieces. The die will cleave along a crystal plane and will be very straight. Typically, only one edge of the two pieces will be overhanging; the other underhanging piece cannot be used and is discarded. The cleaving process tends to "comb" the nanotubes so that they rest perpendicular to the edge(this "combing" is accentuated in SWCNT samples as can be seen in Figure A.1 (b) of Appendix A.) MWCNT samples prepared in this way are shown in Figure 1.1 (b).

1.1.1 *in situ* Mechanical Attachment

Once the carbon nanotube samples are prepared they can be used to attach the tubes to sharp tips. For the sharp tip, we use commercial AFM tips (Mikromasch, http://www.spmtips.com/) or prepare electrochemically etched tungsten STM tips as described in Ref. [159]. The AFM tips tend to give higher yield perhaps because the etch used during fabrication is well-defined and uniform, and results in a smoother surface and therefore improved nanotube adhesion. Stiffer AFM tips (spring constant $\sim$ 1 N/m; Mikromasch NSC-35 and NSC-36 series are a good choice) must be used to avoid having the AFM probe crash into the nanotube sample; tip crashing can be

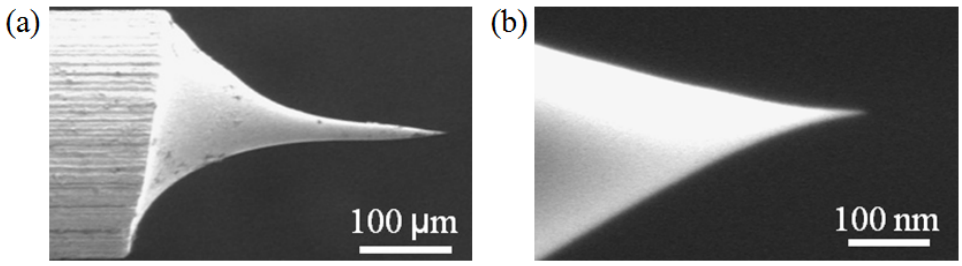

Figure 1.2: (a) STM tip made by electrochemical etching (b) commercial AFM probe

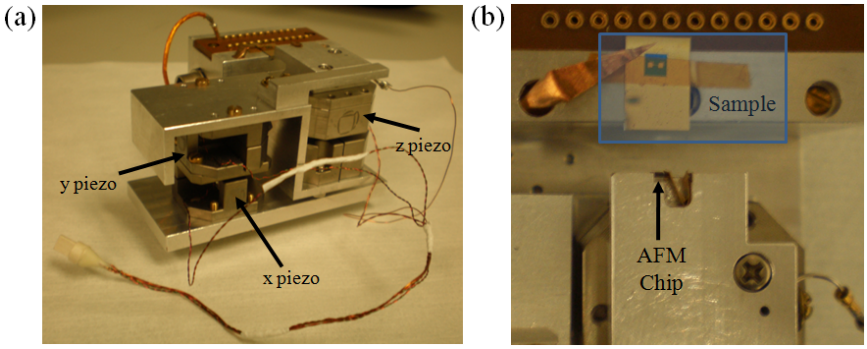

Figure 1.3: Attocube Stage

even more problematic during experimentation because the tip is biased with respect to a counter electrode.

The nanotube sample and the AFM (or STM) tip are mounted onto a piezo-driven 3D nanopositioning stage (see 1.3 (a)). The nanotube sample is clamped to a stationary part of the stage (see 1.3 (b) upper). The AFM tip is secured to the mobile part of the stage (see 1.3 (b) lower) using an elastic metal clip. The position of the AFM tip can now be controlled in three dimensions by X, Y, and Z piezos (Attocube; Zettl Group contact for piezo problems or for repairs: rainer.goetz@attocube.com). The piezos are controlled by a commercial controller (Attocube, see 1.4), which sends sawtooth voltage signal to the piezo causing it to expand or contract and then quickly return to the unstrained state–the "stick-and-slip" mechanism. The piezos can also be controlled by computer; a LabVIEW program was written to control the voltage output of a DAQ (DAQ in 1.4) which is then amplified (amplifier in 1.4) and sent to the piezo to control coarse and fine motions. Computer control fine motion can easily achieve sub-angstrom precision. Detailed instructions for operating the Attocube nanopositioning stage are given in Appendix E.

The sharp probe can now be positioned near the edge of the carbon nanotube sample, and the SEM can be focused on a particular nanotube. Again, longer nan-

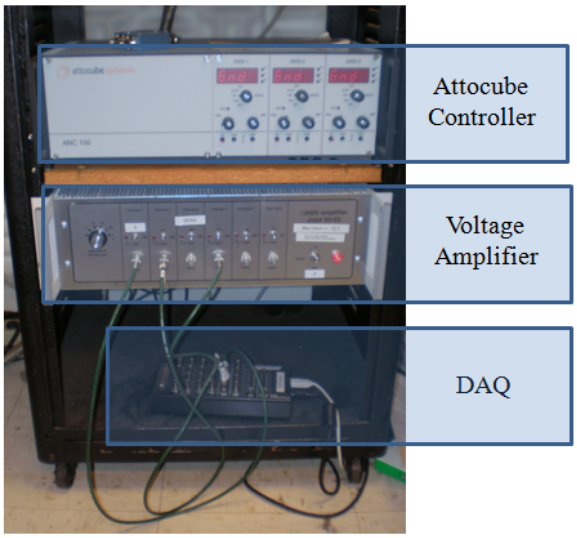

Figure 1.4: Attocube Controller

otubes are more flexible than shorter tubes and are much easier to attach to the probe. Without changing the SEM focus, the probe is moved along the Z-axis until its tip comes into focus. Further adjustments are made along all three axes until the nanotube rests on the surface of the probe tip, as in Figure 1.5. Once the nanotube comes into contact with the probe tip, it can be visibly moved and manipulated by changing the position of the probe.

Although the van der Waals attractions holding the carbon nanotube onto the surface are strong [116], we reinforce the bond by electron beam induced deposition of amorphous carbon or an organometallic compound over the nanotube. By focussing the beam over the nanotube, residual organic species in the SEM vacuum chamber can be deposited over the nanotube-surface junction. The deposition of amorphous carbon in this way can be difficult to control and may lead to several tens of minutes of wait time. Much more predictable bonds can be obtained by injecting an organometallic gas into the SEM chamber. Deposition functions when the organometallic precursor gas adsorbs onto surface and secondary electrons "crack" the adsorbed molecule leaving a metallic deposit. Volatile products are then carried away from the surface by the vacuum. Gas injection can deposit μm of material per minute, and deposits only in regions exposed to the SEM electron beam. The resolution is limited by the scattering of secondary electrons and can achieve 100 nm line widths. Regions where gas injection has been used to deposit platinum onto the nanotube-probe can be see in Figure 1.5 (b).

Once a good bond has been established, the nanotube is supported at both ends with metallic contacts. The length of the suspended nanotube beam can be adjusted by moving the probe toward or away from the carbon nanotube sample edge. The

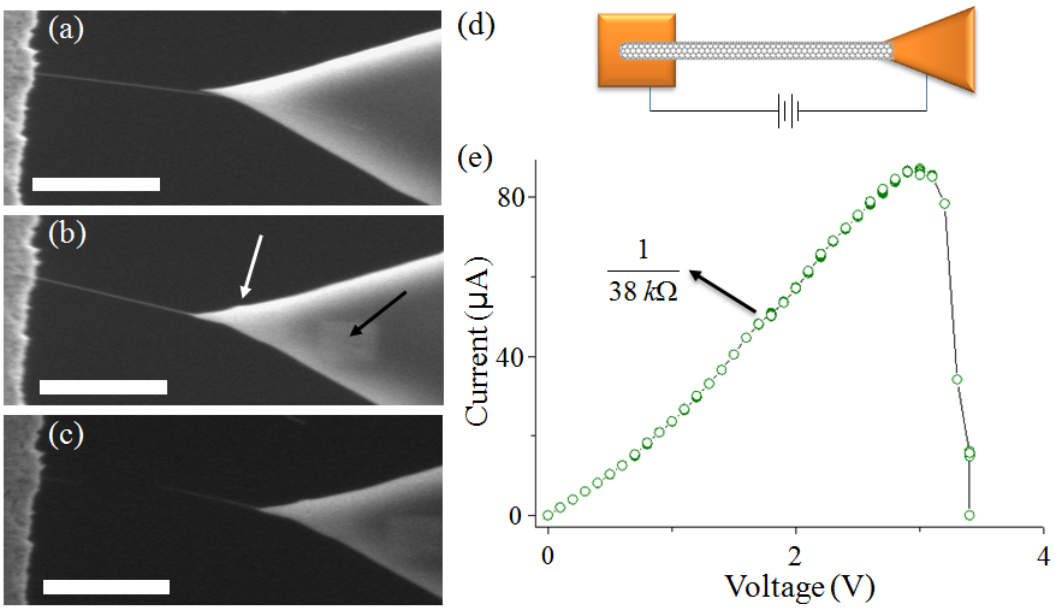

Figure 1.5: Nanotube Resonator Device Fabrication by Mechanical Attachment: (a)-(c) is a sequence. (d) shows the setup for running current through. (d) Shows data for cutting.

eventual length of the nanotube device will be half the length of the doubly-clamped beam, achieved by "cutting" the nanotube, or the total length of the nanotube by pulling it completely away from the substrate. Devices made by pulling the nanotube off of the substrate can be as much as 10 μm in length. Nanotube "cutting" is achieved by running an electrical current through the nanotube (see 1.5 (d)). At sufficiently large currents, Joule heating raises the temperature of the middle of the nanotube past failure and the tube is severed [142]. A LabVIEW program was written to control a Keithley 2400 Sourcemeter to apply and record voltages and currents to the nanotube. A typical current-voltage curve obtained from cutting a nanotube is show in Figure 1.5 (e). From this data, we see that the end contacts are quite good with a device electrical resistance of about 38 kΩ. At approximately 80 μA, the current through the tube abruptly drops to zero indicating that the tube has been cut, which is verified by SEM in Figure 1.5 (c).

1.2 Fabrication II: Lithography

In this section, we summarize the fabrication of nanotube resonator devices by a combination of optical and electron beam lithography. The devices are engineered to be compatible with TEM characterization, so regions near the suspended elec-

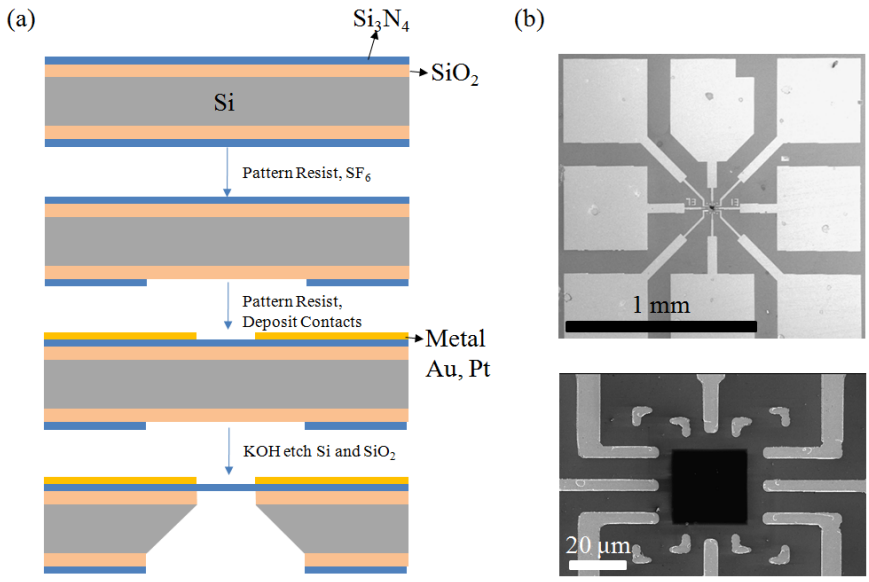

Figure 1.6: Si_3N_4 Membranes with predefined metallic contacts. (a) Process flow diagram for membrane fabrication. (b) *Upper* is zoomed out view of contacts and membrane (center of pattern) and *lower* shows higher magnification of membrane. The membrane appears dark because of its transparency in the electron beam.

trical contacts and the suspended nanotube will be completely void of a substrate. The TEM "transparent" suspended structure is made by performing electron beam lithography on a 20 nm thin silicon-nitride membrane (Si_3N_4) window (approximately 400 μm^2 in area). This round of e-beam lithography defines 200 nm thick metallic contacts on the nanotube used for electrical characterization and probing. The Si_3N_4 is then removed with an SF_6 reactive ion etch, which suspends the electrical contacts and the nanotube.

An individual bare Si_3N_4 membrane window device (see Figure 1.6 (b) upper) is about 2 mm wide on each side and has metallic contacts that are large (500 μm $\times$ 500 μm) near the edge of the die and become narrower as they approach the die's center. The electrode geometry is compatible with the pogo pin layout of the TEM transport stage discussed in §2.3. At the center of the die is located a 20 μm $\times$ 20 μm window (black square in lower part of Figure 1.6 (b)) of Si_3N_4 approximately 10-40 nm in thickness. Alignment markers that are used during e-beam lithography are located at the corners of the membrane window.

Details of the Si_3N_4 membrane device fabrication can be found in Gavi Begtrup's UC Berkeley doctoral thesis [144]. The fabrication is summarized schematically in Figure 1.6 (a). Briefly, 10-40 nm of Si_3N_4 and 200-500 nm of oxide are grown onto both sides of a 200 μm thick (100) Si wafer. Optical lithography is used to define an

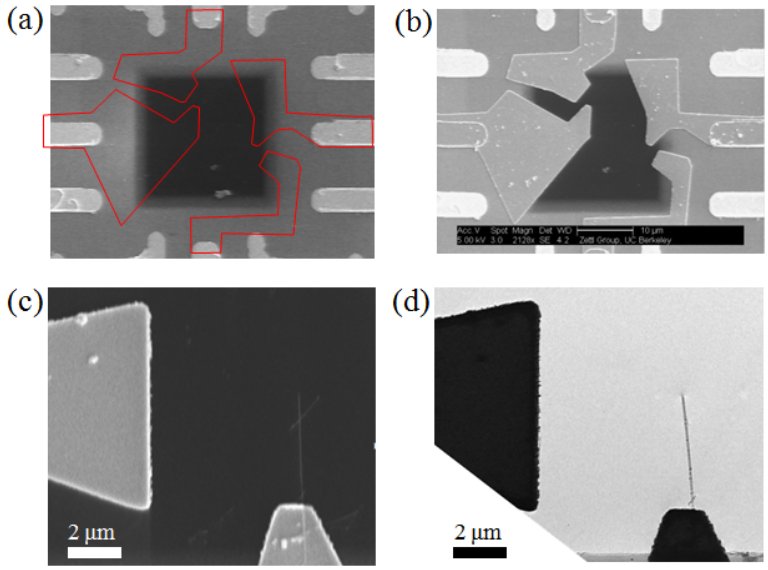

Figure 1.7: Carbon nanotube resonator on using Si_3N_4 membranes. (a) Pre-pattern showing where electrodes will be written. (b) After lithography. (c) SEM and (d) TEM of a completed carbon nanotube resonator.

"etch mask" by etching squares into the Si_3N_4(with SF_6) on one side of the wafer, and to deposit metallic contacts on the other. A KOH (2-1 H_20-KOH) bath then etches pits into the oxide and the Si as defined by the Si_3N_4 etch mask. The KOH etch proceeds to the upper Si_3N_4 layer, resulting in the suspended Si_3N_4 membrane.

Carbon nanotube resonators are fabricated on Si_3N_4 membranes by first spin casting a dilute nanotube solution in isopropyl alcohol onto the Si_3N_4 chip. The location of the nanotubes on the membranes relative to the alignment markers is mapped using SEM. Electrode patterns are then designed using commercial CAD software (DesignCAD) with the aid of the SEM mapping (see Figure 1.8 (a) and Figure 1.7 (a)). An electron sensitive polymer (PMMA A4) is deposited onto the chip. Patterns defined by the CAD files are then written onto the chip using an SEM electron beam controlled with the commercial Nanometer Pattern Generation System (NPGS) software (JC Nabity Lithography Systems). After developing, 150-200 nm of metal (gold or platinum) is deposited onto the chip. "Lift-off" in hot NMP or Acetone leaves the desired electrode pattern on the nanotube (see SEM images in Figure 1.8 (b) and Figure 1.7 (b) and (c).) Approximately 2-3 individual carbon nanotube resonator devices can be assembled per membrane. A thorough outline of the entire electron beam lithography process, including the use of NPGS, is given in Appendix G.

As noted earlier, an SF_6 reactive ion etch removes the Si_3N_4 membrane, and thus produces the suspended nanotube structure, as can be seen the TEM images of Figure

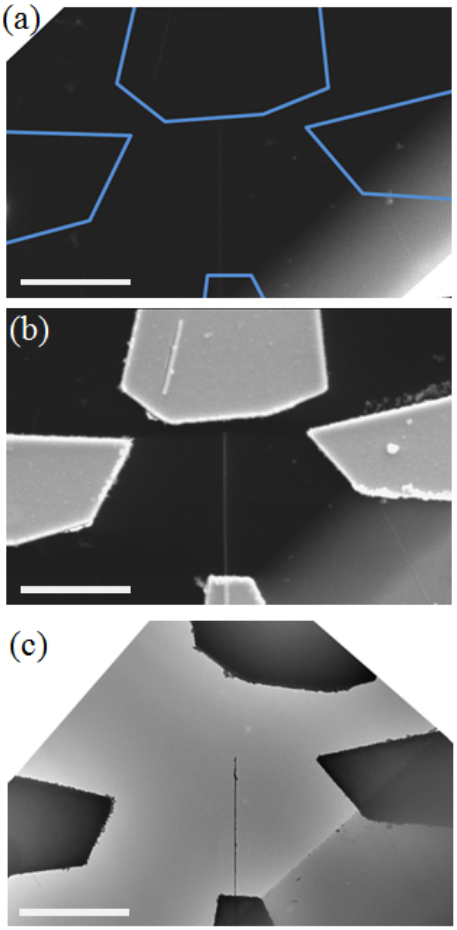

Figure 1.8: Carbon nanotube resonator on using Si_3N_4 membranes. (a) Pre-pattern showing where electrodes will be written. (b) After lithography. (c) In TEM, some contacts have been damaged.

1.8 (c) and Figure 1.7 (d).) Because portions of the electrodes that were over the Si_3N_4 membrane become suspended after the etch, they will bend or collapse if not sufficiently thick. Figure 1.8 (c) shows a device whose electrodes were too thin (they do not appear completely opaque in the TEM beam) and have moved away from the designed position (as seen in Figure 1.8 (b)). The device shown in Figure 1.7 (d) does, however, have sufficiently thick electrodes as can be seen by their black appearance in the TEM image.

Chapter 2

Electromechanics of Carbon Nanotube Resonators

Now we examine how suspended carbon nanotubes behave under applied external electrostatic and electrodynamic forces. First we outline the necessary elasticity theory needed to understand the system response. The background theory is also included here because complete derivations of the important relationships in static and dynamic beams, such as Eigenfrequencies, spring constants, beam shape, *etc.*, are somewhat difficult to find in a compact form in existing texts. We therefore hope that the background theory given in this chapter and in Chapter 3 will be especially helpful for future students pursuing research in this exciting field. Finally, we'll discuss some basic experiments that were performed *in situ* TEM to test the basic elasticity theory. We'll consider static deflections of carbon nanotube beams, and the dynamical response of the resonators under the influence of a time-varying driving force. In both cases, we find that the behavior of our devices are in excellent agreement with the theory.

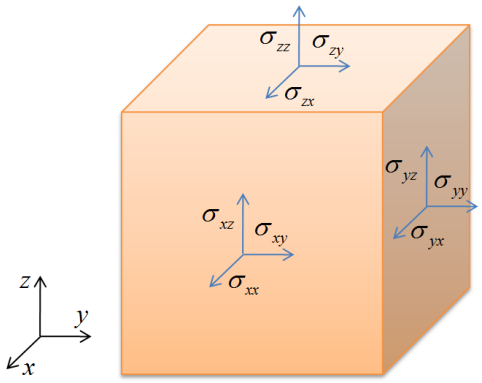

Figure 2.1: Differential Volume Element for Stress Tensor

2.1 Basic Elasticity and Beam Theory

We begin by exploring the basic relationship between stress (the forces on a body element) and strain (the physical response: stretching, compressing, *etc.*) in a solid body.

The stress tensor σ_{ij} gives the normal stress (pressure) on a face for $i = j$, and the shear stress for $i \neq j$, and has units of Pascals, Pa, or N/m^2 in SI units. Figure 2.1 shows the different components of the stress tensor acting on a square body.

Strain is a measure of how much the body extends or compresses when acted upon by some stress, internal or external. Axial strain is defined as

$$\epsilon_{xx} \equiv \frac{u_x(x + \Delta x) - u_x(x)}{\Delta x} = \frac{\partial u_x}{\partial x}$$

where $u_x(x)$ is the displacement in the $\hat{x}$ direction of an element initially located at position x. It is common to omit the second subscript when writing the axial strain, $\epsilon ii = \epsilon_i$. Referring to the body shown in Figure 2.2, body elements located at positions x and $x+\Delta x$ get displaced to $x+u(x)$ and $x+\Delta x+u(x+\Delta x)$, respectively. Positive strain corresponds to the extension (lengthening) of a body, whereas negative strain corresponds to compression.

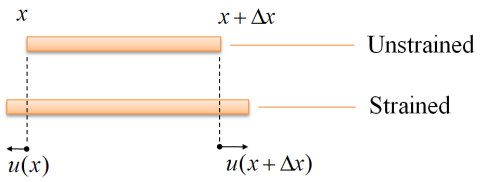

Figure 2.2: Simple 1-D Strain

Shear strain is defined as

$$\epsilon_{xy} = \frac{\partial u_x}{\partial y} + \frac{\partial u_y}{\partial x}$$

The first-order, linear relationship between normal stress and uniaxial strain is

$$\sigma_{ii} = E\epsilon_i \tag{2.1}$$

where E is the Young's modulus. Equation 2.1 is the equivalent of Hooke's law; with $\sigma = F/A$, equation 2.1 gives

$$F = \frac{A}{L} E \Delta L$$

where the Hooke's law spring constant is $k = AE/L$.

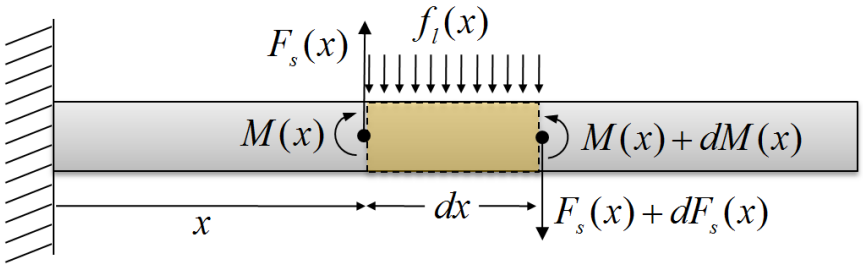

Figure 2.3: Forces and Moments on a Beam

Shear stress and shear strain are connected by the shear modulus G:

$$\sigma_{ij} = G\epsilon_{ij}$$

Uniaxial strain is often accompanied by transverse contraction and related by Poisson ratio, ν,

$$\epsilon_x = -\nu\epsilon_y$$

The differential volume element is assumed to be in static equilibrium, so the that the condition of no net torque gives

$$\sigma_{ij} = \sigma ji$$

for $i, j = x, y, z$. Also, one can relate the shear modulus, Young's modulus, and the Poisson ratio by

$$G = \frac{E}{2(1+\nu)}$$

2.1.1 Static Deformation of Beams

We now use the results from the last section to derive differential equations for the equilibrium displacement of a beam in terms of external loads. Referring to Figure 2.3, the sum of the forces on the differential element dx is

$$f_l(x)dx + (F_s + dF_s) - F_s = 0$$

or

$$\frac{dF_s}{dx} = -f_l(x) \tag{2.2}$$

where $F_s(x)$ is the shear force, and $f_l(x)$ is force per unit length along beam at position x. The sum of the moments on the element is

$$(M(x) + dM(x)) - M(x) - (F_s(x) + dF_s(x))dx - \frac{f_l(x)dx}{2}dx = 0$$

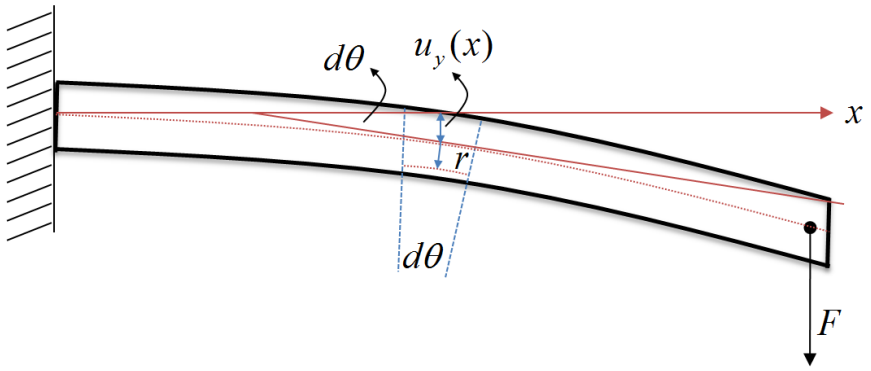

Figure 2.4: A Bending Beam

or

$$\frac{dM(x)}{dx} = F_s(x) \tag{2.3}$$

where $M(x)$ is the moment at position x along beam.

Now we look at the strain in a section of a bent cantilever (Fig. 2.4). At a position x, the beam has a radius of curvature $R(x)$ and the *neutral* axis of the differential element dx has length $dx = R(x)d\theta$ and subtends the angle $d\theta$. At a distance r from the neutral axis, the differential element has length $dl = (R(x) - r)d\theta$. Thus, the length of the differential segment under stress is

$$dl = dx - \frac{r}{R(x)}dx$$

Therefore, the strain is

$$\begin{aligned} \epsilon_x &= \frac{dl - dx}{dx} \\ &= -\frac{r}{R(x)} \end{aligned}$$

and the stress-strain relationship (Equation 2.1) gives

$$\sigma_{xx} == -\frac{r}{R(x)}E$$

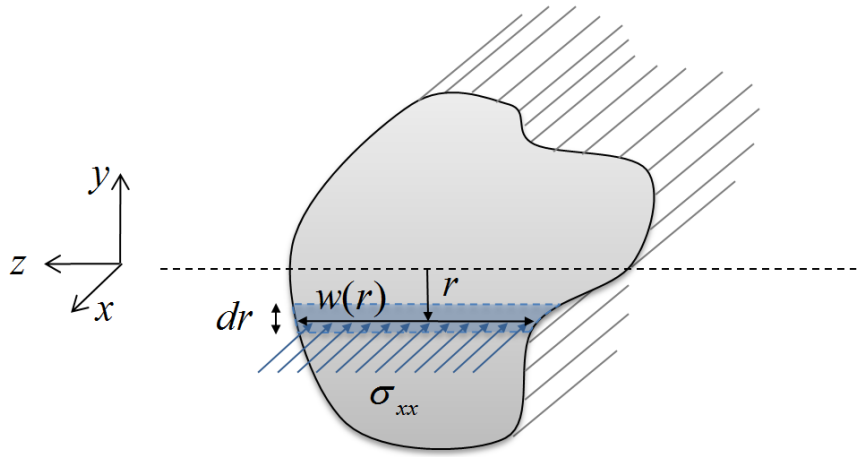

Figure 2.5: A Beam Cross Section

We can now use σ_{xx} to obtain the internal bending moment. From figure 2.5

$$\begin{aligned} M_z &= \int \sigma_{xx} w(r) r dr \\ &= \int \frac{-E}{R(x)} w(r) r^2 dr \\ &= -\frac{E}{R(x)} \int w(r) r^2 dr \\ &= -\frac{E}{R(x)} I \end{aligned} \tag{2.4}$$

where we have used the relation $\sigma_{xx} == -\frac{r}{R(x)} E$, and defined the moment of inertia, I:

$$I = \int w(r) r^2 dr \tag{2.5}$$

The moment thus depends on the local radius of curvature of the beam, $R(x)$, which is given in many introductory texts on differential geometry as

$$\frac{1}{R(x)} = \frac{\frac{d^2 u_y(x)}{dx^2}}{\left(1 + \left(\frac{du_y(x)}{dx}\right)^2\right)^{3/2}}$$

We take the approximation $\frac{1}{R(x)} = \frac{d^2 u_y(x)}{dx^2}$ which hold for many NEMS beams when $\frac{du_y(x)}{dx} << 1$. This approximation holds even for beams that can bend back over

themselves, as in springs, as long as the local tangent line makes a small enough angle. Then using Equation 2.4,

$$\frac{d^2u_y(x)}{dx^2} = \frac{-M(x)}{EI} \tag{2.6}$$

Differentiating Eq. 2.6 and using Eq. 2.3 gives

$$\frac{d^3u_y(x)}{dx^3} = \frac{-F_s(x)}{EI} \tag{2.7}$$

Finally, differentiating a second time and using Eq. 2.2, we obtain the *linear beam equation* which relates the beam deflection, $u_y(x)$, to the force distribution, $f_l(x)$,

$$\boxed{EI\frac{d^4u_y(x)}{dx^4} = f_l(x)} \tag{2.8}$$

This equation is useful when solving for beam shapes when only external loads are present. We will use this result later when we discuss instability in self-oscillating carbon nanotube resonators. Eq. 2.8 neglects internal tensile or compressive stress, such as would exist in a doubly-clamped beam. Modifying Eq. 2.8 to include these additional terms gives (see [20])

$$EI\frac{d^4u_y(x)}{dx^4} - EIT\frac{d^2u_y(x)}{dx^2} = f_l(x) \tag{2.9}$$

which is known as the *Euler beam equation.*

2.1.2 Some Important Examples

Moment of Inertia for Carbon Nanotube

We now calculate the moment of inertia of a carbon nanotube, which has a circular cross-section:

$$\begin{aligned} I &= \int_{r_i}^{r_o}\int_0^{2\pi} \rho^2\sin^2(\theta)(\rho d\theta d\rho) \\ &= \int_{r_i}^{r_o}\int_0^{2\pi} \rho^3\left(\frac{1}{2} - \frac{1}{2}\cos(2\theta)\right)d\theta d\rho \\ &= \pi\frac{{r_o}^4 - {r_i}^4}{4} \end{aligned} \tag{2.10}$$

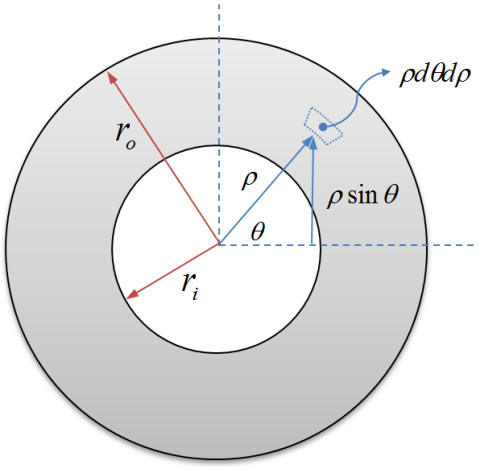

Figure 2.6: A CNT Cross Section

Point Load at Free End of Cantilever

We consider a point load $f_l(x) = -F\delta(x-L)$. Integrating Eq. 2.8 gives $\frac{d^3u_y(x)}{dx^3} = -\frac{F}{EI} + C$ which, by Eq. 2.7, must be equal to a shear at end of the beam. Thus, $\frac{d^3u_y(L)}{dx^3} = +\frac{F}{EI}$ so $C = \frac{2F}{EI}$. Integrating again yields $\frac{d^2u_y(x)}{dx^2} = \frac{F}{EI}x + C$ and, since their are no net torques at position $x = L$, $\frac{d^2u_y(L)}{dx^2} = 0$ and thus $C = -\frac{FL}{EI}$. Another integration gives $\frac{du_y(x)}{dx} = \frac{F}{2EI}x^2 - \frac{FL}{EI}x + C_1$; the slope at beam clamps must be zero, $\frac{du_y(0)}{dx} = 0$, thus $C_1 = 0$. After a final integration, $u_y(x) = -\frac{F}{6EI}x^3 + C\frac{FL}{2EI}x^2 + C_2$. The clamp boundary condition, $u_y(0) = 0$, makes $C_2 = 0$. Then

$$u_y(x) = \frac{F}{EI}\left(\frac{1}{6}x^3 - \frac{L}{2}x^2\right)$$

The effective spring constant is found by solving for F with maximum deflection, which occurs at the end of the beam. The result is

$$F = -\frac{EI}{3L^3}u_y(L)$$

so the effect spring constant is

$$k_{eff} = \frac{3EI}{L^3}$$

Uniform Load on a Cantilever

We assume a uniform load $f_l(x) = -F/L$ acts on a cantilever beam. First, $\frac{d^3u_y(x)}{dx^3} = -\frac{F}{LEI}x + C$, and the condition for a shearless end $\frac{d^3u_y(L)}{dx^3} = 0$ makes $C = \frac{F}{EI}$.

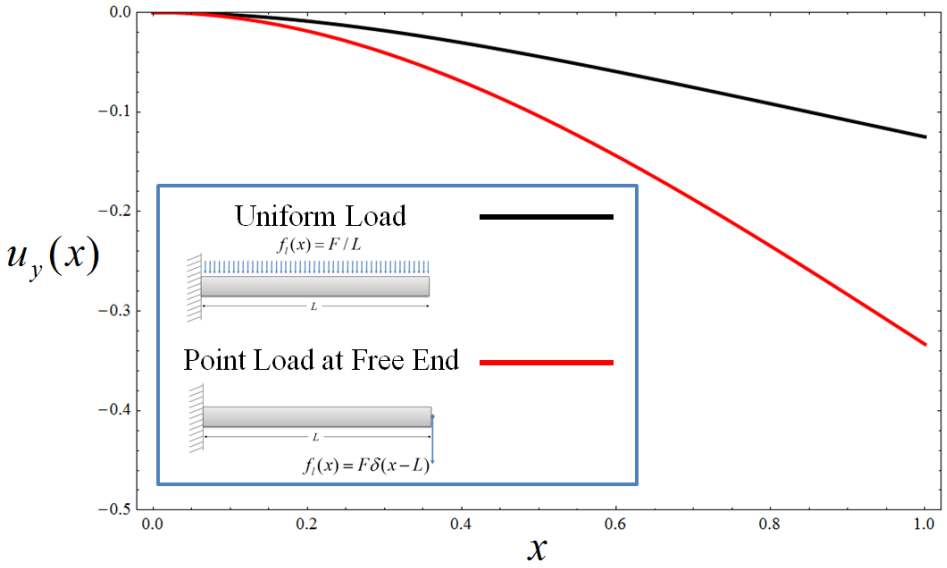

Figure 2.7: Theoretical beam profile $u_y(x)$ vs. x for Point Load and Uniform Load for $E = I = F = L = 1$

$\frac{d^2u_y(x)}{dx^2} = -\frac{F}{2LEI}x^2 + \frac{F}{EI}x + C_1$, and the condition for a torque free end $\frac{d^2u_y(L)}{dx^2} = 0$ gives $C_1 = -\frac{FL}{2EI}$. $\frac{du_y(x)}{dx} = -\frac{F}{6LEI}x^3 + \frac{F}{2EI}x^2 + -\frac{FL}{2EI}x + C_2$, $\frac{du_y(0)}{dx} = 0$ makes $C_2 = 0$. Finally, $u_y(x) = -\frac{F}{24LEI}x^4 + \frac{F}{6EI}x^3 + -\frac{FL}{4EI}x^2 + C_3$ and $u_y(0) = 0$ makes $C_3 = 0$, so

$$u_y(x) = -\frac{F}{24LEI}x^4 + \frac{F}{6EI}x^3 + -\frac{FL}{4EI}x^2$$

The effective spring constant is

$$k_{eff} = \frac{8EI}{L^3}$$

Figure 2.7 shows $u_y(x)$ vs. x for a point load applied to the free end and a uniform load for $E = I = F = L = 1$.

2.2 Flexural Vibrations

Consider again the beam in figure 2.3 without the external load but with the shear forces and moments. During vibration, the differential element's equation of motion is

$$F_s(x) + dF_s(x) - dF_s(x) - \rho A dz \frac{\partial^2 u_y(x)}{dt^2} = 0$$

which is just an application of Newton's second law. Note that the moments still cancel

$$(F_s(x) + dF_s(x))dx + (M(x) + dM(x)) - M(x) = 0$$

Rearranging these expressions gives:

$$\frac{\partial F_s}{\partial x} = \rho A \frac{\partial^2 u_y}{\partial t^2} \tag{2.11}$$

and

$$F_s(x) = -\frac{\partial M(x)}{\partial x} \tag{2.12}$$

Substituting Eq. 2.12 into Eq. 2.11 and using Eq. 2.6($\frac{d^2 u_y(x)}{dx^2} = \frac{-M(x)}{EI}$), we obtain the *wave equation* for beams

$$EI \frac{\partial^4 u(x)}{\partial x^4} = -\rho A \frac{\partial^2 u(x)}{\partial t^2} \tag{2.13}$$

(Note that the y subscript has been dropped.) We would like to solve Equation 2.13 to obtain the mode shapes and frequencies of a vibrating nanotube. Using the trial solutions

$$u(x,t) = e^{i(kx-\omega t)}$$

in Equation 2.13, we see that the wavevector k must satisfy:

$$k^4 = \left(\frac{\rho A}{EI}\right)\omega^2$$

Thus,

$$k = \pm \left(\frac{\rho A}{EI}\right)^{1/4} \omega^{1/2}$$

and

$$k = \pm i \left(\frac{\rho A}{EI}\right)^{1/4} \omega^{1/2}$$

are valid solutions. Setting $\Omega = \left(\frac{\rho A}{EI}\right)^{1/4} \omega^{1/2}$, The general solutions for $u(x,t)$ can be written as

$$u(x,t) = e^{-i\omega t}(Ae^{-i\Omega x} + Be^{+i\Omega x} + Ce^{\Omega x} + De^{-\Omega x})$$

The spatial part of $u(x,t)$ can then be written as:

$$u(x) = a\cosh(\Omega x) + b\sinh(\Omega x) + c\cos(\Omega x) + d\sin(\Omega x) \tag{2.14}$$

We can solve Eq. 2.14 for a cantilevered beam of length L. The appropriate boundary conditions are

$$u(0) = 0 \tag{2.15}$$

$$\frac{du(0)}{dx} = 0 \tag{2.16}$$

$$\frac{d^2u(L)}{dx^2} = 0 \tag{2.17}$$

$$\frac{d^3u(L)}{dx^3} = 0 \tag{2.18}$$

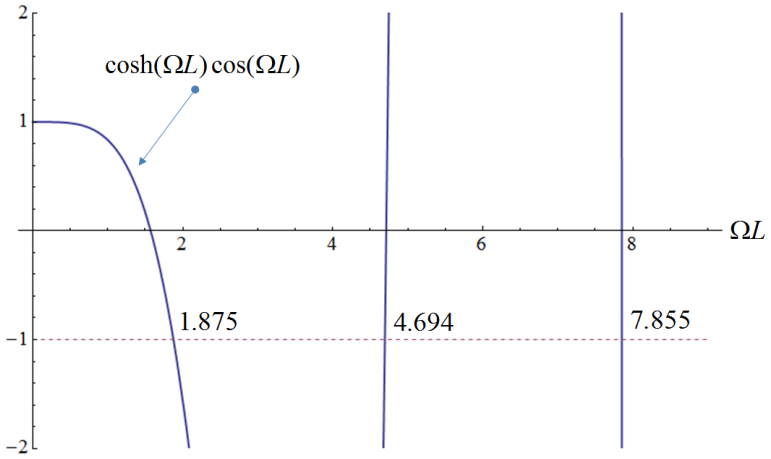

Figure 2.8: Plot of Solutions for ΩL.

The first two boundary conditions correspond to beam clamping (*i.e.* zero displacement and slope at the clamped end) and require that $a = -c$ and $b = -d$. The last two boundary conditions, which follow from Eqs. 2.6 and 2.7 (the beam should have now moment or shear forces at it end), require

$$\begin{pmatrix} \cosh(\Omega L) + \cos(\Omega L) & \sinh(\Omega L) + \sin(\Omega L) \\ \sinh(\Omega L) - \sin(\Omega L) & \cosh(\Omega L) + \cos(\Omega L) \end{pmatrix} \begin{pmatrix} a \\ b \end{pmatrix} = 0 \tag{2.19}$$

We find non-trivial solutions to Eq. 2.19 by setting the determinant of the left-hand-side matrix to zero:

$$\cos(\Omega L)\cosh(\Omega L) + 1 = 0 \tag{2.20}$$

We find solutions for ΩL graphically, as shown in Fig. 2.8. We also label the n^{th} root of Eq. 2.20 as the n^{th} vibrational mode of the beam. Then, $\Omega_n L$=1.875, 4.694, 7.855, and so on. The solutions $\Omega_n L$ also lead to relationships between a_n and b_n which we obtain from Eq. 2.19. For instance, a_n/b_n=-1.3622, -0.9819, -1.008, and so on.

Thus, the shape of the n^{th} vibrational mode is

$$u_n(x) = a_n[\cosh(\Omega_n x) - \cos(\Omega_n x)] + b_n[\sinh(\Omega_n x) - \sin(\Omega_n x)] \tag{2.21}$$

The first few three modes are plotted in Figure 2.9.

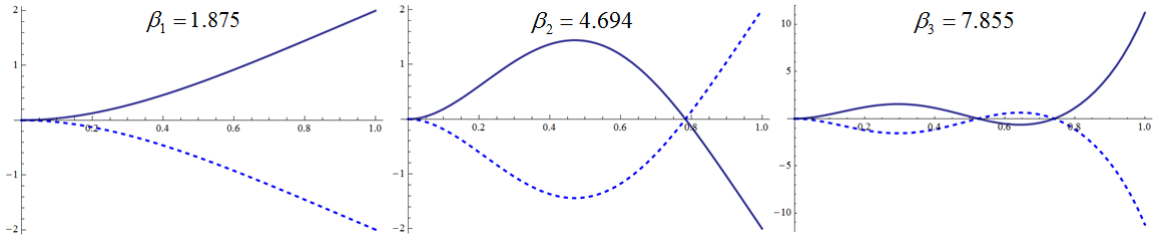

Figure 2.9: Mode shapes given by Equation 2.21

ω_1	1
ω_2	6.267
ω_3	17.68
ω_4	34.53

Figure 2.10: First few vibrational frequencies of cantilever normalized to ω_1.

Writing $\Omega_n L = \beta_n$, the allowed frequencies of oscillation are given by

$$\begin{aligned} \omega_n &= \left(\frac{EI}{\rho A}\right)^{1/2} \Omega_n^2 \\ &= \left(\frac{EI}{\rho A}\right)^{1/2} \frac{\beta_n^2}{L^2} \\ &= \left(\frac{EI}{mL^3}\right)^{1/2} \beta_n^2 \end{aligned} \tag{2.22}$$

With a beam spring constant $k = EI/L^3$ (recall $k = 3EI/L^3$ for a point load at free end of cantilever), then the frequency takes the familiar $\omega = \sqrt{k/m}$ form for a simple harmonic oscillator of mass m and spring constant k. Figure 2.11 plots the vibrational frequency of the fundamental mode, $f_1 = \omega_1/2\pi$, in Hz for a multiwalled nanotube resonator as a function of the nanotube length and radius. Figure 2.10 tabulates the relationship between the first few mode frequencies.

2.3 *In situ* TEM Experimentation with Carbon Nanotube Resonators

We now test the elasticity theory presented above by performing a series of fundamental *in situ* transmission electron microscopy (TEM) experiments. We use the TEM to directly observe the deflection and vibrational dynamics of the carbon nan-

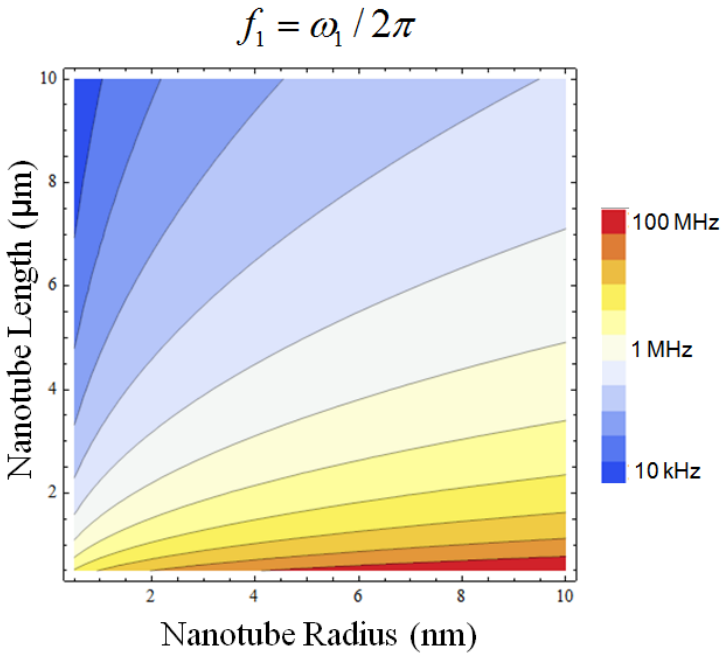

Figure 2.11: Vibrational frequency of the fundamental mode, $f_1 = \omega_1/2\pi$, as a function nanotube length and frequency.

otube NEMS devices discussed in Chapter 1. Further *in situ* TEM experiments exploring self-oscillations, parametric amplification, and non-linear behavior in carbon nanotube NEMS are given in Part III of this dissertation.

TEM uses high energy electrons (E $\approx 100 - 200$ keV), which owing to their small *de Broglie* wavelength $\lambda_e = \frac{h}{p} \approx \frac{h}{\sqrt{2mE(1+E/2mc^2)}}$, to achieve few-angstrom or, in the case of aberration-corrected TEM, sub-angstrom resolution. TEM can be used to obtain real-space images or reciprocal-space diffraction images of sufficiently thin samples ($<$ 100 nm). We will not discuss the theory or operation of TEM in this work. For a deeper discussion of TEM, the reader is referred to the texts by *Fultz and Howe* [161] or by *Williams and Carter* [160].

In situ TEM experiments are performed in a commercial JEOL 2010 TEM (shown in Figure 2.12) using a commercial nanopositioning stage (HS100 STM-Holder^{TM} with SU100 Control System, Nanofactory Instruments AB, Sweden) or a custom-built transport stage (shown in Figure 2.13). The nanopositioning stage is shown in Figure A.1. Both stages have feedthroughs that facilitate electron transport measurements. Currents and voltages were controlled and recorded using a Keithley 2410 and code written in LabVIEW.

Transport studies using the nanopositioning stage are essentially limited to two-terminal measurements. A small metallic wire can be mounted onto the stage and

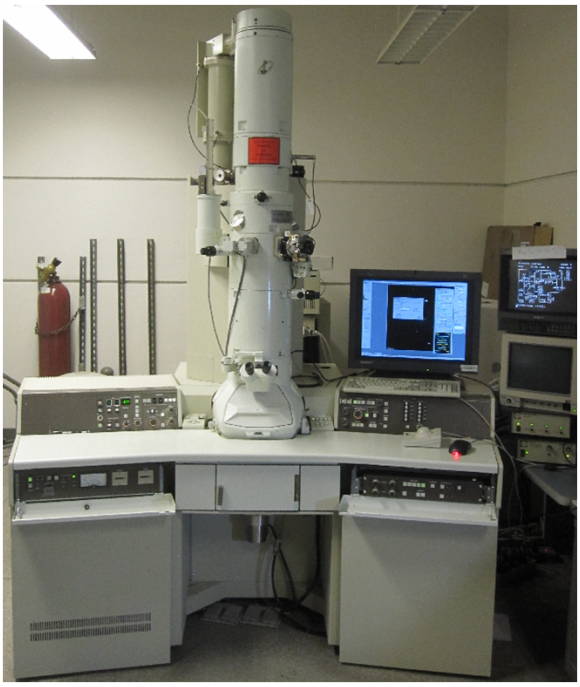

Figure 2.12: Zettl Group TEM: JEOL 2010

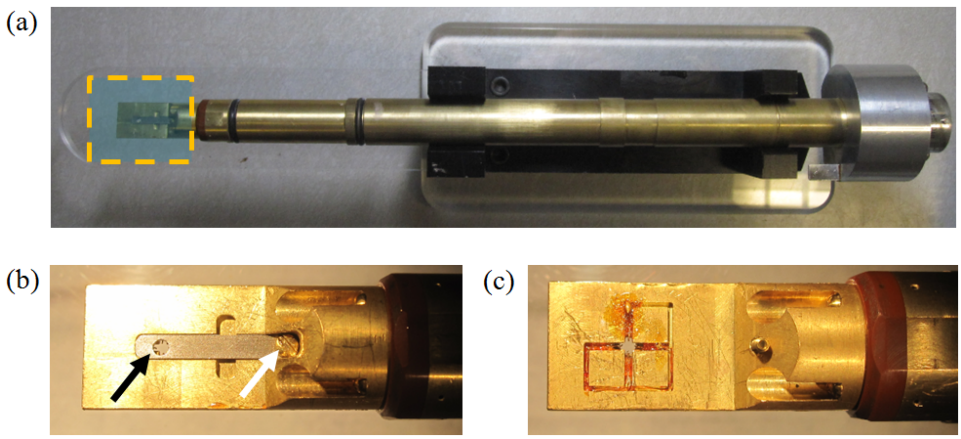

Figure 2.13: TEM Transport Stage. (a) Stage (b) Side showing small beam-path aperture with contact wires (black arrow) and screw (white arrow) for clamping down device. (c) Backside showing wiring of holder.

assumes the role of the stationary counter electrode. A "bottom-up" carbon nanotube device (described in §1.1.1) is mounted to the mobile, piezo-driven part of the stage. Positioning of the nanotube can be controlled in all three physical dimensions with sub-angstrom precision. The nanopositioning stage allows one to look at geometric parameters very easily, but the counter-electrode shape and z-height is uncertain. The Zettl group has a rich tradition with *in situ* TEM measurements of nanomaterials: The Zettl group developed the first nanopositioning stage [164], and has performed many fundamental studies as in, for example, low-friction CNT bearings [165], buckling and kinking force measurements with CNTs [118], high temperature stability of graphene [163], and exploring novel structures such as graphene sandwiches [162].

The transport stage allows one to use up to eight electrodes, and was designed for chip-based devices with the electrodes geometries shown in Figure 1.6. The stage allows for more elaborate measurements, such as exploring the effect of electrostatic gating, and the planar nature of the chip devices results in well-defined (in both shape and position) electrode structures. The electrodes pads (1.6) of the chip are placed on top of the pogo pins of the stage to establish an electrical connection. Similar techniques have been used in previous work to explore fundamental properties of carbon nanotubes [142, 166] and novel nanotube-based archival memory [167].

We now discuss nanoelectromechanical experiments with carbon nanotubes.

2.4 Static Deformation of Carbon Nanotubes

The electrostatic force on the nanotube $F_E(x) = \frac{1}{2}\frac{dC(x)}{dx}V^2$ is predicted to be quadratic in the voltage, where $C(x)$ is the capacitance of the nanotube-counter electrode geometry and x is the nanotube tip deflection. In our experiments, the electrical voltage is applied between the nanotube and a counter electrode (metal wire in nanopositioning stage, lithographically defined electrode in transport stage.) The nanotube deflection, Δx, is linear under an applied *lateral* load (see section 2.1.1), and thus has the form

$$\Delta x = \frac{1}{k(V)}\frac{1}{2}\frac{dC}{dx}V^2$$

where $k(V)$ will be approximately constant, independent of voltage V. Loads *parallel* to the nanotube axis add tension or compression to the nanotube [15, 35], which changes its effective spring constant (in this case, $k(V)$ *will* have voltage dependence) and generates non-linearities in the predicted deflection behavior. To first order in V, $\frac{1}{k(V)} \approx a_0 + a_1 V$ and the deflection becomes

$$\Delta x \approx \frac{1}{2}\frac{dC}{dx}(a_0 V^2 + a_1 V^3)$$

Thus, in the presence of parallel loads, the deflection-voltage behavior at sufficiently large voltages is expected to deviate from pure V^2 behavior.

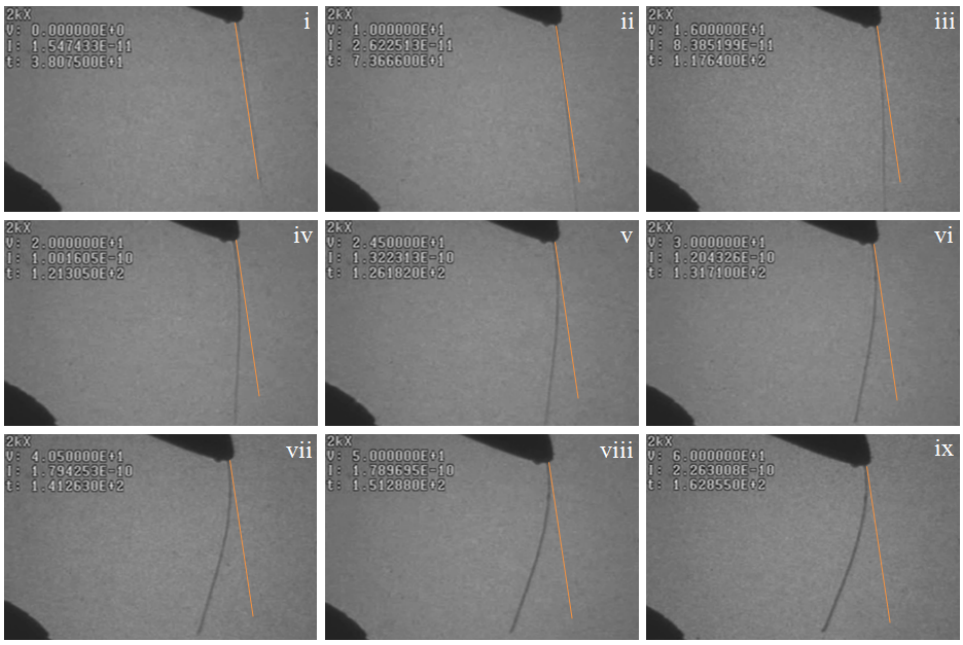

Figure 2.14: Electrostatic actuation of CNT Beam taken in TEM. Sequence (i-ix) shows beam bending under an increasing applied voltage. The nanotube is approximately 5 μm in length.

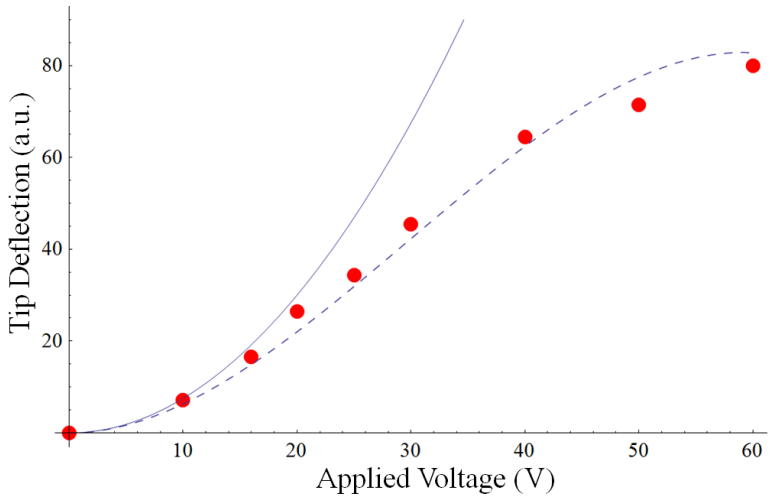

Figure 2.15: Plots of electrostatic actuation of CNT Beam taken in TEM from Fig. 2.14, a $\Delta x = cV^2$ fit (solid blue), and a $\Delta x = c_0V^2 + c_1V^3$ (dashed blue) are shown. The deflection data follows the $\Delta x = c_0V^2 + c_1V^3$ curve for larger voltages.

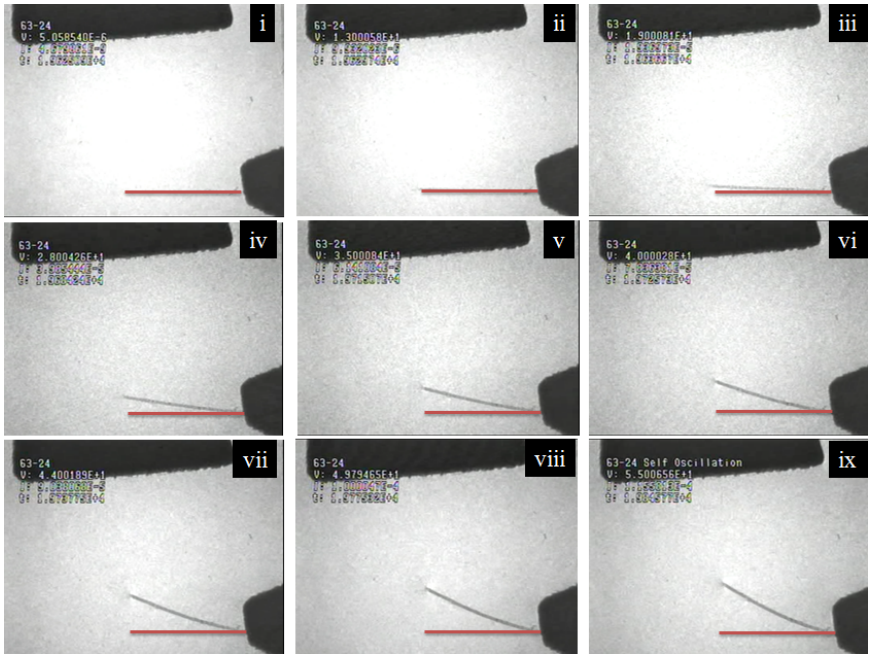

Figure 2.16: Electrostatic actuation of CNT Beam taken in TEM. Sequence (i-ix) shows beam bending under an applied voltage. The nanotube is approximately 4 μm in length.

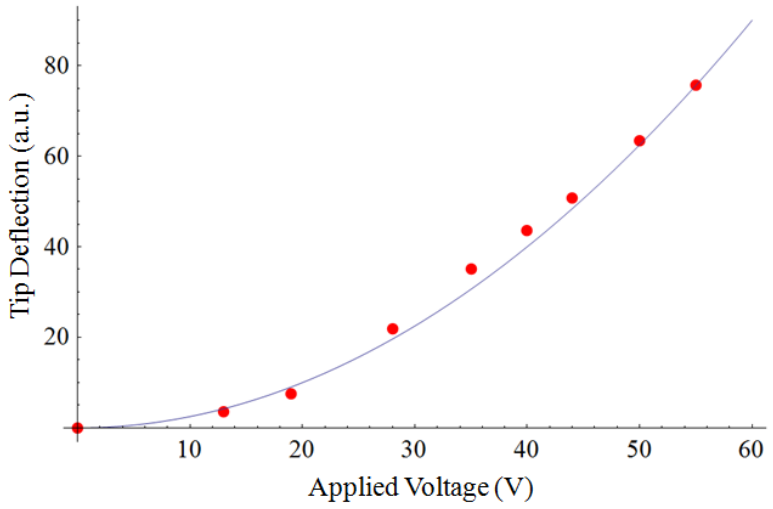

Figure 2.17: Plot of Electrostatic actuation of CNT Beam taken in TEM from Fig. 2.16. The deflection has a clear quadratic voltage dependence.

Fig. 2.14 shows a sequence of TEM images of a carbon nanotube device as the applied voltage is increased. The position of the nanotube is such that lateral and parallel electrostatic forces are acting on the nanotube. Fig. 2.15 shows a plot of the nanotube tip deflection (in arbitrary units) as a function of the applied voltage, along with a $\Delta x = cV^2$ fit (solid blue) and a $\Delta x = c_0V^2 + c_1V^3$ (dashed blue). The deflection follows the quadratic curve for small voltages (< 20 V), but then deviates from this behavior and follows the $\Delta x = c_0V^2 + c_1V^3$ curve nicely, in agreement with the above discussion.

Figure 2.16 shows a similar TEM image sequence of a lithographically fabricated nanotube device being bent electrostatically. The device's well-defined electrode structure ensures that the electrostatic forces are almost purely lateral. Figure 2.17 shows the corresponding deflection vs. voltage data, along with a fit quadratic in voltage. The deflection is quadratic up the highest applied voltage (nearly 60 V). This result highlights the experimental control one can have with lithographically defined carbon nanotube NEMS devices.

2.5 Vibrational Dynamics of Driven Carbon Nanotube NEMS

We now explore some basic properties of carbon nanotube resonators under a applied AC voltage. The AC voltage can be applied directly to the nanotube and has the form $V(t) = V_0 \cos(\omega t + \phi)$. The force acting on the tube in the TEM can originate from charge-charge (capacitive) interactions, which will be of the form

$$F_C(x,t) = \frac{1}{2}\frac{dC}{dx}V(t)^2$$

or from current-magnetic field (Lorentz) interactions, which have the form

$$F_L(t) = I(t)LB$$

where $I(t) \propto V(t)$ is the current in the nanotube induced by the applied voltage, L is the nanotube length, and B is the magnetic field due to the objective lens of the TEM (~ 1 Tesla).

In the limit of high quality factor ($Q >> 1$), the nanotube's amplitude-frequency response can be approximated by that of a driven-damped simple harmonic oscillator [21]. Thus, our nanotube devices, whose quality factors are $Q \sim 500$, will possess a Lorentzian-type response,

$$A(\omega) = \frac{F_0}{k}\frac{\omega_n^2}{\sqrt{(\omega_n^2 - \omega^2)^2 + (\omega\omega_n/Q)^2}},$$

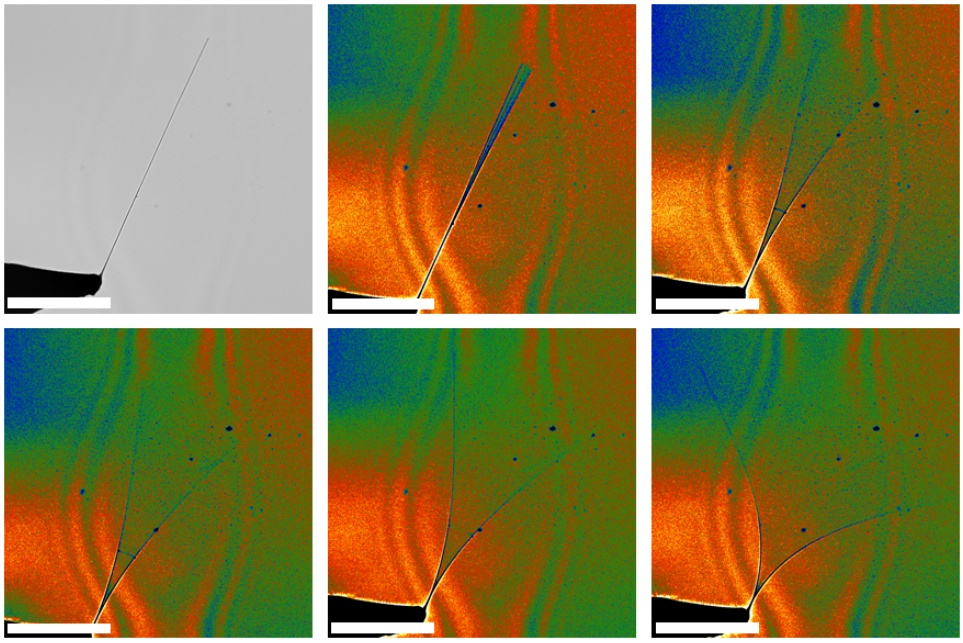

Figure 2.18: TEM of nanotube driven into oscillation near resonance. The driving force frequency is increased from below resonance (upper left) up to resonance (lower right). (Scale bar 2μm)

and resonate near their natural resonance frequencies, ω_n (given by 2.22). In the absence of an additional DC voltage, capacitive forces, because of their V^2-dependence, will drive resonance at $\omega_n/2$, while Lorentzian forces will drive at resonance ω_n.

The amplitude of a carbon nanotube resonator near resonance can be observed directly with TEM. Figure 2.18 shows a sequence of TEM images of a nanotube device while frequency of the applied voltage is swept near resonance. Beginning off resonance (upper-left, gray scale image), the frequency is increased and the amplitude also increases until it reaches a maximum value at resonance (lower-right). Some of the images have color-contrast to make the vibrational envelope easier to visualize (the hour-glass feature in the image background is due to oil deposits on the TEM CCD camera.) As can be seen from these images, rather large amplitudes can be achieved with carbon nanotube resonators. TEM is also useful for observing higher vibrational modes. The first two flexural modes corresponding to ω_1 and ω_2 are shown in Figure 2.19. These mode shapes are in excellent agreement with the classical elastic beam theory presented earlier, as shown in Figure 2.19.

In summary, we have seen that the static and dynamic behavior of cantilevered carbon nanotube mechanical resonators can be described accurately by the physics of classical electrodynamics and elastic continuum mechanics. The basic results that have been reported in this chapter will play an important role later in our discussion

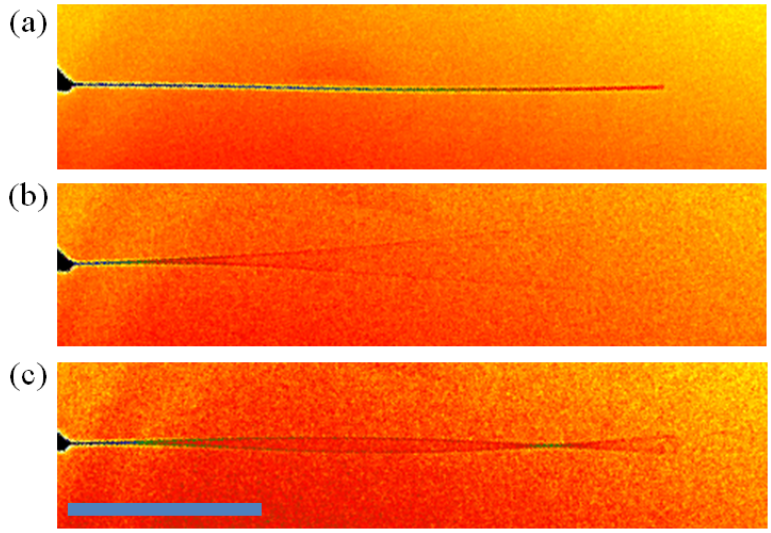

Figure 2.19: Transmission Electron Microscopy (TEM) Profiles of Driven CNT Resonators. (a) Non-driven tube. (b) Driven near ω_1. (c) Driven near ω_2. (Scale bar $2\mu m$)

of parametric amplification, self-oscillations, and non-linear behavior of our carbon nanotube NEMS devices.

Chapter 3

Field Emission from Carbon Nanotube Electrodes

Electron field emission occurs in metals when a sufficiently high electric field near the surface allows electrons to "tunnel" through metal's work function barrier. Field emission of electrons is a purely quantum mechanical phenomenon. Sharp metallic objects with a high aspect-ratio and a small radius of curvature, such as carbon nanotubes (length-to-diameter ratio as high as 132,000,000:1, and radii as small as 5 Å) can have very high electric fields at their surface, and can exhibit field emission at voltages less than 100 V. As we'll explore in Part III of this dissertation, field emission current can couple strongly to the mechanical motion of carbon nanotube resonators producing a novel transduction mechanism and generating novel quantum-electromechanical phenomenon. Therefore, a thorough understanding of the field emission process is useful for those interested in studying this particular class of carbon nanotube based NEMS.

In this chapter, we review the theory of field emission and explore the specifics of the effect in carbon nanotubes through analytical and finite-element methods. Furthermore, we demonstrate field emission experimentally with single carbon nanotubes using both "top-down" and "bottom-up" devices (see Chapter 1.) and obtain current densities as high as $\mu A/nm^2$. Our demonstration of field emission using "top-down" (*i.e.* fabricated lithographically) devices is the first such demonstration with planar devices, and paves the way for applications requiring chip-based, stand-alone field-emitting nanotube devices, such as the nanotube radio [35] and mass spectrometer [28]. We also report field emission current quantization in single carbon nanotube field emitters, and present a model that attributes the observed step-like current behavior to discrete charge states of the nanotube.

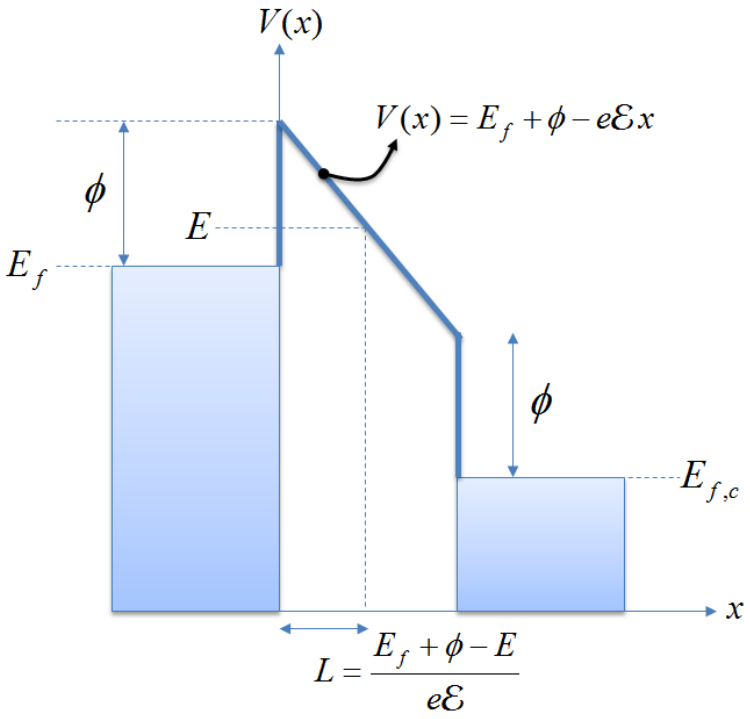

Figure 3.1: Fowler Nordheim Energy Diagram

3.1 Introduction to Field Emission of Electrons

Field emission occurs when electrons quantum mechanically "tunnel" through the potential barrier near an object's surface into a nearby vacuum [36, 37]. Field emission differs from other electron emission mechanisms, such as photoemission and thermionic emission, where electrons are excited over the energy barrier of the surface. Also, as we will see later, the field emission tunneling current is greatly enhanced in one-dimensional structures, such as nanotubes, because of higher local electric fields found at their tips. We will now give a derivation of the Fowler-Nordheim equation, which predicts the field emission current as a function of the electric field. For a more thorough discussion of the Fowler-Nordheim theory, the reader is referred to the text by Gomer [36] and the review by Jensen *et al.* [143].

The current density due to electrons traveling in one-dimension (the x direction, say) with velocity v_x is $J = nev_x$, where e is the electron charge and n is the electron number density. The number density in the one-dimensional tunneling problem is equal to the product of the number of electronic states with wavevector k_x (the $\hat{k}_x$ direction is assumed to be normal to the metal surface), given by the Fermi-Dirac distribution $f(k_x)$, and the tunneling probability $T(k_x)$. Therefore, the total tunneling current is given by integrating over k_x space,

$$J = \frac{q}{2\pi}\int_0^\infty \frac{\hbar k_x}{m^*} T(k_x) f(k_x) dk_x \tag{3.1}$$

where we have used the quantum result for the velocity $v_x = \frac{\hbar k_x}{m^*}$. Using the quantum relation $E_x(k_x) = \frac{\hbar^2 k_x^2}{2m^*}$ (and, thus, $dE_x = \frac{\hbar^2 k_x}{m} dk_x$) and dropping the x subscript, we have

$$J = \frac{q}{2\pi\hbar}\int_0^\infty T(E) f(E) dE \tag{3.2}$$

The distribution $f(E)$ is obtained by integrating out wavevectors for electrons traveling along the surface,

$$\begin{aligned} f(E) &= \frac{1}{2\pi}\int \frac{dk_y dk_z}{1+\exp[\beta(\mu - E(\vec{k}))]} \\ &= \frac{m^*}{\pi\beta\hbar^2}\ln[1+\exp[\beta(\mu - E)] \end{aligned} \tag{3.3}$$

In the low temperature limit, $1/\beta = k_b T << E_f$, Eq. 3.3 becomes

$$f(E) = \frac{m^*}{\pi\hbar^2}(E_f - E) \tag{3.4}$$

where E_f is the fermi level of the emitting metal. Figure 3.1 shows an energy diagram for the field emission tunneling process; an electron with energy E "sees" a triangular barrier of width $\frac{E_f+\phi-E}{e\mathcal{E}}$ formed by the work function ϕ and the electric potential $\mathcal{E}x$. In our calculation, we assume that the emitter and counter electrodes have the same work function, and the Fermi levels are given by E_f and $E_{f,c}$, respectively.

The tunneling transmission probability is given by the Wentzel-Kramers-Brillouin (WKB) approximation (see, for example, Ref. [168]), $T(E) = \exp(-\frac{2}{\hbar}\int_0^L p(x)dx)$, where L is the "turning point" on the field side. Referring to Figure 3.1, $L = \frac{E_f+\phi-E}{e\mathcal{E}}$, and thus

$$\begin{aligned} T(E) &= \exp\left(-\frac{2}{\hbar}\int_0^L \sqrt{2m^*(V(x)-E)}dx\right) \\ &= \exp\left(-\frac{2}{\hbar}\int_0^L \sqrt{2m^*(E_f+\phi-e\mathcal{E}x-E)}dx\right) \\ &= \exp\left(\frac{4\sqrt{2m^*}}{3\hbar e\mathcal{E}}(E_f+\phi-e\mathcal{E}x-E)^{3/2}\Big|_0^L\right) \\ &= \exp\left(-\frac{4\sqrt{2m^*}}{3\hbar e\mathcal{E}}(E_f+\phi-E)^{3/2}\right) \end{aligned} \tag{3.5}$$

We Taylor expand the exponent in Eq.3.5 around the Fermi energy, E_f, and obtain

$$T(E) \approx \exp\left(-\frac{4\sqrt{2m^*}}{3\hbar e\mathcal{E}}(\phi^{3/2} - \frac{3}{2}\phi^{1/2}(E - E_f))\right)$$

The current density, Eq.3.2, becomes

$$J = \frac{em^*}{2\pi^2\hbar^3}\exp\left(-\frac{4\sqrt{2m^*}}{3\hbar e\mathcal{E}}\phi^{3/2}\right)\int_{E_{f,c}}^{E_f}(E_f - E)\exp\left(\frac{2\sqrt{2m^*}\phi^{1/2}}{\hbar e\mathcal{E}}(E - E_f)\right)dE$$

Using the formula $\int xe^{ax}dx = \frac{1}{a^2}e^{ax}(ax - 1)$, we have

$$\begin{aligned} J &= -\frac{em^*}{2\pi^2\hbar^3}\exp\left(-\frac{4\sqrt{2m^*}}{3\hbar e\mathcal{E}}\phi^{3/2}\right)\frac{\hbar^2e^2\mathcal{E}^2}{8m^*\phi}\exp\left(\frac{2\sqrt{2m^*}\phi^{1/2}}{\hbar e\mathcal{E}}(E - E_f)\right) \\ &\quad \times\left(\frac{2\sqrt{2m^*}\phi^{1/2}}{\hbar e\mathcal{E}}(E - E_f) - 1\right)\Big|_{E_{f,c}}^{E_f} \end{aligned}$$

In the limit $E_f \gg E_{f,c}$, which holds when large potentials are applied between the emitter and the counter electrodes, the field emission tunneling current density becomes

$$J = \frac{e^3\mathcal{E}^2}{16\pi^2\hbar\phi}\exp\left(-\frac{4\sqrt{2m^*}\phi^{3/2}}{3\hbar e\mathcal{E}}\right) \tag{3.6}$$

This is the celebrated Fowler-Nordheim equation for field-emitting electron current. A more complete derivation that includes image charge effects and other corrections can be found in [36, 143]. These more complete derivations, however, leave the general dependence on the field $\mathcal{E}$ unchanged.

In general, one defines the electric field in terms of the experimentally controlled voltage, V, and the anode-cathode separation distance, L, as $\mathcal{E} = V/L$. In this derivation we have assumed that the anode-cathode configuration is one-dimensional, like a parallel plate capacitor. However, for curved anodes, such as carbon nanotubes tips or graphene edges, the local field can be much greater than $\mathcal{E} = V/L$ and is written as $\mathcal{E}_{local} = \beta\mathcal{E} = \beta V/L$ where β is known as the field enhancement factor. Then, the Fowler-Nordheim equation is often written as

$$J = a\beta^2\mathcal{E}^2\exp\left(-\frac{b}{\beta\mathcal{E}}\right) \tag{3.7}$$

3.2 Field Emission from Carbon Nanotubes: Electrostatics Modeling

In systems with high curvature, such as carbon nanotubes, β can be as high as 10^3. Thus, for a nanotube biased to 100 V and with a anode-cathode separation of 1

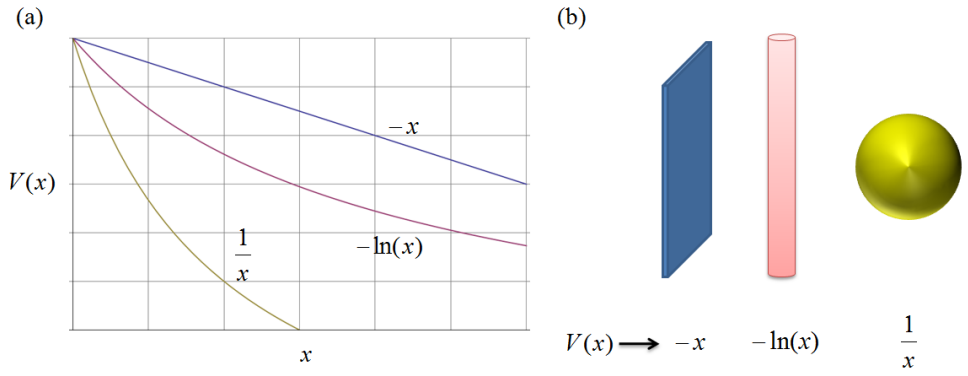

Figure 3.2: Field Enhancement with Different Geometries

μm, the electric field at the tip can easily be 10^9 V$\cdot$ cm^{-1}. These high fields require that the nanotube field emission experiments be carried out in high vacuum ($< 10^{-6}$ torr).

In terms of nanotube radius, r, and length, l, the field enhancement factor for the nanotube is given approximately by [50]:

$$\beta = 3.5 + \frac{l}{r} \tag{3.8}$$

Thus, for typical nanotube geometries ($r = 10^{-9}$ m and $l = 10^{-6}$ m), $\beta \approx 10^3$, as stated earlier.

Figure 3.2 illustrates how, according to elementary electrostatics, the local field and energy differs with curved geometries. The potential energy $V(x)$ drops off faster from a surface with a higher local field. Thus, a higher local field effectively decreases the barrier width for tunneling which then leads to a larger field emission current.

Finite-element analysis (FEA) simulations (using the commercial FEA solver COMSOL Multiphysics) are useful for solving the electrostatic Poisson equation, $\nabla^2 V(\overrightarrow{r}) = \frac{\rho}{\epsilon_0}$, for carbon nanotube device geometries used in actual experiments. From these simulations, one can gain valuable insight into the behavior of the electric fields near the nanotube apex as a function of the device's geometric parameters. One can also use the simulations to calculate surface charge densities, electrical potentials, and the capacitance of the exact device geometry, which is a task not easily performed using purely analytical methods. An extremely fine mesh (densest value permitted by computer memory capacity) was used near the tip of the CNT (Figure 3.3 (d).) in all calculations in order to improve their accuracy.

Figure 3.3 shows the results of FEA simulations for the electrical potential near a 10 nm diameter, 1 μm long nanotube. The tube is grounded with respect to a nearby counter-electrode (a semi-infinite plane), which is held at 100 V. The nanotube-counter-electrode distance is 100 nm in Figure 3.3 (a) and 1 μm in Figure 3.3 (b), and

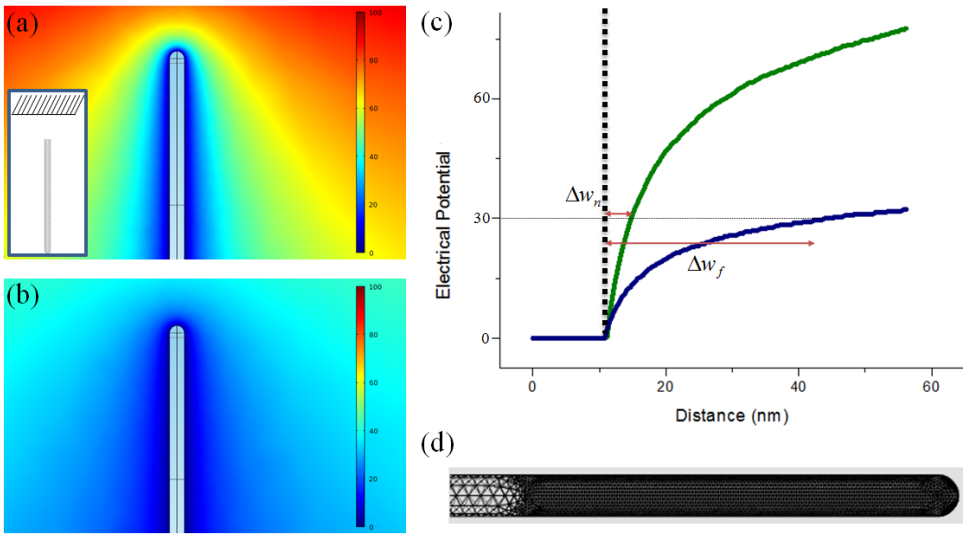

Figure 3.3: Finite-element Modeling for Straight Nanotube. 100 V bias for all. (a) 100 nm anode-cathode distance. Inset shows configuration for simulations. (b) 1 μm anode-cathode distance. (c) Electrical potential profiles from (a) and (b). (d) Meshing on tube used for simulations. Extremely fine mesh is used from tip and 100 nm away from tip.

has a clear effect on the corresponding electrical potential, dropping off much more quickly for the tube positioned 100 nm away from the counter-electrode. The gradient of the potential (AKA the electric field) and the width of the tunneling barrier for electrons that would exist at the nanotube tip can be seen in Figure 3.3 (c). For example, the width at 30 V for the 100 nm case is $\Delta w_n \approx 9$ nm and $\Delta w_f \approx 43$ nm for the 1 μm case. The disparity in the barrier widths at 60 V is even greater.

This simulation result illustrates the electric field's strong dependence on the position of the nanotube. In general, for a fixed electrical potential, the electric field at the tip of a nanotube electrode and the resulting tunneling current will increase as it is brought closer to the counter-electrode. Thus, a strong coupling will exist between the field emission current and the mechanical motion of the nanotube, and suggests a novel mechanical motion transduction mechanism. This novel transduction mechanism in carbon nanotube NEMS has been explored previously by the Zettl group's Kenny Jensen [35, 28], and further experimental work related to this effect will be discussed in Part III.

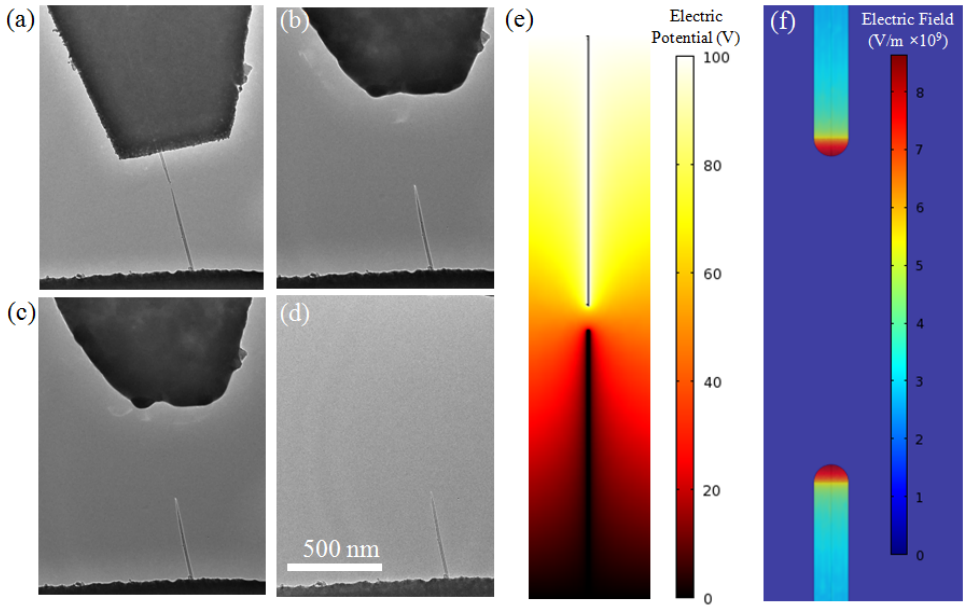

Figure 3.4: Field emission sequence of CNT burning nanotube and counter electrode. (a)-(d) sequence. (e) Electrical potential of two tubes at 100 V, (f) Electric field of same tubes. Simulations are 10 nm tube, 1μm apart, 100 nm apart.

3.3 Field Emission from Carbon Nanotubes: *in situ* Experiments

We now report TEM observations of chip-based carbon nanotube field emission devices. The emitter itself can be pre-fabricated or it can be produced *in situ* by severing a CNT beam via Joule heating. A freshly severed CNT beam is shown in Figure 3.4 (a). We then bias the nanotube into field emission (data shown in Figure 3.5). The field near the nanotube emitter is reduced when it is close to another sharp object, as can be seen in the FEA simulation in Figure 3.4 (e) and (f), and the current is focused onto this sharp object (in this case another nanotube.) The 100 eV field emission electrons degrade the nanotube counter-electrode and eventually destroy it completely (Figure 3.4 (b)), and the current increases as expected (blue section of Figure 3.5.) The intensity of the 100 eV electrons continues, and the gold counter-electrode begins to degrade, likely evaporating due to the energy transfer of emitter electron beam. The field decrease that occurs once the gold electrode evaporates can also be seen from the decrease in the TEM image intensity near the nanotube tip.

The electronic transport behavior of the chip-based carbon nanotube emitter agrees well with the Fowler-Nordheim equation. Figure 3.6 shows a current-voltage

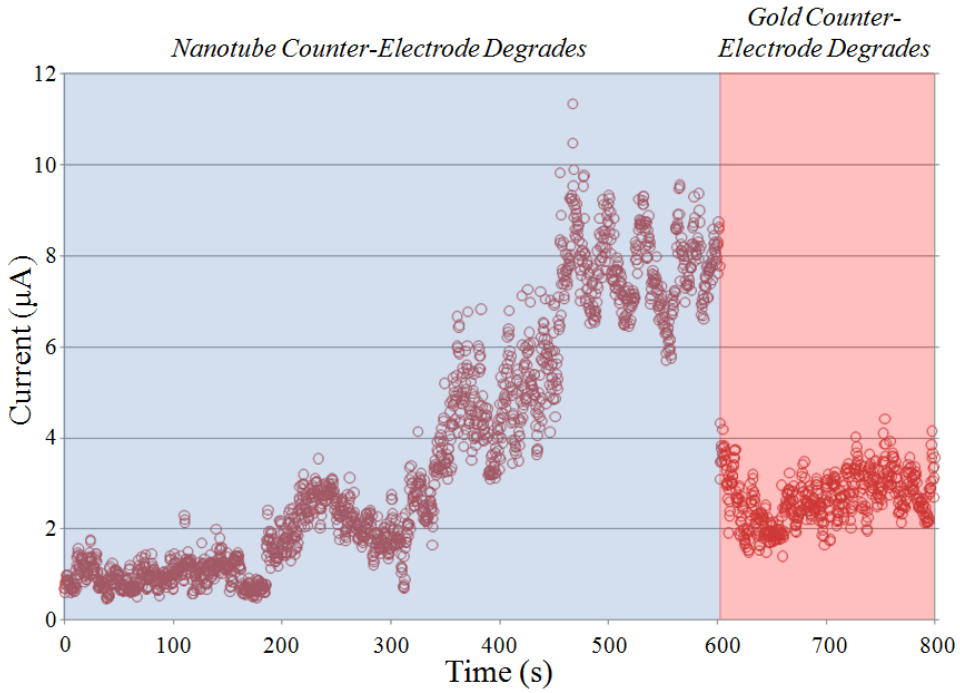

Figure 3.5: Field Emission Data During CNT Counter-electrode Failure. Corresponds to TEM sequence in Figure 3.4 (a)-(d). The initial slow increase in current at constant voltage is due to the degradation of the CNT counter-electrode, which results in a higher field. The sudden current drop corresponds to the gold counter-electrode melting away reducing the effective field at the nanotube tip.

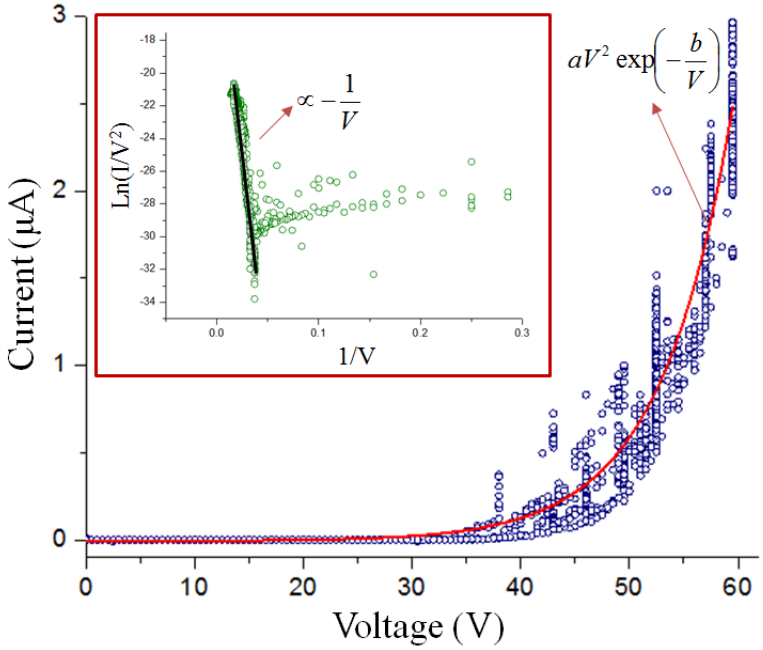

Figure 3.6: Field emission data from carbon nanotube field emitter. I-V curve and inset shows $\ln\left(\frac{I}{V^2}\right)$ vs. $\frac{1}{V}$.

curve during field emission along with a fit of the form

$$I = aV^2 \exp\left(-\frac{b}{V}\right)$$

According to the Fowler-Nordheim theory, a plot of $\ln(I/V^2)$ vs. $1/V$ should produce a straight line with negative slope, a signature of true field-emission. The inset of Figure 3.6 shows such a plot, indicating that the nanotube device is indeed field emitting. The current noise that occurs at a fixed bias is apparent in Figure 3.6. We now report and develop a model to account for step-like current behavior that can be observed in this noise.

3.4 Observation of Room Temperature Single Electron Effects: Current Switching Behavior in CNT Field Emitters

Figure 3.7 (a) shows a current-voltage curve for a single multi-walled carbon nanotube (length $\sim$ 2 μm, diameter $\sim$ 10 nm) field emitter. Figure 3.7 (b) shows a plot

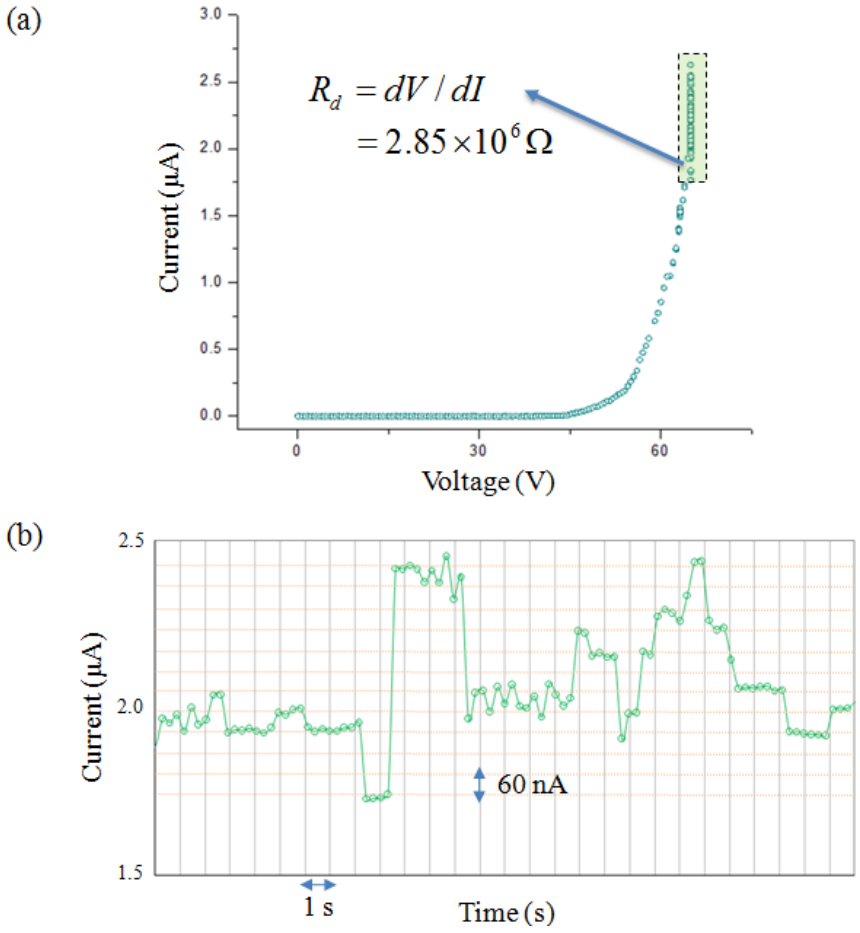

Figure 3.7: Current steps data. (a) I-V curve corresponding to device with current steps. (b) Time dependence of current for data shown in boxed region in (a). The tube is held at 66 V during this time. The current step height is ≈ 60 nA.

of the fixed-bias current time-dependence corresponding to the "noise" (green highlighted region) in the I-V curve of Figure 3.7 (a). Interestingly, while at this fixed bias (∼66 V) the field emission current exhibits *step-like* behavior: the measured current occurs only at fixed, discrete levels. The discrete levels have been highlighted by horizontal lines in Figure 3.7 (b), and are separated by approximately 60 nA of current. The current value can switch by a single (60 nA) step or by as many as 10 steps. Data acquisition rates limited temporal resolution to about 100 ms, so switching events faster than this could not be observed. The measured time between switching events could be as little as 100 ms and as high as 10 s. The step-like switching behavior has been observed reproducibly in dozens of devices and can apparently persist for an indefinite amount of time.

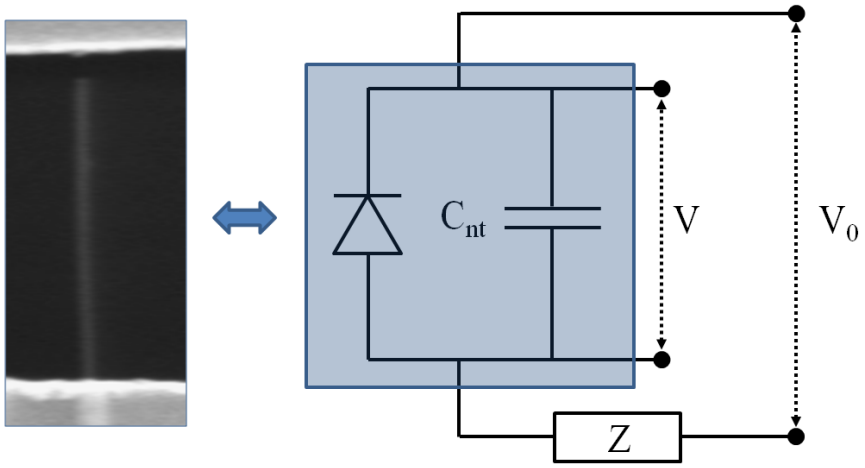

Figure 3.8: Equivalent Circuit for CNT Field Emitter. The nanotube is both a Fowler-Nordheim diode and a capacitor. Fluctuations of the number of electrons on the nanotube lead to large voltage changes, $\Delta V = \Delta Q/C_{nt}$ across the diode due to the small capacitance of the nanotube. V_0 is the applied voltage and V is the voltage across the nanotube. Z is the equivalent impedance of the rest of the circuit.

Similar step-like, switching behavior has been previously reported [54, 55, 56] and attributed to individual linear atomic carbon chains protruding from the CNT tip and chemisorption/desorption and unraveling events on these chains [54], or interactions between neighboring field emission sites [55]. These models were speculative and qualitative in nature, and were not used to generate quantitative predictions to describe the step-like current behavior. Furthermore, the model described in Ref. [55] relies on the presence of several closely spaced, field-emitting nanotubes; since our devices are composed of single nanotubes, this model is fundamentally inconsistent with our experimental configuration. In the remainder of this chapter, we'll describe a simple model that gives *quantitatively* accurate predictions for the observed step-like current behavior observed in carbon nanotube field emission devices.

3.4.1 A Capacitor-Diode Model

The discrete current steps observed in our carbon nanotube field emitters can be understood by modeling the carbon nanotube as a capacitor, whose capacitance is given by the nanotube/counter-electrode geometry, in parallel with a diode (with a Fowler-Nordheim I-V characteristic). This is equivalent to modeling the nanotube system as a tunnel junction of finite capacitance and resistance. Figure 3.8 shows a nanotube device and the corresponding equivalent electronic circuit, where C_{nt} is the nanotube capacitance, V_0 is the bias applied by an external supply, V is the voltage

across the nanotube, and Z represents the lumped impedance of the remainder of the circuit.

Since the capacitor is in parallel with the diode in the circuit, the current through the diode gives a direct measure of the charge on the capacitor through the relation $Q(t) = C_{nt}R_dI(t)$, where R_d is the differential resistance, $R_d = \frac{dV}{dI}$, of the field emitter diode. Thus, charge fluctuations on the nanotube capacitor will result in current fluctuations through the diode given by

$$\Delta I = \frac{\Delta Q}{C_{nt}R_d} \tag{3.9}$$

Because of discrete nature of charge, $\Delta Q = ne$, where $n = 0, 1, 2, \ldots$ and $e = 1.6 \times 10^{-19}$ Coulombs, ΔI in our system will also be discrete. Assuming $\Delta Q = e$ and with $R_d \approx 2.85 \times 10^6\ \Omega$ (from Figure 3.7), the model predicts a nanotube capacitance of $C_{nt} = 1.6 \times 10^{-19}/(2.85 \times 10^6 \cdot 60 \times 10^{-9}) \approx 10^{-18}$ F (1 aF) in order to account for the observed current quanta $\Delta I \approx 60$ nA. Thus, the capacitor-diode model gives a simple, quantitatively accurate explanation for the current steps observed in our experiments, given that the capacitance of the nanotube/counter-electrode system is on the order of 1 aF. Later, we will show that this capacitance is indeed on this order.

According to Equation 3.9, current changes through *any* capacitor-diode junction should be discrete since charge itself is discrete. For instance, a junction with capacitance $C = 10^{-12}$ F and resistance $R = 1$ kΩ will have a minimum current step separation (that due to a single electron) of $\Delta I = 1.6 \times 10^{-19}/10^{-12}10^3 = 1.6 \times 10^{-10}$ A. Currents of 100 pA are readily measurable with modern electronics. In general, however, it is quite difficult to fabricate parallel junctions composed of a capacitor and other circuit elements (*i.e.* diodes, resistors, *etc.*) while preserving a small capacitance; physical interconnects in a circuit can easily add stray capacitance many orders of magnitude larger than the intended small (*e.g.* less than 1 pF) capacitance. In practice, the best single-electron devices that can be fabricated are tunnel junctions (see Refs. [53, 59]) whose capacitance is limited by lithography (even at 50 nm resolution) to values larger than 1-10 fF. The system formed by the counter electrode and the nanotube represents the class of such tunnel junctions taken to the extreme of ultrasmall capacitance, approximately three orders of magnitude smaller than the state-of-the-art.

Even more important than fabrication challenges are the constraints placed on the system by thermal noise and fundamental physical limitations on the temporal resolution of the measurement. These constraints often complicate or preclude the observation of single electron effects at room temperature or even the lowest temperatures achievable by modern methods. These constraints can be understood by considering the energy fluctuations present in the nanotube device as given by the quantum energy uncertainty relation $\delta E = h/\delta t$ (for a similar argument to that given here see Kittel [60].) The relevant time scale for unbalanced electrons on the carbon nanotube is RC_{nt}, where R is the resistance of the nanotube device and C_{nt} the

capacitance. Thus, $\delta E = \frac{h}{\delta t} = \frac{h}{RC}$ or

$$\delta E = \left(\frac{h}{e^2}\frac{1}{R}\right) \times \left(\frac{e^2}{C}\right) \tag{3.10}$$

If energy fluctuations are on the order of the single electron charging energy, that is if $\delta E \sim \frac{e^2}{C}$, then the energy levels corresponding to discrete charge states will be smeared out. Therefore, according to Eq. 3.10, one constraint is placed on the resistance R of the nanotube device (or the capacitor-diode device):

$$R \gg \frac{h}{e^2} = R_Q$$

The device resistance must be greater than the resistance quanta, R_Q ~25.8 $k\Omega$. Also, to preserve the discreteness of the capacitor energy levels, the single-electron charging energy must be greater than the thermal energy,

$$\frac{e^2}{C} \gg k_B T$$

To observe single-electron effects at room temperature, the capacitance must be less than $C = (1.6 \times 10^{-19})^2/(1.38 \times 10^{-23} \times 300) \approx 60$ aF.

Single-electron devices similar to our nanotube capacitor-diode have been previously studied and demonstrated. Examples include the single-electron transistor (SET) [53], coulomb-controlled tunneling in a freely suspended metallic island [57], among others. A good review of single-electron devices is given in Ref. [59]. The theory of single electron field emission devices has also been explored to some extent in Ref. [58]. In the case of the SET, state-of-the-art fabrication techniques yield a device capacitance on the order of 10 fF (10^{-14} F), which require temperatures $T < 100$ mK in order to observe single-electron effects. The tunnel junction resistance of these devices is similar to ours, and easily exceeds R_Q.

3.4.2 Capacitance of a Carbon Nanotube Field-Emission Tunnel Junction

The capacitance of the carbon nanotube device can be approximated by the formula [40]

$$C_{nt} = \frac{2\pi\epsilon_0}{\ln\left(\frac{4d_0}{r}\right)} L \tag{3.11}$$

where L is the nanotube length, r is the nanotube radius, and d_0 the nanotube/counter-electrode separation distance. For a typical experiment, $L = 1\,\mu$m, $r = 5$ nm, and $d_0 = 1 - 10\,\mu$m, we have $C_{nt} = 6.1 - 8.3$ aF.

FEA simulations can also be used to calculate the capacitance of our devices. Figure 3.9 (b) shows the simulation results for the surface charge density of a nanotube.

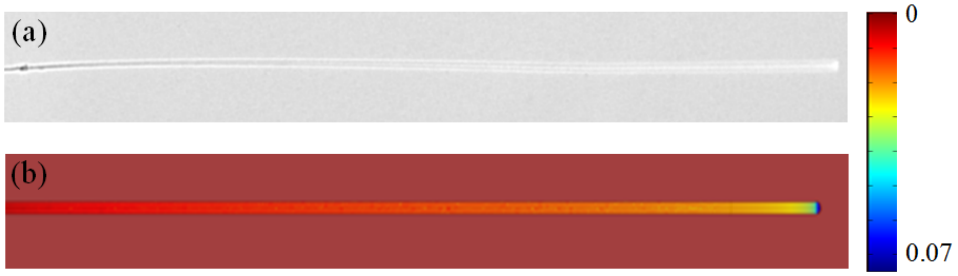

Figure 3.9: Nanotube during field emission. (a) TEM (b) FEA of 1μm tube located $d_0 = 1\mu$m from a counter electrode held at 100 V. Scale bar for surface charge density is in C/m^2.

The surface charge density agrees well with the intensity of the TEM image of the 1 μm nanotube shown in Figure 3.9 (a), which is brighter near the tip and the sides due to the increased presence of charge. Integrating the surface charge density yields a capacitance $C \approx 10$ aF, in good agreement with Eq. 3.11.

The nanotube capacitance calculations using Eq. 3.11 and by simulation agree reasonably well (within a factor 6.1) with 1 aF result obtained from the experimental data, thus supporting the validity of our model. In either case, the capacitance calculations are an order of magnitude less than the 60 aF room-temperature limit. Therefore, we would expect the charging energy levels of the nanotube to be well-defined at room temperature. We would also expect the current to demonstrate the step-like behavior observed in our experiments. Further agreement between the experimental and theoretical capacitance values can be made by using a more appropriate value for the experimental differential resistance and by including space-charge effect in the calculations. Besides the error associated with the $R_d = dV/DI$ measurement, we have also neglected the contact resistance and a 1 MΩ resistor (used to prevent electrostatic damage discharge damage to the device) present in the circuit. Since the value $R_d \approx 2.85 \times 10^6\,\Omega$ includes both of these resistance terms, the true resistance of the nanotube tunnel junction is likely closer to 1 MΩ, giving $C_{nt} = 3$ aF.

Space-charge will lead to further reductions of the theoretical capacitance calculations. The field emission current in the vacuum can be written as $I = A\rho v_e$, where ρ is the charge density, v_e is the electron velocity, and A is the cross-sectional area. We calculate v_e from energy conservation, $\frac{1}{2}m_e v_e^2 = q_e V$, where m_e is the electron mass, q_e is the electron charge, and V is the applied voltage. Then, $v_e = \sqrt{\frac{2q_eV}{m_e}}$, and $\rho = \frac{I}{Av_e} = \frac{I}{A}\sqrt{\frac{m_e}{2q_eV}}$. For typical voltages, currents, and a 10 nm $\times$ 10 nm emitter area, we have $\rho \approx 10^3$ C/m^2. Placing this charge density near the tip of the nanotube, finite-element simulations yield capacitance values on the order of $C_{nt} = 1$ aF, in accord with experiment.

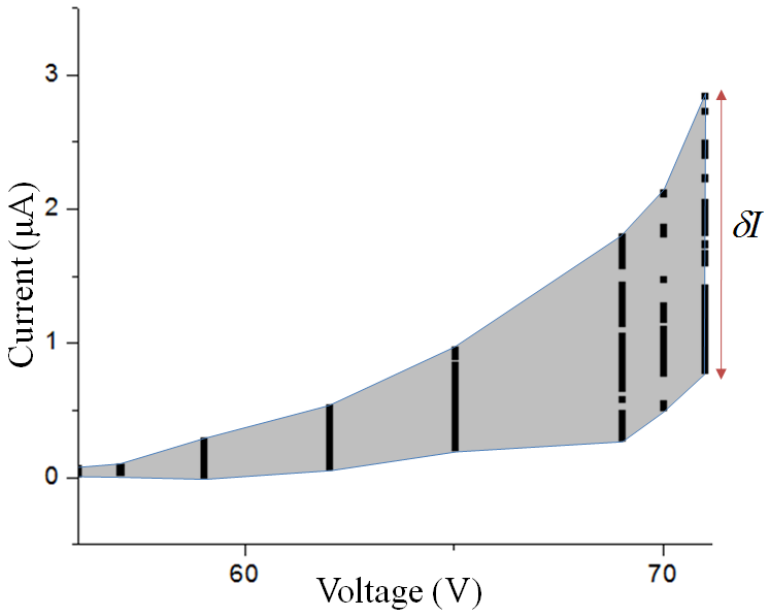

Figure 3.10: Variation in Current in Field Emitter. The variation increases with applied voltage. This is in qualitative agreement with $\Delta I = \Delta V/R_d$. For selected voltage values, we held the voltage fixed for several seconds and recorded the current.

3.4.3 Current Variations

The step-like current behavior is only observed in experiments when the tube is held at sufficiently high bias. This observation is in agreement with our model because the differential resistance of a Fowler-Nordheim diode is expected to decrease with increased voltage, and $\Delta I \propto \frac{1}{R_d}$. Similarly, as the charge state of the nanotube switches between the various levels, the model would predict a greater overall variation in current, δI, with increasing voltage, which will appear as more "noise" at a fixed bias. This current variation does indeed occur and can be seen in Fig. 3.10. As expected, range of this current variation increases with voltage. Furthermore, the observed current step spacing, ΔI, at lower voltage values is correspondingly smaller, as predicted by the model and in agreement with previous observations [56].

3.4.4 Conclusion

In conclusion, we have reported step-like behavior in the current signal of a field-emitting carbon nanotube device at room temperature. We have presented a quantitative model that accurately predicts the observed behavior in which the nanotube forms a capacitor-diode or tunnel junction. We attribute the current plateaus to single-electron charge states on the carbon nanotube capacitor, which is directly cou-

pled to and controls the current through the carbon nanotube field emission diode. We calculate a nanotube device capacitance of order aF, which agrees with the requirements for room-temperature observation of single-electron effects, our model predictions, and our experimental results.

Part III

Self-Oscillations, Parametric Amplification, and Non-linear Dynamics in Carbon Nanotube Resonators

The field emission properties (chapter 3) of carbon nanotubes can demonstrate a strong electromechanical coupling that is in addition to the conventional coupling in MEMS and NEMS, as is necessary, for example, for electromechanical actuation. The basis for this coupling is the field emission current's sensitivity to the position of the nanotube, and is unique only to systems possessing similar nanoscale dimensions. Because of the quantum nature of this coupling, we will refer to it as a quantum-electromechanical coupling. In this chapter, we'll examine how this quantum-electromechanical coupling together with non-linear behavior can lead to curious new behavior and novel applications in carbon nanotube NEMS. First, we report a self-oscillation phenomenon in carbon nanotube resonators that occurs with only a fixed DC bias. We then explore a carbon nanotube NEMS parametric amplifier that, because of the quantum-electromechanical coupling, can be utilized in a surprisingly broad range of applications. Finally, we report the *in situ* TEM observation of non-linear behavior in carbon nanotube resonators.

Chapter 4

A Self-Oscillation Phenomenon in Carbon Nanotube Mechanical Resonators

In this chapter, we'll explore a self-oscillation phenomenon that occurs in carbon nanotube NEMS devices. For a carbon nanotube device with the proper configuration (Fig. 4.1), we can observe sustained mechanical oscillations by applying only a fixed DC (i.e. not time-varying) voltage to the nanotube. We'll use an electromechanical model to calculate the voltage necessary to drive these self-oscillations and come to a deeper understanding of some of the other experimental observations. We then use the predictive power of our model to engineer and fabricate self-oscillating devices with well-defined characteristics, and suggest a few possible technological uses for these devices.

4.1 Introduction

To achieve sustained oscillations in a mechanical system, such as a mass on a spring, or an electronic system, such an LCR circuit, one must commonly supply an external, time-varying drive, such as a driving force or AC current or voltage. The dependence on an external drive exists for macroscopic electromechanical systems as well as for those at the micro- and nanoscale. Although Nanoelectromechanical systems (NEMS) based on vibrating mechanical elements have demonstrated excellent performance for many applications including chemical sensing[25, 26, 27], mass sensing[28], and high frequency signal generation[29], capturing the full potential size, power and performance benefits for these NEMS is often undermined by their functional reliance on an external drive or control. For active and passive systems, the external components may include driving forces as well as feedback circuitry that are produced by relatively large, high-power, high-frequency external electronics such as

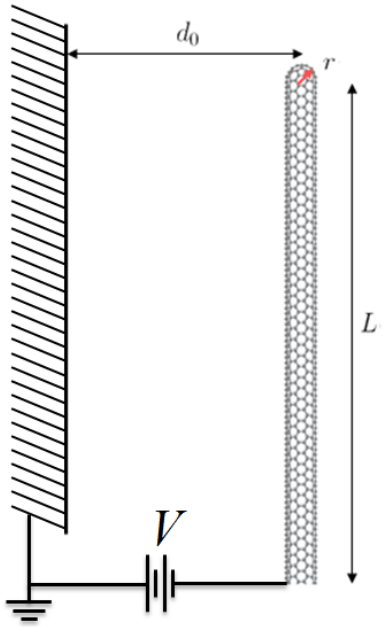

Figure 4.1: Schematic of Self-Oscillation Device. A nanotube of length L, radius r, a distance d_0 from a counter electrode is biased to potential V. Self-oscillations depend sensitively on the counter electrode position. Schematic of setup used to test self-oscillations in carbon nanotubes. A DC bias voltage is applied between the nanotube and the counter electrode causing field emission from the nanotube to the counter electrode. An ammeter is used to measure the field emission current.

signal sources[30, 31], amplifiers and integrated circuits[29]. We report the use of Transmission Electron Microscopy (TEM) to observe the controllable self-oscillations of singly-clamped, field-emitting carbon nanotubes that operate with only a single DC bias voltage. Furthermore, we formulate an electromechanical model that predicts the voltage necessary to induce oscillations solely in terms of device geometry and material properties, and we use this model to successfully fabricate, for the first time, top-down self-oscillating NEMS amenable to large-scale integration.

A number of self-oscillation approaches have been explored[29, 32, 33] in resonant NEMS devices which, to some extent, circumvent the need for bulky control electronics that commonly detriment many of the size and power benefits derived from the device's nanoscaled dimensions. Observations of self-oscillations in nanowires [34] have been reported, but a clear understanding of the underlying drive mechanism or the requisite geometry to enable reliable, self-oscillation-based NEMS devices are still in need. We here elucidate the requisite geometry for NEMS self-oscillators, and our quantitative model establishes comprehensive design parameters for scalable devices. We'll begin by describing our experimental observations in detail.

4.2 Experimental Observations

The main experimental result is the initiation of sustained flexural vibrations of the nanotube when a sufficiently high DC bias is applied between the nanotube and a nearby counter electrode. Because no time-varying external control is necessary for these vibrations, the system is said to "self-oscillate." In our experiments, we employ a singly-clamped cantilevered field-emitting carbon nanotube[35] as a prototypical oscillator element, as shown schematically in Fig. 4.1. A critical feature in achieving reliable self-oscillations is the angle between the nanotube's longitudinal axis and the counter electrode: a nanotube oriented parallel to the surface can self-oscillate while one oriented perpendicular to the surface cannot. This orientation specificity exists because the tunneling current (field emission current) must be able to couple to lateral electromechanical forces.

Transmission electron microscope (TEM) images of a multi-walled carbon nanotube devices are shown in Fig. 4.2. Fig. 4.2 (b) and (e) show "bottom-up" devices formed by attaching a MWCNT to a conducting atomic force microscope tip, and Fig. 4.2 (c) and (f) show "top-down" devices fabricated using lithography. The fabrication of these devices is discussed in Chapter 1. As the bias voltage is increased from zero the nanotube bends toward the counter electrode (Figs. 4.2 (b), (c)) and the field emission current (see section 3.1) may rise to detectable levels. Typically, several tens of nanoamperes of current will be observed around 10 Volts. The electrostatic bending is identical to the results in §2.4. Subsequent increases in the bias voltage result in an increase in the field emission current (typically between 0.1-1 μA) and flexural bending. Above a critical, device-specific bias threshold or onset voltage, V_{th}, sustained self-oscillations occur, as can be seen in Figs. 4.2 (e) and (f) where a TEM image is shown of a vibrating nanotube biased beyond V_{th} into the continuous self-oscillation mode. Due to the high frequency of the vibrations (typical resonant frequencies of devices are 1-100 MHz, as shown in Fig. 2.11) the images of the nanotube are blurred and only the oscillation envelope is observable; the red arrows in Fig. 2.11 (e) point to the edges the oscillation envelope of the nanotube.

There is strong coupling between the quantum mechanical field emission current and the observed self-oscillations in our system. In fact, if a device is reverse-biased (so that electronic tunneling is suppressed) no self-oscillations will be observed. Therefore, our device is part of a novel class of NEMS that incorporates quantum mechanical functionality, a new class we coin Q-NEMS or Quantum-Nanoelectromechanical Systems.

This quantum-electromechanical coupling manifests itself in the experimentally observed field emission current. A plot of field emission current and applied voltage over time for the device in Fig. 4.2 (b) is shown in Fig. 4.3 (c). These data illustrate an important and consistent observation in our experiments: the onset of self-oscillations is associated with a current spike at V_{th}. We'll explore the cause of these current spikes semi-quantitatively in this section and more quantitatively in section 4.4, in which we

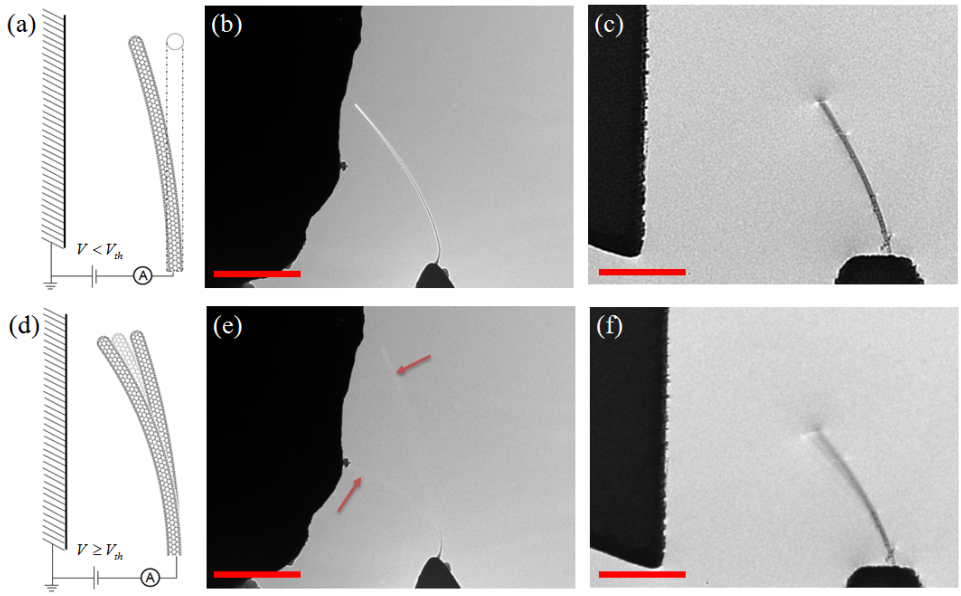

Figure 4.2: TEM of Self-Oscillation Phenomenon with two different devices. (a) Schematic and TEM ((b),(c)) of nanotube device when biased below the threshold voltage for self-oscillations, $V < V_{th}$, and (d)-(f) biased above this threshold, $V \geq V_{th}$. The nanotube is not easily visible while it is vibrating in (c); the dashed lines, which delineate the vibration amplitude, have been added for clarity. Although the nanotube appears to touch the counter electrode, it does not. The vibration plane is located behind the visible edge of the counter electrode.Scale bars are 2μm.

examine the quantum-electromechanical coupling (as governed by electronic transport and the mechanical equation of motion) of the system. We remark that the data of Fig. 4.3 (c) have been acquired using the inherently low sampling rate of the Keithley source meter used for measurements. Hence the response signal is coarse-grained and does not directly reflect the oscillatory response for $V > V_{th}$. Chapter **??** will discuss some ongoing efforts in the Zettl group to increase the temporal resolution of our measurements in order to detect the high-frequency behavior of this system.

4.3 Electromechanical Modeling

The nature of the self-oscillations can be understood qualitatively by examining the forces acting on the nanotube and the effect of these forces on the field emission current. When the nanotube is biased below V_{th}, it is attracted to the counter electrode by the electrostatic force resulting from charge accumulations on the nanotube and the counter electrode. This attractive force is balanced by the repulsive mechan-

ical restoring force of the bent nanotube cantilever. It is understandable why the tube must have the proper orientation described above, since only transverse forces will cause bending of the carbon nanotube. As is observed experimentally, vibrations begin when a burst of electrons discharges from the nanotube, which is evident from the current spikes in Fig. 4.3 (c). This rapid discharge temporarily reduces the attractive electrostatic force and, consequently, the mechanical restoring force suddenly dominates. Because of the significant resistance and capacitance of the system, there is a time delay in recharging the nanotube, and thus the nanotube is quickly pulled away from the counter electrode. Additional temporary reduction of the attractive electrostatic force will occur due to the increase in space charge near the nanotube; this space charge is a direct consequence of the field emission process and serves to screen the nanotube from the counter electrode. The step-like forcing function initiates nanotube mechanical vibrations. The rapid discharge of electrons is analogous to the plucking of a guitar string. It is *possible*, in the case of the nanotube, that the vibrations are sustained indefinitely because the cycle of rapid discharge and repulsion (i.e. the plucking) repeats itself, much like the continuous strumming of a guitar string. However, this explanation is correct only if the time-scales of the mechanical and electronic relaxation are in the correct range, which, to a certain extent, can be tuned experimentally. While this plucking explanation is possible in some systems, a more likely and general explanation for the self-oscillation phenomenon will be apparent when we examine the time-dependence of system parameters, such as resonance frequency or spring constant, and the corresponding parametric modulation in Chapter 5. In any case, the initial plucking event, whether or not is repeated, occurs because of an energetic instability and is essential to the self-oscillations observed in our system.

We now turn to a closer examination of field emission from cantilevered and mechanically flexed nanotubes. This serves to explain the origin of the current spike which initiate self-oscillations and allows us, based on geometrical device parameters alone, to predict the onset voltage for self-oscillations. Field emission occurs when electrons tunnel through the potential barrier near an object's surface into a nearby vacuum [36, 37] as described in section 3.1. The tunneling current is greatly enhanced in one-dimensional structures, such as nanotubes , because of higher local electric fields found at their tips. Fig. 4.4 (a) shows a finite-element simulation of the field of a straight nanotube near a flat, conducting electrode. The increased field at the tip, relative to the less curved nanotube sidewall or, more so, to a flat surface (see Fig. 3.2), is clearly evident. Fig. 4.4 (b) shows the field of the same nanotube bent toward the counter electrode. The field near the tip significantly increases as the distance to the counter electrode is reduced. This increased field ($\mathcal{E}$) leads to a reduced potential barrier at the tip, as shown in Fig. 4.4 (c), which in turn causes the field emission current to increase as the tube nears the counter electrode as predicted

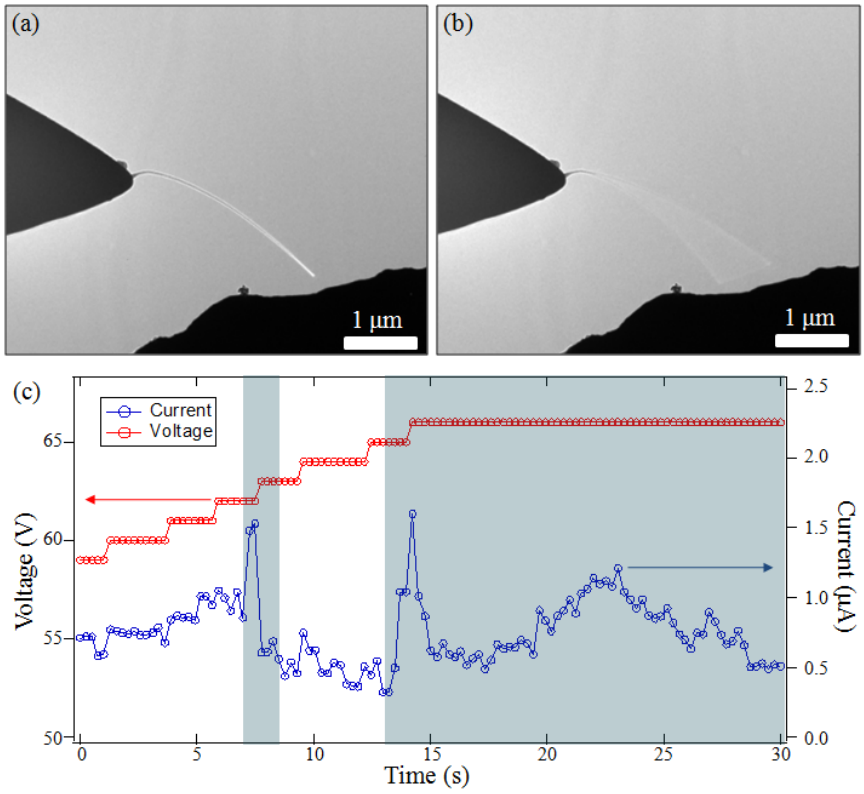

Figure 4.3: Current data showing onset spikes. (a) No self-oscillations and (b) self-oscillations. (c) Current and voltage data during experiment. The shaded part of data shows spikes and when tube is oscillating as in (b).

by the Fowler-Nordheim equation (Eq. 3.6),

$$J(\mathcal{E}) = a\beta^2\mathcal{E}^2 \exp\left(-\frac{b}{\beta\mathcal{E}}\right)$$

The current spike associated with the onset of self-oscillations is caused by the nanotube quickly moving closer to the counter electrode, and therefore being in a state where the electric field at the tip, and thus the field emission current, is much higher. This rapid movement can be quantified by analyzing in greater detail the total force acting on the nanotube. As was mentioned earlier, we'll discover that this rapid motion toward the counter electrode is due to an imbalance in the electrostatic and elastic forces acting on the nanotube.

The electrostatic forces acting on the nanotube are primarily capacitive in nature, and given by the simple expression $F(x) = \frac{1}{2}\frac{dC(x)}{dx}V^2$. Other forces, such as Van der Waals and Casimir forces can be ignored [41, 42] because the relatively large nanotube-counter electrode separation distance. Since obtaining an expression for

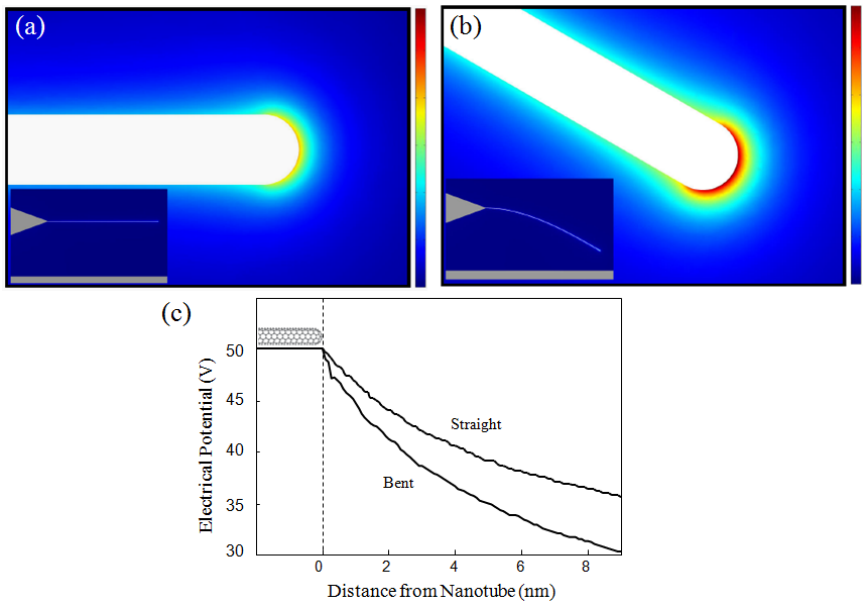

Figure 4.4: Finite Element Analysis of Nanotube Bending toward Counter Electrode. (a) Not bent. Inset lower magnification view of device., (b) Bent. Inset lower magnification view of device., (c) Voltage profile of (a) and (b). Simulations assumed a 3 μm long, 5 nm radius, carbon nanotube biased at 50 volts. The nanotube is 1.5 μm from the counter electrode in (a)

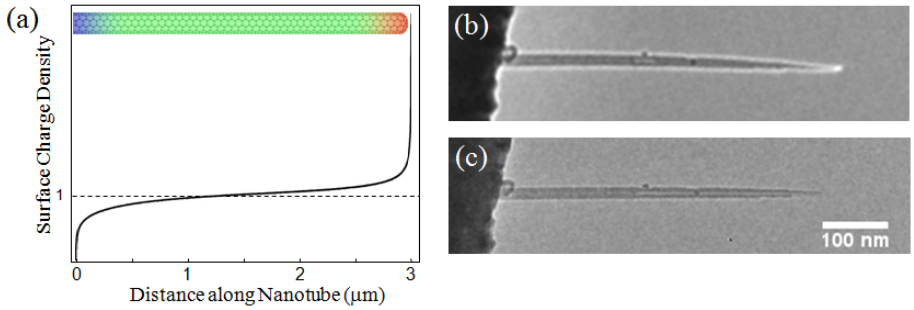

Figure 4.5: Current Density of Nanotube and TEM of Charged/Uncharged Tube. (a) FEA of surface charge density of 3μm long tube normalized to surface charge density of infinitely long cylinder. (b) Charged tube and (c) uncharged tube. Simulations assumed a 3 μm long, 5 nm radius, carbon nanotube biased at 50 volts.

the capacitance in our system is non-trivial, finite element analysis (FEA) methods can serve as a useful starting place in making appropriate approximations to the true capacitance of our system. Fig. 4.5 (a) shows a FEA simulation performed with commercial software (COMSOL Multiphysics) of the surface charge density of a biased nanotube; the horizontal line in the graph shows the surface charge density of an infinite cylinder in the identical geometric configuration as the system in question. Guided by this simulation, we approximate the total charge as the combination of a sidewall charge, as given by an infinitely long cylinder, and a tip charge. We utilize standard techniques, such as the method of images[39, 40, 41], to solve for the capacitive sidewall force,

$$F_s(x,V) = \frac{\pi\epsilon_0 L\sin\theta}{\sqrt{(d_0-x/2)((d_0-x/2)+2r)}\arccos^2\left(1+\frac{d_0-x/2}{r}\right)}V^2 \tag{4.1}$$

Here x is the displacement of the nanotube tip, d_0 is the initial distance (i.e. when $V=0$) from the tip to the counter electrode, L is the length of the nanotube, r is the nanotube radius, V is the voltage of the nanotube with respect to the counter electrode, θ is the initial angle the longitudinal axis of the tube makes with the normal to the ground plane, and ϵ_0 is the permittivity of vacuum.

The tip charge is approximated with a parametrically derived expression for flat-end nanocylinders [42] modified to account for the closed end of the nanotube [43]. The expression is essentially an empirical fit to simulations by varying L and r and comparing the result to the sidewall force, Eq. 4.1. The resulting electrostatic force acting on the tip of the nanotube is

$$F_t(x,V) = \frac{0.85\pi\epsilon_0((d_0+r)^2 r)^{1/3}\sin\theta}{2\sqrt{(d_0-x)((d_0-x)+2r)}\arccos^2\left(1+\frac{d_0-x}{r}\right)}V^2 \tag{4.2}$$

The elastic response of the nanotube in the presence of the above electrostatic loads can be ascertained by solving the linear beam equation, $EI\frac{d^4u_y(x)}{dx^4} = f_l(x)$ (Eq. 2.8), which gives two components corresponding to the applied sidewall and tip forces. We can use the methods outlined in §2.1 to obtain effective spring constants of an elastic linear response. The resulting spring constants associated with the electrostatic sidewall and the tip forces are, respectively, $k_s = \frac{8EI}{L^3} = \frac{8\pi Er^4}{4L^3}$ and $k_t = \frac{3EI}{L^3} = \frac{3\pi Er^4}{4L^3}$, where E is the Young's modulus ($E \sim 1$ TPa for a carbon nanotube[44]), and $I = \frac{\pi r^4}{4}$ is the areal moment of inertia of a multiwalled nanotube as derived in Eq. 2.10.

Eqs. 4.1 and 4.2 govern the rapid nanotube deflection that initiates self-oscillations. The equilibrium tip deflection is obtained by finding a self-consistent solution to

$$x = \frac{F_s(x)}{k_s} + \frac{F_t(x)}{k_t} \tag{4.3}$$

Eq. 4.3 is a sum the individual deflections caused by each load on the carbon nanotube, and follows from the linearity of Eq. 2.8. Although an approximation, solutions to Eq.4.3 are consistent with simulations obtained from finite-element analysis, which solves Eq. 2.8, $EI\frac{d^4u_y(x)}{dx^4} = f_l(x)$, directly. The equilibrium tip deflection is plotted in Fig. 4.6(b) for selected values of initial tip-counter electrode separation d_0. The plots reveal that the tip position becomes unstable at a critical voltage, identified by the vertical lines in Fig. 4.6(b). At this critical voltage V_{th} the attractive electrostatic force overwhelms the repulsive elastic force and the nanotube is rapidly drawn to the counter electrode. This runaway deflection has been previously observed in MEMS/NEMS switches [45, 46, 20], but here the nanotube is positioned such that it cannot reach the counter electrode.

The instability of a nanotube at the critical voltage can also be seen from plots of the total potential energy of the nanotube, Fig. 4.6 (a), which includes electrostatic, $\frac{1}{2}C(x)V^2$, and elastic, $\frac{1}{2}k_{eff}x^2$, contributions. For low voltages there exists a deep well for stable equilibrium. As the voltage is increased, this well becomes shallower and eventually disappears completely, removing the stable equilibrium position altogether. Another source for the electrostatic instability in our system is evident from the position (x) dependence of Eqs. 4.1 and 4.2, which creates positive feedback in the system. That is, a given electrostatic force causes a deflection which in turn causes a larger electrostatic force, a larger deflection, and so on. This positive feedback is inherent to this particular class of electromechanical systems[20], and essential to many MEMS/NEMS devices such as electrostatic actuators and switches [45, 46, 20]. Fig. 4.6(b) was produced by allowing the deflection to converge to a self-consistent solution of 4.3, so that each data point corresponds to a position of static equilibrium of the nanotube. The vertical lines in Fig. 4.6 (b) marks the threshold where no self-consistent solution is possible, that is, where static equilibrium in the system cannot be achieved.

The threshold voltage V_{th} at which the nanotube position becomes unstable and

self-oscillations commence can be evaluated directly from geometric device parameters (r, L, d_0, θ). This threshold voltage is equivalent to the "pull-in" voltage known to researchers in the MEMS/NEMS switch community[20]. A plot of the total potential energy is shown in Fig. 4.6 (a) for bias voltages V ranging from 5 to 60 volts at 5 volt intervals. The minimum of each curve corresponds to the stable equilibrium deflection of the nanotube for a given V; this equilibrium deflection increases with increasing voltage. The instability voltage, V_{th}, of the system is given by the lowest voltage for which no minimum exists, and can be calculated by finding a V such that $\frac{dU(x,V)}{dx} > 0$ for all x in the region of interest. Note that the statement $\frac{dU(x,V)}{dx} > 0$ is equivalent to the total force, $F_{tot} = -\frac{dU(x,V)}{dx}$, being nonzero, a condition that precludes static equilibrium. In general, the model predicts that the threshold voltage for self-oscillations, V_{th}, increases for shorter tubes, larger tube radii, and larger initial tip-to-counter-electrode distances. For the device geometry shown in Fig. 4.3 (a), the model predicts $V_{th} \sim 55$V, which, given the uncertainty in the position of our bottom-up devices and the approximations of the model, is in excellent agreement with the experimentally observed V_{th} of 66 volts.

Based on the energetic instability of the system, we can now revisit the description of self-oscillations in terms of the strummed-guitar analogy given early. Sustained self-oscillations will occur for applied bias voltage $V > V_{th}$, but only if the decay time for mechanical oscillations, given by $2Q/\omega_0$ where Q is the quality factor and ω_0 is the natural frequency of oscillation, is greater than or on the order of the recharging time, given by the RC time constant of the circuit. For the experiments described above, we estimate $2Q/\omega_0 \sim 10^{-4}$ and $RC \sim 10^{-5}$, consistent with this interpretation of the model. We note further that if the system is biased very near to, but just below V_{th}, fluctuations (such as those associated with field emission current noise or with k_BT thermal noise) can temporarily kick the system into self-oscillation mode. While such oscillations may last for several seconds, they are not sustainable. We will give alternative, more general descriptions of the self-oscillation phenomenon in §4.4 and Chapter 5.

4.4 A Electronic Circuit Model for Self-oscillations: Charge Transport and Nanotube Motion Coupling

In the above analysis, we were concerned with calculating the threshold voltage, V_{th}, for the onset of self-oscillations in electromechanical systems similar to that shown in Fig. 4.1. In this section, we investigate self-oscillations by considering the quantum-electromechanical coupling in our system, and do this by looking directly at charge transport, where quantum mechanical tunneling of electrons plays an important role, and its relation to the electromechanical forces. The tunneling current

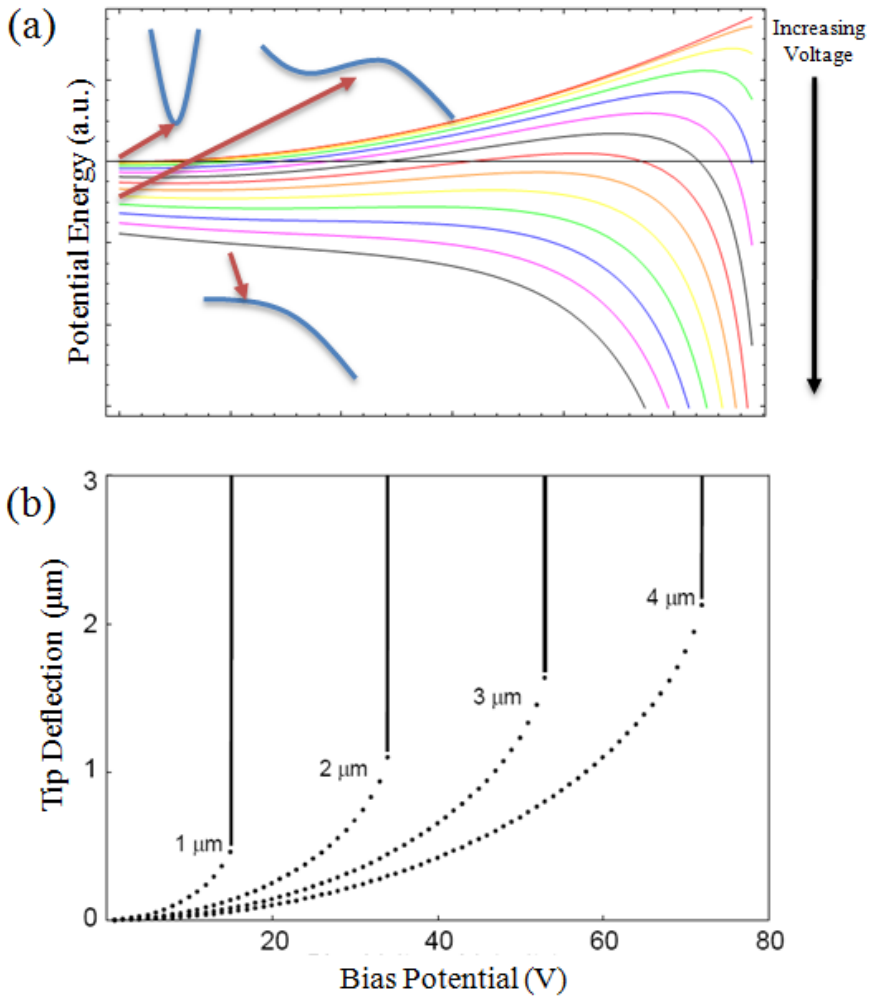

Figure 4.6: Total Potential Energy and Tip Deflection as a function of bias voltage. (a) Potential energy and (b) tip deflection as a function of bias voltage, for several values of d_0 (1,2,3,4 μm). Electromechanical modeling of self-oscillating carbon nanotubes. a) The equilibrium deflection of 10 nm radius nanotube tip as a function of bias voltage is shown for a tube of length 3 m at various initial tip-surface distances (1 μm, 2 μm, 3 μm, and 4 μm.) The vertical lines for each curve represent the voltage at which no equilibrium deflection exists for the tube and the tube becomes unstable.Here $r = 10$ nm, $\theta = \pi/2$, and $L = 3$ μm.

(field emission current) is coupled strongly to the electromechanical forces since both are governed by the electrical voltage applied to the tube. Thus, through a simple examination of the electrical and mechanical forces, by way of Newton's Second Law, and elementary charge transport, by way of Kirkoff's circuit rules, we will gain insight

into the dynamics of the self-oscillation process and be able to predict some of the observed properties. In particular, the current spikes observed at the onset of the self-oscillations and the self-oscillations themselves are predicted by this model.

The electrostatic force is written simply as the product of the charge on the tube, $q(x,V)$, and the electric field on the tube, $E(x,V)$, both a function of the nanotube tip position, x, and voltage, V. The elastic response of the nanotube is written as $m\omega_0^2 x$, where the resonance frequency, ω_0, of the nanotube would be dependent on the spring constant of the system. Including the conventional loss term, $m(\omega_0/Q)\dot{x}$, Newton's Second gives:

$$m\ddot{x} + m\omega_0^2 x + m(\omega_0/Q)\dot{x} - q(x,V)E(x,V) = 0 \tag{4.4}$$

We make linear approximations for the charge and the field, so

$$E(x,V) = (k_1 + k_2 x)V$$

and

$$q(x,V) = c(x)V = (k_3 + k_4 x)V \tag{4.5}$$

In terms of electric circuit components, we model a field-emitting nanotube as a capacitor-diode parallel junction, where the diode has a Fowler-Nordheim current-voltage characteristic. This model was presented in §3.4 when we looked at current switching behavior. A diagram of corresponding equivalent circuit for our field-emitting nanotube is shown in Fig. 4.7. Applying Kirkoff's voltage and current sum rules to this circuit, we obtain

$$V_0 = I_R R + V \tag{4.6}$$

and

$$I_R = I_{FN} + I_C \tag{4.7}$$

Here, we have set the load impedance to a pure resistance, $Z = R$, and have written the current through the resistor, diode, and capacitor as I_R, I_{FN}, and I_C, respectively. The current I_{FN} is given by the Fowler-Nordheim equation (Eq. 3.6),

$$I_{FN} = a(\beta E)^2 \exp\left(-\frac{b}{\beta E}\right)$$

The capacitor current, $I_C = \dot{q} = c(x)\dot{V} + \dot{c}(x)V$, combines with Eqs. 4.6 and 4.7 to yield

$$c(x)\dot{V} + V\dot{c}(x) + I_{FN}(V,x) + (V - V_0)/R = 0 \tag{4.8}$$

Eqs. 4.4 and 4.8 are a set of coupled differential equations which can be solved to obtain $x(t)$ and $V(t)$. We solve this by Taylor expanding the general expression for the electrostatic force,

$$F = \frac{1}{2}\frac{dC(x)}{dx}V^2 \approx a_0 + a_1 x + a_2 x^2 \ldots$$

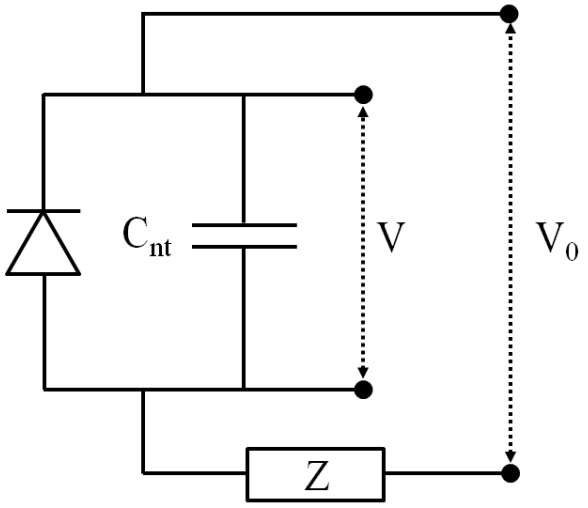

Figure 4.7: Equivalent Circuit for CNT Field Emitter. The nanotube is both a Fowler-Nordheim diode and a capacitor. V_0 is the applied voltage and V is the voltage across the nanotube. Z is the equivalent impedance of the rest of the circuit.

and comparing to the earlier expression,

$$F = q(x,t)E(x,t) = k_1k_3 + (k_1k_4 + k_3k_2)x + k_2k_4x^2$$

Also, the capacitance is $C(x) \approx c_0 + c_1x = k_3 + k_4x$, using Eq. 4.5. We obtain these constants, k_i, from Eq. 4.1, for example, and the corresponding equation for the capacitance. The next chapter gives a slightly different, and cleaner analytically, formula for the capacitance of the system, which we reproduce here

$$C(x) = \frac{2\pi\epsilon_0}{\ln\left(\frac{4d_0(1+x/d_0)}{r}\right)}L \tag{4.9}$$

from which all of these constants can be obtained. Using parameters appropriate for our system and/or obtaining them from experimental data (as is necessary for constants in IFN), we solve Eqs. 4.4 and 4.8 computationally (code is written in Mathematica, a commercial computational software program for technical computing and programming). Fig. 4.8 shows one such solution for the position of the nanotube, $x(t)$. From this particular solution, we see that this model captures the essential properties of the system including the current spike and oscillations. The initial large amplitudes seen in Fig. 4.8 will cause the spike in the field emission current, and the inset shows the onset of smaller amplitude oscillations. Thus, the current spike can be, as argued earlier, ascribed to transients in the system. We note that these transients and the oscillations do not occur if the V_0 input parameter is not above V_{th}

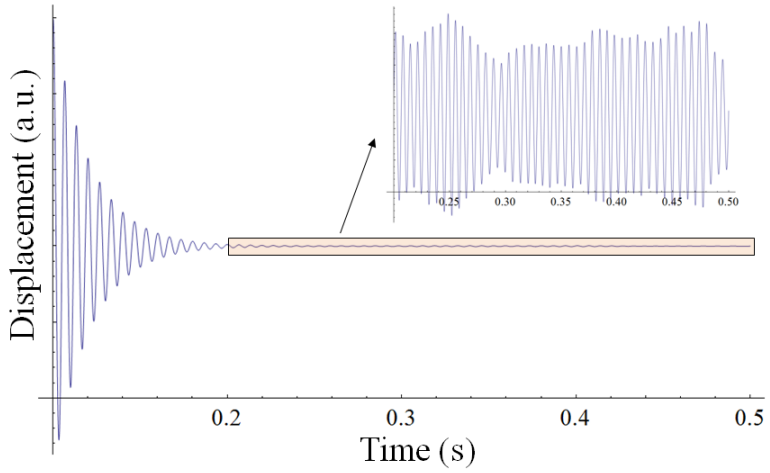

Figure 4.8: Simple Electromechanical Model II. Displacement of nanotube showing transients and "steady-state" oscillations.

for the system, in accord with the modeling presented in §4.3. Instead, the deflection curve, $x(t)$ vs. t, is a straight line (*i.e.* the nanotube is in static equilibrium).

4.5 Engineering Self-Oscillating NEMS

Our model explicitly outlines the role geometric parameters play in self-oscillations, and can thus facilitate the engineering and design of self-sustaining NEMS oscillators. Since the patterned growth and deposition of carbon nanotubes is now quite common[48, 49, 51], our model will be useful for the design of self-oscillating NEMS amenable to large-scale fabrication. To this end, Fig. 4.9 summarizes the geometric requirements (assuming $L = d_0$) for designing self-oscillating cantilevered devices that operate within a certain desired DC bias voltage range and for a range of practical nanotube dimensions. The data comprising Fig. 4.9 was generated directly from the analysis given above in §4.3. The graph indicates, for example, that a 10 μm long carbon nanotube will self-oscillate for an applied bias of 10V if $r < 7$ nm, while a 1μm long tube will oscillate for similar values of V if $r < 2.5$ nm. It is worth noting that over 75% (the red and yellow area in Fig. 4.9) of devices in this parameter space have operation (self-oscillation) voltages less than 25 Volts. These low operating voltages and the low power necessary for their operation ($P = IV \sim 1\mu A \times 10V = 10\mu W$) make these devices compatible with many of the specifications of modern electronics, including with those of ultra-low-power portable electronics.

We now employ scalable methods to fabricate fully integrated self-oscillating NEMS structures with pre-determined performance characteristics. We use standard optical and electron-beam lithography, microfabrication processing, and simple

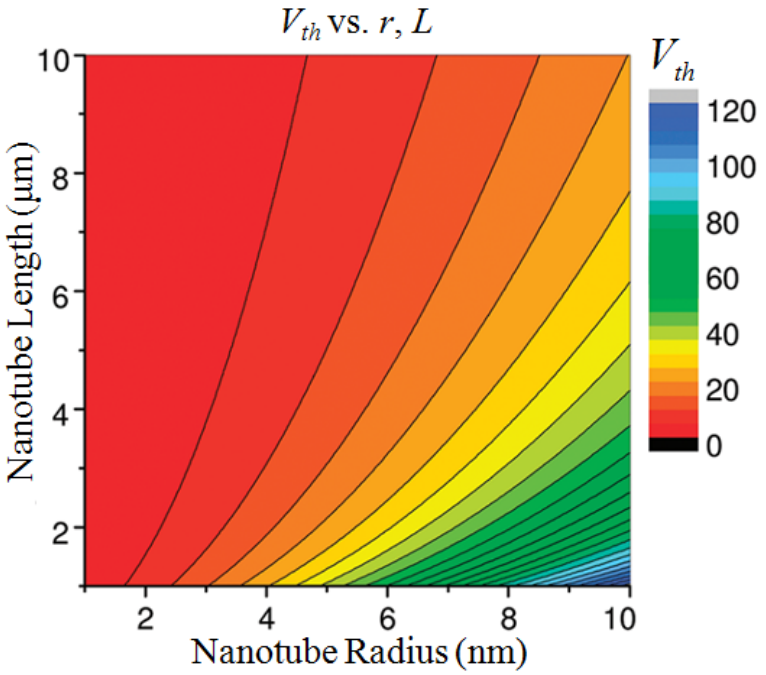

Figure 4.9: Self-Oscillation Threshold Voltage. A contour plot the self-oscillation onset voltage given for $L = d_0$ ranging from 1-10 μm and r between 1-10 nm.

nanotube deposition techniques (spin casting) to produce fully suspended nanotube-based oscillators with well-defined L, d_0, r, and θ. The details of this fabrication can be found in Chapter 1 and Appendix G. Figure 4.2(c) shows a TEM micrograph of an unbiased device composed of a suspended multi-walled carbon nanotube and a lithographically defined counter-electrode. Fig. 4.2(f) shows the same device biased into self-oscillations. For this device, V_{th} was determined experimentally to be 40 V, which agrees within 10% of model predictions.

The device architecture shown in Fig. 4.2 (b),(f) was chosen to facilitate TEM characterization and was realized by performing all processing on a thin Si_3N_4 membrane that was then etched using an SF_6 plasma to produce the suspended structure. Of course, TEM-transparent devices are not necessary for most applications and so much simpler, membrane-free approaches are available. Examples of alternatives include those that suspend nanotubes over trenches[47] and that exploit techniques for the controlled placement of highly-aligned SWCNT[48] or MWCNT[49] on substrates such as Si or SiO_2. A suspended MWCNT nanotube on SiO_2 is shown in Fig. 4.10; an HF etch followed by critical point drying (CPD) gently suspends the nanotube and avoids stiction. Techniques that grow SWCNT on predefined contacts, which avoids the CPD step altogether and results in ultra-clean devices, have been developed [52] and are completely amenable to fabrication at the wafer scale. Therefore,

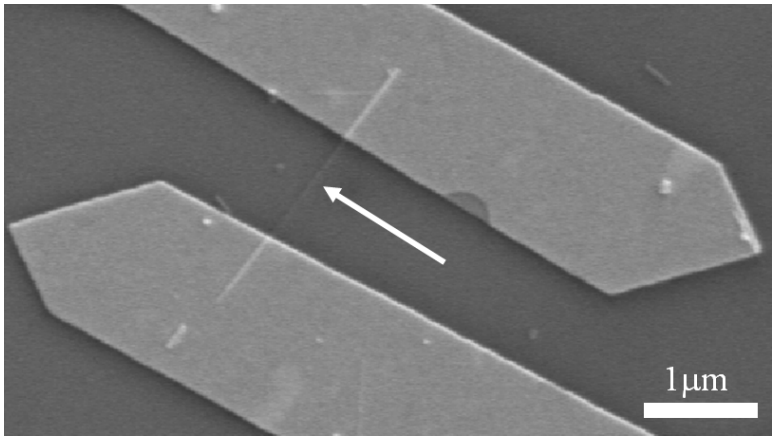

Figure 4.10: Multiwalled Carbon Nanotube on SiO_2 with source and drain electrodes. An HF will suspend the tube and the tube can be severed to produce a singly-clamped CNT device by passing sufficient current through the tube.

one could use existing technologies and techniques to mass-produce self-oscillating carbon nanotube NEMS for myriad commercial or scientific applications.

4.6 Summary

In summary, we have demonstrated controllable, sustained self-oscillations with carbon nanotube NEMS. Because of the strong coupling between quantum mechanical tunneling currents and nanomechanical motion that is required for these self-oscillations, these particular CNT NEMS form a novel class of NEMS, quantum-NEMS or Q-NEMS. Furthermore, we have used an electromechanical model to develop a comprehensive understanding of this behavior and have described the parameters necessary for designing proper device architectures. In addition, the model that we presented can be applied to similar devices composed of other materials, such as nanowires and graphene, and is likely applicable to previous observations of self-oscillation[34]. With these design parameters we have fabricated operational top-down devices. The successful top-down fabrication of NEMS self oscillators has important implications for future highly-integrated, chip-based systems, such as sensors[28], logic and memory elements[29], and high frequency NEMS switches[46], which can in principle be tailored to operate at DC bias voltages less than 25 V.

Chapter 5

Parametric Amplification in Carbon Nanotube Resonators

This chapter is dedicated to the description of a parametric amplifier based on a single suspended carbon nanotube field-emitter. This novel electromechanical nanotube device acts as a phase-sensitive, variable-gain, band-pass-filtering amplifier for electronic signal processing and, at the same time, can operate as a variable-sensitivity, tuneable detector and transducer of radio frequency electromagnetic waves. The amplifier can exhibit "infinite" gain at pumping voltages much less than 10 Volts. Additionally, the amplifier's low overhead power consumption (10-1000 nW) make it exceptionally attractive for ultra-low-power electronics applications. Apart from detailing our nanoscaled parametric amplifier and some important applications, we will use some of the tools developed in this chapter to revisit and gain insight into the phenomenon of self-oscillation that can occur in these devices.

5.1 Introduction

The phenomenon of parametric amplification, such as occurs in a child's swing[1], has been studied since the early 19^{th} century[2, 3] and occurs in oscillating systems in which a parameter (i.e. resonance frequency, spring constant, degree of dissipation, etc.) is modulated at a sub-multiple of twice the resonance frequency, $2\omega_0/n$, to produce amplification in the response of the system. It is the child's up-and-down leg motion, for example, that provides a temporal modulation of the resonance frequency of the swing (through a change in the effective length of the swing), which in turn is responsible for large (amplified) amplitude of the swing. A theoretical amplitude-frequency response of a parametric amplifier is shown in Fig. 5.1.

Several experimental implementations of parametric amplifiers have been demonstrated, including in electronic systems, using varactors[7] and Josephson junctions[8], optical systems, using nonlinear materials[9], and electromechanical systems[10]. Para-

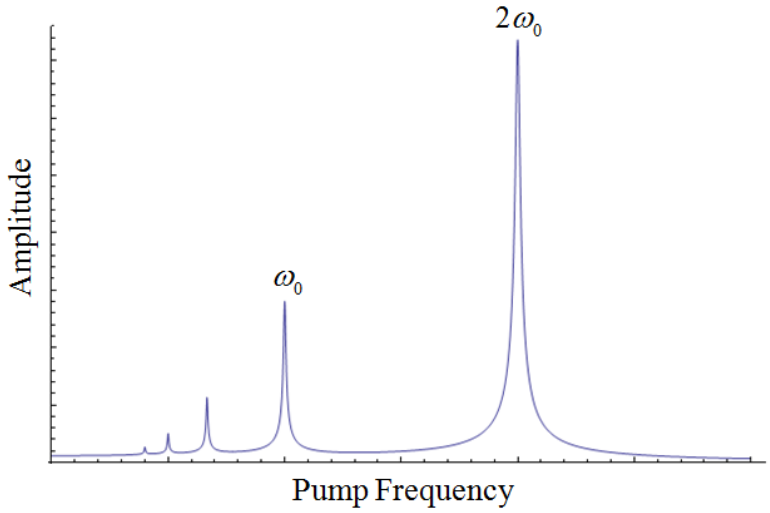

Figure 5.1: **Theoretical Amplitude-Frequency Response of Parametric Amplifier**. A parametric amplifier, when pumped at $2\omega_0$, will resonate at the submultiples $2\omega_0$, ω_0, $2\omega_0/3$, $\omega_0/2, \ldots$, with a diminished response at the lower frequencies[21].

metric amplifiers, or "paramps", have captured the interest of researchers partly because of their inherent non-linear properties, but also because of their usefulness in the amplification of electron and optical signals. Most importantly, however, this amplification, though not necessarily accompanied by high gain, has amplifier noise that can approach the quantum-limit[4, 5, 6]. In this chapter, we explore the parametric amplification of mechanical oscillations in a suspended carbon nanotube resonator (Fig. 5.2 (a)). Additionally, we show that by operating the device in the limit of strong coupling between mechanical vibrations and field emission tunneling current, the device behaves as a tuneable, high-gain, phase-sensitive amplifier of AC current and voltage signals. The same device possesses a surprisingly versatile utility, finding potential uses as a tuneable, highly-sensitive detector (or transmitter) of electromagnetic radiation(from low-frequency to radio-frequency), a band-pass filter, a particle detector, or even a thermometer.

At the heart of this novel device and its technological versatility is the same *quantum-electromechanical* coupling–the quantum mechanical tunneling current (field emission current) in these devices is sensitive to the position (and mechanical motion) of the nanotube relative to the counter electrode–that arose in our discussion of self-oscillations in field-emitting CNT resonators (Chapter 4). Thus, suspended carbon nanotube field emitters show exceptional promise as resonators[15] in nanoelectromechanical systems (NEMS) with applications to radio wave detection[35], atomic-resolution inertial mass sensing[28], and as self-sustained RF oscillators[18]; they have also proven useful as electron sources[11, 12, 13] and Fowler-Nordheim

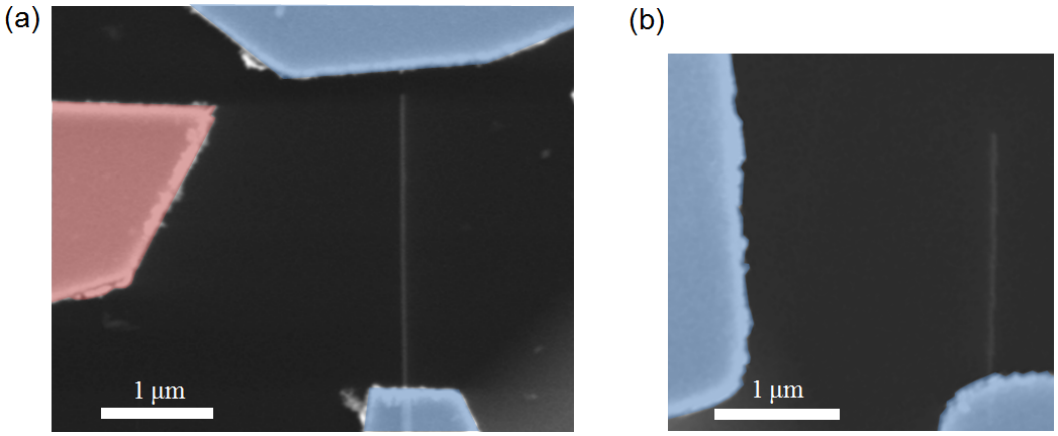

Figure 5.2: **Prototypes for a carbon nanotube parametric amplifier**. (a) A false-color scanning electron micrograph of a lithographically-defined multiwalled carbon nanotube device. The source and drain electrodes (upper and lower in blue) maintain and measure the field emission current and the side pumping electrode (left in red) generates the modulation of the effective elastic spring constant of the nanotube. (b) Two-terminal device

diodes[14]. Therefore, the quantum tunneling current adds to the existing electromechanical functionality by coupling directly into the motion of the nanotube resonator(as seen in Chapter 4), while simultaneously providing a mechanism for "reading out" or transducing nanoscale vibrational information into detectable electronic signals. The combination of tunneling current transduction and parametric amplification of mechanical vibrations enables all of the amplification and detection functionality of our system.

We begin by briefly describing prototype devices that possess the requisite transduction and parametric amplification properties. We then develop the modeling for the transduction and parametric amplification functions, and discuss some of the notable predictions made by the model. Finally, we discuss some the applications of these novel nanoscaled parametric amplifiers and explore the connection between parametric amplification and the self-oscillation phenomenon described Chapter 4.

5.2 Device Description and Electromechanical Modeling

The generic parametric amplifier requires drive and "pump" (the generator of parametric modulation) input signals to produce the amplification effect. In order to monitor the output of the parametric amplification, one must also provide a sep-

arate mechanism to "see" or measure the signal amplification. Our nanoscaled parametric amplifier incorporates all the necessary functionality into a single suspended, singly-clamped carbon nanotube electrode and a few nearby metallic electrodes. The nanotube serves as the mechanical resonator element, a metallic electrode, and the active field-emitter. Since the mechanical motion transduction is facilitated by the field-emission process, a second electrode–the counter electrode–is required in order to "drain" and measure the corresponding current. An additional electrode is required to introduce parametric modulation (in the form of an AC voltage) into the system, which may also supply a driving signal. As we will see later, the drive signal can be produced thermally, electronically, mechanically, or radiatively, and therefore this function doesn't necessarily demand its own separate electrode. Hence, it is possible to integrate amplification, transduction, and driving signal supply using as few as two electrodes (the nanotube itself and a second auxiliary electrode).

Scanning electron microscopy (SEM) images of three- and two-terminal device prototypes are shown in Figure 5.2 (a) and (b), respectively. These devices were fabricated using the methods described in Chapters 1 and 4. Briefly, MWCNTs were drop-cast onto a Si_3N_4 membrane, electrodes and contacts were defined by electron-beam lithography, and the membrane is etched away to leave a suspended structure. For the device shown in Fig. 5.2 (a), one possible functioning configuration would have the upper (blue) electrode serve as the drain, while the left (red) electrode introduces parametric modulation and drive signals to interact with the nanotube. The only strict geometric requirement applies to the pump electrode; in order to pump energy into, and thus amplify, lateral flexural vibrations of the nanotube, the pump electrode must be oriented next to the sidewall (as opposed to the tip) of the nanotube, as in Fig. 5.2 (b) and Fig. 5.3 (a). We'll the discuss the benefits and disadvantages of the many different electrode and signal configurations in §5.4.

5.2.1 Field Emission as a Mechanism for Mechanical Motion Transduction

Transduction of the nanotubes mechanical motion is achieved by measuring the field emission current produced by the biased nanotube. The process is analogous to the topographical mapping of a conducting surface using scanning tunneling microscopy(STM), where the value of the tunneling current is sensitive the relative height of the STM tip above the surface. The height(nanotube position)-current relationship in our system is captured by the Fowler-Nordheim equation (Eq. 3.6)

$$J(x) = \frac{e^3 \mathcal{E}(x)^2}{16\pi^2 \hbar \phi} \exp\left(-\frac{4\sqrt{2m^*}\phi^{3/2}}{3\hbar e \mathcal{E}(x)}\right)$$

which gives the field emission current as a function of the electric field $\mathcal{E}(x)$, which is itself a function of the nanotube tip position x. Referring to Fig. 5.3 (a), a one-

dimensional model yields the simple relation $E(x) = V/(d_0 + x)$, where V is the electrical potential applied to the tube, d_0 is position at $V = 0$, and x is the position of the tube. Thus, if the position, $x(t)$, varies at a temporal frequency ω, so will the field emission current (though the non-linear behavior of field emission process will rectify the current signal[35].) Fig. shows the amplitude-frequency response of a CNT device obtained by reading the tunneling current.

The efficiency of this transduction mechanism, for a given nanotube oscillation amplitude, is maximized for a nanotube-counter electrode configuration that maximizes the corresponding electrode separation distance. So, the device in Fig. 5.2 (b), which field emits in the lateral direction, will transduce mechanical motion much more efficiently than the device in Fig. 5.2 (a), which field emits in the longitudinal direction.

5.2.2 Parametric Amplification in an Electromechanical System

Parametric amplification in our system occurs because the carbon nanotube capacitively couples to a nearby electrode. The spatial dependence of the associated capacitive force, given by the expression $F(x, V) = \frac{1}{2}\frac{dC(x)}{dx}V^2$, leads to a host of non-linear behavior, including parametric modulation. In terms of the electrostatic potential energy, the capacitive coupling changes the landscape of the elastic mechanical potential energy in such a way that the effective spring constant of the system is now a function of the electric potential difference, V, between the nanotube and the electrode. We will now give a theoretical analysis of the parametric amplification that arises from this capacitive coupling.

We model our singly-clamped carbon nanotube device as a capacitively-coupled, driven-damped simple harmonic oscillator. A schematic for the model device and its parallel-plate analog is shown in Figure 5.3. The capacitive coupling is tunable through the applied voltages, $V_p(t)$ and V_0, which represent time-varying and DC bias, respectively. The nanotube is held at electrostatic ground. Geometric parameters for our model include the zero-bias nanotube-electrode distance, d_0, and the nanotube length, L, radius, r, and tip deflection, x.

The potential energy associated with the capacitive coupling is given by the classical relation, $U_C(x) = \frac{1}{2}C(x)V^2$, where V includes $V_p(t)$ and V_0, and $C(x)$ is the capacitance of the nanotube-electrode system. The corresponding force is then $F_C(x) = -\frac{1}{2}\frac{dC(x)}{dx}V^2$. Taylor expanding $C(x)$ to second order, $C(x) = C(0) + \frac{dC(0)}{dx}x + \frac{1}{2}\frac{d^2C(0)}{dx^2}x^2 + \cdots$, and setting $V = V(t) = V_0 + V_p \sin(2\omega_0 t)$ yields the approximate capacitive force

$$F_C = -\frac{1}{2}\left(\frac{dC(0)}{dx} + \frac{d^2C(0)}{dx^2}x\right)(V_0^2 + 2V_0V_p \sin(2\omega_0 t) + V_p^2 \sin^2(2\omega_0 t)) \qquad (5.1)$$

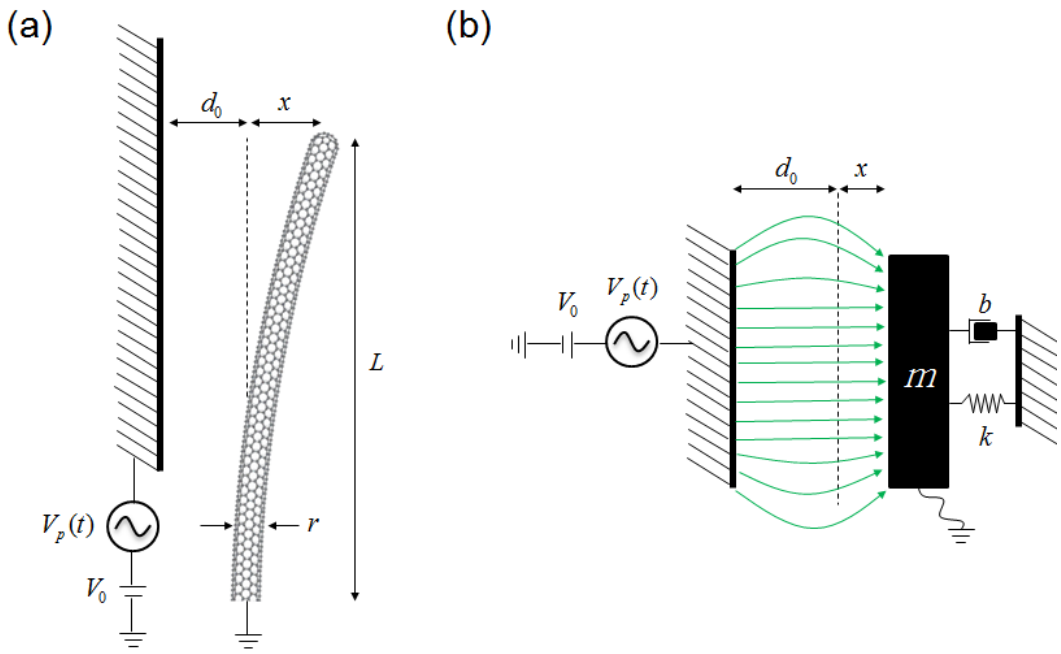

Figure 5.3: **A Schematic for Modeling**. (a) A schematic of the device highlighting the interaction with the pump electrode and the basic electrical circuit wiring. (b) A schematic of the equivalent electromechanical system for the pump-nanotube interaction shown in (a). The pump electrode-nanotube interaction is modeled as a position variable capacitor of mass m connected to a rigid support by a spring of spring constant k and dissipation b.

We have set the frequency of the pumping voltage, $V_p(t)$, to $2\omega_0$ in anticipation of maximizing the effect of parametric amplification. The terms involving $\frac{dC(0)}{dx}$ or $\sin^2(2\omega_0 t)$ lead to off-resonant driving terms or static deflections and can be neglected. Hence, retaining terms involving products of x with V_0^2 or $\sin(2\omega_0)$, and including dissipative, elastic, and driving force terms, the equation of motion of the nanotube becomes

$$m\frac{d^2x}{dt^2} + m\frac{\omega_0}{Q}\frac{dx}{dt} + [k + \Delta k \sin(2\omega_0 t)]x = F\cos(\omega t + \phi) \tag{5.2}$$

where m is the nanotube mass, Q is the resonator quality factor, ω is the driving frequency, ϕ is the relative phase between the pumping ($2\omega_0$) and driving (ω) terms, and $\omega_0 = \omega_0(k)$ is the mechanical resonance frequency. We have defined

$$k \equiv k_0 + \frac{1}{2}\frac{d^2C(0)}{dx^2}V_0^2 \tag{5.3}$$

as the electrostatic spring constant of the nanotube, where $k_0 = \frac{3\pi E r^4}{4L^3}$ is the bias-free value given by elastic beam theory (see [20] or §2.1.1) and $E \approx 1$ TPa is the Young's modulus of a carbon nanotube. Eq. 5.2 is similar to the equation-of-motion of a driven-damped simple harmonic oscillator except for the time-dependent term $\Delta k \sin(2\omega_0 t)x$, where we define

$$\Delta k \equiv \frac{d^2C(0)}{dx^2}V_0 V_p \tag{5.4}$$

This time-dependent term controls the degree of parametric modulation in our system, and is responsible for the amplification effect that we will see shortly.

Eq. 5.2 is in the form of the driven *Mathieu* equation, and its solutions have two unique features. First, the amplitude-frequency response will display resonance peaks(Fig. 5.1) at the *pump* frequencies $\omega_p = 2\omega_0/n$, where n is any positive, non-zero integer [21]; this contrasts the single resonance peak observed in the simple harmonic oscillator. We have already set $\omega_p = 2\omega_0$ in Eq. 5.2. Second, the amplitude at resonance exhibits amplification governed by the strength of the modulation term (Δk), the spring constant (k), and the relative phase (ϕ). However, Δk and k are themselves functions of the $d^2C(0)/dx^2$, V_0, and V_p, and therefore the amplification is governed by the device geometry, through the capacitance, and the experimentally variable bias voltages. In the limit $Q >> 1$, the gain of this amplification is

$$G(\Delta k, k, \phi) = \left[\frac{\cos^2(\phi)}{(1 + Q\Delta k/2k)^2} + \frac{\sin^2(\phi)}{(1 - Q\Delta k/2k)^2}\right]^{1/2} \tag{5.5}$$

The amplitude response itself is just $A = F\frac{Q\omega_0}{k}G(\Delta k, k, \phi)$ [10, 21].

The general phase-dependence of the gain formula (Eq. 5.5) is shown in Fig. 5.4. *Amplification* occurs for values of phase with a corresponding gain that is greater

than unity, $G(\phi) > 1$, while *deamplification* occurs when $G(\phi) < 1$. The gain itself is relative to the unmodulated (*i.e.* $\Delta k = 0$) simple harmonic oscillator, whose gain is defined to be unity. Referring to Fig. 5.4, amplification will occur for $\phi > 5°$ and reaches a maximum at $\phi = 90°$. Deamplification will occur for $\phi < 5°$; this deamplification effect has been used to prepare thermomechanically squeezed states[10, 22], in which one quadrature of a mechanical resonator's thermal noise is reduced below $k_B T$ and so appears to be "cooler". The gain's dependence on the modulation strength, Δk, and the spring constant, k, for our model system will be discussed below(§5.3.)

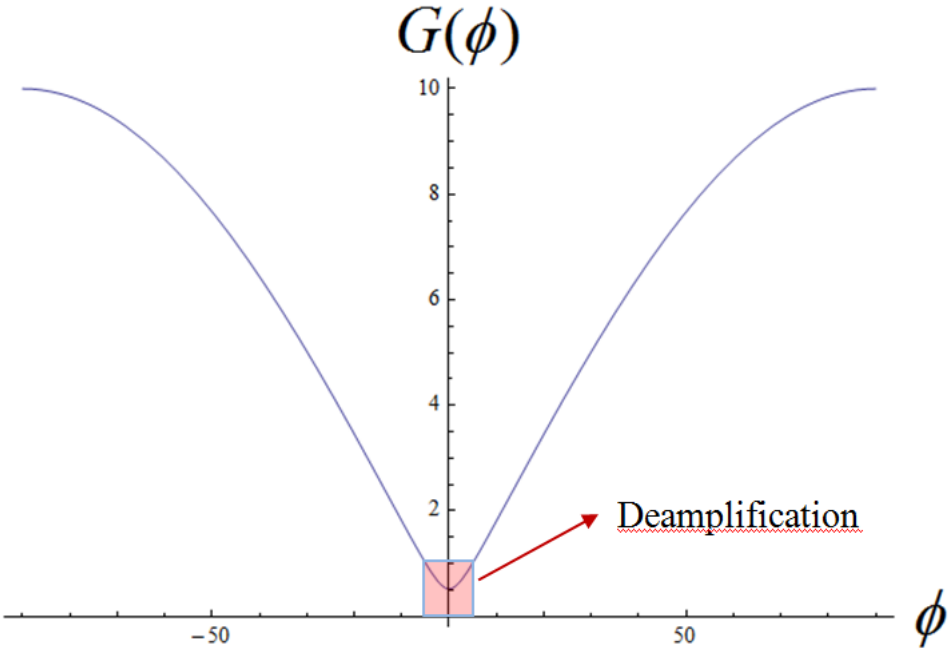

Figure 5.4: Gain as a function of phase, ϕ.

5.2.3 Solution to Mathieu Equation

We now give a brief derivation of Eq. 5.5. First we introduce the complex variables

$$a = \frac{dx}{dt} + i\omega_1^* x \tag{5.6}$$

$$a^* = \frac{dx}{dt} - i\omega_1 x \tag{5.7}$$

where $\omega_1 = \omega_0[(1 - 1/4Q^2)^{1/2} + i/2Q]$. Solving for x and $\frac{dx}{dt}$ in Eqs. 5.6 and 5.7 gives

$$x = \frac{a - a^*}{i(\omega_1^* + \omega_1)} \tag{5.8}$$

$$\frac{dx}{dt} = \frac{\omega_1 a + \omega_1^* a^*}{\omega_1^* + \omega_1} \tag{5.9}$$

Substituting Eqs. 5.8 and 5.9 into Eq. 5.2 and setting $\omega = \omega_0$ and $k = m\omega_0^2$ gives the expression

$$\frac{da}{dt} = i\omega_1 a + i\frac{\Delta k \sin(2\omega_0 t)}{m}\frac{a - a^*}{\omega_1^* + \omega_1} + \frac{F\cos(\omega_0 t + \phi)}{m} \tag{5.10}$$

We look for harmonic solutions to Eq. 5.10. Then, substituting the solution $a(t) = A\exp(i\omega_0 t)$ into Eq. 5.10 and retain terms proportional to $e^{i\omega_0 t}$ gives

$$\left[i(\omega_1 - \omega_0)A - \frac{\Delta k}{2m(\omega_1^* + \omega_1)}A^* + \frac{F}{2m}e^{i\phi}\right]e^{i\omega_0 t} = 0 \tag{5.11}$$

In the high-Q limit, $\omega_1^* + \omega_1 \approx 2\omega_0$ and $\omega_1 - \omega_0 \approx i\omega_0/2Q$, Eq. 5.11 gives

$$-\frac{\omega_0}{2Q}(\mathbf{Re}A + i\mathbf{Im}A) - \frac{\Delta k}{4m\omega_0}(\mathbf{Re}A - i\mathbf{Im}A) + \frac{F}{2m}(\cos\phi + i\sin\phi) = 0 \tag{5.12}$$

Equating the real and imaginary parts of Eq. 5.12, we obtain

$$A = F\frac{Q\omega_0}{k}\left[\frac{\cos(\phi)}{1 + Q\Delta k/2k} + i\frac{\sin(\phi)}{1 - Q\Delta k/2k}\right] \tag{5.13}$$

which yields Eq. 5.5

5.3 Amplification Gain for Carbon Nanotube Mechanical Resonators

Most of the analysis presented so far is applicable to any electromechanical system possessing a capacitive coupling similar to that shown in Fig. 5.3. We now apply the results to the specific geometry of our carbon nanotube devices. For the capacitance of our nanotube device, we'll use the classical expression for a metallic cylinder of radius r and length L situated a distance d_0 from a conducting plane[19],

$$C(x) = \frac{2\pi\epsilon_0}{\ln\left(\frac{4d_0(1+x/d_0)}{r}\right)}L \tag{5.14}$$

where $\epsilon_0 = 8.85 \times 10^{-12} C^2 N^{-1} m^{-2}$ is the vacuum permittivity, and x is the displacement of the entire nanotube away from d_0 (see Fig. 5.3). Here we will approximate x as the tip deflection; this approximation agrees well (within 18 %) with finite-element simulations performed on a nanotube bending under the appropriate electrostatic load. Some error cancelation is expected since we have neglected the capacitive contribution of the highly charged nanotube that was used earlier (Chapter 4.)

Taking the second derivative of Eq. 5.14, we obtain,

$$\frac{d^2C(0)}{dx^2} = \frac{\pi\epsilon_0 L}{d_0^2}\frac{(2+\ln(4d_0/r))}{\ln^3(4d_0/r)} \tag{5.15}$$

Now we use Eqs. 5.3, 5.4, and with $f = f(r, L, d_0) = d^2C(0)dx^2$ together with Eq. 5.5:

$$G(V_0, V_p, \phi) = \left[\frac{\cos^2\phi}{\left(1+\frac{2QfV_0V_p}{2k_0+fV_0^2}\right)^2} + \frac{\sin^2\phi}{\left(1-\frac{2QfV_0V_p}{2k_0+fV_0^2}\right)^2}\right]^{1/2} \tag{5.16}$$

The amplifier gain is therefore specified by the experimental parameters V_p , V_0, and ϕ, and also by the device parameters Q, r, L, d_0. Figure 5.5 (a) shows a contour plot of the gain as a function of both V_p and V_0, and Fig. 5.5 (b) shows the gain behavior as a function of V_p for several fixed values of V_0. Of particular interest is the divergence of the gain, $G \to \infty$, which causes the system to become unstable and enables self-oscillation behavior[10, 8]. In terms of the applied voltages, the gain diverges when

$$V_p = \frac{2k_0 + fV_0^2}{2QfV_0} \tag{5.17}$$

Fig. 5.5 plots $V_p = \frac{2k_0+fV_0^2}{2QfV_0}$ vs. V_0 for $L = d_0 =$ 1, 2, 3, 4, 5 μm, $r =$ 5nm, and $Q = 1000$. From this plot we see that nanotube devices will exhibit infinite gain when the applied voltage are in the range $V_0 =$ 10-100 V and $V_p \leq 50$ mV. The devices will never exhibit true infinite gain, but instead will have high gain below the threshold defined by Eq. 5.17 and instability above this threshold. In practice, the maximum gain achieved by our devices will be limited by other non-linear effects and damping. However, it is worth noting the low voltages required to enable high amplification gain in our system.

5.4 Applications of Carbon Nanotube Parametric Amplifier

The sensitivity of the carbon nanotube resonator to a diversity of incoming signals leads to a large number of exciting potential applications. The carbon nanotube NEMS device will respond to any "signal" that induces mechanical vibrations of the nanotube. These vibrations are then amplified (as discussed above) and transduced for readout as an electrical signal–a current. The device's response has a frequency dependence: The device is sensitive to the Fourier components of any signal that are both centered within the bandwidth ($\Delta\omega_0 = \omega_0/Q$) of the nanotube's vibrational resonance frequency and capable of exciting the nanotube's vibrational modes into

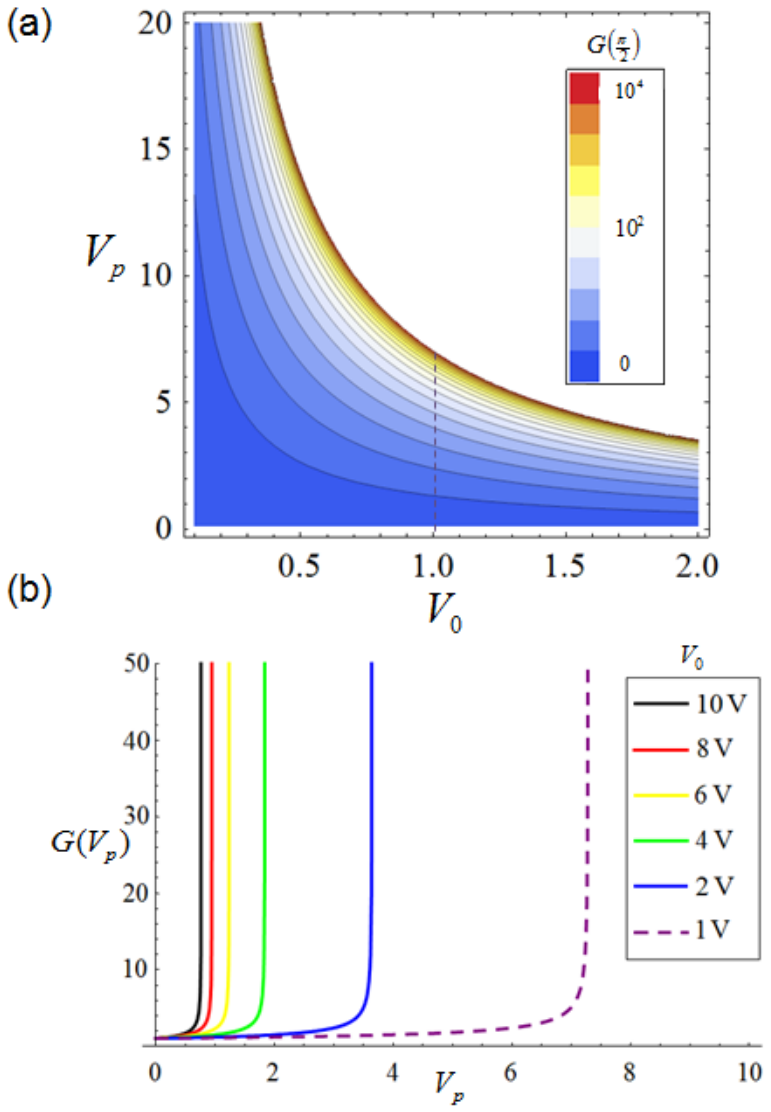

Figure 5.5: Amplifier Gain: (a) Gain of amplifier as a function of V_0 and V_p. The upper white portion of the graph is a region of resonator instability. (b) Shows gain as a function of V_p for several fixed values of V_0. The dashed line at $V_0 = 1$ V in (a) corresponds to the rightmost dashed line in this plot and aids in visualizing the rapid change in gain near a critical value (about 7.25 V for the dashed curve) of V_p. In all the curves, the gain is near unity for lower values of V_p and then quickly diverges to infinity. In all plots, $L = d_0 = 1\mu m$, $r = 5$ nm, $Q = 500$, and $\phi = \pi/2$.

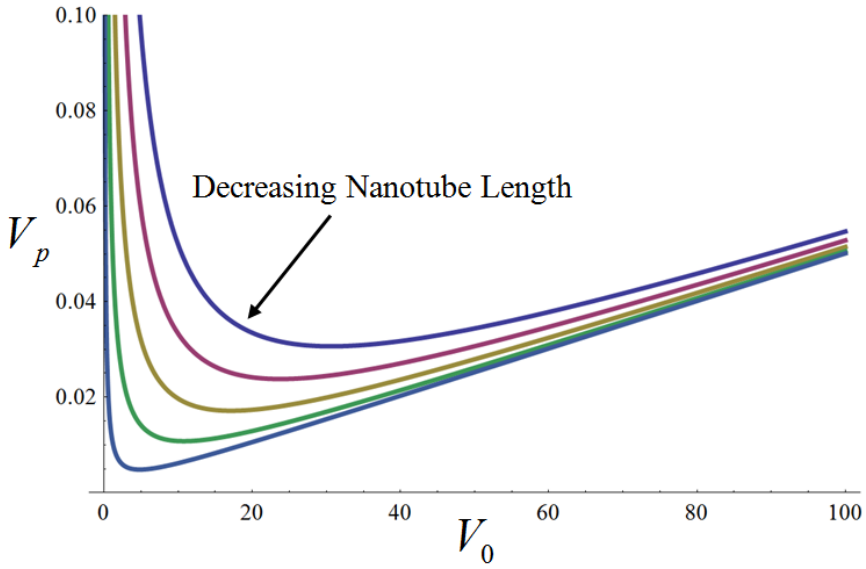

Figure 5.6: Gain Divergence, $V_p(V_0) = \frac{2k_0+fV_0^2}{2QfV_0}$, for $L = d_0 = 1, 2, 3, 4, 5$ μm, $r = 5$nm. The black arrow indicates the direction of decreasing nanotube length, L.

motion. In this way, our device functions as a band pass filter while simultaneously serving as a detector and an amplifier(Figure 5.7). Chip-based devices, as shown in Fig. 5.2, can be readily fabricated and engineered to operate in the 100 kHz - 1 GHz frequency band. We now look at a few examples of "signals" that can serve as inputs for our device.

5.4.1 A Tunable Electronic Band-pass Filter and Amplifier

The filtering properties of our device allow it to be used as an electronic bandpass filter. A sinusoidal voltage input, $V(t) = V_{in} \sin \omega t$, applied either to the nanotube electrode or the counter electrode in Fig. 5.3 will result in a force $F_{in} \propto \sin \omega t$. This force will have no effect on the motion of the nanotube, or the corresponding tunneling current output, unless its frequency is within $\Delta\omega_0$ of the resonance frequency of the nanotube, ω_0. Voltage signals within $\Delta\omega_0$ of ω_0 drive mechanical oscillations of the nanotube and result in time varying tunneling currents. This discriminatory behavior characterizes the filtering process.

The center frequency of the bandpass filter is voltage-tunable; Eq. 5.3 and the relation $k = m\omega_0^2$ yield

$$\omega(V_0) = \sqrt{\frac{1}{m}}\sqrt{k_0 + \frac{1}{2}\frac{d^2C(0)}{dx^2}V_0^2} \tag{5.18}$$

where m is the nanotube mass, and k_0 is unperturbed spring constant of the nanotube

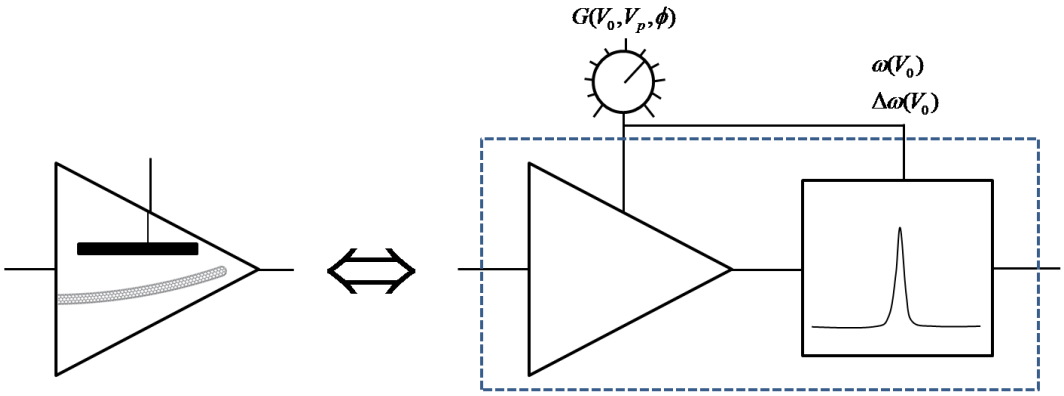

Figure 5.7: Schematic and Circuit Symbol of Carbon Nanotube-based NEMS Parametric Amplifier. A proposed circuit (left) symbol for our nanoelectromechanical carbon nanotube paramp which serves as a band-pass-filtered, variable-gain, phase-sensitive amplifier (right).

resonator, given by $k_0 = \frac{3\pi E r^4}{4L^3}$. The frequency can be increased by over 100% by tuning V_0 from 0 to 50 V, so that the center frequency can be easily tuned over the range ω_0 to $2\omega_0$, as reported for similar nanostructures in Ref. [23]. Note that this capacitive frequency tunability is in addition to the electrostatic tensioning of the nanotube that has been reported previously[15, 35]. The bandwidth of this filter, $\Delta\omega_0 = \omega_0/Q$, will also decrease with increasing frequency, and will be roughly 0.05-0.1 % of the center frequency. Thus, a 100 MHz filter with 100 kHz bandwidth (assuming a quality factor $Q = 1000$) can quite easily be voltage tuned to 200 MHz with 50 kHz bandwidth.

By turning on the parametric modulation (*i.e.* applying a non-zero V_p), the carbon nanotube device will now amplify current signals or serve as a voltage-current converter, given that the respective input signals are in the appropriate band. For instance, applying an AC voltage to the pump probe or the nanotube electrode at ω_0 will drive the nanotube into resonance (with an amplified response do to Δk) resulting in an AC current through the source-drain circuit path. Similarly, a current driven through the nanotube at ω_0 will modulate the static charge on the tube and, because of V_0, excite oscillations which are in turn amplified by the parametric pump.

The power required to operate the device is provided by the external battery (DC) supply. The power gain acquired by amplified signals comes from this external power supply. For a typical device, the power, $P = IV$, can be as high as $100\mu A \times 100V = 10$ mW, or as low as $10nA \times 10V = 100$ nW. The power gain in our device can be controlled by the source-drain current and/or by the pump voltage V_p. Also, the operational range for incoming signals will be limited by the current capacity of the nanotube, which is typically $\sim 10 - 100$ μA.

5.4.2 A Parametrically Amplified Nanotube Radio

Because of the voltage applied to the carbon nanotube, it is electrically charged and therefore sensitive to electromagnetic radiation. Detection of RF electromagnetic radiation by a suspended, field-emitting carbon nanotube has been reported in previous work [35]. Signal transduction in the so-called "nanotube radio" [35] occurs as describe above: The RF wave drives the nanotube into oscillation resulting in a current signal at the output of the device. As reported in [35], power gain, provided by DC voltage source, can be as high as 50 dB; this amplification is due entirely to details of the field emission process, and not any parametric modulation.

Parametric modulation adds improvements to the nanotube radio by adding a low-noise amplification stage–mechanical preamplification–prior to signal transduction. In principle, the sensitivity to incoming RF photons can be enhanced by several orders of magnitude, possibly by as much as a factor of $10^5 - 10^8$. Furthermore, a high-frequency device operated in the limit of high gain, in order to induce parametric self-oscillations, could conceivably be used to generate detectable RF dipole radiation. The device operated in the same high-gain, self-oscillation limit could also be used for time-keeping applications; for example, our device could function as a clock for digital microelectronics with frequencies as high as a few Gigahertz.

5.4.3 A Nanoelectromechanical Thermometer

Thermal noise in the nanotube device ultimately limits its fundamental sensitivity. However, the parametric amplification of the corresponding thermomechanical vibrations can prove quite useful. For instance, one can produce thermomechanically *squeezed* states [10, 22] by operating on one quadrature of the thermal noise. Here, we propose *dilating* one quadrature of the thermal noise for thermomechanical thermometry.

Reading out thermomechanical vibrations, whose amplitude is given by the classical relation $x_{rms} = (k_B T/k^2)^{1/2} = (k_B T/m\omega_0^2)^{1/2}$, can be quite challenging at low temperatures because of the small amplitudes involved and complications of measurement back-action. The parametric modulation in our system offers a method of amplifying the thermal noise with high gain and minimal back-action, and thus allows our system to function as a thermometer. The useful range of our carbon nanotube paramp thermometer would roughly be from 100 nK to 500 K (or the melting point of the metallic contacts used in the device.) As an example, a 10 μm long tube, 5 nm in radius and at a temperature of 100 mK will oscillate at about 1 nm; 50 dB of gain would make these vibrations about 150 nm, whose corresponding field emission current fluctuation would be much larger.

5.5 Parametric Amplification of Self-generated Voltage Fluctuations: Self-Oscillations Revisited

Parametric amplification offers a powerful way to analyze the phenomenon of self-oscillations seen in Chapter 4. We have already seen, as exemplified in Fig. 5.5, that in the presence of a large enough DC bias, V_0, a rather small AC pump amplitude, V_p, is required to produce large gain in the response. Given the device geometries that have been utilized in our experiments, the model predicts that this large gain can be achieved for $V_p < 10$ mV. We will now show that in the presence of an applied DC voltage, V_0, the position dependence of the field emission current creates self-generated *pump* and *drive* signals that, through a process of positive-feedback, can produce self-sustained oscillatory motion–self-oscillations.

The current of a field-emitting nanotube is sensitive to the position of the tip relative to the counter electrode (see §5.2.1.) For a nanotube device whose counter electrode is positioned in the lateral direction of the longitudinal axis of the nanotube (*i.e.* one in the "self-oscillation" configuration, as in Fig. 5.3), the Fowler-Nordheim equation (Eq. 3.6) predicts that the frequency of an oscillating nanotube will match the frequency of the field emission current signal. Therefore, a field-emitting nanotube oscillating at its nature frequency ω_0 will generate a current signal which varies at ω_0. As this alternating current passes through the rest of the circuit, the voltages at different nodes of the circuit will vary according to their resistance, capacitance, and inductance characteristics. In particular, ohmic drops across resistors in the circuits, given by $\Delta V = IR$, will cause the voltage across the nanotube to vary at ω_0. For example, a 100 nA AC current across a 100 KΩ nanotube contact resistance will generate a $\Delta V = 10$ mV variation across the nanotube. In this simple way, nanotube vibrations at ω_0 generate voltage variations across the nanotube at the frequency ω_0. Other sources of time varying potentials could be space-charge.

Including a DC bias ,V_0, and a field-emission induced AC voltage of amplitude V_f and frequency ω_0, the voltage across the nanotube is

$$V(t) = V_0 + V_f \sin(\omega_0 t) \tag{5.19}$$

The capacitive force corresponding to this voltage is,

$$\begin{aligned} F_C &= -\frac{1}{2}\left(\frac{dC(0)}{dx} + \frac{d^2C(0)}{dx^2}x\right) \\ &\quad \times \left(V_0^2 + 2V_0V_f \sin(\omega_0 t) + \frac{1}{2}V_f^2 - \frac{1}{2}V_f^2 \cos(2\omega_0 t)\right) \end{aligned} \tag{5.20}$$

where we have used the relation $\sin^2 x = \frac{1}{2}(1 - \cos 2x)$. Discarding constant and

off-resonant terms, we can write

$$\begin{aligned} F_C &= -V_0 V_f \frac{dC(0)}{dx}\cos(\omega_0 t - \pi/4) - \frac{1}{2}\frac{d^2C(0)}{dx^2}(V_0^2 + \frac{1}{2}V_f^2)x \\ &\quad -V_0 V_f \frac{d^2C(0)}{dx^2}\sin(\omega_0 t + \pi/4)x - \frac{1}{4}V_f^2\frac{d^2C(0)}{dx^2}\sin(2\omega_0 t)x \end{aligned} \tag{5.21}$$

Including damping terms, we obtain:

$$m\frac{d^2x}{dt^2} + m\frac{\omega_0}{Q}\frac{dx}{dt} + [k + \Delta k_1 \sin(\omega_0 t + \pi/4) + \Delta k_2 \sin(2\omega_0 t)]x = F\cos(\omega t - \pi/4) \tag{5.22}$$

where now

$$k \equiv k_0 + \frac{1}{2}\frac{d^2C(0)}{dx^2}(V_0^2 + \frac{1}{2}V_f^2) \tag{5.23}$$

$$\Delta k_1 \equiv V_0 V_f \frac{d^2C(0)}{dx^2} \tag{5.24}$$

$$\Delta k_2 \equiv \frac{1}{4}V_f^2\frac{d^2C(0)}{dx^2} \tag{5.25}$$

$$F \equiv -V_0 V_f \frac{dC(0)}{dx} \tag{5.26}$$

We recognize that Eq. 5.22 is in the form of the Mathieu equation studied earlier. Unlike the case studied in §5.2.2, the parametric modulation and driving terms are *not* provided by an *outside* supply, but generated from *within* the system. This "self-generation" is a unique consequence of the field emission current coupling strongly to the mechanical motion of the nanotube, and requires the dimensions of the device to be nanoscale.

The terms involving Δk_1 and Δk_2 will contribute independent amplification gain to the motional response of the nanotube nanocantilever. The Δk_1 term varies at ω_0 and corresponds to a relatively weaker sub-harmonic; however, its phase relative to the driving term is $\pi/2$, so its gain will be at its maximum possible value. The Δk_2 term corresponds to the fundamental harmonic ($2\omega_0$), though its gain will not be maximized because of its phase is $\pi/4$. Furthermore, the Δk_1 term will likely dominate since its pumping strength is proportional to $V_0 V_f$, as opposed to V_f^2, and experimentally $V_0 \gg V_f$.

We can now give a scenario in which parametric amplification can cause self-oscillations in our carbon nanotube NEMS device. We apply a DC bias, V_0, to the nanotube and approach the instability threshold voltage, V_{th}, given in Chapter 4. In this state, a typical device may field-emit around 1 μA of current at a bias of 40 V. Above V_{th}, the nanotube is pulled in toward the counter electrode, suddenly emits much more current, and then begins to vibrate due to the momentary drop

in its potential. So far, this description is analogous to plucking a guitar string a single time and allowing it ring, an analogy presented in Chapter 4. However, as the nanotube rings the voltage across it will have a time-varying component, and this component will generate an on-resonance driving force, whose amplitude is given by Eq. 5.26, which will sustain the oscillations, as small as they may be. The time-varying voltage will also generate parametric modulation, whose strength is given by Eq. 5.24, which then amplifies the mechanical vibrations. These larger mechanical vibrations then increase the amplitude of the time-varying voltage signal, which in turn gives rise to a larger driving force and pump strength. This process of positive feedback continues, and the amplitude of mechanical vibrations increases until the system reaches a limit cycle.

It is likely that during this feedback process the modulation strength Δk_1 will exceed levels that cause instability that is generally associated with self-oscillations [10, 15]. According to our model, values of V_f as small as 10 mV can drive the system into instability. This voltage is quite small compared to the voltage fluctuation that occurs when the nanotube gains or loses an excess electron, which, due the small capacitance of the nanotube system ($C \sim 1$ aF), is $\Delta V = e/C = 1.6 \times 10^{-19}/10^{-18}\, V = 160$ mV.

5.6 Summary

We have described a novel electromechanical nanotube-based parametric amplifier that integrates detection, amplification, and transduction functionality into a single, cantilevered carbon nanotube. The amplification and detection properties of the device are variable gain, phase-sensitive, low-noise, and voltage-tunable, whereas the device's bandwidth is determined by the quality factor of the nanotube mechanical resonator. In terms of applications, this device is quite versatile; it acts as a bandpass filter, an amplifier, an electromagnetic wave detector, or even as a thermometer. We have also argued that, under the right conditions, the parametric amplification in our system can explain the self-oscillations observed in previous studies (Chapter 4.)

The broad range of operation frequencies that are attainable in our system (100 kHz 10 GHz) make it versatile and attractive for a wide range of applications. Furthermore, most amplifier devices can exhibit "infinite" gain at pumping voltages less than 50 mV, and can have overhead power consumption as low as 100 nW, making them exceptionally low-power devices. In addition, the device's phase-sensitivity facilitates phase-filtering of signals, and the ability to operate in "self-oscillation mode can remove the reliance on external high-frequency inputs. Thus, this novel nanoscaled parametric amplifier has the potential to fill the need for voltage-controlled, ultra-low-power, ultra-low-noise, high-gain, room-temperature-operable amplifiers and detectors in the fields of electronics, wireless communications, optics, and thermometry.

Chapter 6

Non-Linear Behavior in Carbon Nanotube Mechanical Resonators

In this chapter, we report the *in situ* transmission electron microscopy (TEM) observation of dynamic non-linear behavior in carbon nanotube mechanical resonators. *In situ* TEM observation of static non-linear behavior was discussed in §2.4. Here, we observe the bifurcation phenomenon characteristic of a system obeying the Duffing equation by directly monitoring the vibrational amplitude of the carbon nanotube resonator using TEM. The nonlinear behavior likely originates from the capacitive coupling of the system and from the strain energy of the bent nanotube.

6.1 Introduction and Experimental Observations

The carbon nanotube mechanical resonators used in these experiments are composed of a single cantilevered multiwalled carbon nanotube; the nanotubes are typically 3-10 nm in radius and 1-5 μm in length. This carbon nanotube cantilever is then placed within 10 μm from a laterally-positioned metallic electrode. A schematic of the devices used in these experiments is shown in Figure 6.1. Devices are then mounted onto a TEM stage (manipulation or transport) for high resolution TEM observation. The stage is also equipped with electronic feedthroughs so that electrical signals can be sent in to probe the system.

To observe non-linear behavior, we first apply a DC bias to the metallic electrode which causes the nanotube to bend. In this bent state, we then apply a separate AC bias (using an AC-DC bias "T") and sweep the frequency around the fundamental vibrational frequency of the nanotube. As we sweep from below resonance, the amplitude of the vibrating nanotube increases in a way similar to the Lorentzian response of a simple harmonic oscillator. However, as the frequency is increased beyond resonance, the amplitude of the nanotube quickly decreases. In a reverse sweep (*i.e.* starting from above resonance and decreasing the frequency), the nanotube's

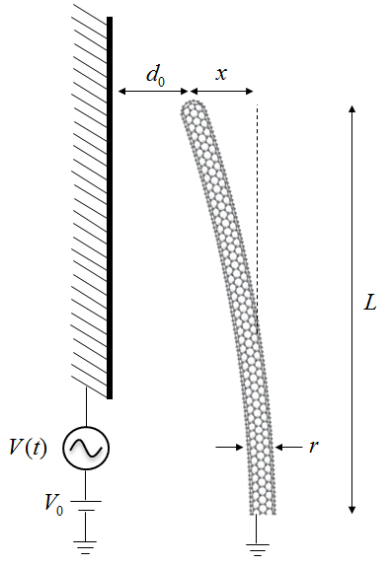

Figure 6.1: Device Schematic for Carbon Nanotube Resonator

vibrational amplitude increases slowly and then suddenly jumps to a higher value. Continuing the sweep, the amplitude then gradually decreases until no vibrations are observed. The sudden changes in oscillation amplitude, sometimes referred to as bifurcation "jumps", are indicative of a system possessing some degree of non-linearity. Figure 6.2 shows TEM images of the nanotube in the bent state (a), vibrating with maximum amplitude during upward sweep (b), and vibrating with maximum amplitude before the jump to a higher amplitude (c).

Bifurcation jumps can occur in a system when its elastic response becomes "softened" or "hardened". Such a system will deviate from pure linear (*i.e.* Hookean) behavior as higher order terms begin to contribute to its response. We now summarize a few general properties of non-linear systems, and then we discuss possible sources of non-linearity in our system.

6.2 Basic Nonlinear Behavior: The Duffing Equation

Bifurcation jumps in the amplitude-frequency response can arise when a force cubic in the displacement acts on the system. Adding a cubic force to the driven simple harmonic oscillator yields the driven *Duffing* equation:

$$\frac{d^2x}{dt^2} + \gamma\frac{dx}{dt} + \omega_0^2 x + \omega_0^2 K x^3 = \frac{f_0}{m}\cos(\omega t) \tag{6.1}$$

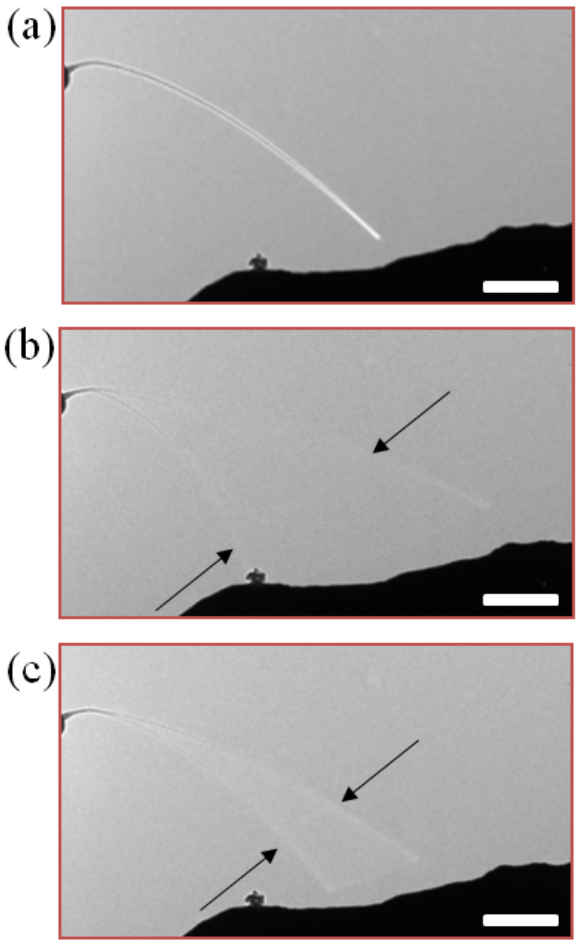

Figure 6.2: TEM Sequence of Hysteretic Behavior in CNT Resonators. (a) Biased CNT (b) Maximum Amplitude during upward sweep. (c) Maximum amplitude before jumping to higher state.

For solutions of the form $x = A\cos(\omega t+\phi)$, the oscillation energy E ($E \propto A^2$) satisfies

$$E^3 - \frac{4\delta}{\kappa}E^2 + \left(\frac{1}{Q^2\kappa^2} + \frac{4}{\kappa^2}\delta^2\right)E - \frac{f_0^2}{m^2\kappa^2} = 0 \tag{6.2}$$

and the phase ϕ satisfies

$$\begin{aligned} \tan\phi &= \frac{\gamma(1+\delta)}{2\omega_1\delta - 3\omega_1 K_3 E/4} \\ &= \frac{1}{Q}\frac{1+\delta}{2\delta - \kappa E} \end{aligned} \tag{6.3}$$

where the detuning parameter, δ, is defined by $\omega = \omega_0(1+\delta)$, $\kappa = 3K/4$, and $Q = \omega_0/\gamma$. Appendix C gives a derivation of Eqs. 6.2 and 6.3.

Figure 6.3 shows E vs. ϕ for a fixed driving force, f_0, and varying degrees of nonlinearity, K. The center blue curve shows the response in the linear ($K = 0$) regime. With increasing K, the curve leans to the left (curves in Fig. 6.3 correspond to a softened spring, this is $K < 0$, so we speak of increasing magnitude; a stiffened spring, $K > 0$, would cause curves to lean toward positive δ.) resulting in multi-valued solutions for E. This multi-valued solution causes the system to jump discontinuously from one branch of the curve to another and describes the jumps we observe in our experiments.

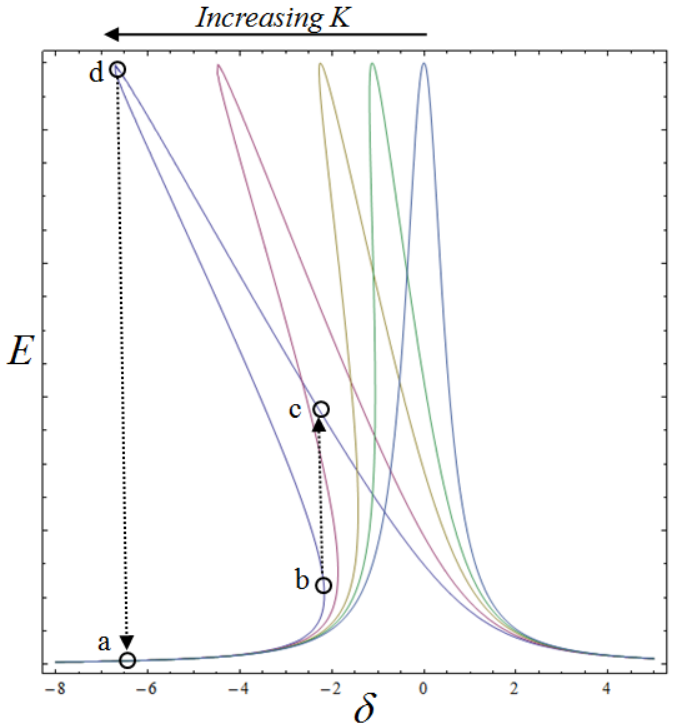

Figure 6.3: Amplitude-Frequency Response for a Softened Spring given by Duffing Equation, E vs. δ. The graphs increase (right to left) in degree of nonlinearity, K. At sufficiently high nonlinearity strength, the response curve becomes multi-valued. The labeled points on the left most curve indicate where the system would transition (jump) discontinuously from one stable amplitude to another. From a to b the system is stable, then jumps from b to c. The system is then stable on the upper branch of the curve near c. Decreasing the frequency from c to d, the system will then jump to the lower curve.

The response possesses hysteresis. The labeled points on the left most curve indicate where the system would transition (jump) discontinuously from one stable amplitude to another. From a to b the system is stable, then jumps from b to c.

The system is then stable on the upper branch of the curve near c. Decreasing the frequency from c to d, the system will then jump to the lower curve. The portion of the curve between b and d is unstable.

6.3 Sources of Nonlinearity

The cubic term in Eq. 6.1 can arise from the nonlinear nature of the capacitive force. The capacitance for the device configuration in Fig. 6.1 can be approximated with the expression

$$C(x) = \frac{2\pi\epsilon_0}{\ln\left(\frac{4d_0(1-x/d_0)}{r}\right)}L \tag{6.4}$$

This expression can be Taylor-expanded around the equilibrium position of the nanotube, x_0,

$$\begin{aligned} C(x) = C(x_0) + \frac{dC(x_0)}{dx}(x-x_0) + \frac{1}{2}\frac{d^2C(x_0)}{dx}(x-x_0)^2 \\ + \frac{1}{3!}\frac{d^3C(x_0)}{dx}(x-x_0)^3 + \frac{1}{4!}\frac{d^4C(x_0)}{dx}(x-x_0)^4 + \cdots \end{aligned} \tag{6.5}$$

Eq. 6.5 can be used to obtain the cubic term in the capacitive force:

$$F(\Delta x) = -\frac{1}{2}\frac{1}{3!}\frac{d^4C(x_0)}{dx}V^2\Delta x^3 \tag{6.6}$$

where we can evaluate

$$\frac{d^4C(x_0)}{dx} = f(x_0)\frac{1}{\left(1-\frac{x_0}{d_0}\right)^4} \tag{6.7}$$

where $f(x_0)$ is a relatively slowly increasing function of x_0. From Eq. 6.7, we see that as the tube bends in closer to the biased electrode (i.e. as $x_0 \to d_0$), the strength the cubic term increases dramatically. Thus, in the bent state (Fig. 6.2 (a)) the nanotube is in an extremely nonlinear state, given that x_0 is very close to d_0.

The flexing of the beam can also introduce additional nonlinearity. The motion of a vibrating beam was discussed in Chapter 2; the displacement of the beam at position z along the length of the beam is $U(z,t) = a(t)u(z)$ where $u(z)$ are normalized mode shapes plotted in Fig. 2.9 and $a(t)$ contains information regarding amplitude and time-dependence. The elastic strain energy density for a bending beam is approximately $\frac{1}{2}E\epsilon^2$ (Recall from Chapter 2 that the compression spring constant of a beam is $k = AE/L$, where A is the cross-sectional area, L is the length, and E is the Young's Modulus; then the energy is $\frac{1}{2}kx^2 = \frac{1}{2}\frac{AE}{L}\Delta L^2 = \frac{1}{2}EAL\frac{\Delta L^2}{L^2} = \frac{1}{2}E\epsilon^2AL$, giving the strain energy density $\frac{1}{AL}\frac{1}{2}kx^2 = \frac{1}{2}E\epsilon^2$.) For a bending beam, the strain is approximately [21]

$$\epsilon = -x\frac{d^2U(z,t)}{dz^2}$$

Performing the volume integral over the differential arclength of the beam $dl = \sqrt{dz^2 + dU(z)^2} = \sqrt{1 + \left(\frac{dU}{dz}\right)^2}\, dz$, the total potential energy due to strain is

$$\begin{aligned} V &= \frac{E}{2}\int x^2 \left(\frac{d^2U(z,t)}{dz^2}\right)^2 dl\, dA \\ &\approx \frac{E}{2}\int x^2 \left(\frac{d^2U(z,t)}{dz^2}\right)^2 \left(1 + \frac{1}{2}\left(\frac{dU(z,t)}{dz}\right)^2\right) d\mathbf{r} \\ &= \frac{E}{2}\int x^2 \left(\frac{d^2U(z,t)}{dz^2}\right)^2 d\mathbf{r} + \frac{E}{4}\int x^2 \left(\frac{d^2U(z,t)}{dz^2}\right)^2 \left(\frac{dU(z,t)}{dz}\right)^2 d\mathbf{r} \\ &= \frac{Ea^2(t)}{2}\int x^2 \left(\frac{d^2u(z)}{dz^2}\right)^2 d\mathbf{r} + \frac{Ea^4(t)}{4}\int x^2 \left(\frac{d^2u(z)}{dz^2}\right)^2 \left(\frac{du(z)}{dz}\right)^2 d\mathbf{r} \\ &= \frac{EI_1}{2}a^2(t) + \frac{EI_2}{4}a^4(t) \end{aligned} \tag{6.8}$$

Under the Lagrangian formalism, the force associated with this energy, $F_V = -\frac{dV}{da}$, is

$$F_V = -EI_1 a(t) - EI_2 a^3(t) \tag{6.9}$$

The first term in Eq. 6.9 is the linear term, and the second is the cubic term that causes the nonlinear behavior in our system. Note that this term arises from the beam stretching so that $dl \neq dz$. One could calculate the strength of the this nonlinearity by using Eq. 2.21, which gives $u(z)$ explicitly, to evaluate the integral I_2. I_2 will increase as the nanotube beam becomes more curved, and thus is expected to increase as the nanotube is bent. Electrostatic tensioning, as discussed in §2.4, would lead also lead to beam lengthening and a similar non-linearity.

6.4 Summary

In conclusion, we have reported the TEM observation of bifurcation jumps in the amplitude of a vibrating carbon nanotube mechanical resonator. We have modeled the system with the driven Duffing equation, and see that multi-valued solutions for the amplitude-frequency response function occur when the system contains a cubic nonlinearity. These multi-valued solutions describe the hysteresis and discontinuous jumping that we observe in our experiments. Cubic terms in our system are seen to arise from the capacitive coupling of the nanotube to a nearby electrode, and also from the stretching of the nanotube beam that occurs under flexural bending. The strength of these nonlinearities increases with beam bending, in accord with our experiments.

Part IV

Graphene NEMS

Graphene's large surface area, low mass, and high strength make graphene membranes ideal resonant elements for NEMS. In the next chapters, we report two novel, high-yield methods to fabricate suspended graphene membranes, and use optical interferometry to demonstrate their use as NEMS resonators. The membrane's lack of a backing substrate facilitate characterization by transmission electron microscopy (TEM) which allows, for the first time, one to correlate atomic and molecular scale physical properties of the graphene membrane to its performance as a mechanical resonator. We exploit this capability, and show that nanoscale contamination, membrane defects, and folded membrane structures as seen in TEM can explain an observed vibrational mode degeneracy splitting. Apart from the graphene membrane's clear utility as a TEM sample support, we demonstrate their durability by using them as a platform for atomic force microscopy (AFM) studies.

Chapter 7

Suspended Graphene Membranes

The preparation of suspended graphene structures has been a great focus of researchers attempting to probe the two-dimensional properties of graphene[62, 63, 64, 65]. These structures facilitate the exploration of graphene's fundamental properties [6-16] as well as nanomechanical [69, 79] and electronic [76, 74, 67] applications not possible with substrate-bound graphene. Until the advent of CVD graphene[82], suspended graphene structures[68, 69, 71, 74] were fabricated using low-yield, serial processes from mechanically exfoliated graphene[62]. In this chapter, we present two simple methods that produce high-quality single-layer graphene membranes in high yield. The first method forms graphene membranes by directly patterning the copper support used to grow CVD graphene, and thus avoids the use of secondary substrates (such as silicon) or graphene transfer. This transfer-free method is scalable and produces graphene membranes in high yield (> 75 %) with controllable diameters ranging from 20-60 μm. The second method creates suspended graphene structures by transferring CVD graphene without the use of polymers to a pre-patterned perforated substrate, and is useful for smaller width graphene structures ranging from 1-7 μm. The suspended graphene structures generated by these methods will facilitate access to the two-dimensional physics of graphene that are suppressed by substrate interactions, and enable the widespread use of graphene-based sample supports for electron, optical, and scanning probe microscopy. In chapter 8, we demonstrate the use of these graphene membranes as NEMS resonators.

7.1 Graphene Synthesis by Chemical Vapor Deposition

Graphene was first isolated by mechanical exfoliation[62]. In this simple process, researchers used scotch tape to remove thin graphite flakes from pieces of graphite, and then rubbed these flakes onto silicon dioxide in order to optical identify single layer graphene. Although mechanical exfoliation has produced relatively pristine

specimens of graphene, the serial nature of the process precludes the possibility of large-scale graphene production. Epitaxial graphene, generated by the high temperature reduction of silicon carbide[94], is scalable but doesn't easily produce suspended graphene structures. In 2009, Li *et al.* [82] reported a scalable process to produce large-area poly-crystalline graphene films on copper by low pressure chemical vapor deposition (CVD). The suspended graphene structures that we fabricate in this chapter were produced using CVD graphene. We now give a brief overview of this CVD-growth process.

The CVD synthesis of graphene on copper is facilitated by carbon's low solubility in copper at elevated temperatures ($\sim$1000° C). At these high temperatures, copper absorbs just enough carbon (carbon is produced by "cracking" a hydrocarbon gas, such as methane, in the high temperatures of a CVD furnace) to produce a floating monolayer in the near-molten surface of the copper substrate. Upon cooling, the carbon monolayer crystalizes to form mostly single layer graphene on the surface of the copper.

In this work, we place 10 μm or 25 μm thick Cu foils (99.8 % Alfa Aesar, Ward Hill, MA 01835, USA) into a CVD furnace evacuated to a base pressure of $\sim$ 50 mTorr under a steady 2 sccm flow of H_2 gas. The furnace is ramped up to 1000 ° C over 30 minutes and then CH_4 gas is introduced at 35 sccm for 30 minutes during which graphene growth occurs. The furnace is then allowed to cool and the graphene-copper foil is removed.

7.2 Fabrication of Suspended Graphene Membranes: Transfer-Free Batch Fabrication Method

We demonstrate a process for batch production of large-area (100 - 3000 μm^2) patterned free-standing graphene membranes on Cu scaffolds using chemical vapor deposition (CVD)-grown graphene. This technique avoids the use of silicon and transfers of graphene. As one application of this technique, we fabricate transmission electron microscopy (TEM) sample supports. TEM characterization of the graphene membranes reveals relatively clean, highly TEM-transparent single-layer graphene regions (50% by area) and, despite the polycrystalline nature of CVD graphene, membrane yields as high as 75-100%. This high yield verifies that the intrinsic strength and integrity of CVD-grown graphene films is sufficient for sub-100 ?m width membrane applications. Elemental analysis (electron energy loss spectroscopy (EELS) and X-ray energy-dispersive spectroscopy (EDS)) of the graphene membranes reveals some nanoscaled contamination left over from the etching process, and we suggest several ways to reduce this contamination and improve the quality of the graphene for electronic device applications. This large-scale production of suspended graphene

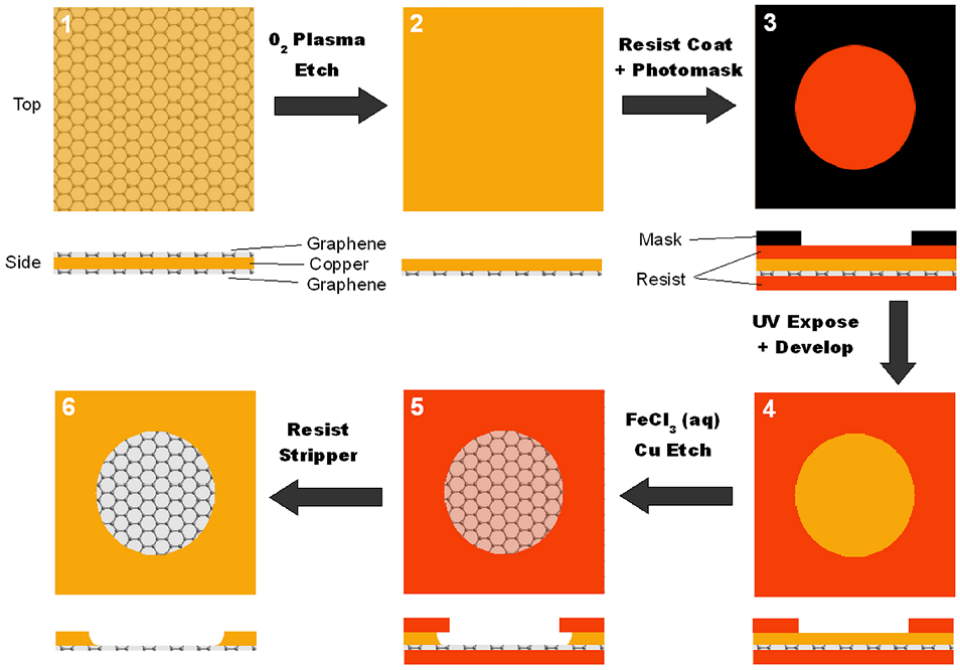

Figure 7.1: Process flow diagram for transfer-free suspended graphene membrane fabrication on Cu. The top and bottom of each image corresponds to the plan view and side view of the substrate, respectively. 1) CVD synthesized graphene grown on Cu. 2) Graphene from one side of Cu is removed with an oxygen plasma etch and 3) both sides of the substrate are coated in photoresist. Conventional photolithography is used to pattern the resist on the Cu side of the substrate to 4) expose the mask-defined regions of the Cu. 5) A ferric chloride solution etches the Cu down to the underlying graphene resist. The remaining photoresist is stripped resulting in 6) a patterned, suspended graphene membrane.

membranes facilitates access to the two-dimensional physics of graphene that are suppressed by substrate interactions, and enables the widespread use of graphene-based sample supports for electron and optical microscopy.

7.2.1 Details of Fabrication

Our suspended graphene membrane fabrication process (scheme shown in Figure 7.1) begins with low pressure chemical vapor deposition (CVD) of methane and hydrogen to grow graphene on 10 μm and 25 μm thick Cu foils as described above. Since the CVD process coats both sides of the foil with graphene, we remove the graphene from one side of the Cu foil using an oxygen reactive ion etch(Plasma Etch, Inc., USA); 50 sccm of O_2 at 50 Watts for 20 seconds removes the top-side graphene.

Both sides of the foil are then coated with positive photoresist: 1 μm of resist (Rohm & Haas Megaposit SPR 955-CM-0.9, MicroChem Corp., Newton, MA, USA) is spun onto substrates at ∼2000 rpm and baked at 110° C for 90 seconds. A photomask with the desired dark-field pattern is placed over the resist/Cu side of the substrate, which is then given an appropriate UV exposure (175 mJ/cm^2 i-Line dose). The samples are then post-baked at 110° C for 90 seconds and then immersed in wet developer(1-3.5% TMAH (OPD 4262, Arch Chemicals, USA)) for 60 seconds. The resulting exposed patterned regions of the Cu surface are then etched by submersing the foil in an aqueous solution of $FeCl_3$(0.1 g/mL aqueous solution of iron(III) chloride hexahydrate (ACS reagent grade 97%, Sigma-Aldrich, USA)), followed by light agitation with a small stir rod. The etching process is complete when the etch reaches the graphene, approximately 7 minutes for 10 μm thick Cu foils and 20 minutes for 25 μm thick Cu foils. Longer etching times cause the hole diameters to further dilate, and local variations in foil thickness and solution agitation lead to some variation in hole diameters (see Figure 7.2 (b), (c)). Finally, the patterned foil is thoroughly rinsed in deionized water to remove traces of the etchant, immersed in hot acetone (60° C) to strip photoresist, rinsed in isopropyl alcohol, and allowed to air dry.

7.2.2 Proof-of-Concept: Fabrication of TEM Sample Supports

As a proof-of-concept, we use this direct patterning technique to fabricate conventional TEM sample supports (TEM "grids") consisting of 3.1 mm diameter Cu disk with suspended graphene spanning a centered 9 x 9 array of patterned circular holes (Figure 7.2 (b)). After fabrication, the sample supports remain connected to the foil by two small tabs that can be cut to free the TEM grid. The area of the Cu foils used in this work was limited by the inner-tube radius of CVD quartz tubes to about 2 cm^2, which generated four loosely spaced TEM grids. The total substrate real-estate of a TEM grid is about 0.1 cm^2, so using a tighter spacing than was used in this work could produce as many as 20 TEM grids per 2 cm^2 foil. With larger diameter tube furnaces or by inserting rolls of Cu sheets into a furnace, our process could be used with much larger area foils to produce thousands of graphene-based TEM sample supports on a single 100 cm^2 foil. This increase in yield is a several-orders-of-magnitude improvement over conventional serial preparation of graphene TEM grids or suspended graphene membranes.

The yield of intact graphene membranes depends strongly on the hole diameter. For 30-60 μm diameter holes (area ∼ 1000-3000 μm^2), we were able to attain yields–that is, regions of intact suspended graphene–of 75% using 25 μm thick foil, while nearly all the membranes on the 10 μm thick foils had failed. However, when hole diameters are reduced to about 20 μm (area ∼ 300 μm^2) the 10 μm thick foil yield improves to ∼ 60% and the 25 μm thick foil yield surpasses 90% . For hole diameters

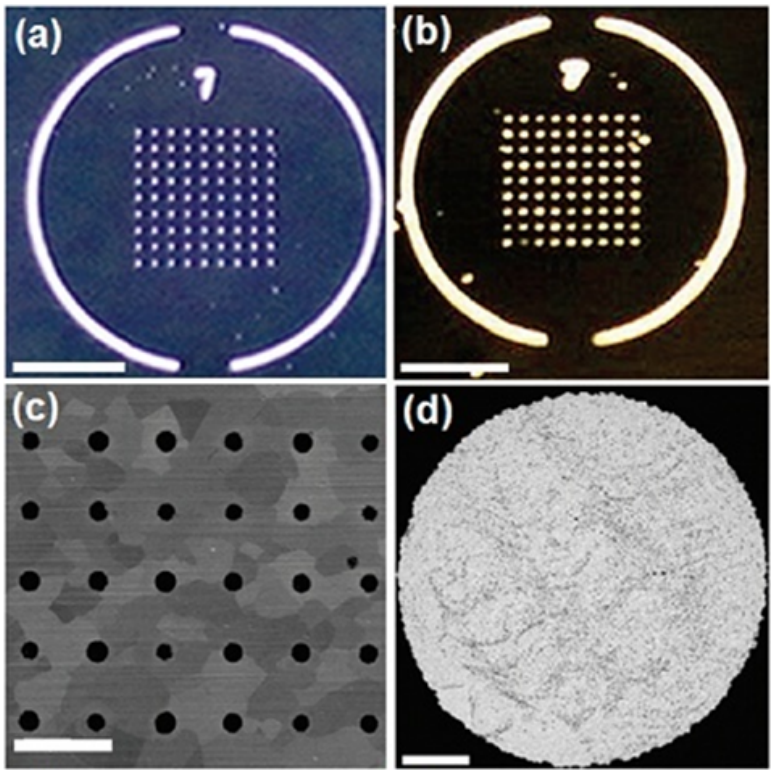

Figure 7.2: Lithographically defined graphene TEM sample supports. (a) One of the repeating elements of the photomask used to create an array of TEM grids (scale bar: 1 mm). (b) A back-side illuminated optical image of 3.1 mm diameter TEM grid produced using the procedure outlined in Scheme 1 with the photomask from (a). The Cu tabs can be cut with a razor blade to remove the grid to be used in a conventional TEM sample stage. The patterned "7" indicates the graphene side of the grid (scale bar: 1 mm). (c) Scanning electron micrograph shows etched holes and Cu grains on 25 μm thick foils (scale bar: 200 μm). (d) TEM of a 55 μm diameter graphene membrane. Cu nanoparticles left from an incomplete etching process help visualize the graphene. A small tear in the lower left side of the membrane contrasts vacuum with clean regions of the membrane (scale bar: 10 μm).

> 15 μm, we observe that both 10 μm and 25 μm thick foils produce intact graphene membranes nearly 100% of the time. The yield's dependence on foil thickness may be related to the disparate Cu grain sizes seen in the 10 μm and 25 μm thick foils, a result of different foil manufacturing conditions. We found that the annealed (post-graphene growth) 10 μm and 25 μm thick Cu foils have grains on the order of 10 μm^2 and 100-1000 μm^2, respectively, as can be seen from the SEM micrographs in Figure 7.2 (c) for the 25 μm thick foil. Smaller Cu grains may lead to smaller graphene domains and/or a higher graphene "wrinkle" density, producing weaker graphene films which are more easily destroyed during wet processing. Previous work[66, 67] on exfoliated single-crystal graphene generated membranes up to several tens of microns in width by using critical point drying techniques. We note here that suspended CVD-grown polycrystalline graphene survives rather harsh wet chemical etching and drying without the use of critical point techniques, confirming not only the robustness of single grains but also the interaction strength between adjacent grains.

Many membranes are fully intact or have tears that remove only 5-35% of membranes, as can be seen in Figure 7.2 (d), although tear-free membranes are more prevalent when their width is on the order of 15 μm or less. In Figure 7.2 (d), the graphene sheet is made visible at low magnification by small Cu particles left by an incomplete etch. Despite the contamination shown in Figure 7.2 (d), the sample is often highly clean on the nanoscopic scale (see Figure 7.7, with atomically clean single layer graphene regions on the order 10^4 nm^2. We note that these atomically clean regions are as large as or larger than have been previously reported[66, 67, 80, 83, 84] and that the Cu particulate contamination can be further abated with a post-etch HCl bath.

Variations in hole diameter are mainly caused by the isotropic nature of the $FeCl_3$ etch, which under ideal conditions (precise timing, controlled etchant concentration and temperature, uniform fluid agitation, *etc.*) would lead to radial dilation equal to the Cu foil thickness - thus, suspended graphene regions with a diameter equal to the mask-defined diameter plus twice the Cu foil thickness. The dilation can be seen from the SEM image shown in Fig. 7.3. Non-uniform fluid agitation (especially near the resist etch mask) causes non-uniformities across the foil, with smaller features often being under-etched. Since we used large, uniformly-etched features as a visual gauge to cease etching, we often observe unusually low dilation in the array of small suspended graphene regions. As shown in Figure 7.2 (c), we see dilation of approximately 21 ± 5 μm compared to the 50 μm diameter dilation expected for 25 μm thick Cu foils, in addition to the 15 μm diameter holes defined by the photomask. Variations in the foil thickness, determined by atomic force microscopy to be less than 100 nm (Figure 7.4), have a negligible contribution to the overall hole diameter variations. Also, scanning electron micrographs of hole underside (see Fig. 7.3) show that the etched pits of the Cu are not smooth but contain grains as large as 3 μm in diameter; this roughness can also be seen in the edges of the membrane shown in Figure 7.2 (d). This roughness puts a lower bound on the size of suspended

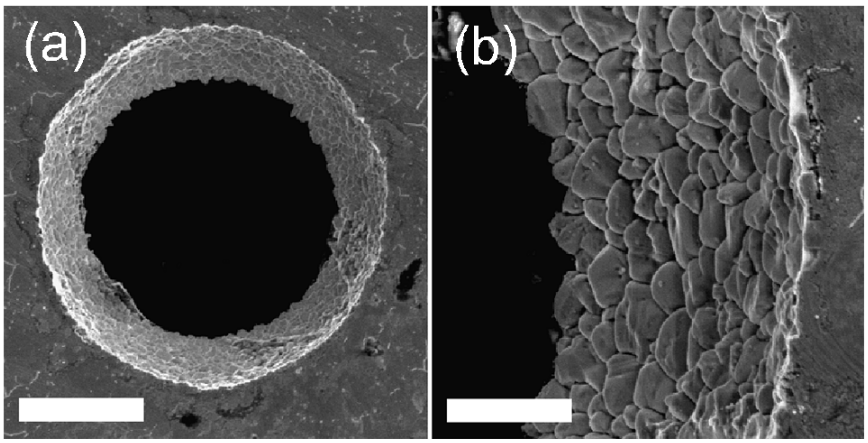

Figure 7.3: . (a) Scanning electron micrograph of the backside an etched 25 μm thick copper foil (scale bar: 20 μm). (b) Higher magnification scanning electron micrograph of the backside of an etched feature shows that the sidewalls of the feature are fairly coarse. This coarseness sets a lower limit on the feature resolution one could obtain using the technique outlined in the main manuscript (scale bar: 5 μm).

graphene regions that can be reproducibly fabricated with this technique. However, a slightly more complex microfabrication pathway would lead quite easily to more precisely defined suspended structures. For example, by the appropriate use of a thin-film material and its corresponding etchant (e.g. silicon dioxide/HF), one could define a secondary support scaffold with features approaching the current limitations of photolithography or electron beam lithography.

7.3 Fabrication of Suspended Graphene Membranes II: Transfer to Commercial TEM Grid

The transfer-free approach described above is a viable method for large-scale production of graphene membranes. However, this method is currently most useful for creating large diameter (¿15 μm) membranes. Therefore, we develop a method for the fabrication of small diameter graphene membranes that, although involving a graphene transfer step, utilizes CVD graphene and still retains the potential for scalability. In this method, CVD graphene is transferred from the copper foil to a substrate pre-patterned with holes. In principle, the substrate can have holes, trenches, or wells of any size and shape with very little material composition restrictions. A similar transfer technique has produced graphene membranes in high-yield over trenches in silicon dioxide[96], though the presence of a substrate underneath

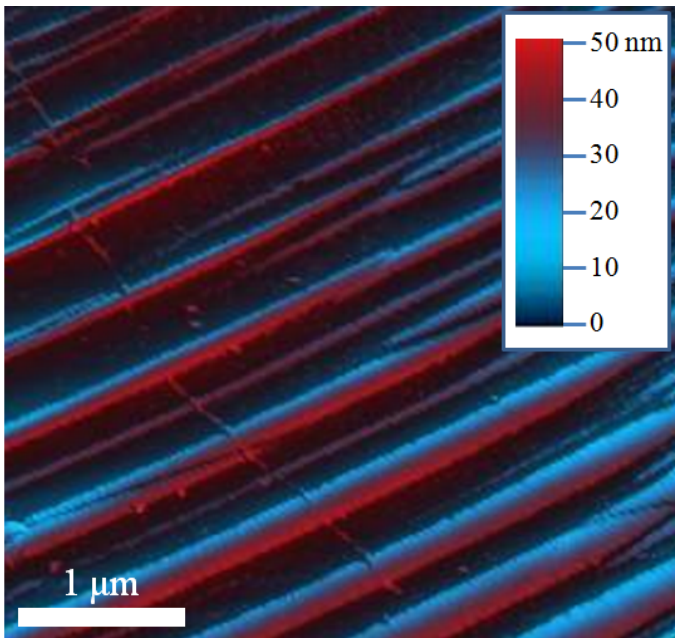

Figure 7.4: AFM of Copper Surface After Graphene Deposition

the suspended graphene structure precludes the possibility of TEM characterization. Furthermore, transfer to silicon (or other hard substrates) requires that the graphene first be transferred to a flexible polymer, such as PMMA. Transfers involving polymers often contaminate the graphene surface in a nearly irreversible way. Therefore, we utilize a polymer-free direct-transfer of CVD graphene to commercial TEM grids developed by Regan *et al.* [95] that produces circular and square membranes ranging from 1-7 μm in width in high yield, without excess polymer contamination, and compatible with TEM *and* AFM.

The polymer-free direct-transfer method is summarized in Figure 7.5. We begin with a bare gold-coated commercial TEM grid with a carbon mesh pre-patterned with circular holes or squares (QUANTAFOIL® Holey Carbon Grids, Ted Pella, www.tedpella.com). Circular holes come in 1.2 μm and 2 μm sizes, and squares are 7μm on a side. The grid is positioned over a piece of graphene/copper foil from the CVD growth process and covered with drop of isopropyl alcohol. As the alcohol dries, the grid and foil bind together; the graphene likely π-stacks with the carbon film to form a strong bond. The grid/foil is now placed into copper etchant (aqueous solutions of iron chloride or sodium perchlorate both work well). The copper foil is allowed to etch away completely, leaving the graphene adhered to the grid. The graphene grid is then rinsed in deionized water and isopropyl alcohol, and allowed to dry.

Figure 7.6 shows SEM images of TEM grids after graphene transfer. From Figure

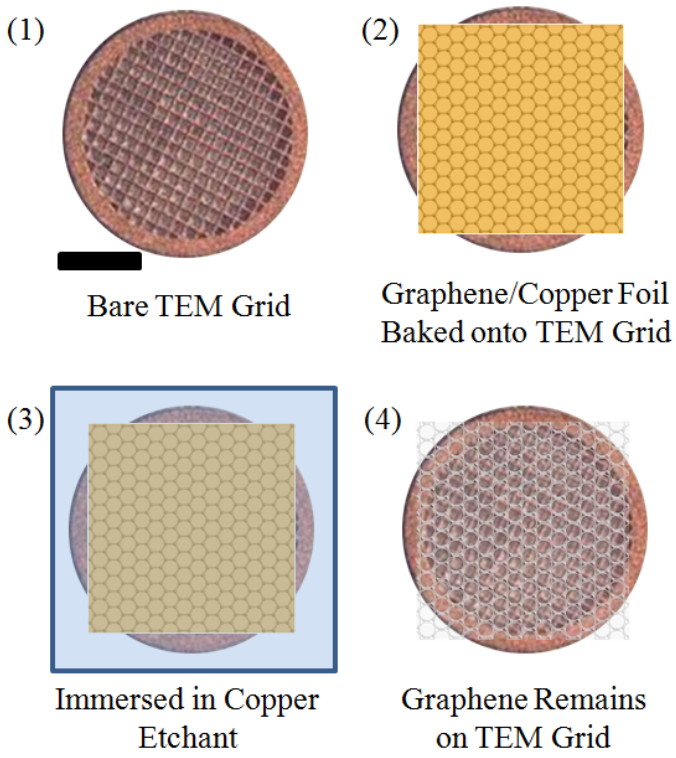

Figure 7.5: Transfer of CVD Graphene to TEM Grid. Step (1) Bare TEM grid (scale bar 1 mm), (2) Graphene/Copper adhered to TEM grid first by placing drop of isopropyl alcohol onto grid and then foil then baked, (3) immersed into copper etchant, (4) graphene is transferred to TEM grid with no remaining copper.

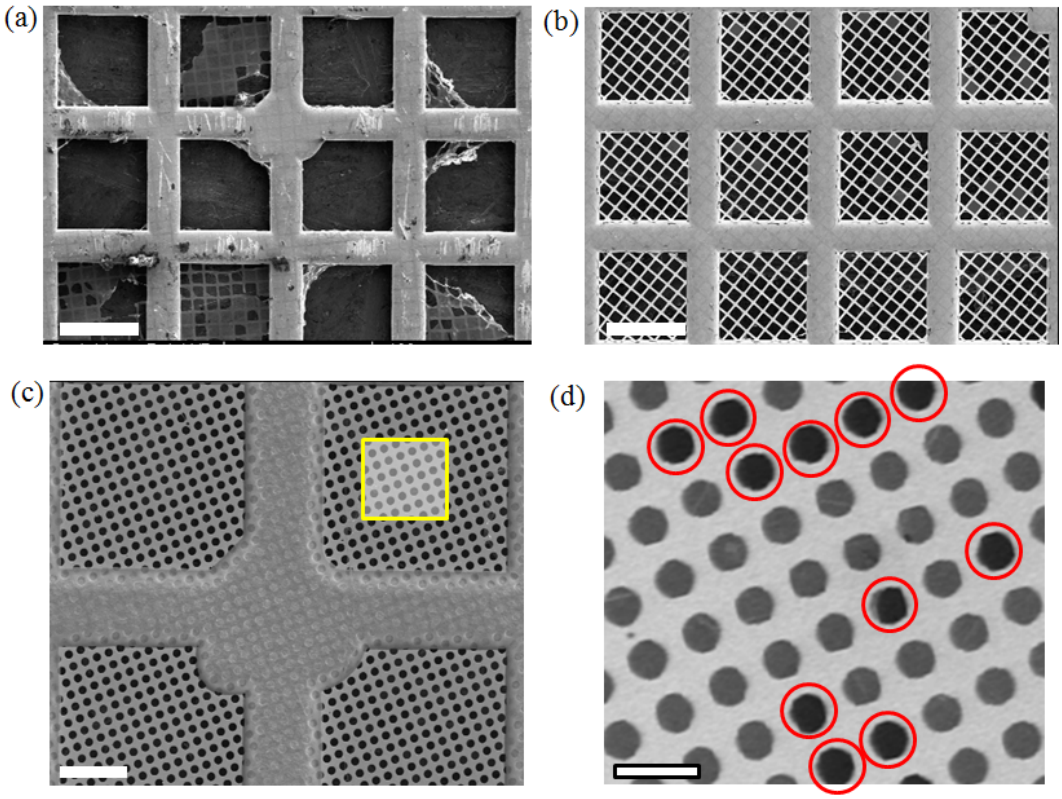

Figure 7.6: SEM of Graphene Membranes Made by Graphene Transfer. (a) No metal-reinforcement (scale bar 50 μm), (b) metal-reinforced (scale bar 50 μm), (c) 2 μm holes (scale bar 20 μm) and (d) higher magnification of 2 μm holes showing high yield (scale bar 5 μm).

7.6 (a), it is clear that the yield of intact 7 μm squares is quite low. The low-yield is due to the amorphous carbon film collapsing during the transfer process. The carbon film can be reinforced by evaporating material ($\sim$100 nm Au used here) onto its backside before the transfer process, leaving the other side of the carbon film free to bind with the graphene. The increase in yield is evident form Figure 7.6 (b). The carbon film with 2 μm circles survives the transfer process more efficiently, with nearly all regions remaining intact ((Figure 7.6 (c)). SEM can be utilized to differentiate intact graphene membranes from broken membranes, as can be seen in Figure 7.6 (d); intact membranes appear light gray while broken membranes appear black (outlined in red circles for clarity). Yield of intact membranes using the transfer process generates more than 10,000 individual graphene membranes.

7.4 TEM characterization of Membranes

We characterize the quality and crystallinity of the graphene membranes fabricated using the two above techniques using high-resolution TEM and electron beam diffraction. We find that approximately 50% of the graphene surface is covered with islands of amorphous material (Fig. 7.7 (a)), which is similar to earlier reports on graphene TEM grid preparation[84]. Electron diffraction analysis (Fig. 7.7 (b)) in such clean regions of the membranes indicates that it has the hexagonal crystal structure of graphene's honeycomb lattice, though additional rotated diffraction spots do appear in some regions which suggest the presence of complex lattice orientations, most likely from multiple graphene grains, graphene multilayers, or pleaded graphene structures ("grafolds"[97]) intersecting the beam path. Furthermore, we observe a weak monotonic character of the diffraction peak intensities with tilt angle, which establishes the suspended regions as mostly single-layer graphene, in accord with Meyer *et al.* [67].

The TEM transparency of clean single-layer graphene is evident from Figure 7.8(a) which shows a membrane near a region of free space. The image's grayscale intensity distribution in regions of graphene (red dot/curve in Figure 7.8 (a)/(b)) closely resembles regions of free space (blue dot/curve in Figure 7.8 (a)/(b)). The shift from vacuum and broadness of the intensity distribution of the amorphous regions (gray dot/curve in Figure 7.8 (a)/(b)) is similar to that of commercial amorphous carbon and Si_3N_4 thin film sample supports and makes it difficult to image low-contrast entities such as biological molecules or low atomic number elements. Graphene's relatively narrow intensity bandwidth and well-defined crystallinity thus enable TEM and diffraction of low contrast objects.

For some applications, such as for TEM imaging, the membranes fabricated by the methods described above can be used directly, while for others, such as for sensing or electronic device applications[87], it may be desirable to reduce certain kinds of surface contamination. Therefore, it is instructive to know what contaminants remain

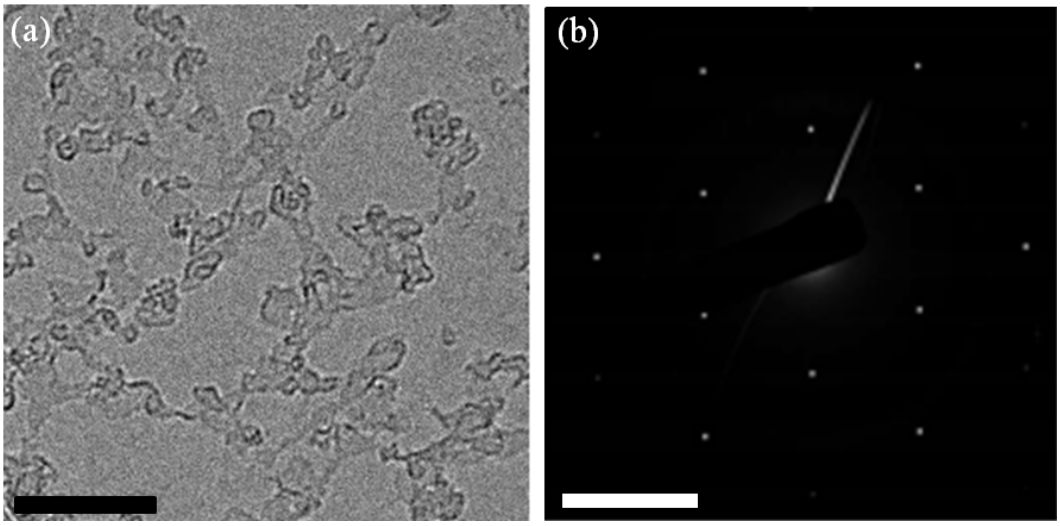

Figure 7.7: High-resolution transmission electron micrograph of a suspended graphene membrane. (a) Higher magnification TEM of a large clean region of a graphene membrane with sparse amorphous contamination (scale bar: 10 nm). (b) A selected area electron diffraction pattern of the membrane, confirming the known hexagonal crystal structure of graphene (scale bar: 5 nm^{-1}).

following the ferric chloride etch process. Figure 7.9 (a) is a color-contrast TEM micrograph showing graphene (orange) with a typical amount of amorphous carbon contamination (yellow/light green) and evidence of a polycrystalline contaminant (blue/green). High-resolution TEM of this contamination is shown in Figure 7.9 (b) and illustrates its crystallinity.

We obtain an elemental fingerprint of the contamination through the use of electron energy loss spectroscopy (EELS) and X-ray energy-dispersive spectroscopy (EDS) in a TEM (X-ray spectrometry (INCAEnergyTEM 250, Oxford) and electron energy loss spectroscopy (Tridiem, Gatan) were performed at 120 keV in a JEOL 2100-F.) Spectroscopic analysis was performed in regions with contamination similar to that shown in Figure 7.9 (a) and (b). EELS data (Figure 7.9 (c)) reveals the presence of carbon, oxygen, and iron in our sample with an approximate atomic ratio (C:O:Fe) of 5:3:1. EDS data (Figure 7.9 (d)) confirms the existence of carbon, oxygen, and iron, but also detected small amounts of copper and chlorine. The atomic percentages determined through EDS are: C (55%), O (32%), Fe (12%), Cl (1 %), and Cu (less than 1%). The Cl, Cu, and some of the Fe are likely left over from the etching and may be in the form of $FeCl_3$, copper oxides, copper chlorides, or more complex compounds. However, the high concentration of Fe and O relative to Cl and the correlation of their locations suggest that some of the Fe from the etchant has formed an oxide and has produced the nano-sized crystals on the graphene surface seen in Figure 7.9 (b).

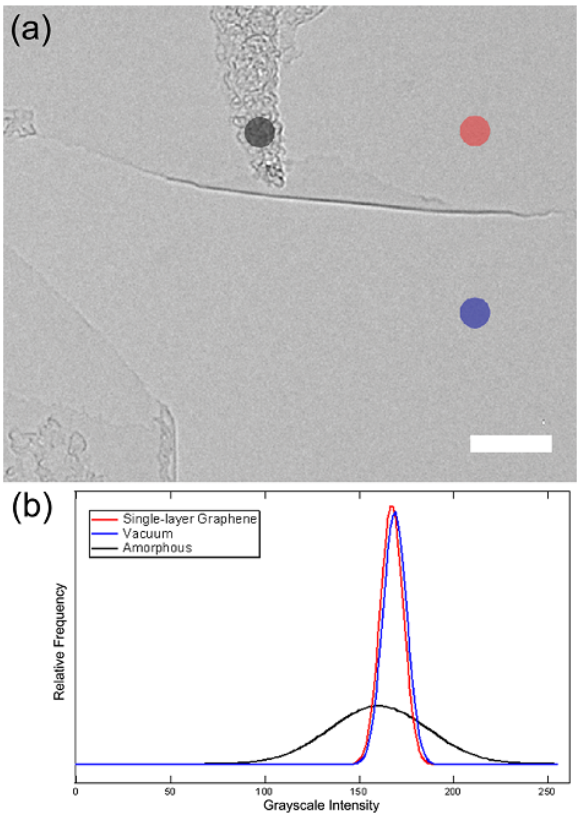

Figure 7.8: TEM transparency of graphene membranes. (a) Clean regions of single-layer graphene (red dot) near a tear in the membrane are compared to vacuum (blue dot) and amorphous debris (black dot) (scale bar: 10 nm). (b) The grayscale intensity distributions of single-layer graphene (red curve), vacuum (blue curve), and amorphous (black curve) regions. The graphene and vacuum have nearly indistinguishable contrast signatures, while the amorphous region's distribution is shifted and much broader. This contrast difference makes graphene far superior to amorphous carbon in resolving low contrast entities.

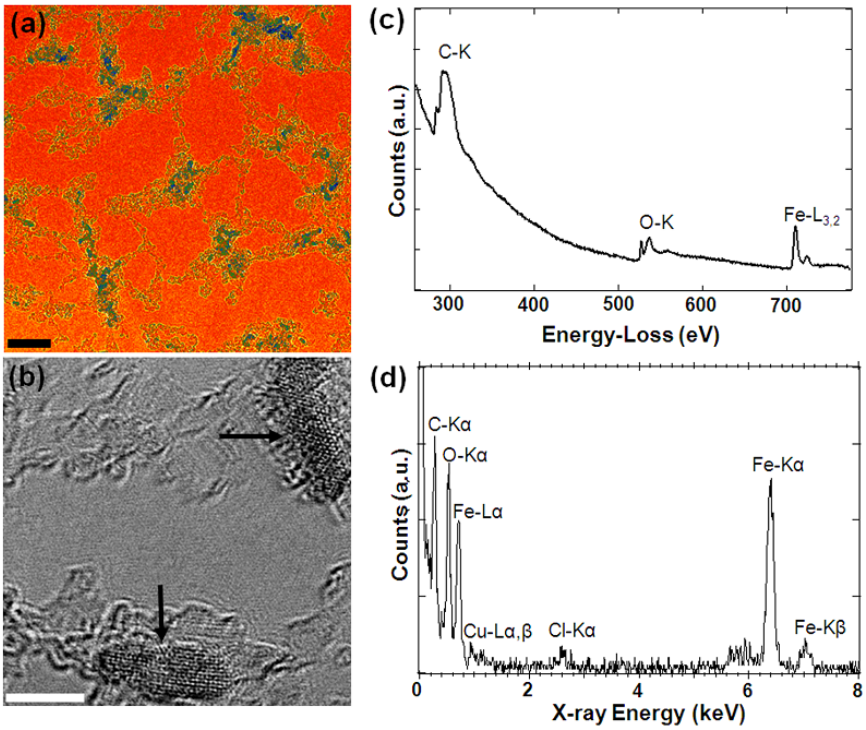

Figure 7.9: TEM and elemental microanalysis of iron-containing contamination on the surface of FeCl3 etched CVD graphene. (a) Color-contrast TEM micrograph showing regions of pristine graphene (orange-yellow), amorphous carbon (yellow-light green), and iron-containing contaminant (dark green-blue) (scale bar: 20 nm). (b) High-resolution TEM of iron-containing contamination (scale bar: 5 nm). (c) Electron energy loss spectroscopy (EELS) data and (d) X-ray energy-dispersive spectroscopy (EDS) data obtained from sample regions containing contamination similar to that shown in (a) and (b). EELS data clearly shows the presence of carbon, oxygen, and iron. X-ray spectroscopy data confirms the presence of carbon, oxygen, and iron, but also shows traces of copper and chloride.

Rinsing the samples in a solution that can dissolve iron oxide (acetic acid, citric acid, etc.) may remove part of this contamination. To avoid the formation of iron oxides altogether, one could also employ alternative Cu etchants such as sodium persulfate, ammonium persulfate, or organic acids such as citric, glycolic, acetic, malic, and oxalic acids. In fact, we have found that sodium persulfate (MG-Chemicals Product # 4101-1KG) is indeed effective at removing nearly all of this contamination, as can be seen from Figures 7.7 (a) and 7.8.

Chapter 8

Optical Detection of Vibrations in Graphene NEMS

In this chapter, we report the detection of mechanical vibrations in graphene membrane NEMS by optical interferometry. The amplitude-frequency response of the resonators is in excellent agreement with predictions made by modeling the system with the two-dimensional wave equation. The symmetry of the square geometry resonators used in our study leads to a vibrational mode degeneracy. However, we observe a lifting of this degeneracy and, through TEM and AFM characterization, discover that mass distribution, strain, or geometry inhomogeneities of the membrane can account for the splitting.

8.1 Detection and Actuation of Vibrations in Graphene Resonators

Actuation and detection of vibrations in our graphene NEMS membranes is accomplished using an all-optical technique. The experimental setup is shown schematically in Figure 8.1. A pair of co-aligned lasers and broad spectrum white light are focused onto the sample by adjusting the relative position between the sample and a 40X optical objective; typically, light beams are focused down to a spot 2-4 μm in diameter. The sample is position by a 3D micromanipulation stage connected to the vacuum chamber housing the graphene sample. A small glass port on the vacuum chamber allows optical probing of the sample. The beam focussing is achieved by redirecting (using a set of retractable mirrors) light beams into a CCD camera; a second lens focuses the light before it enters the camera and forms a simple light microscope. We first focus the image formed from white light (see Figure 8.2 (b)), then switch to the lasers, mark the spot for reference, then switch back to the white light image and adjust the sample so the beams are centered on a graphene membrane.

Detection of membrane vibrations in our experiment is performed by Fabry-Pérot

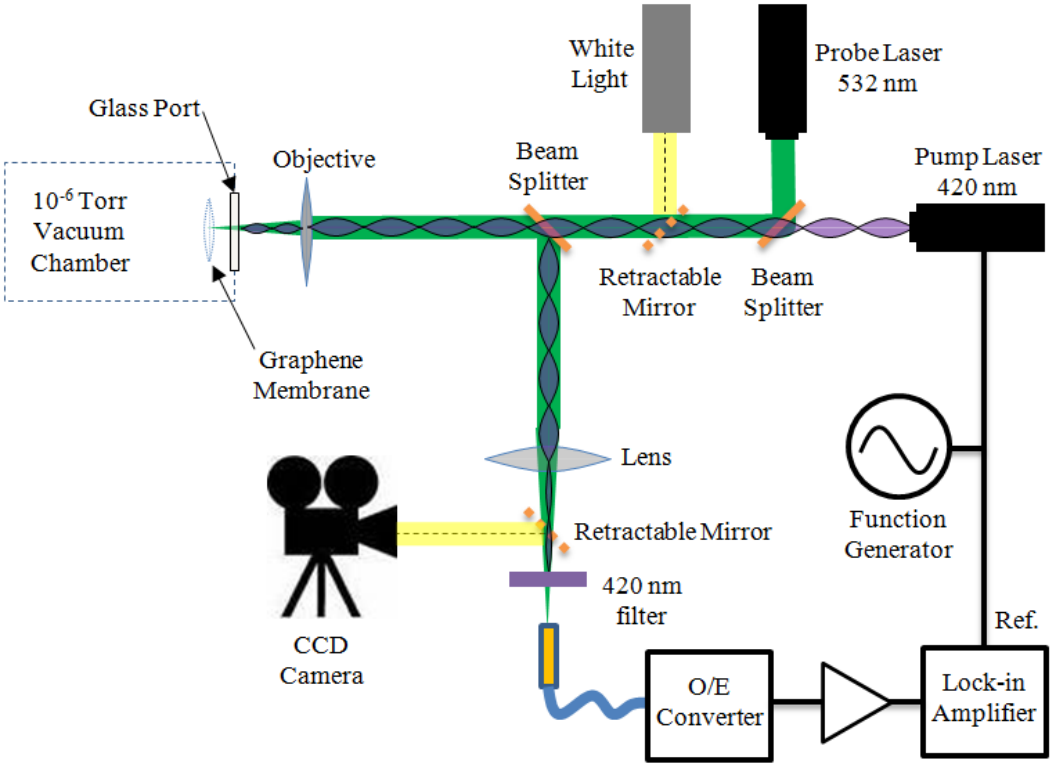

Figure 8.1: Setup for Graphene membrane vibration detection

interferometry. A 532 nm (green) laser(JDS Uniphase μ-green-slm laser; power 0.1 mW) reflects off the graphene membrane and then is redirected (using a beam splitter) and focused into a fiber optic cable that guides the light into a fast, high-gain/bandwidth photodiode (CP Model 310B O/E Converter with Silicon APD Detector: 1GHz bandwidth, 25000 V/W gain). Reflections off the surface of the glass vacuum port serve as a reference beam for interferometry. The intensity of the total reflected signal (off graphene and glass) is a function of the relative path length traveled by each beam. The time-dependent part of the reflected intensity is given by the expression $I(t) = 2\sqrt{I_g I_{ref}}\cos\left(\phi(t) + \phi_0\right)$, where $\phi(t) = \frac{4\pi}{\lambda}x(t)$ is the phase due to position of the membrane $x(t)$, $\phi_0 = \frac{4\pi}{\lambda}d$ is phase from light traveling a distance d to unperturbed position of membrane, and I_g and I_{ref} are the individual reflected light intensities from the graphene and glass surfaces, respectively. For oscillatory motion $x(t) = x_0\cos(\omega_0 t)$ and in the limit of small displacement ($x_0 \ll \lambda$), the intensity is

$$\begin{aligned} I(t) &= 2\sqrt{I_g I_{ref}}\left(\cos\phi(t)\cos\phi_0 - \sin\phi(t)\sin\phi_0\right) \\ &\approx 2\sqrt{I_g I_{ref}}\left(\cos\phi_0 - \sin\phi_0\frac{4\pi}{\lambda}x_0\cos(\omega_0 t)\right) \end{aligned} \tag{8.1}$$

Thus, variations in the reflected intensity will have frequency ω_0, the oscillation frequency of the membrane, and are monitored by analyzing the photodiode output voltage.

The membrane is driven with a second 420 nm (purple)laser (Thorlabs laser diode model TCLDM9 and Thorlabs LDC 500 controller) with power ranging between 1-5 mW. This laser follows the same beam path as the green laser, but is filtered to avoid entering the photodetector optical fiber. The intensity of this laser is modulated by an externally applied RF signal at frequency ω provided by a signal generator. The resulting modulated intensity drives graphene membrane vibrations when operated near one of the eigenfrequencies of the membrane. Detection of membranes is achieved by feeding the output of the photodiode into a lock-in amplifier with the same RF drive from the signal generator as a reference. For 7 μm square resonators, the signal generator frequency is swept between 500 kHz and 2 MHz in order to resolve the amplitude-frequency response of the first few harmonics.

The vibrations of the graphene resonators arise from thermal expansion/contraction [101] of the graphene membrane and also from radiation pressure. Both of these processes are driven by the modulated 420 nm laser and are dominated by radiation *absorption* (reflection of light from graphene, approximately 0.01%[98], is negligible). The elevated temperatures that occur because of this absorption (and the obvious degradation of the quality factor that would occur otherwise) require that the resonator be tested under vacuum, normally held at or below 7×10^{-6} torr. Interestingly, the absorption in graphene[98] is determined by the fine-structure constant α as $(1-T) \approx \pi\alpha \approx 0.023$, or 2.3%. In the thermally-driven process, the absorption of the strobed laser causes the periodic heating and cooling of the graphene; when strobed

at resonance, the resulting expansion and contraction of the membrane causes the membrane to vibrate[101]. Radiation pressure is also an important drive mechanism; the radiation force on the membrane is $F_r = \pi\alpha\frac{\mathcal{P}}{c}$, where the total laser power $\mathcal{P}$ is approximately 1 mW, and c is the speed of light. Driven at resonance, this force gives an amplitude $A_r = \frac{QF_r}{k} = \frac{\pi\alpha Q\mathcal{P}}{cm\omega_0^2} = \frac{\pi\alpha Q\mathcal{P}}{c\sigma A\omega_0^2}$, where $k = m\omega_0^2 = \sigma A\omega_0^2$ is the spring constant of the graphene membrane, $\sigma = 7.6 \times 10^{-7}\text{kg/m}^2$ is the area mass density, and A is the area of our membrane. The radiation force becomes important when it is larger than thermal oscillations, given by the expression $A_{th} = \sqrt{\frac{k_BT}{k}} = \sqrt{\frac{k_BT}{m\omega_0^2}}$. For the $7 \times 7\,\mu\text{m}^2$ square graphene membranes used in our experiments, $A_r \approx 100$ nm and $A_{th} \approx 10$ nm. Thus, we expect radiation pressure to contribute to the vibrations that we observe.

8.2 Experimental Results

Figure 8.2 shows devices used in our membrane vibration detection measurements. Figure 8.2 (a) shows a TEM image of an array of such devices. These devices have metal-reinforced amorphous carbon scaffolding (see Chapter 7) which appears black in the TEM images. Figure 8.2 (b) shows the device array as it is captured in the CCD camera used for focusing and positioning the lasers onto the graphene resonators. Here the support scaffolding appears light gray because it reflects incoming the incoming light better than the graphene (dark inner squares). Figure 8.2 (c) shows TEM of an individual device used for measurements. Long dark lines spanning the membrane (blue arrows point to a few) are due the increased contrast of folds in the graphene–grafolds[97]. A higher magnification image of the blue shaded region in Figure 8.2 (c) is given in Figure 8.3. These grafolds, as appear in Figure 8.3, cause inhomogeneities in the mass distribution and strain in the membrane.

The amplitude-frequency and phase-frequency characteristic for the fundamental mode for a typical 7 μm square device is shown in Figure 8.4. The resonance frequency of this mode is 695 kHz with a Q (quality factor) of about 150. The response agrees well with that of a driven simple harmonic oscillator.

The measured resonance frequencies of the devices was found to be quite consistent; for several dozen devices that were tested, the fundamental resonance frequency was 718 $\pm$ 20 kHz with Q ranging from 100-200. This consistency can be seen in Figure 8.5, which shows the amplitude-frequency response of four different 7 μm square devices.

We were able to observe as many as six higher harmonics in our experiments. The amplitude-frequency response of a typical 7 μm square graphene resonator is shown in Figure 8.6, and includes three peaks, labeled f_{11}, f_{12}, f_{21}, and f_{22}, corresponding to the first four vibrational modes. The measured values of these peaks are $f_{11} = 685$ kHz, $f_{12} = f_{21} = 1158$ kHz, $f_{22} = 1357$ kHz.

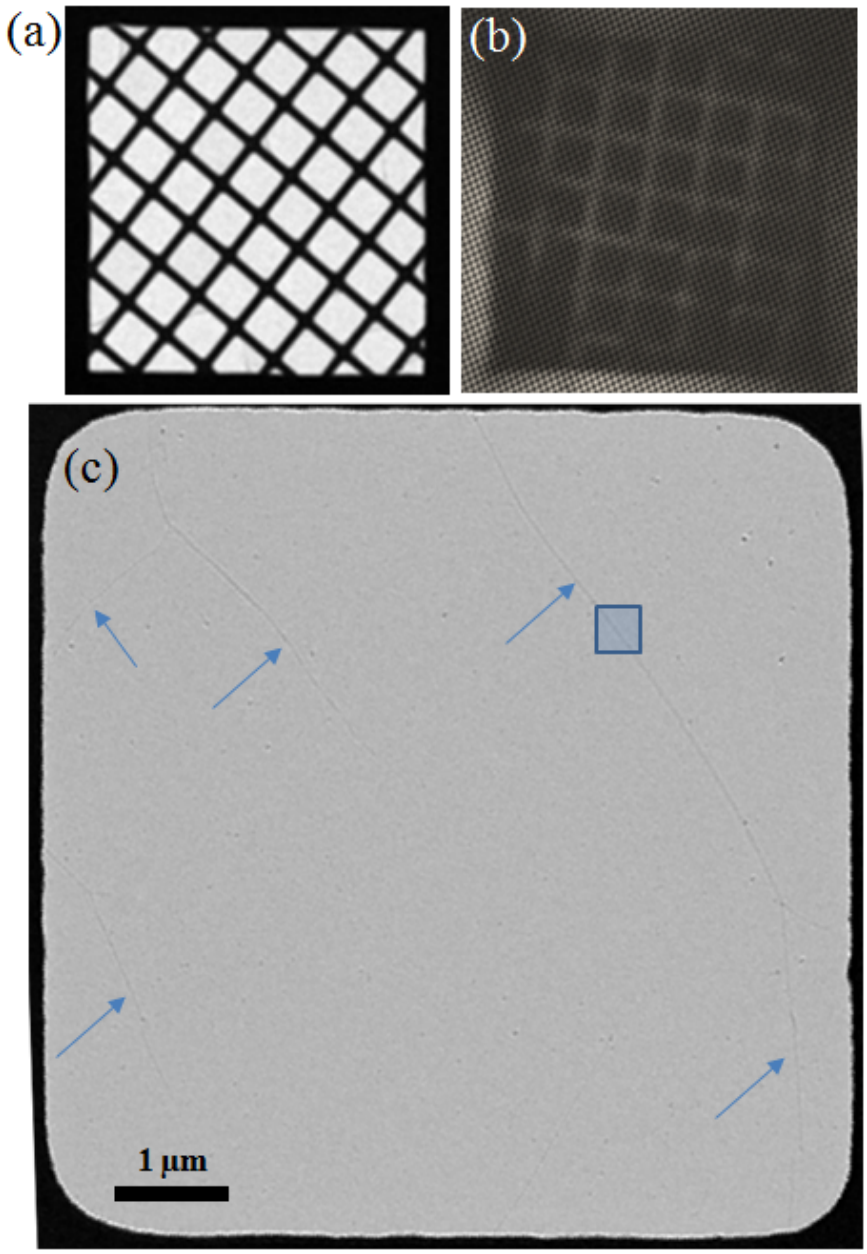

Figure 8.2: TEM and Optical Images of Graphene Membrane Resonators. (a) Low-magnification TEM image of array of resonator devices. (b) Optical image taken with CCD camera during experiment. (c) Higher magnification TEM image of individual 7 μm square graphene membrane resonator. Long dark lines spanning the membrane (blue arrow point to a few) are due the increased contrast of folds in the graphene–grafolds[97]. A higher magnification image of the blue shaded region containing a grafold is given in Figure 8.3. These grafolds cause inhomogeneities in the mass distribution and strain in the membrane.

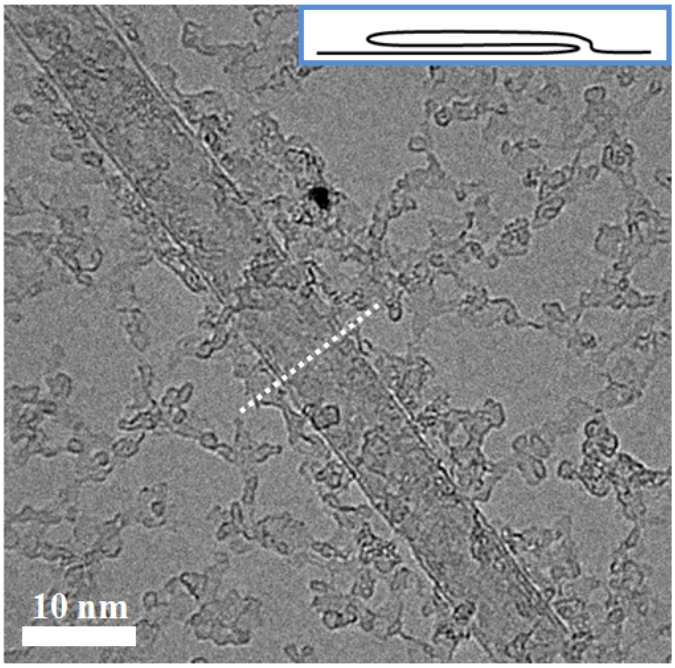

Figure 8.3: High Magnification TEM Image of Folded Graphene–Grafold. Inset shows theoretical structure of the folded region. Single dark lines suggest this structure.

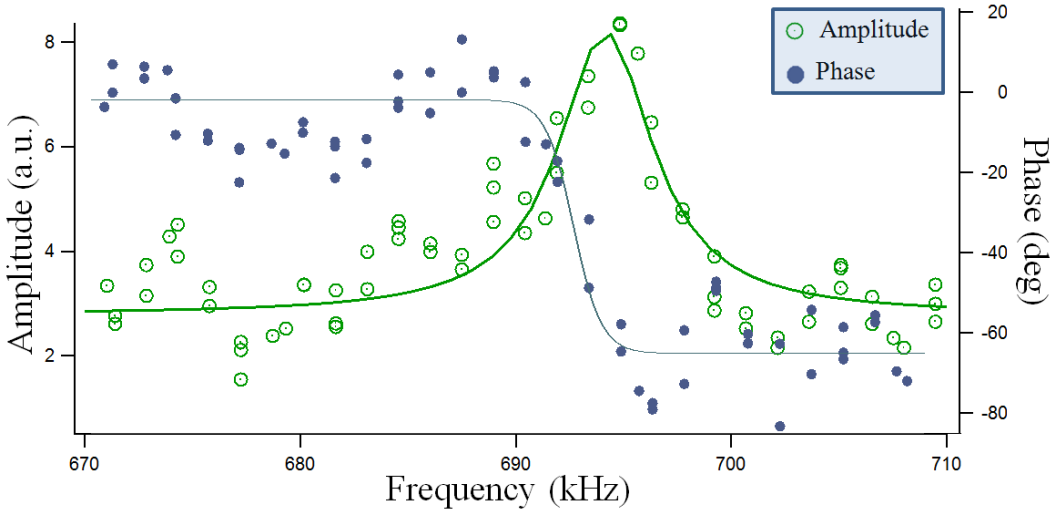

Figure 8.4: Amplitude-Frequency Response of Fundamental Mode in Graphene Resonator. Shows phase and amplitude as a function of frequency. Agrees well with result from simple harmonic motion; $Q = 150$ and peaked at 695 kHz.

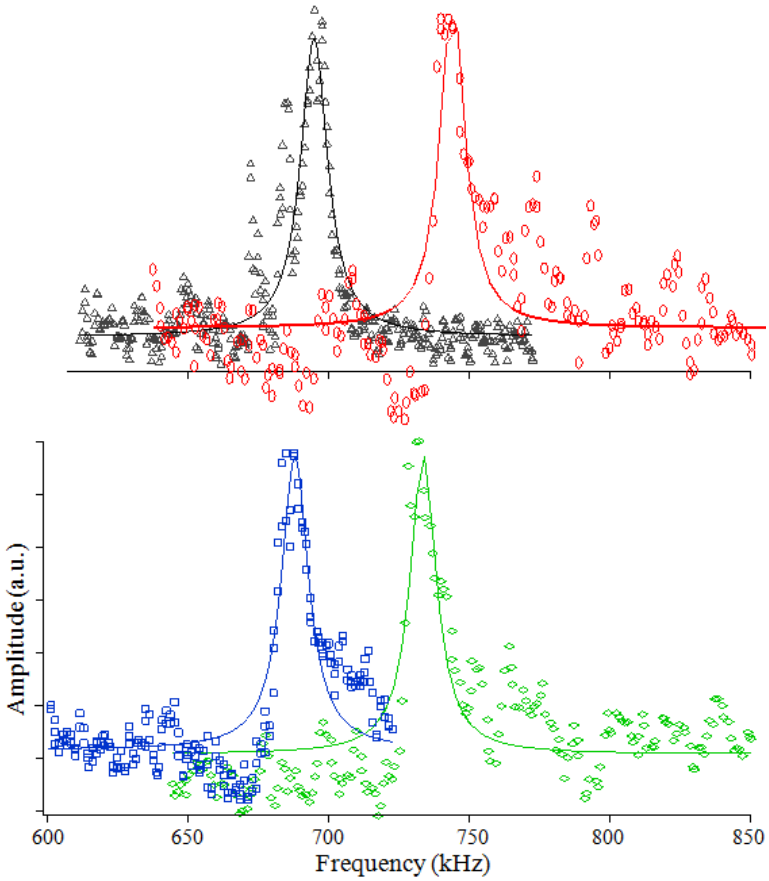

Figure 8.5: Amplitude Response Curves of Four Different Graphene Resonator 7 μm square Devices.

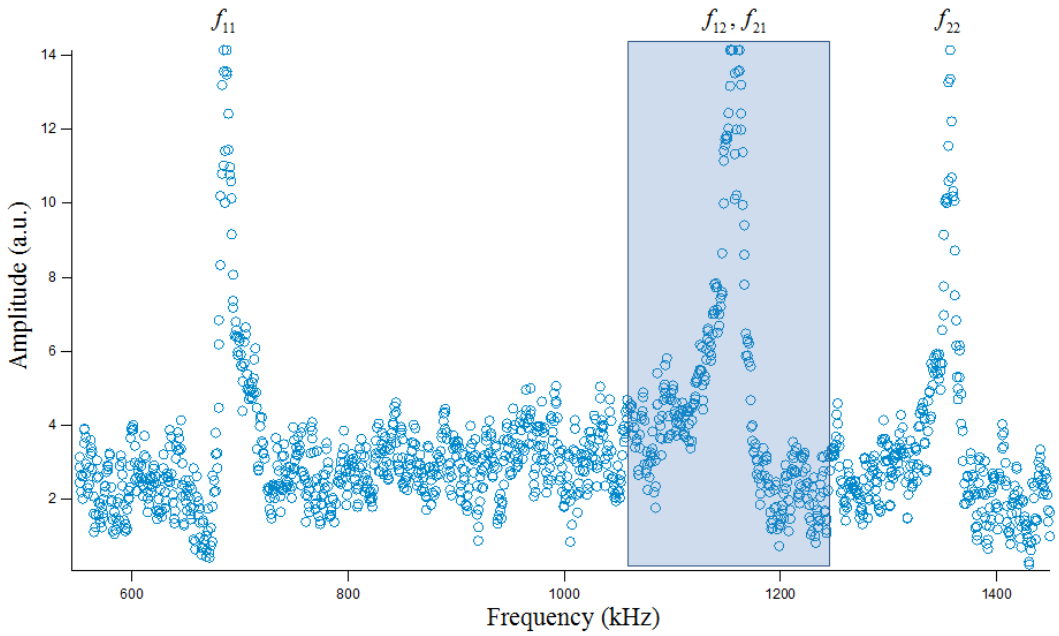

Figure 8.6: Amplitude-Frequency Response of Graphene Resonator showing first 4 modes. The highlighted mode is degenerate and is shown in Figure 8.8. The measured values $f_{11} = 685$ kHz, $f_{12} = f_{21} = 1158$ kHz, $f_{22} = 1357$ kHz agree well with expected are $f_{12} = f_{12} = \sqrt{5/2} f_{11} \approx 1083$ kHz, and $f_{22} = 2f_{11} \approx 1370$ kHz

Modeling the graphene resonator as a membrane satisfying the two-dimensional wave equation,

$$\frac{\partial^2 z}{\partial x^2} + \frac{\partial^2 z}{\partial y^2} = \frac{\sigma}{S}\frac{\partial^2 z}{\partial t^2}\,, \tag{8.2}$$

yields predictions that agree exceptionally well with the experimentally measured resonance frequencies. Assuming a square geometry with sides of length L and clamped boundary conditions, Eq. 8.2 can be solved(A complete solution is given in Appendix D) to give the deflection of the membrane

$$z_{pq}(x, y, t) = [A_{pq}\cos(\omega_{pq}t) + B_{pq}\sin(\omega_{pq}t)]\sin\left(\frac{p\pi x}{L}\right)\cos\left(\frac{q\pi y}{L}\right) \tag{8.3}$$

and the resonance frequencies

$$\omega_{pq} \equiv \frac{\pi}{L}\sqrt{\frac{S}{\sigma}}\sqrt{p^2 + q^2} \tag{8.4}$$

Here, S is the surface tension and σ is the area mass density of the graphene membrane. The theoretical mode shapes, z_{mn}, for several harmonics are shown in Figure 8.7. Equation 8.4 can be used to predict the higher harmonics from the fundamental,

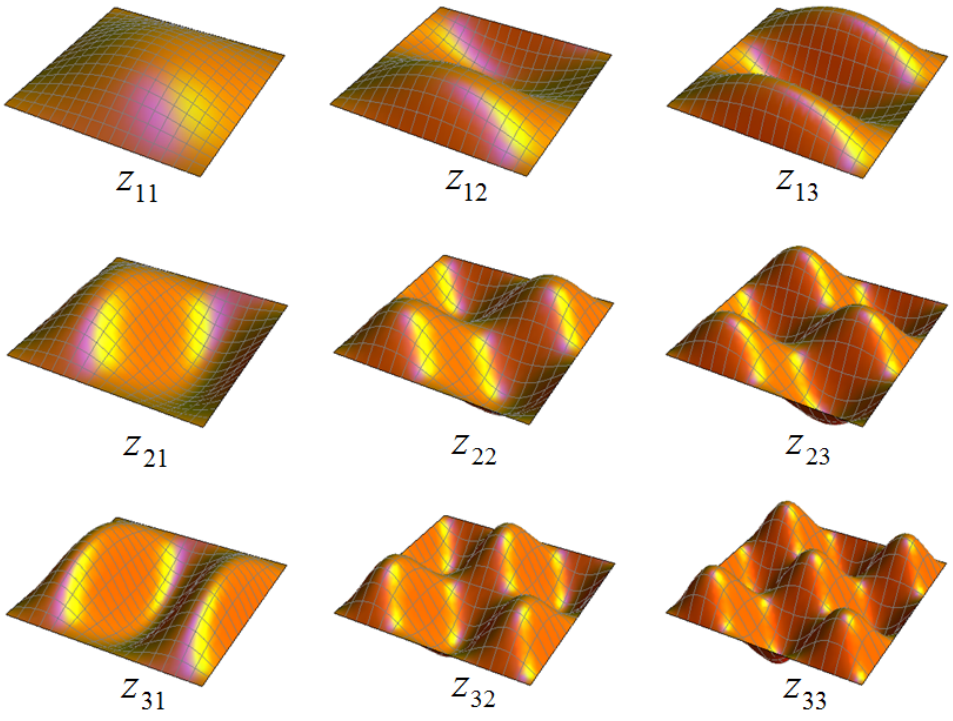

Figure 8.7: Mode Shapes, z_{pq}, for Square Membrane

$f_{11} = \omega_{11}/2\pi$. Using the data from Figure 8.6, we see the measured values $f_{11} = 685$ kHz, $f_{12} = f_{21} = 1158$ kHz, $f_{22} = 1357$ kHz agree well (within 0.9 %) with expected values $f_{12} = f_{12} = \sqrt{5/2} f_{11} \approx 1083$ kHz, and $f_{22} = 2f_{11} \approx 1370$ kHz. Assuming $\sigma = 7.6 \times 10^{-7} \mathrm{kg/m^2}$ for graphene, we can also use the model to calculate the surface tension, $S = 38 \pm 4\,\mu\mathrm{N/m}$, or a tension of $266 \pm 28\mathrm{pN}$ along each 7 μm side.

The symmetry of the square geometry leads to frequency degeneracies, $f_{mn} = f_{nm}$, whenever $n \neq m$. Thus, the second peak in Figure 8.6 (shaded in blue) contains two modes with frequencies f_{12} and f_{21}. Interestingly, we find that this degeneracy is often ''broken", so that the two modes have distinct resonance frequencies. A narrow sweep near the second peak in Figure 8.6 is shown in Figure 8.8 and unveils a degeneracy splitting of about 5 kHz. We have observed similar degeneracy breaks in nearly all devices that we tested.

These degeneracy breaks are likely caused by inhomogeneities in mass density and strain, as well as geometric imperfections, all of which break the symmetry of the system. We can use Equation 8.4 to explore how small variation in resonator mass, surface tension, and geometry can lead to the frequency shifts that cause the degeneracy splitting. The frequency shift due adding mass to the resonator of initial frequency f_0 and mass m_0 is approximately

$$\Delta f_m = -\frac{f_0}{2m_0}\delta m\,,$$

From Figure 8.8, $f_0 = 1083$ kHz and $\Delta f = 5$ kHz, so that a fractional change of mass $\frac{\Delta m}{m_0} \approx 0.9\,\%$ would be sufficient to cause this splitting. This could be caused, for example if a single 30 nm wide grafold were to asymmetrically span the length of the membrane. TEM images of graphene resonators with an exceptionally high density of mass defects (*i.e.* grafolds, holes, nanoparticle contamination, *etc.*) is shown in Figure 8.9. The fact that these graphene membranes can be fabricated on a very large scale and the density of optically-detected graphene resonators can easily approach 1 membrane per 4 $\mu\mathrm{m}^2$ suggests potential archival memory applications. For example, one could tune the frequency of the resonator via mass loading to correspond to some piece of information (*e.g.* an alphanumeric character). Since mass loading is a continuous process, information stored in this way would have a much higher density than conventional two-state systems (bits). The memory capacity of the graphene membrane arrays presented here would already be competitive with modern optical storage media, such as DVDs and CDRs, and could be read optically.

A variation in the width of the membrane, δL, leads to the frequency shift

$$\Delta f_L = -\frac{f_0}{L}\delta L\,,$$

For $L = 7\,\mu$m, a variation of $\delta L = 63$ nm would be sufficient to cause a 5 kHz frequency shift.

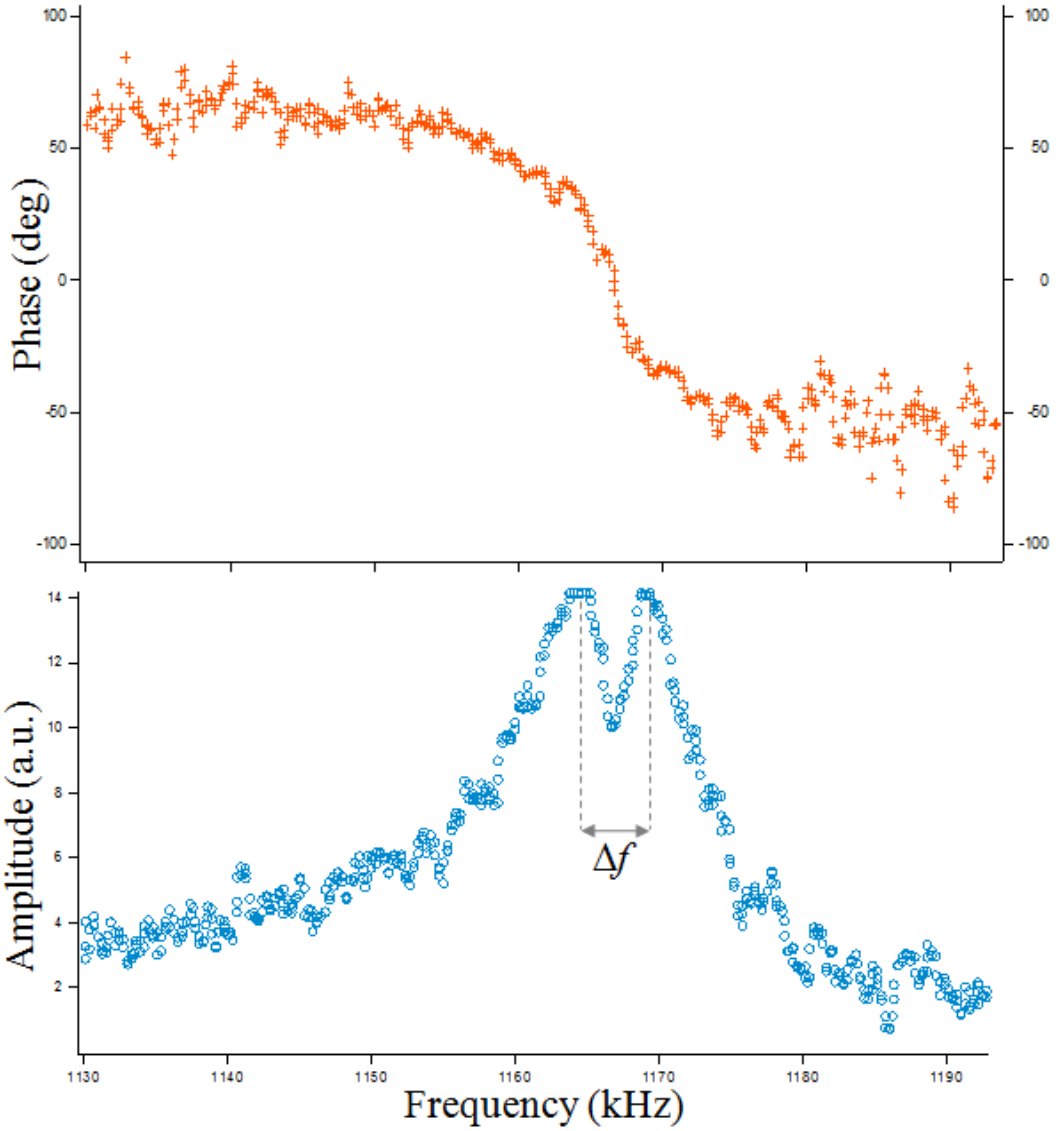

Figure 8.8: Amplitude-Frequency Response of Double Peak in Graphene Resonator. Phase and amplitude. $\Delta f \sim 5$ kHz.

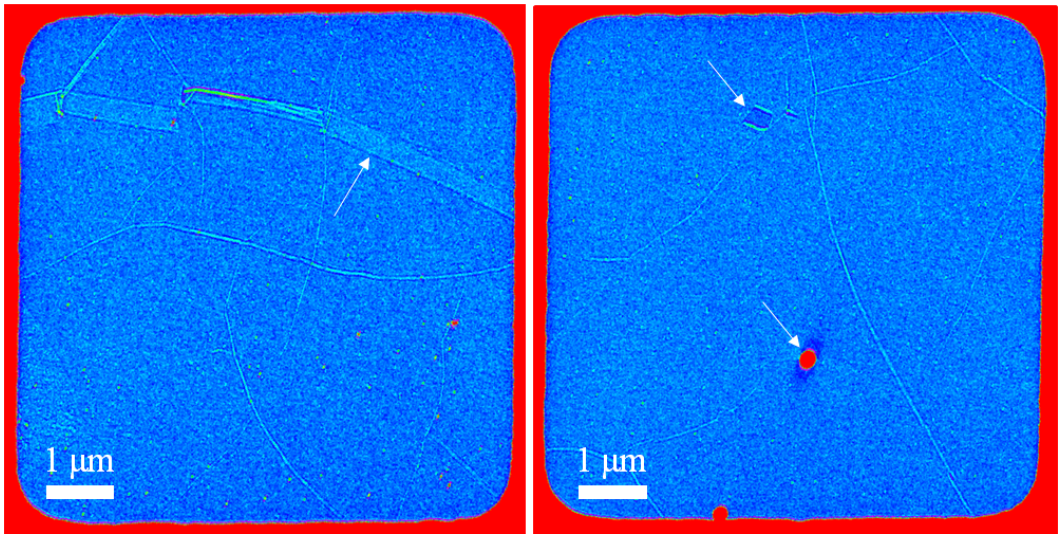

Figure 8.9: Color Contrast TEM of Graphene Resonators. Small and large (left) "grafold" defects, holes(right, upper arrow), and particle contaminants (right, lower arrow).

Similarly, surface tension variations also lead to frequency shifts,

$$\Delta f_S = \frac{f_0}{2S}\delta S\,,$$

Thus a tensile force of 2.4 pN applied to one of membrane edges would again account for the 5 kHz frequency shift. The symmetry-dependence of this degeneracy splitting could be useful for mapping relative strain in two dimensions.

Despite their atomic-scale thickness, we are able to characterize the membranes using tapping mode and contact mode AFM. AFM images of an array of graphene resonators is shown in Figure 8.10. The details of preparing the samples for AFM imaging are discussed in Appendix B. Here, AFM allows us to characterize some of the membrane defects, such as the grafold structure shown in Figure 8.10 (b) and (c). These devices give a powerful way to study mechanical properties using the optical techniques, while simultaneously performing TEM-AFM (or TEM-SPM) parallel studies (see Appendix B for an explicit example of an TEM-AFM parallel study.)

Furthermore, we have observed that AFM imaging can be performed in repulsive mode with set-point percentages approaching 97% of the target amplitude (this corresponds to extremely low dissipation and energy transfer to the sample, which minimizes damage to both the tip and the sample). In light of atomic thickness of the graphene membrane, this extremely soft tapping capability is consistent with the small tip-surface interactions forces. Thus, as an ideal AFM substrate, graphene

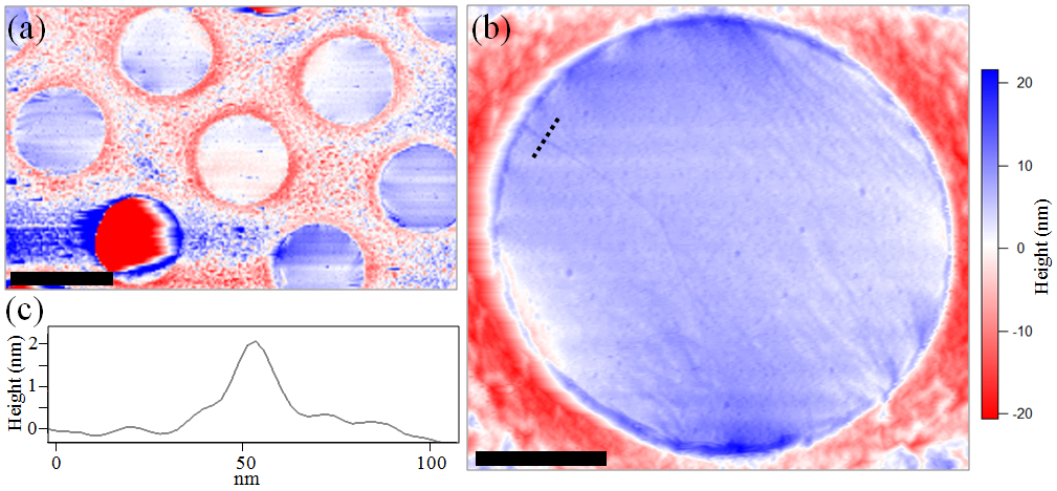

Figure 8.10: AFM of Circular Graphene Resonators: (a) Array with damaged membrane (bright red) (scale bar: 2 μm), (b) single resonator with grafold defect (scale bar: 500 nm). Some rippling and small particle contamination can be seen on membrane. Profile along dotted line given in (c)

membranes should facilitate many future AFM studies.

Bibliography

[1] Tai L. Chow, *Classical Mechanics*. Wiley, New York, 1995.

[2] Faraday. *M Phil. Trans. Roy. Soc.* 121:299-318, 1831.

[3] Strutt J and Rayleigh L. *Phil. Mag.* 16:50-53, 1883.

[4] Caves C. *Phys. Rev. D* 26:1817, 1982.

[5] Hatridge M, Vijay R, Slichter D, Clarke J and Siddiqi I. *Phys. Rev. B* 83:134501, 2011.

[6] R. Vijay, M.H. Devoret., I. Siddiqi. Invited Review Article: The Josephson bifurcation amplifier. *Rev. Sci. Instrum.* 80:111101, 2009.

[7] Mortenson K. *J. Appl. Phys.* 30:1542, 1959.

[8] Yurke B, Corruccini L, Kaminsky P, Rupp L, Smith A, Silver A, Simon R and Whittaker E. *Phys. Rev. A* 39:2519, 1989.

[9] Giordamaine J and Miller. *R Phys. Rev. Lett.* 14:973, 1965.

[10] Rugar D and Grütter P. *Phys. Rev. Lett.* 67: 699-702, 1991.

[11] Collins P and Zettl A. *Appl. Phys. Lett.* 69:1969, 1996.

[12] Collins P and Zettl A. *Phys. Rev. B* 55:9391, 1997.

[13] de Heer W, Chatelain A and Ugarte D. *Science* 270:1179-1180, 1995.

[14] Fowler R and Nordheim L. *Proc. R. Soc. London*, Ser. A 119:173-181, 1928.

[15] Poncharal P, Wang Z, Ugarte D and de Heer W. *Science* 283:1513-1516, 1999

[16] Jensen K, Weldon J, Garcia H and Zettl A. *Nano Letters* 7(11):3508-3511, 2007.

[17] Jensen K, Kim K and Zettl A. *Nature Nanotech.* 3(9):533-537, 2008.

[18] Weldon J, Alemn B, Sussman A, Gannett W and Zettl A. *Nano Lett.* 10:1728-1733, 2010.

[19] Hayt W and Buck J. *Engineering Electromagnetics*. McGraw-Hill, Boston, 2006.

[20] Senturia S. *Microsystem Design*. Springer, New York, 2001.

[21] Cleland A. *Foundations of Nanomechanics: from Solid-State Theory to Device Applications*. Springer, New York, 2003.

[22] T. Rocheleau, K.C. Schwab, *et al. Nature* 463:72-75, 2009.

[23] Vera Sazonova, Yuval Yaish, Hande Ustunel, David Roundy, Tomas A. Arias, and Paul L. McEuen. A tunable carbon nanotube electromechanical oscillator. *Nature* 431, 2004.

[24] Craighead, H. *Science* 290:15321535, 2000.

[25] Wan, Q.; Li, Q.; Chen, Y.; Wang, T.; He, X.; Li, J.; Lin, C. *Appl. Phys. Lett.* 84:36543656, 2004.

[26] Waggoner, P.; Craighead, H. *Lab Chip* 7:12381255, 2007.

[27] Li, M.; Tang, H.; Roukes, M. *Nat. Nanotechnol.* 2:114120, 2007.

[28] Jensen, K.; Kim, K.; Zettl, A. *Nat. Nanotechnol.* 3:533537, 2008.

[29] Feng, X. L.; White, C. J.; Hajimiri, A.; Roukes, M. L. *Nat. Nano- technol.* 3:342346, 2008.

[30] Unterreithmeier, Q.; Weig, E.; Kotthaus, J. *Nature* 458:10011004, 2009.

[31] Mahboob, I.; Yamaguchi, H. *Nat. Nanotechnol.* 3:369369, 2008.

[32] Durand, C.; Casset, F.; Renaux, P.; Abele, N.; Legrand, B.; Renaud, D.; Ollier, E.; Ancey, P.; Ionescu, A.; Buchaillot, L. *IEEE Electron Device Lett.* 29:494496, 2008.

[33] Sekaric, L.; Zalalutdinov, M.; Turner, S.; Zehnder, A.; Parpia, J.; Craighead, H. *Appl. Phys. Lett.* 80:36173619, 2002.

[34] Ayari, A.; Vincent, P.; Perisanu, S.; Choueib, M.; Gouttenoire, V.; Bechelany, M.; Cornu, D.; Purcell, S. *Nano Lett.* 7:2252 2257, 2007.

[35] Jensen, K.; Weldon, J.; Garcia, H.; Zettl, A. *Nano Lett.* 8:374374, 2008.

[36] Gomer, R. *Field Emission and Field Ionization*. Harvard University Press, Cambridge, MA, 1961.

[37] Fursey, G. *In Field Emission in Vacuum Microelectronics.* Kluwer Academic/PlenumPublishers, New York, 2005.

[38] Deheer,W. A.; Chatelain, A.; Ugarte, D. *Science* 270:1179 1180, 1995.

[39] Jackson, J. D. *Classical Electrodynamics, 3rd. Edition.* Wiley, New York, 1999.

[40] Hayt, W. H.; Buck, J. A. *Engineering Electromagnetics, 7th ed.*. McGraw-Hill Higher Education, Boston, 2006.

[41] Dequesnes, M.; Rotkin, S.; Aluru, *N. Nanotechnology* 13:120131, 2002.

[42] Ke, C.; Espinosa, H. *J. Appl. Mech.* 72:721725, 2005.

[43] Keblinski, P.; Nayak, S. K.; Zapol, P.; Ajayan, P.M. *Phys. Rev. Lett.* 89:255503-4, 2002.

[44] Wong, E. W.; Sheehan, P. E.; Lieber, C. M. *Science* 277:19711975, 1997.

[45] Ke, C. H.; Espinosa, H. D. *Appl. Phys. Lett.* 85:681683, 2004.

[46] Ke, C. H.; Espinosa, H. D. *Small* 2:14841489, 2006.

[47] Peng, H. B.; Chang, C. W.; Aloni, S.; Yuzvinsky, T. D.; Zettl, A. *Phys. Rev. B* 76:035405, 2007.

[48] Huang, L. M.;White, B.; Sfeir, M. Y.; Huang, M. Y.; Huang, H. X.; Wind, S.; Hone, J.; OBrien, S. *J. Phys. Chem. B* 110:11103 11109, 2006.

[49] Yuzvinsky, T. D.; Fennimore, A. M.; Kis, A.; Zettl, A. *Nanotechnology* 17:434438, 2006.

[50] Wang, X. Q.; Wang, M.; He, P. M.; Xu, Y. B.; Li, Z. H. Model calculation for the field enhancement factor of carbon nanotube. *J.Appl. Phys.* 96:6752-6755, 2004.

[51] Ado Jorio, Gene Dresselhaus, Mildred Dresselhaus. *Carbon Nanotubes: Advanced Topics in the Synthesis, Structure, Properties, and Applications.* Spring-Verlag, Berlin, Heidelberg, 2008.

[52] Steele GA, Httel AK, Witkamp B, Poot M, Meerwaldt HB, Kouwenhoven LP, van der Zant HS. Strong coupling between single-electron tunneling and nanomechanical motion. *Science* 325(5944):1103-7, 2009.

[53] Michel H. Devoret, Robert J. Schelkopf, Amplifying Quantum Signals with the Single-Electron Transistor. Nature 406:1039-1046, 2000.

[54] A. G. Rinzler, J. H. Hafner, P. Nikolaev, L. Lou, S. G. Kim, D. Tomnek, P. Nordlander, D. T. Colbert, R. E. Smalley, Unraveling Nanotubes: Field Emission from an Atomic Wire. *Science* 269(5230):1550-1553, 2000.

[55] Philip G. Collins, A. Zettl. Unique Characteristics of Cold Cathode Carbon-nanotube-matrix Field Emitters. *Physical Review B* 55(15):9391-9399. 1997.

[56] J. -M. Bonard, J.-P. Salvetat, T. Stöckli, L. Forró, A. Châtelain. Field Emission from Carbon Nanotubes: Perspectives for Applications and Clues to the Emission Mechanism. *Appl. Phys. A* 69:245-254, 1999.

[57] Chulki Kim, Hyun S. Kim, Hua Qin, Robert H. Blick. Coulomb-controlled Single Electron Field Emission va a Freely Suspended Metallic Island. *Nano Letters* 10:615-619, 2010.

[58] O. E. Raichev. Coulomb blockade of Field Emission from Nanoscale Conductors. *Physical Review B* 73:195328, 2006.

[59] Yukinori Ono, Akira Fujiwara, Katsuhiko Nishiguchi, Hiroshi Inokawa, and Yasuo Takahashi. Manipulation of detection of single electrons for future information processing. *Journal of Applied Physics* 97:031101, 2005.

[60] Charles Kittel. *Introduction to Solid State Physics*. Wiley, New York, 2005.

[61] J-M. Bonard, T. Stöckli, F. Meier, W. A. de Heer, A. Châtelain, J.-P. Salvetat, L. Forró. Field-Emission-Induced Luminescence from Carbon Nanotubes. *Phys. Rev. Lett.* 81:1441-1444, 1998.

[62] Novoselov, K. S.; Geim, A. K.; Morozov, S. V.; Jiang, D.; Zhang, Y.; Dubonos, S. V.; Grigorieva, I. V.; Firsov, A. A., Electric Field Effect in Atomically Thin Carbon Films. *Science* 306:666-669, 2004.

[63] Novoselov, K. S.; Jiang, D.; Schedin, F.; Booth, T. J.; Khotkevich, V. V.; Morozov, S. V.; Geim, A. K., Two-Dimensional Atomic Crystals. *Proceedings of the National Academy of Sciences of the United States of America* 102:10451-10453, 2005.

[64] Geim, A. K.; Novoselov, K. S., The Rise of Graphene. *Nature Materials* 6:183-191, 2007.

[65] Neto, A. H. C.; Guinea, F.; Peres, N. M. R.; Novoselov, K. S.; Geim, A. K., The Electronic Properties of Graphene. *Reviews of Modern Physics* 109:62, 2009.

[66] Zhang, Y. B.; Brar, V. W.; Girit, C.; Zettl, A.; Crommie, M. F., Origin of Spatial Charge Inhomogeneity in Graphene. *Nature Physics* 6:74-74, 2010.

[67] Meyer, J. C.; Geim, A. K.; Katsnelson, M. I.; Novoselov, K. S.; Booth, T. J.; Roth, S., The Structure of Suspended Graphene Sheets. *Nature* 446:60-63, 2007.

[68] Booth, T. J.; Blake, P.; Nair, R. R.; Jiang, D.; Hill, E. W.; Bangert, U.; Bleloch, A.; Gass, M.; Novoselov, K. S.; Katsnelson, M. I.; Geim, A. K., Macroscopic Graphene Membranes and Their Extraordinary Stiffness. *Nano Letters* 8:2442-2446, 2008.

[69] Bunch, J. S.; Verbridge, S. S.; Alden, J. S.; van der Zande, A. M.; Parpia, J. M.; Craighead, H. G.; McEuen, P. L., Impermeable Atomic Membranes From Graphene Sheets. *Nano Letters* 8:2458-2462, 2008.

[70] Du, X.; Skachko, I.; Barker, A.; Andrei, E. Y., Approaching Ballistic Transport in Suspended Graphene. *Nature Nanotechnology* 3:491-495, 2008.

[71] Frank, I. W.; Tanenbaum, D. M.; Van der Zande, A. M.; McEuen, P. L., Mechanical Properties of Suspended Graphene Sheets. *Journal of Vacuum Science and Technology B* 25:2558-2561, 2007.

[72] Lee, C.; Wei, X. D.; Kysar, J. W.; Hone, J., Measurement of The Elastic Properties and Intrinsic Strength of Monolayer Graphene. *Science* 321:385-388, 2008.

[73] Nair, R. R.; Blake, P.; Grigorenko, A. N.; Novoselov, K. S.; Booth, T. J.; Stauber, T.; Peres, N. M. R.; Geim, A. K., Fine Structure Constant Defines Visual Transparency of Graphene. *Science* 320:1308-1308, 2008.

[74] Bolotin, K. I.; Sikes, K. J.; Jiang, Z.; Klima, M.; Fudenberg, G.; Hone, J.; Kim, P.; Stormer, H. L., Ultrahigh Electron Mobility in Suspended Graphene. *Solid State Communications* 146:351-355, 2008.

[75] Bolotin, K. I.; Ghahari, F.; Shulman, M. D.; Stormer, H. L.; Kim, P., Observation of The Fractional Quantum Hall Effect in Graphene. *Nature* 462:196-199, 2009.

[76] Du, X.; Skachko, I.; Duerr, F.; Luican, A.; Andrei, E. Y., Fractional Quantum Hall Effect and Insulating Phase of Dirac Electrons in Graphene. *Nature* 462:192-195, 2009.

[77] Girit, C. O.; Meyer, J. C.; Erni, R.; Rossell, M. D.; Kisielowski, C.; Yang, L.; Park, C. H.; Crommie, M. F.; Cohen, M. L.; Louie, S. G.; Zettl, A., Graphene at The Edge: Stability and Dynamics. *Science* 323:1705-1708, 2009.

[78] Bunch, J. S.; van der Zande, A. M.; Verbridge, S. S.; Frank, I. W.; Tanenbaum, D. M.; Parpia, J. M.; Craighead, H. G.; McEuen, P. L., Electromechanical Resonators from Graphene Sheets. *Science* 315:490-493, 2007.

[79] Garcia-Sanchez, D.; van der Zande, A. M.; Paulo, A. S.; Lassagne, B.; McEuen, P. L.; Bachtold, A., Imaging Mechanical Vibrations in Suspended Graphene Sheets. *Nano Letters* 8:1399-1403, 2008.

[80] Meyer, J. C.; Girit, C. O.; Crommie, M. F.; Zettl, A., Hydrocarbon Lithography on Graphene Membranes. *Applied Physics Letters* 92:3, 2008.

[81] Kim, K. S.; Zhao, Y.; Jang, H.; Lee, S. Y.; Kim, J. M.; Ahn, J. H.; Kim, P.; Choi, J. Y.; Hong, B. H., Large-Scale Pattern Growth of Graphene Films for Stretchable Transparent Electrodes. *Nature* 457:706-710, 2009.

[82] Li, X. S.; Cai, W. W.; An, J. H.; Kim, S.; Nah, J.; Yang, D. X.; Piner, R.; Velamakanni, A.; Jung, I.; Tutuc, E.; Banerjee, S. K.; Colombo, L.; Ruoff, R. S., Large-Area Synthesis of High-Quality and Uniform Graphene Films on Copper Foils. *Science* 324:1312-1314, 2009.

[83] Park, H. J.; Meyer, J., Roth, Siegmar; Skakalova, V., Growth and Properties of Few-Layer Graphene Prepared by Chemical Vapor Deposition. *Carbon* 48:1088-1094, 2010.

[84] Meyer, J. C.; Girit, C. O.; Crommie, M. F.; Zettl, A., Imaging and Dynamics of Light Atoms and Molecules on Graphene. *Nature* 454:319-322, 2008.

[85] Meyer, J. C.; Kisielowski, C.; Erni, R.; Rossell, M. D.; Crommie, M. F.; Zettl, A., Direct Imaging of Lattice Atoms and Topological Defects in Graphene Membranes. *Nano Letters* 8:3582-3586, 2008.

[86] Gass, M. H.; Bangert, U.; Bleloch, A. L.; Wang, P.; Nair, R. R.; Geim, A. K., Free-standing Graphene at Atomic Resolution. *Nature Nanotechnology* 3:676-681, 2008.

[87] Levendorf, M. P.; Ruiz-Vargas, C. S.; Garg, S.; Park, J., Transfer-Free Batch Fabrication of Single Layer Graphene Transistors. *Nano Letters* 9:4479-4483, 2009.

[88] Pernel, C.; Farkas, J.; Louis, D., Copper in Organic Acid Based Cleaning Solutions. *Journal of Vacuum Science and Technology B* 24:2467-2471, 2006.

[89] Reina, A.; Jia, X. T.; Ho, J.; Nezich, D.; Son, H. B.; Bulovic, V.; Dresselhaus, M. S.; Kong, J., Large Area, Few-Layer Graphene Films on Arbitrary Substrates by Chemical Vapor Deposition. *Nano Letters* 9:30-35, 2009.

[90] Land, T. A.; Michely, T.; Behm, R. J.; Hemminger, J. C.; Comsa, G., STM Investigation of Single Layer Graphite Structures Produced on Pt(111) by Hydrocarbon Decomposition. *Surface Science* 264:261-270, 1992.

[91] Coraux, J.; N'Diaye, A. T.; Busse, C.; Michely, T., Structural Coherency of Graphene on Ir(111). *Nano Letters* 8:565-570, 2008.

[92] Craighead, H. G., Nanoelectromechanical Systems. *Science* 290:1532-1535, 2000.

[93] A.A. Balandin, S. Ghosh, W. Bao, I. Calizo, D. Teweldebrhan, F. Miao and C.N. Lau, Superior thermal conductivity of single-layer graphene. *Nano Letters* 8:902, 2008.

[94] Sutter, P. Epitaxial graphene: How silicon leaves the scene. *Nature Materials* 8(3):171, 2009.

[95] W. Regan, N. Alem, B. Alemn, B. Geng, C. Girit, L. Maserati, F. Wang, M. Crommie, and A. Zettl. A direct transfer of layer-area graphene. *Appl. Phys. Lett.* 96(9):113102, 2010.

[96] Arend M. van der Zande, Robert A. Barton, Jonathan S. Alden, Carlos S. Ruiz-Vargas, William S. Whitney, Phi H.Q. Pham, Jiwoong Park, Jeevak M. Parpia, Harold G. Craighead, and Paul L. McEuen. Large-scale arrays of single-layer graphene resonators. *Nano Letters* 10(12):48694873, 2010.

[97] K.Kim, Z. Lee, B.D. Malone, K.T. Chan, B. Alemn, W. Regan, W. Gannett, M.F. Crommie, M.L. Cohen, and A. Zettl. Multiply folded graphene. *Phys. Rev. B* 83:245433, 2011.

[98] R. R. Nair, P. Blake, A. N. Grigorenko, K. S. Novoselov, T. J. Booth, T. Stauber, N. M. R. Peres, and A. K. Geim. Fine Structure Constant Defines Visual Transparency of Graphene, *Science* 320(5881):1308, 2010.

[99] S. Bae, H. Kim, Y. Lee, X. Xu, J.-S. Park, Y. Zheng, J. Balakrishnan, T. Lei, H. Ri Kim, Y.I. Song, Y.-J. Kim, K.S. Kim, B. zyilmaz, J.-H. Ahn, B.H. Hong, and S. Iijima, Roll-to-roll production of 30-inch graphene films for transparent electrodes. *Nature Nanotechnology* 5:1-5, 2010.

[100] Y. Lee, S. Bae, H. Jang, S. Jang, S.-E. Zhu, S.H. Sim, Y.I. Song, B.H. Hong, and J.-H. Ahn, Wafer-scale synthesis and transfer of graphene films. *Nano letters* 10:490-493, 2010.

[101] B. Ilic, S. Krylov, K. Aubin, R. Reichenbach, and H.G. Craighead. Optical excitation of nanoelectromechanical oscillators. *Applied Physics Letters* 86:193114, 2005.

[102] Binnig, G., Quate, C. F. & Gerber, C. Atomic Force Microscope. *Physical Review Letters* 56:930-933, 1986.

[103] Chen, J. & Anandarajah, A. Van der Waals attraction between spherical particles. *Journal of Colloid and Interface Science* 180:519-523, 1996.

[104] Chen, L. W., Cheung, C. L., Ashby, P. D. & Lieber, C. M. Single-walled carbon nanotube AFM probes: Optimal imaging resolution of nanoclusters and biomolecules in ambient and fluid environments. *Nano Letters* 4:1725-1731, 2004.

[105] Chen, X., Kis, A., Zettl, A. & Bertozzi, C. R. A cell nanoinjector based on carbon nanotubes. *Proceedings of the National Academy of Sciences of the United States of America* 104:8218-8222, 2007.

[106] Cheung, C. L., Hafner, J. H. & Lieber, C. M. Carbon nanotube atomic force microscopy tips: Direct growth by chemical vapor deposition and application to high-resolution imaging. *Proceedings of the National Academy of Sciences of the United States of America* 97:3809-3813, 2000.

[107] Chin Li, C., Hafner, J. H., Odom, T. W., Kim, K. & Lieber, C. M. Growth and fabrication with single-walled carbon nanotube probe microscopy tips. *Applied Physics Letters* 76:3136-3138, 2000.

[108] Cumings, J., Collins, P. G. & Zettl, A. Materials - Peeling and sharpening multiwall nanotubes. *Nature* 406:586-586, 2000.

[109] Dai, H. J., Franklin, N. & Han, J. Exploiting the properties of carbon nanotubes for nanolithography. *Applied Physics Letters* 73:1508-1510, 1998.

[110] Dedkov, G. V. & Rekhviashvili, S. S. Nanotubes and force interactions in an atomic force microscope. *Technical Physics* 44:982-985, 1999.

[111] Hafner, J. H., Cheung, C. L. & Lieber, C. M. Direct growth of single-walled carbon nanotube scanning probe microscopy tips. *Journal of the American Chemical Society* 121:9750-9751, 1999.

[112] Hafner, J. H., Cheung, C. L. & Lieber, C. M. Growth of nanotubes for probe microscopy tips. *Nature* 398:761-762, 1999.

[113] Hafner, J. H., Cheung, C. L., Oosterkamp, T. H. & Lieber, C. M. High-yield assembly of individual single-walled carbon nanotube tips for scanning probe microscopies. *Journal of Physical Chemistry B* 105:743-746, 2001.

[114] Hafner, J. H., Cheung, C. L., Woolley, A. T. & Lieber, C. M. Structural and functional imaging with carbon nanotube AFM probes. *Progress in Biophysics & Molecular Biology* 77:73-110, 2001.

[115] Harper, J. D., Wong, S. S., Lieber, C. M. & Lansbury, P. T. Assembly of A beta amyloid protofibrils: An in vitro model for a possible early event in Alzheimer's disease. *Biochemistry* 38:8972-8980, 1999.

[116] Hertel, T., Walkup, R. E. & Avouris, P. Deformation of carbon nanotubes by surface van der Waals forces. *Physical Review B* 58:13870-13873, 1998.

[117] Hongjie, D., Hafner, J. H., Rinzler, A. G., Colbert, D. T. & Smalley, R. E. Nanotubes as nanoprobes in scanning probe microscopy. *Nature* 384:147-150, 1996.

[118] Jensen, K., Mickelson, W., Kis, A. & Zettl, A. Buckling and kinking force measurements on individual multiwalled carbon nanotubes. *Physical Review B* 76(5):195436, 2007.

[119] Kalinin, S. V., Bonnell, D. A., Freitag, M. & Johnson, A. T. Carbon nanotubes as a tip calibration standard for electrostatic scanning probe microscopies. *Applied Physics Letters* 81:754-756, 2002.

[120] Lee, S. I. et al. Nonlinear tapping dynamics of multi-walled carbon nanotube tipped atomic force microcantilevers. *Nanotechnology* 15:416-421, 2004.

[121] Lee, S. I. et al. Complex dynamics of carbon nanotube probe tips. *Ultramicroscopy* 103:95-102, 2005.

[122] Maeda, Y. et al. Reduction of long-range interactions using carbon nanotube probes in biological systems. *Japanese Journal of Applied Physics Part 1-Regular Papers Short Notes & Review Papers* 40:1425-1428, 2001.

[123] Marin, C., Serrano, M. D., Yao, N. & Ostrogorsky, A. G. Evidence for a bundle of 4 angstrom single-walled carbon nanotubes. *Nanotechnology* 14:L4-L5, 2003.

[124] Martinez, J. et al. Length control and sharpening of atomic force microscope carbon nanotube tips assisted by an electron beam. *Nanotechnology* 16:2493-2496, 2005.

[125] Meyer, J. C., Girit, C. O., Crommie, M. F. & Zettl, A. Hydrocarbon lithography on graphene membranes. *Applied Physics Letters* 92:123110, 2008.

[126] Nguyen, C. V. et al. High lateral resolution imaging with sharpened tip of multi-walled carbon nanotube scanning probe. *Journal of Physical Chemistry B* 108:2816-2821, 2004.

[127] Nguyen, C. V. et al. Carbon nanotube scanning probe for profiling of deep-ultraviolet and 193 nm photoresist patterns. *Applied Physics Letters* 81:901-903, 2002.

[128] Nishijima, H. et al. Carbon-nanotube tips for scanning probe microscopy: Preparation by a controlled process and observation of deoxyribonucleic acid. *Applied Physics Letters* 74:4061-4063, 1999.

[129] San Paulo, A. & Garcia, R. High-resolution imaging of antibodies by tapping-mode atomic force microscopy: Attractive and repulsive tip-sample interaction regimes. *Biophysical Journal* 78:1599-1605, 2000.

[130] Snow, E. S., Campbell, P. M. & Novak, J. P. Single-wall carbon nanotube atomic force microscope probes. *Applied Physics Letters* 80:2002-2004, 2002.

[131] Solares, S. D., Easplandiu, M. J., Goddard, W. A. & Collier, C. P. Mechanisms of single-walled carbon nanotube probe-sample multistability in tapping mode AFM imaging. *Journal of Physical Chemistry B* 109:11493-11500, 2005.

[132] Solares, S. D., Matsuda, Y. & Goddard, W. A. Influence of the carbon nanotube probe tilt angle on the effective probe stiffness and image quality in tapping-mode atomic force microscopy. *Journal of Physical Chemistry B* 109:16658-16664, 2005.

[133] Stevens, R. M. D. et al. Carbon nanotubes as probes for atomic force microscopy. *Nanotechnology* 11:1-5, 2000.

[134] Uchihashi, T. et al. Carbon-nanotube tip for highly-reproducible imaging of deoxyribonucleic acid helical turns by noncontact atomic force microscopy. *Japanese Journal of Applied Physics Part 2-Letters* 39:L887-L889, 2000.

[135] Uchihashi, T. et al. Identification of B-form DNA in an ultrahigh vacuum by noncontact-mode atomic force microscopy. *Langmuir* 16:1349-1353, 2000.

[136] Wade, L. A., Shapiro, I. R., Ma, Z. Y., Quake, S. R. & Collier, C. P. Correlating AFM probe morphology to image resolution for single-wall carbon nanotube tips. *Nano Letters* 4:725-731, 2004.

[137] Wang, N., Tang, Z. K., Li, G. D. & Chen, J. S. Single-walled 4 angstrom carbon nanotube arrays. *Nature* 408:50-51, 2000.

[138] Wei, H. Y. et al. Control of length and spatial functionality of single-wall carbon nanotube AFM nanoprobes. *Chemistry of Materials* 20:2793-2801, 2008.

[139] Wong, E. W., Sheehan, P. E. & Lieber, C. M. Nanobeam mechanics: Elasticity, strength, and toughness of nanorods and nanotubes. *Science* 277:1971-1975, 1997.

[140] Woolley, A. T., Cheung, C. L., Hafner, J. H. & Lieber, C. M. Structural biology with carbon nanotube AFM probes. *Chemistry & Biology* 7:R193-R204 ,2000.

[141] Wu, Y. et al. Determination of the Young's Modulus of Structurally Defined Carbon Nanotubes. *Nano Letters* 8:4158-4161, 2008.

[142] Yuzvinsky, T. D. et al. Imaging the life story of nanotube devices. *Applied Physics Letters* 87:3, 2005.

[143] K.L. Jensen, *J. Vac. Sci. Tech. B*, 21:1528, 2003.

[144] Begtrup, G. *Silicon Nitride Membranes for Electrical and Thermal Transport Studies of Nanotubes*, PhD thesis, University of California, Berkeley, Fall 2008.

[145] Neil R. Wilson & Julie V. Macpherson. Carbon nanotube tips for atomic force microscopy. *Nature Nanotechnology* 4:483-491, 2009.

[146] Ernst Meyer, Hans Josef Hug, Roland Bennewitz. *Scanning probe microscopy : the lab on a tip*. Springer, Berlin, New York, 2004.

[147] Kislon Voïtchovsky, Jeffrey J. Kuna, Sonia Antoranz Contera, Erio Tosatti, & Francesco Stellacci. Direct mapping of the solidliquid adhesion energy with subnanometre resolution. *Nature Nanotechnology* 5:401405, 2010.

[148] Leo Gross, Fabian Mohn, Nikolaj Moll, Peter Liljeroth, and Gerhard Meyer. The Chemical Structure of a Molecule Resolved by Atomic Force Microscopy. *Science* 325(5944):1110-1114, 2009.

[149] K. R. Williams, K. Gupta, Etch Rates for Micromachining Processing–Part II, *Journal of Microelectromechanical Systems* 12(6), 2003.

[150] Iijima, Sumio. Helical microtubules of graphitic carbon. *Nature* 354(6348):5658, 1991.

[151] Guo, Ting; Nikolaev, Pavel; Rinzler, Andrew G.; Tomanek, David; Colbert, Daniel T.; Smalley, Richard E. "Self-Assembly of Tubular Fullerenes". *J. Phys. Chem.* 99(27):1069410697, 1995.

[152] José-Yacamán, M.; Miki-Yoshida, M.; Rendón, L.; Santiesteban, J. G. "Catalytic growth of carbon microtubules with fullerene structure". *Appl. Phys. Lett.* 62(6): 657, 1993.

[153] Postma, Henk W. Ch.; Teepen, T; Yao, Z; Grifoni, M; Dekker, C. "Carbon Nanotube Single-Electron Transistors at Room temperature". *Science* 293(5527):76, 2001.

[154] Pop, Eric; Mann, David; Wang, Qian; Goodson, Kenneth; Dai, Hongjie. "Thermal conductance of an individual single-wall carbon nanotube above room temperature". *Nano Letters* 6(1):96100, 2005.

[155] Zhou, X., Park, J.-Y., Huang, S., Liu, J. & McEuen, P. *Phys. Rev. Lett.* 95:146805, 2005.

[156] Dai, H. Javey, A., Pop, E., Mann, D. & Lu, Y. *NANO: Brief Reports and Reviews* 1:14, 2006.

[157] Wallace, P. R. "The Band Theory of Graphite". *Physical Review* 71(9):622, 1947.

[158] Matthew J. Allen, Vincent C. Tung, and Richard B. Kaner,"Honeycomb Carbon: A Review of Graphene" *Chem. Rev.*, 110(1):132145, 2010.

[159] Inger Ekvall, Erik Wahlstrom, Dan Claesson, Hakan Olin and Eva Olsson. "Preparation and characterization of electrochemically etched W tips for STM". *Meas. Sci. Technol.* 10(11), 1999.

[160] Williams, D and Carter, C. B. *Transmission Electron Microscopy.* Plenum Press, 1996.

[161] Fultz,B and Howe, J. *Transmission Electron Microscopy and Diffractometry of Materials.* Springer, 2007.

[162] J.M. Yuk, K. Kim, B. Alemán, W. Regan, J.H. Ryu, J. Park, P. Ercius, H.M. Lee, A.P. Alivisatos, M.F. Crommie, J.Y. Lee, and A. Zettl. Graphene veils and sandwiches. *Nano Lett.* 11(8):32903294, 2011.

[163] K. Kim, W. Regan, B. Geng, B. Alemán, B.M. Kessler, F. Wang, M.F. Crommie, and A. Zettl. High-temperature stability of suspended single-layer graphene. *Phys. Status Solidi RRL* 4(11):302-304, 2010.

[164] S. Chen, R.O. Ritchie, A. Zettl, and U. Dahmen. In-situ bending deformation of carbon nanotubes in HVEM. *Electron Microscopy* 3:75, 1998.

[165] J. Cumings and A. Zettl. Low-friction nanoscale linear bearing realized from multiwall carbon nanotubes. *Science* 289:602-604, 2000.

[166] G.E. Begtrup, K.G. Ray, B.M. Kessler, T.D. Yuzvinsky, H. Garcia, and A. Zettl. Probing nanoscale solids at thermal extremes. *Phys. Rev. Lett.* 99:155901, 2007.

[167] G.E. Begtrup, W. Gannett, T. D. Yuzvinsky, V. H. Crespi and A. Zettl. Nanoscale reversible mass transport for archival memory. *Nano Lett.* 9(5):1835-1838, 2009.

[168] David Griffiths. *Introduction to Quantum Mechanics, 2nd ed.*, Addison Wesley, 2004.

[169] A.D. O'Connell, M. Hofheinz, M. Ansmann, R.C. Bialczak, M. Lenander, E. Lucero, M. Neeley, D. Sank, H. Wang, M. Weides, J. Wenner, J.M. Martinis, A.N. Cleland. "Quantum ground state and single-phonon control of a mechanical resonator." *Nature* 464:697-703, 2010.

[170] K. L. Ekinci, M. L. Roukes. Nanoelectromechanical Systems. Review of Scientific Instruments 76:061101, 2005.

[171] Changyao Chen, Sami Rosenblatt, Kirill I. Bolotin, William Kalb, Philip Kim, Ioannis Kymissis, Horst L. Stormer, Tony F. Heinz, James Hone, "Performance of Monolayer Graphene Nanomechanical Resonators with Electrical Readout," *Nature Nanotechnology* 4:861-867, 2009.

[172] Jensen, K.; Mickelson, W.; Kis, A.; Zettl, A. Buckling and kinking force measurements on individual multiwalled carbon nanotubes. Phys. Re . B: Condens. Matter 2007,76.

[173] Timoshenko, S., Gere, J. Theory of Elastic Stability; McGraw-Hill: New York, 1961.

Part V

Appendices

Appendix A

Ultrahigh Resolution AFM with Carbon Nanotube Tips

We fabricate high-aspect-ratio, mechanically robust atomic force microscopy (AFM) probes with tip radii on the order of 5 Å and with zero cone angle. Our method uses a sub-angstrom precision positioning stage in a transmission electron microscope (TEM) to directly attach a single-walled carbon nanotube to the apex of an AFM probe tip. This method gives, for the first time, direct control over several vital parameters of nanotube AFM probes: The nanotube length, radius, and tilt angle. The carbon nanotube probes are then utilized to image gold nanoparticles and DNA with tapping-mode AFM in ambient conditions. We report nearly 8 nm resolution enhancement compared to commercially available super sharp Si AFM probes when imaging gold nanoparticles. We also measure DNA widths as low as 5.4 nm and observe, in some cases, the fine structure associated with the DNA double-helix, with a pitch of 3.32 nm, which agrees well with the theoretical value of 3.4 nm.

A.1 Introduction

Since the invention of atomic force microscopy (AFM) in 1986 [102], advancements in system components (electronics, scanners, and piezos), sample preparation, and techniques (FM, AM, Dual AC, *etc.*) have led to great improvements in the spatial resolution of AFM [146], which has, under special circumstances (*e.g.* with atomically flat crystals in fluid[147] or in UHV with single-molecule terminated probes[148]) reached true atomic-scale resolution. However, under nearly all ambient experimental conditions, the lateral image resolution of AFM remains ultimately limited by the scanning probe tip geometry. Because the topographic images generated by AFM are a convolution of the tip with the sample surface, the ideal probe tip should have a high aspect-ratio, a small radius of curvature, and be oriented along the axis normal to the substrate (*i.e.* have zero cone angle.) Furthermore, the imaging of soft, sensitive

samples, such as proteins and DNA, requires that long-range and short-range tip-sample forces be minimized[104, 122], so, given that these forces scale linearly with probe radius [110], the use of sub-nanometer radius tips becomes essential.

Fabrication limitations have limited conventional microfabricated AFM probes to tip radii above 2 nm and less-than-optimal aspect ratios. Furthermore, material constraints often generate tips with limited longevity due to tip crashing, which drastically reduces lateral resolution. One route to addressing these resolution limitations has been to use carbon nanotubes as the tip of AFM probes. The properties of carbon nanotubes– high-aspect ratio, high young's modulus [51], elastic response to deformation [118, 139], small diameter (as low as 4-5 Å) [123, 137], chemical inertness, and hollow character–make them a truly ideal tip material for AFM probes [117]. In order for CNT probes to achieve true molecular-scale resolution AFM, one must precise control over the nanotube's radius, length, and the tilt angle (the angle between the tube and the axis normal to the substrate).

Poor control over the nanotube radius (R), length (L), and tilt angle (ϕ) invariably leads to broadening of images, image artifacts and distortion, or unstable feedback [130, 131, 136]. The tube radius, R, sets a lower limit on the lateral resolution which will be, at best, twice the tip radius, $2R$. Furthermore, both attractive tip-surface interactions, which lead to additional image broadening and distortion [104, 129] (especially in soft materials), and repulsive interactions scale linearly with R [110, 131, 103]. Thus, it is desirable to have R as small as possible while adjusting the nanotube length, L, in order to offset the resulting increase in thermal oscillations, $A_{th} = \sqrt{\frac{4k_BT}{3\pi E}}\frac{L^{3/2}}{R^2}$, which increase the effective radius of the tube (for example, to achieve $A_{th} < 1$ Å with a 1 nm tube requires a tip length of 18 nm.) Decreasing L is also desirable in order to increase the maximum buckling force[173] $F_b = \frac{\pi^3 ER^4}{4L^2}$. An insufficient F_b precludes stable feedback during AFM imaging[145]. Lastly, large tilt angles, ϕ, cause convolution broadening (especially in high-aspect ratio surfaces [130, 136]) and increase the bending response to compressive response ratio $\sim \frac{4L^2}{3r^2}\tan\phi$ [130] which can cause image contraction, premature buckling, and excessive lateral bending (enough even to cause the tube sidewall to snap into contact with the surface. A tilt angle of $\phi < 40°$ has been shown to preclude stable imaging [136]. Some of the specifics of AFM imaging (i.e. adjusting parameters such as driving amplitude, set point amplitude, different imaging environments) with carbon nanotube AFM probes are given in [104, 131, 145].

Many carbon nanotube AFM probe fabrication methods have been explored, including mechanical assembly via optical microscopy [117] and scanning electron microscopy[128, 124, 122], CVD tube growth on the probe[111, 107] and inside etched pores [106, 112], dielectrophoretic deposition [138], electrical arc discharge [133], and the so-called "pick-up" method [113, 136]. However, these methods often fail to control the nanotube tip radius, length, cone angle, and, in many cases, the number of nanotubes on the probe, and thus have not realized the true resolution enhancement

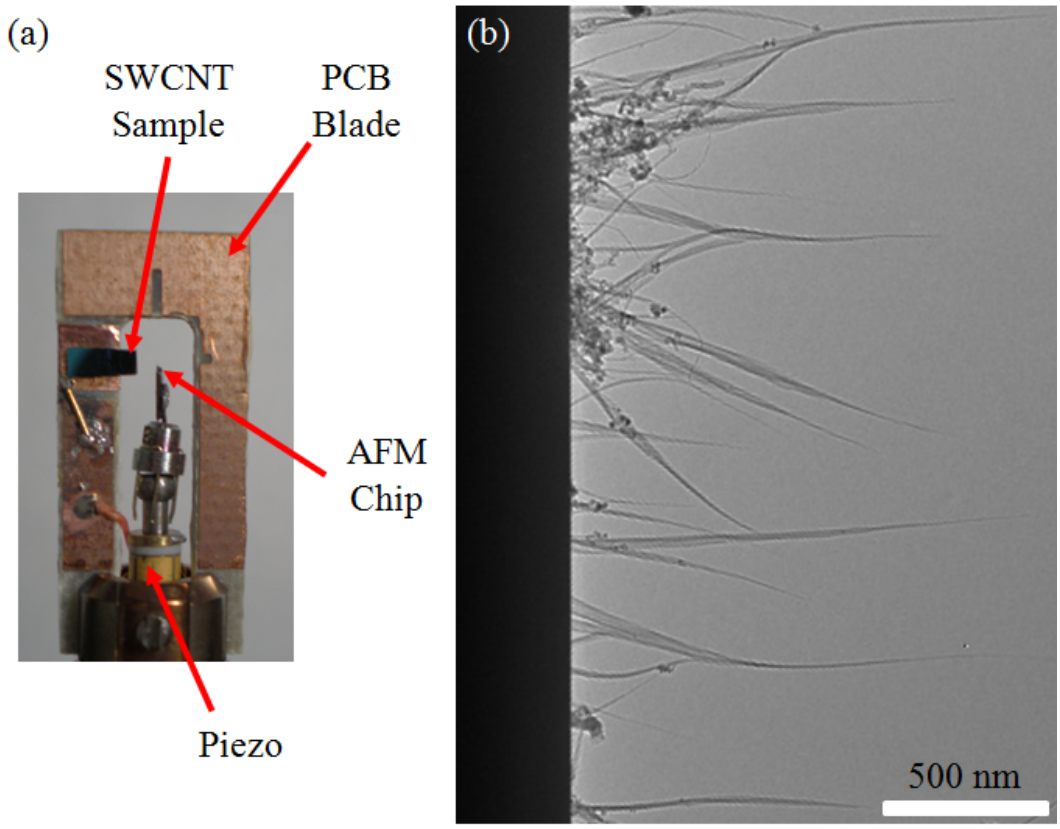

Figure A.1: TEM Blade for CNT AFM Tip Fabrication. (a) The blade, (b) the sample.

potential of the nanotube probes. In this chapter, we present a novel technique to fabricate carbon nanotube AFM probes that offers precise control over the nanotube radius, length, and tilt angle.

A.2 Materials and Methods

We now give the details of carbon nanotube AFM probe fabrication via *in situ* TEM mechanical attachment. We also describe the preparation of gold nanoparticle and DNA samples used to test the performance of the probes.

A.2.1 TEM-assisted mechanical attachment

Our method involves the attachment of a single-walled CNT (SWCNT) to the apex of a commercial Si AFM probe (Nanosensors; Mikromasch) using a manipulation stage (HS100 STM-Holder with SU100 Control System, Nanofactory Instruments AB,

Sweden) viewed using a TEM (JEM 2010, JEOL, Japan) operated at 100 keV. The AFM chip is mounted onto a modified sample holder and secured with a small amount of graphite conductive adhesive (Electron Microscopy Sciences GC adhesive 154), which is then attached to the manipulation stage head (see Figure A.1 (a)), allowing the chip to be manipulated over a few millimeters along each axis with sub-angstrom precision.

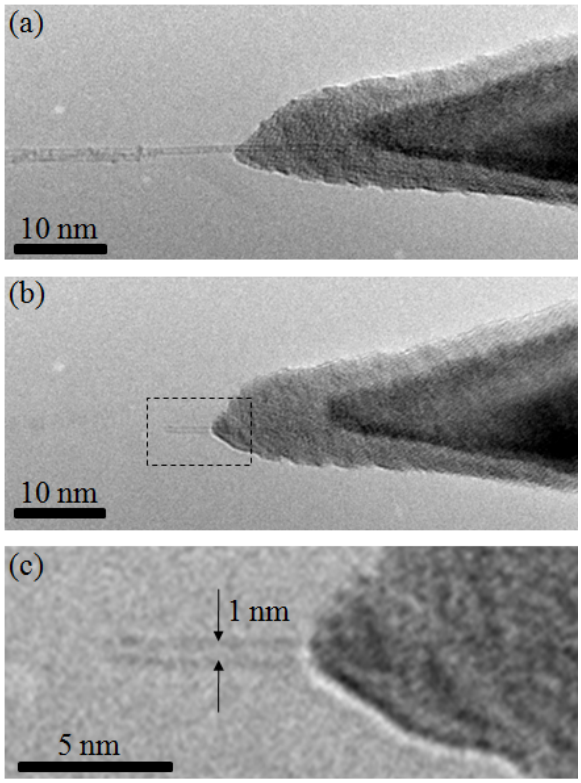

Figure A.2: *In situ* TEM Fabrication of SWCNT AFM Probe. (a) Approaching, (b) Cut, (c) Close-up.

A sample is then prepared with carbon nanotubes protruding off the edge of a Si or Si_3N_4 chip, as described in Chapter 1. This sample is made by spin coating a concentrated solution of electric arc-discharge SWCNTs (Carbon Solutions, Inc., P2-SWNT Purified low functionality $>$ 90% carbonaceous content) or MWCNTs in isopropyl alcohol onto a small piece of degenerately doped Si, followed by cleaving; this method produced many suspended CNT bundles "combed" perpendicular to the silicon edge, which typically have single isolated tubes at their ends. Figure A.1 (b) shows a SWCNT sample. The nanotube sample is then attached to a custom-fabricated TEM blade using a small amount of conductive adhesive. The custom blade, shown in A.1 (a), is made by milling a UHV-compatible printed circuit board

using the techniques in Appendix F.

Using the manipulator, the AFM tip is carefully positioned near the nanotube sample edge. Isolated suspended SWCNTs of reasonable length will not be visible because of large thermal vibrations but are typically found at the end of bundles. We then scan the region near a bundle until contact is made with a tube, at which point it becomes visible (Figure A.2 (a).) One can select tubes with diameters less than 1 nm and adjust the length of the tube that is in contact with the probe surface in order to maximize surface binding energy, which for a 1 nm diameter tube is on the order of 0.8 eV/Å[116]. The tip can be retracted to detach the tube and repositioned until the desired tube length and orientation is acquired. The nanotube is detached from the bundle by passing current (using a Keithley 2400 Sourcemeter) through the nanotube until it fails at its midpoint(Figure A.2 (b).) The higher current capacity of the bundle ensures that failure occurs on the single tube, thus the tube length will be half the original distance between the Si probe apex and where the single tube meets the bundle. Finally, the stage and user are grounded to prevent electrostatic discharge and the AFM chip is removed and placed in a conductive box.

Figure A.2 (c) shows a typical nanotube AFM tip produced using the above technique; for this specimen, $R \approx 5\mathring{A}$, $L \approx 7$ nm, and $\phi \approx 0°$. With good samples, the authors are able to produce a customized tip in about 1 hour, comparable to preparation times for the pick-up method.

A.2.2 Gold Nanoparticle Sample Preparation

Freshly cleaved ruby muscovite mica (grade V2, Ted Pella Prod. #50) was incubated with 15 ml of 0.1 % poly-L-lysine (Ted Pella, Prod. #18021 and #18026) for 1 minute, then rinsed with double distilled water and dried under ultra high purity compressed nitrogen. Immediately after drying, 10 ml of a 3.3×10^{10} particles/ml aqueous gold colloid (Ted Pella, Prod. #15702) is deposited onto the poly-lysine coated mica and allowed to incubate for 18 minutes. The mica was then rinsed with 1 ml of double distilled water and dried under a nitrogen stream for 90 seconds. The samples were allowed to dry overnight at 55° C, and then stored in a desiccator prior to the AFM scan.

A.2.3 DNA Sample Preparation

A DNA solution is prepared which consists of:

- 20 mM HEPES (4-(2-hydroxyethyl)-1-piperazineethanesulfonic acid), must be kept out of light and at 4° C.
- 40 mM KCl

- 5-10 mM $MgCl_2$ (can be kept for up to one month, and must be filtered through the buffer solution using 0.2μm filter because the salts begin to fall out of solution, pH should be about 7.6-7.8)
- 2.5 nM DNA (598 bp dsDNA is obtained from 19 kbp plasmid DNA. The plasmid is spliced using restriction enzymes, PCRed, passed through a Gel, and then separated and purified. DNA is kept concentrated at 50 nM until ready to use)

DNA and buffer is kept on ice (at 4°C) prior to mixing and mixed cold. Pipetting of DNA during mixing is done slowly and carefully to avoid damage or shock to DNA, and unused portion of DNA is immediately returned to ice and can be used for up to one month. After mixing, let dilution sit at room temperature for 5 minutes before use. All solutions are stored in highly sterile, RNAse/DNAse-free, research grade vials(ISC Bioexpress: No Stick hydrophilic microtubes, capacity 0.65 μl, reorder # c-3300-1, www.bioexpress.com). Micropipettes are "supercleaned" and only superclean pipette tips are used (Aerosol resistant tips, ART 10 Pipet Tips, catalog # Ref 2139, www.mbpinc.com)

We use the "German" mica preparation method, which gives superior, single sheet mica with minimal cracking; sharp tweezers are forced into the thin side of a piece of mica, separating into two pieces. Mica pieces are placed face up on clean absorbent filter paper (Whatman Prod. #1004-070, 70 mm circular grade 4 qualitative filters (VWR part number 28460-041)) and covered, then place on double sided tape to be used later.

We then deposit 2 μl of 2.5 nM DNA solution on mica, being careful not to pull DNA from bottom of vial. The drop should not wet the hydrophobic mica; if wetting occurs, mica is discarded and the process is repeated. Let solution stand for 60-90 seconds, then rinse with clean, filtered water and blot excess with filter paper. Dry immediately with dry nitrogen perpendicular to surface for 30 seconds.

A.3 AFM with CNT AFM probes

We utilize tapping-mode AFM (Asylum MFP-3D Bio) with carbon nanotube probes (bare probe is Nanosensors PPP-NCH) and commercial supersharp probes (Nanosensors, PPP-NCH, $R \approx 1$ nm) to image gold nanoclusters and DNA on mica as prepared above. In all cases, the target amplitude was kept to a minimum (5-10 nm), and the set-point amplitude was adjusted to tap as softly as possible in order to minimize damage to the probe and the surface but still allow stable imaging. All imaging was performed in ambient conditions and in repulsive mode, whenever possible.

Representative AFM images of gold nanoparticles using a nanotube probe and a commercial probe are shown in Figure A.3. The dilation due to the larger tip radius

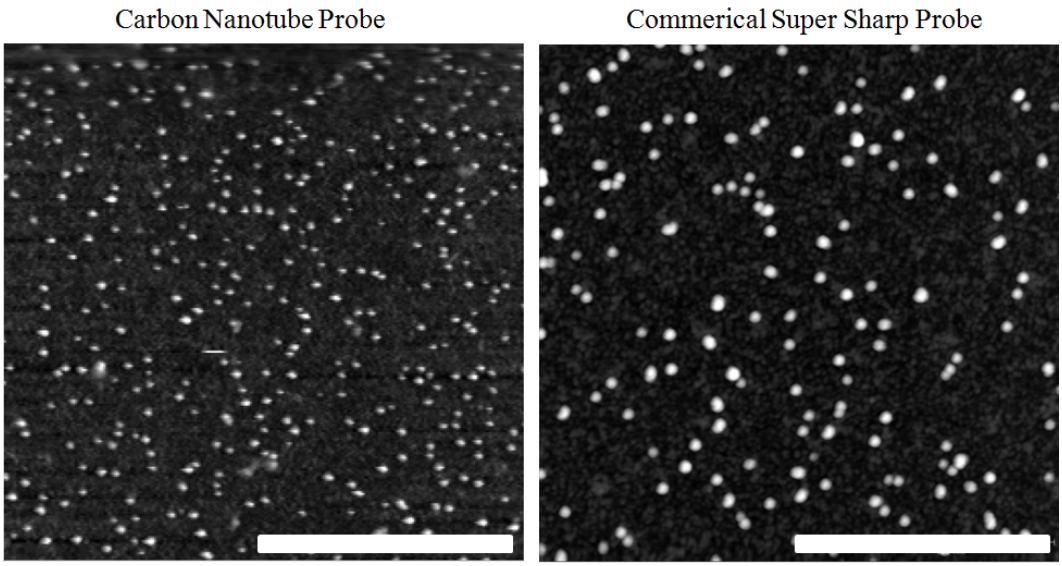

Figure A.3: AFM of Gold Nanoparticles. (Left) Carbon Nanotube Probe (data scale: 0 to 7.4 nm). (Right) Commercial super sharp probe (data scale: 0 to 6.7 nm). (Image scale bar: 500 nm)

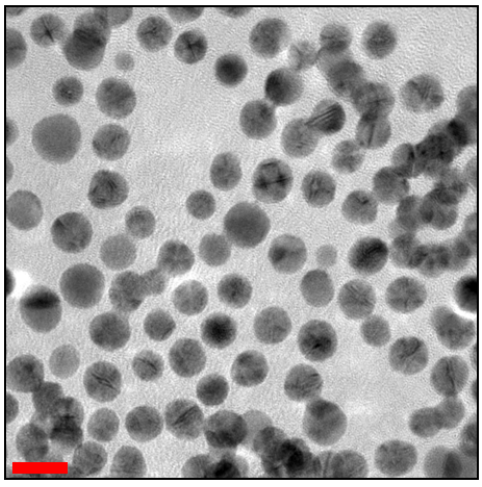

Figure A.4: TEM of Nanoparticles (scale bar: 10 nm)

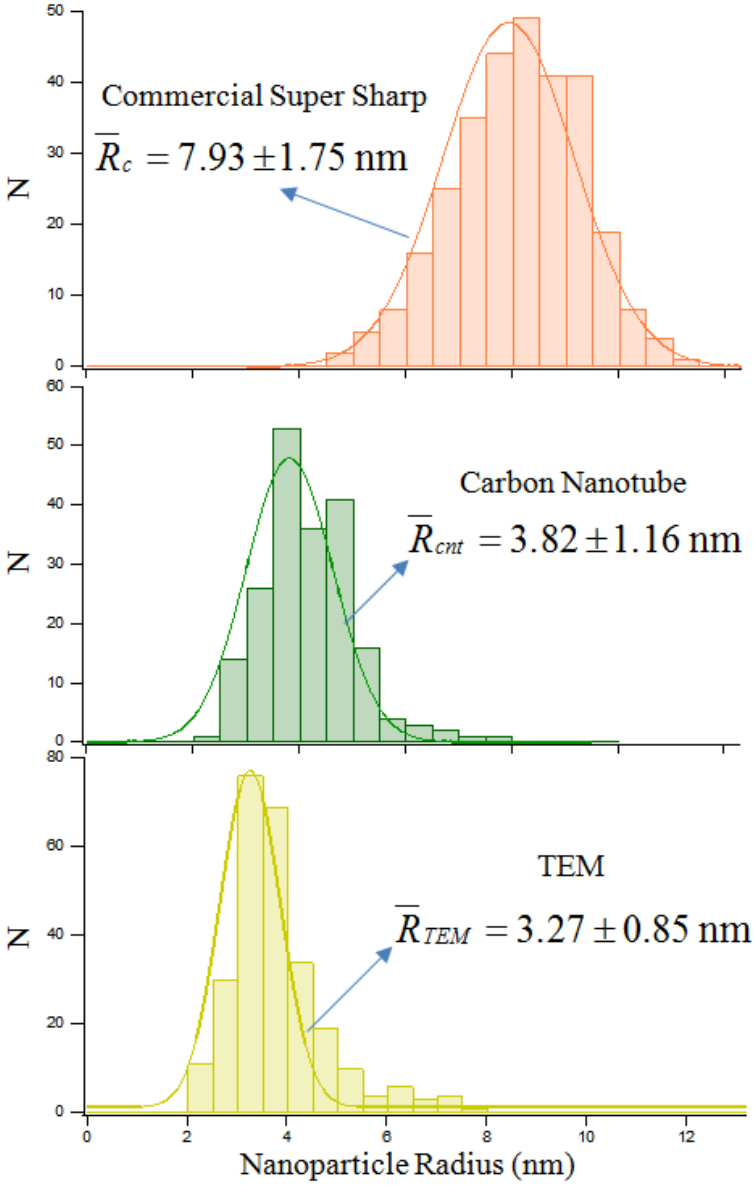

Figure A.5: Nanoparticle AFM Data. TEM, Commercial, and CNT probe data are shown. $R_{cnt} = 3.82 \pm 1.16$ nm, $R_c = 7.93 \pm 1.75$ nm, $R_{TEM} = 3.27 \pm 0.85$ nm. Difference between TEM and CNT AFM gives the approximate probe radius of curvature, $R \approx 0.55$ nm.

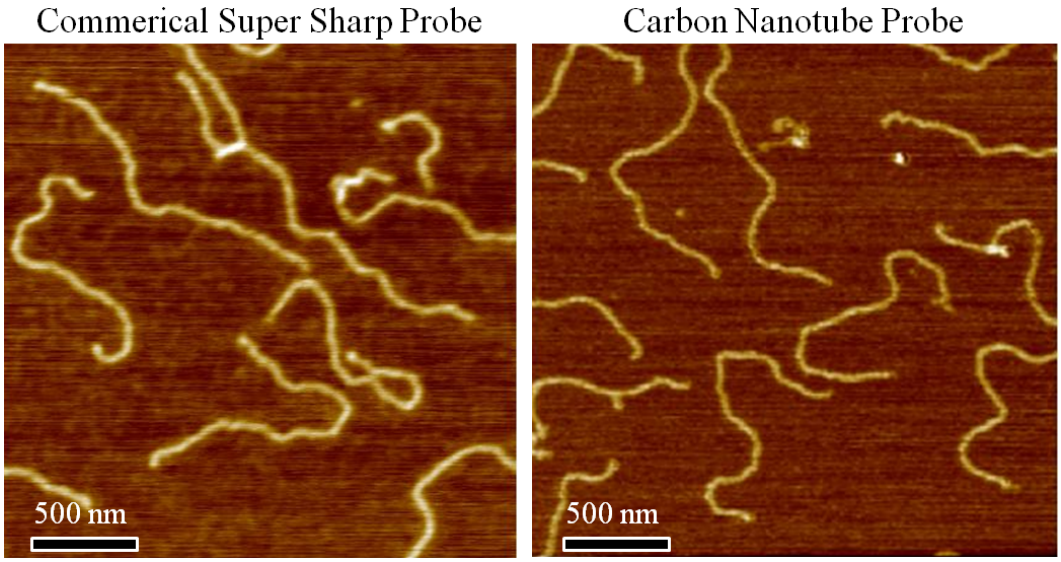

Figure A.6: Commercial (left) vs. Nanotube (right) Probe AFM of DNA. Resolution enhancement is on the order of 20 nm.

of the commercial tip is clear from these images. TEM of gold nanoparticles (on a graphene support) is shown in Figure A.4; particle analysis from these images was used to obtain the "true" nanoparticle diameters to compare to diameters measured from AFM images. Histograms of the measured full-width of the nanoparticles from multiple scans is shown in Figure A.5. The top histogram shows data from the commercial tip, which has an average measured particle radius of $R_c = 7.93 \pm 1.75$ nm. The middle and bottom histograms correspond to the carbon nanotube probe and the TEM particle analysis, with measured radii of $R_{cnt} = 3.82 \pm 1.16$ nm and $R_{TEM} = 3.27 \pm 0.85$ nm, respectively. The difference between R_{TEM} and R_{cnt} gives the approximate probe radius of curvature, $R \approx 0.55$ nm. When imaging nanoparticles, the nanotube probe can achieve about 8.22 nm resolution enhancement over the supersharp commercial probe.

A similar comparison for DNA images is shown in Figure A.6. In this case, the resolution enhancement is approximately 20 nm. Higher magnification images using a nanotube tip are shown in Figure A.7. Figure A.7 (a) shows the periodicity of DNA double-helix on one part of the DNA strand and is measured to be approximately 3.32 nm. Figure A.7 (b) measures full-width of DNA to be approximately 5.5 nm, which, according to simulations (Figure A.8), corresponds to a tip radius of order 1 nm. Figure A.8 (a) shows AFM simulations assuming a parabolic tip geometry. Figure A.8 (b) shows profiles of these images and is useful in estimating expected tip radii.

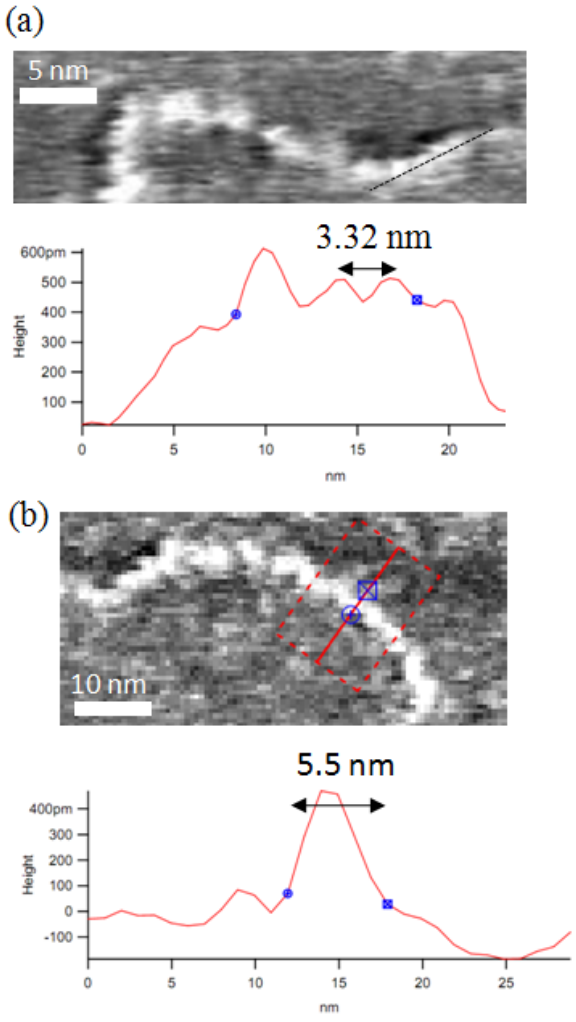

Figure A.7: Resolving DNA Fine-structure with Carbon Nanotube Probe. (a) Periodicity of DNA double-helix is measured to be approximately 3.32 nm. (b) Measured full-width of DNA is approximately 5.5 nm, which, according to simulations (Figure A.8), corresponds to a tip radius of order 1 nm.

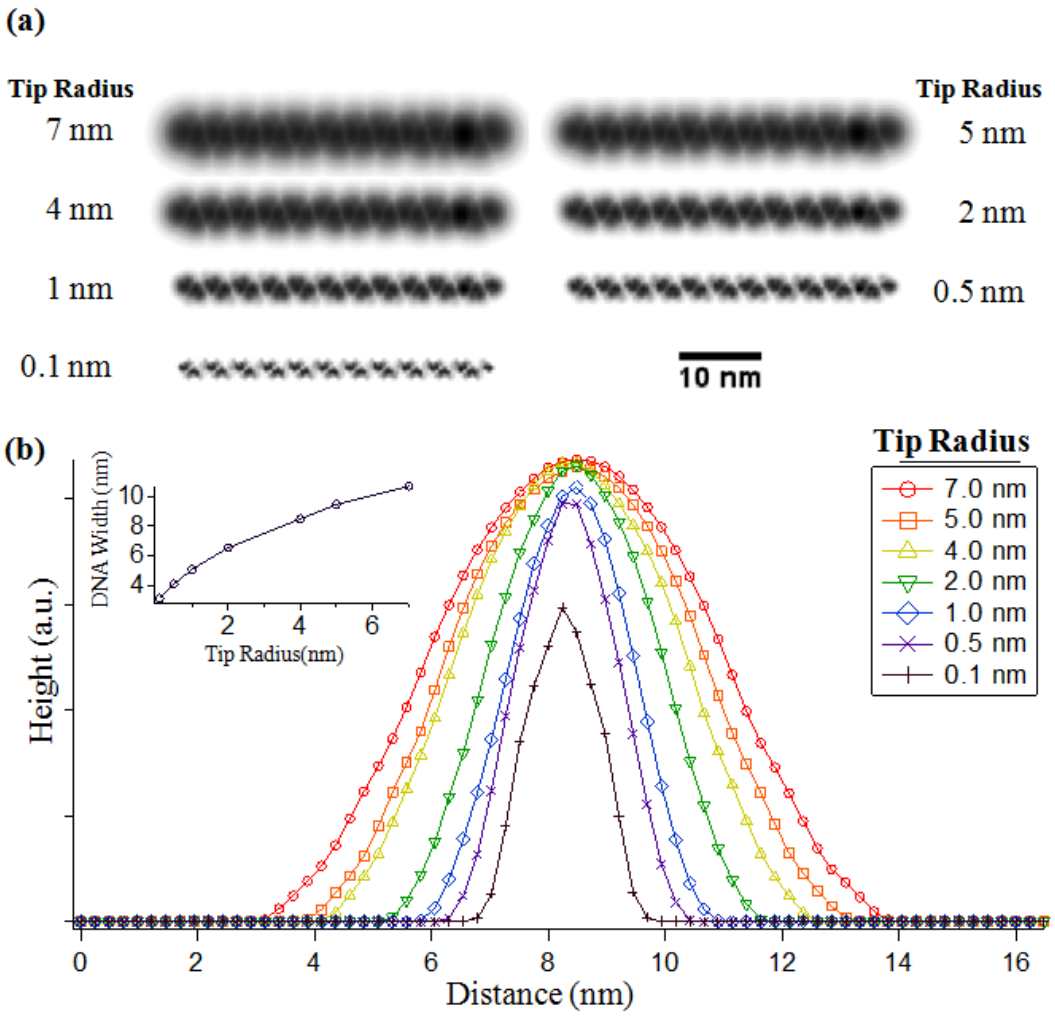

Figure A.8: AFM Simulation of DNA. (a) Topographic AFM simulations of DNA. (b) DNA profile for different radius tip (inset shows maximum width vs. tip radius)

Appendix B

Graphene as a Platform for AFM/TEM Characterization

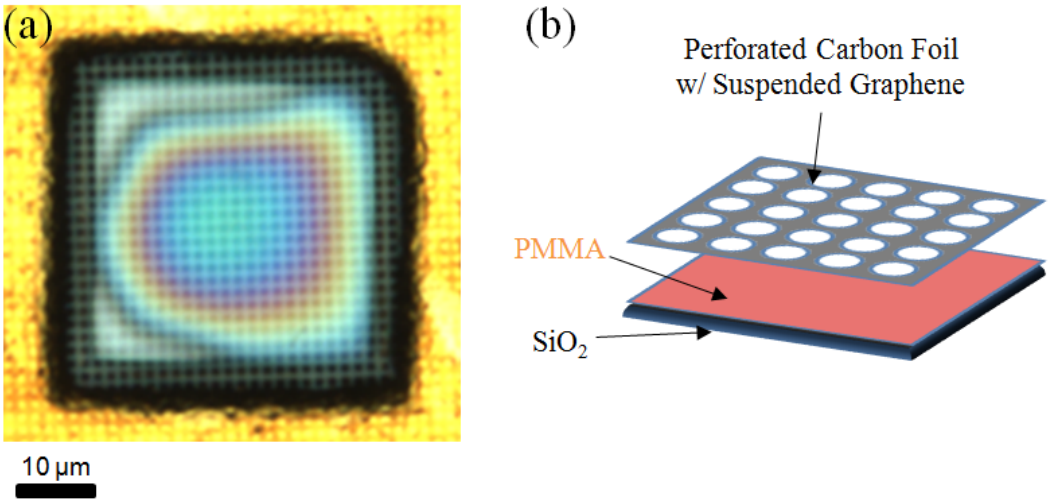

Figure B.1: Transfer of TEM Grid to PMMA/Silicon Substrate for AFM Studies. (a) Optical image. Fringes from sinking of metal frame causing PMMA thickness to change. (b) Schematic sideview of structure.

The graphene membranes fabricated in Chapter 7 used as resonators in Chapter 8 can be made compatible with AFM characterization. In order to do this, the metal frame of the TEM grid must be made completely flat and bound to a substrate. Any non-flat regions can be caused by parts of the frame not being supported by a substrate, which makes AFM characterization, where a sharp tip is attempting to touch the surface, impossible.

AFM requires the surface to be flat locally (on the order of 1-5 μ) and firmly

bound to a hard substrate. The metal frame of the TEM grid is about 25 μm thick, so the roughness of most tape cannot be used since the tape surface may come into contact with the graphene membrane. A technique was developed to stick the grid to a sticky, flat surface. We spin PMMA A4 (1800 rpm for 25 seconds, maximum deceleration) onto clean silicon dioxide dies. The graphene TEM grid is carefully flattened by sandwiching between freshly cleaved mica and pressing firmly with the thumb. The flattened grid is placed graphene-side up onto the PMMA as soon as it is finished spinning down (within 1 second). The timing of this process is crucial: if the PMMA is too "wet" and soft, the metal support of the grid will sink into it and the graphene will touch the PMMA; too dry, the grid will not stick sufficiently or will stick unevenly. When optimized, the metal support is pulled into the PMMA so that the entire frame (or large fractions of it) of the TEM grid are held down and bonded to the PMMA, but the graphene remains suspended, untouched by the polymer. Figure B.1 shows an optical image and a schematic of a successful transfer. The AFM image of the suspended membrane seen in Figure 8.10 was prepared using this technique.

Because this process avoids putting strain on the graphene or its amorphous carbon support scaffold, preparing specimens for AFM studies in this way is minimally invasive. As one application of this technique, we prepare a gold nanoparticle graphene "sandwich" structure, which is gold nanoparticles dispersed between to layers of graphene. Details of the fabrication can be found in Ref. [162]. We can correlate TEM to AFM images and we see that upper layer of graphene forms pyramidal shapes with near perfect symmetry over the gold nanoparticles. TEM selected-area diffraction suggests that the pyramids have a preferred orientation along one of the graphene lattice directions.

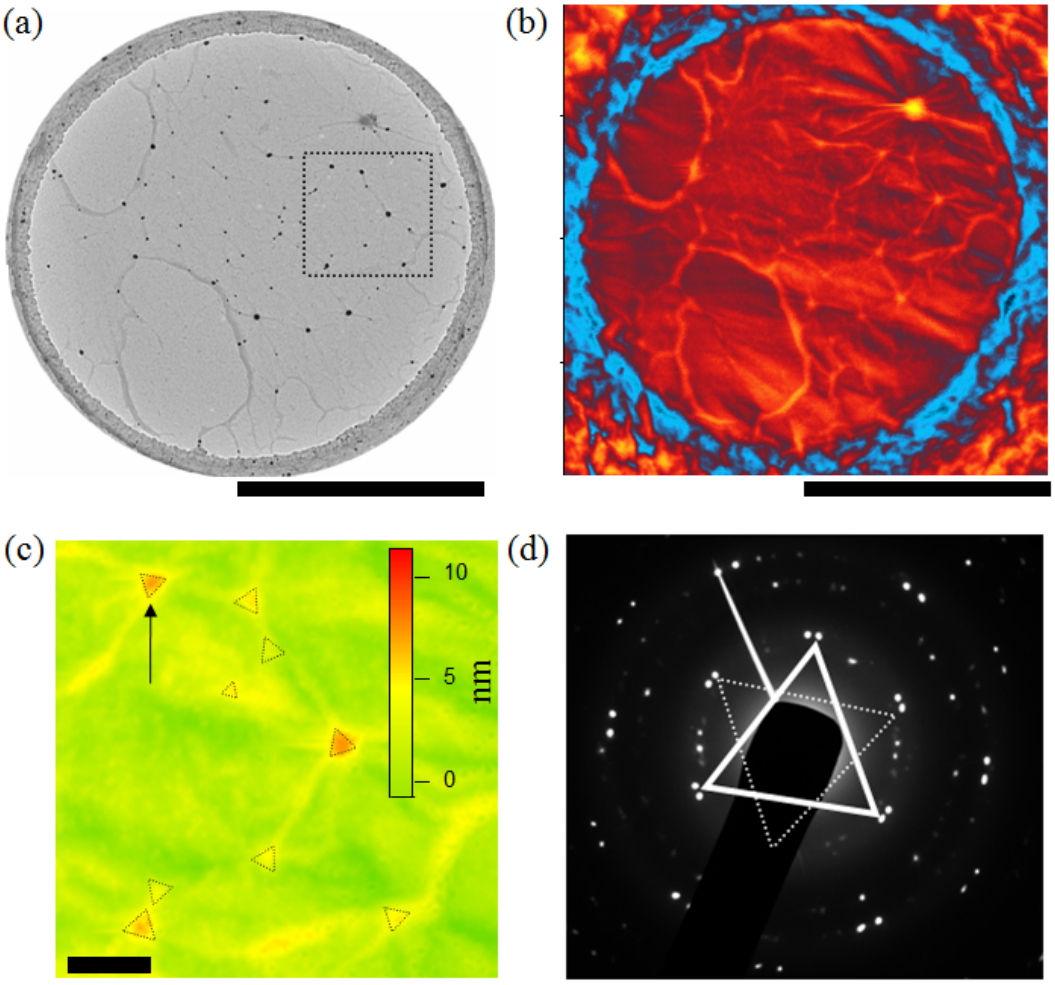

Figure B.2: TEM and AFM of Graphene Sandwich Structure. (a) TEM (scale bar: 1 μm) and (b) AFM (scale bar: 1 μm) of the same graphene "sandwich". (c) shows higher magnification of boxed region in (a) (scale bar: 100 nm); pyramidal shapes are formed over gold nanoparticles. (d) Diffraction in same boxed region. Dashed triangle corresponds to triangle indicated with arrow in (c), suggesting preferential alignment along a crystal axis.

Appendix C

Solution to the Duffing Equation

This derivations follows that given in Refs. [8] and [21]. The Duffing equation is

$$\frac{d^2x}{dt^2} + \gamma\frac{dx}{dt} + \omega_0^2 x + \omega_0^2 K_3 x^3 = \frac{f_0}{m}\cos(\omega t) \tag{C.1}$$

We use the trial solutions $x = \frac{1}{2}(a_0 e^{i(\omega_c t+\phi)+c.c.})$ and define $\omega_c = \omega_0(1+\delta)$, where ω_0 is the natural resonance frequency and δ is a detuning parameter. Drop terms $e^{\pm i3\omega_c t}$ and matching terms $e^{i\omega_c t}$, we find

$$-\omega_c^2 a_0 + i\omega_c\gamma a_0 + \omega_0^2 a_0 + \frac{3}{4}\omega_0^2 K_3 |a_0|^2 a_0 = \frac{f_0}{m}$$

Including an explicit phase in the amplitude, $a_0 = a_0 e^{i\phi}$, gives

$$\left(\omega_0^2 - \omega_c^2 + \frac{3\omega_0^2 K_3}{4}a_0^2 + i\omega_c\gamma\right) a_0 = \frac{f_0}{m}e^{-i\phi} \tag{C.2}$$

We now look at Eq. C.2 near resonance, $|\delta| << 1$, and set $E = a_0^2$

$$\left(-\omega_0^2\delta + \frac{3\omega_0^2 K_3}{4}E\right)^2 E + \omega_0^2\gamma^2 E = \left(\frac{f_0}{m}\right)^2$$

Lastly, with the definitions $Q = \omega_0/\gamma$ and $\kappa = 3K_3/4$, we have the final results:

$$E^3 - \frac{4\delta}{\kappa}E^2 + \left(\frac{1}{Q^2\kappa^2} + \frac{4}{\kappa^2}\delta^2\right)E - \left(\frac{f_0}{\kappa m}\right)^2 = 0 \tag{C.3}$$

and

$$\tan\phi = \frac{\gamma(1+\delta)}{2\omega_0\delta - 3\omega_0 K_3 E/4} \tag{C.4}$$

$$= \frac{1}{Q}\frac{1+\delta}{2\delta - \kappa E} \tag{C.5}$$

Plots of E vs. δ result in leaning Lorentzian curves and lead to multivalued solutions.

Appendix D

Modeling Membrane Vibrations: A Solution to the 2D Wave Equation

In this appendix, we solve the two dimensional wave equation for a square geometry and clamped boundary conditions along the entire perimeter. The two-dimensional wave equation is:

$$\frac{\partial^2 z}{\partial x^2} + \frac{\partial^2 z}{\partial y^2} = \frac{1}{\nu^2}\frac{\partial^2 z}{\partial t^2}$$

We use the method of separation of variables:

$$z(x, y, t) = X(x)Y(y)T(t)$$

Thus

$$YT\frac{\partial^2 X}{\partial x^2} + XT\frac{\partial^2 Y}{\partial y^2} = \frac{1}{\nu^2}XY\frac{\partial^2 T}{\partial t^2}$$

and

$$\frac{\nu^2}{X}\frac{\partial^2 X}{\partial x^2} + \frac{\nu^2}{Y}\frac{\partial^2 Y}{\partial y^2} = \frac{1}{T}\frac{\partial^2 T}{\partial t^2}$$

The time dependent part, $\frac{1}{T}\frac{d^2T}{dt^2} = -\omega^2$, has a solution

$$T(t) = C_\omega \cos(\omega t) + D_\omega \sin(\omega t)$$

Now,

$$\frac{\nu^2}{X}\frac{\partial^2 X}{\partial x^2} + \frac{\nu^2}{Y}\frac{\partial^2 Y}{\partial y^2} = -\omega^2$$

Then we have for X,

$$\frac{1}{X}\frac{d^2X}{dx^2} = -\frac{1}{Y}\frac{d^2Y}{dy^2} - \frac{\omega^2}{\nu^2} \equiv -k_x^2$$

and

$$\frac{1}{Y}\frac{d^2Y}{dy^2} = k_x^2 - \frac{\omega^2}{\nu^2} \equiv -k_y^2$$

where $k_x^2 + k_y^2 = \frac{\omega^2}{\nu^2}$. We find

$$X(x) = E\cos(k_x x) + F\sin(k_x x)$$

$$Y(y) = G\cos(k_y y) + H\sin(k_y y)$$

Applying the boundary conditions $z(0, y, t) = 0$ and $z(x, 0, t) = 0$ gives $E = G = 0$. Similarly, $z(L_x, y, t) = 0$ and $z(x, L_y, t) = 0$ establish the condition $L_x k_x = p\pi$ and $L_y k_y = q\pi$ for integers p and q. Then, $k_x = \frac{p\pi}{L_x}$ and $k_y = \frac{q\pi}{L_y}$. Finally, we write

$$z_{pq}(x, y, t) = [A_{pq}\cos(\omega_{pq}t) + B_{pq}\sin(\omega_{pq}t)]\sin\left(\frac{p\pi x}{L_x}\right)\cos\left(\frac{q\pi y}{L_y}\right) \tag{D.1}$$

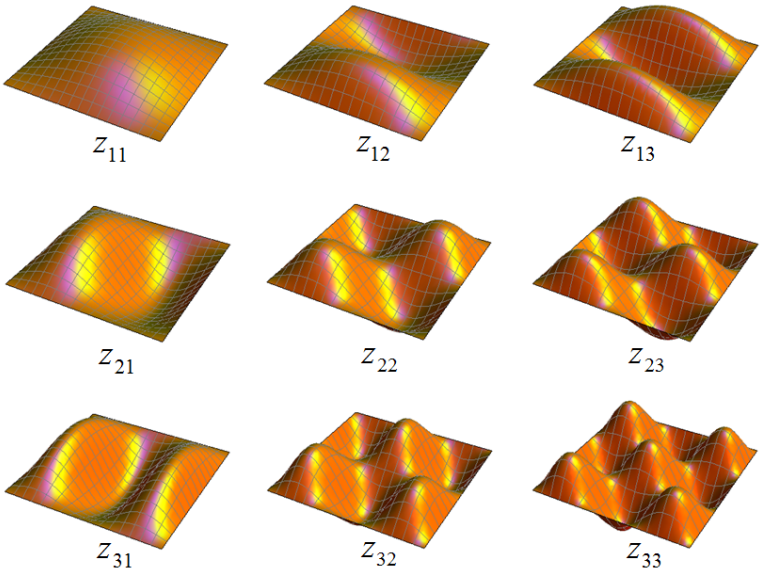

Figure D.1: Mode Shapes, z_{pq}, for Square Membrane

The general solution is

$$z_{pq}(x, y, t) = \sum_{p=1}^{\infty}\sum_{q=1}^{\infty}[A_{pq}\cos(\omega_{pq}t) + B_{pq}\sin(\omega_{pq}t)]\sin\left(\frac{p\pi x}{L_x}\right)\cos\left(\frac{q\pi y}{L_y}\right) \tag{D.2}$$

where

$$\omega_{pq} \equiv \pi\nu\sqrt{\left(\frac{p}{L_x}\right)^2 + \left(\frac{q}{L_y}\right)^2} \tag{D.3}$$

Plots of the vibrational mode shapes z_{pq} are shown in Figure D.1.

Appendix E

Attocube

We now give detailed instructions for operating the Attocube nanopositioning stage:

- Mount sharp probe and nanotube sample onto Attocube stage and load stage into vented SEM. Attach piezo control and biasing feed-through connector (1 inch diameter) to SEM port, and attach corresponding connector (white 6 pin) to Attocube stage. Confirm a good biasing connection; BNC ground (signal) should be connected to nanotube sample (sharp probe). Check stage height, carefully close SEM chamber door(DO NOT TOUCH POLE PIECE), and evacuate.

- Make sure `Axis Mode` of Attocube controller for each axis is set to "Off". Also, make sure all channels (*i.e.* 1, 2, and 4) of the amplifier are "off". After SEM reaches a pressure of 3×10^{-5} mBar, turn on power supply to Attocube controller and amplifier. Turn on EDAX computer and make sure USB-DAQ card (Data Translation, USB-DT9834 Series) is connected to a USB bus and receiving power.

- Turn SEM beam on, find your mobile tip, and align beam as normal. DO NOT MOVE Z-AXIS OF SEM STAGE ANY FARTHER THAN ITS LOWEST POSITION.

- To control Attocube stage without a computer, switch `Axis Mode` on controller to `Run`; now move switch position to `cont` for continuous motion or `step` for single steps. The `infinity` (∞) position allows continuous motion without having to hold down switch. Only use `infinity` when traveling large distances and be sure to watch stage CAREFULLY. Attempts to move an axis past the limits of its position range (several millimeters for each axis) will result in IRREPARABLE damage to the piezos. If an axis stops moving, DO NOT MOVE IT IN THAT DIRECTION ANY MORE. `Frequency` controls how often

the piezos cause motion, and `Amplitude` sets how far the piezos expand per cycle. The motion of an individual axis is cause by the piezo expanding and then rapidly contracting. The scaffold hugging the piezo stick-and-slips during each of the expand-contract cycles.

- To control Attocube stage with computer, open up the `Attocube.exe` LabVIEW VI on EDAX desktop. Select `The following user:` with user name `Attocube` and the universal Zettl Group password. Now switch `Axis Mode` on controller to `CCON` for `C`omputer `CON`trol. Now use joystick (X,Y fine and coarse, and Z coarse) and rotational trackball (Z fine) to control the Attocube position. This LabVIEW program sends commands to the DAQ to send out DC (fine) and AC (coarse) voltage signals to the piezos. Users can adjust the speed and precision of motion with additional joystick controls.

Appendix F

Optical Lithography

Single-process lithography has been set up in our lab with relatively inexpensive equipment. Resist deposition is done with a commercial spin-coater, and exposure is performed using the UV light from a commercial UV-Ozone substrate cleaning system. When performed properly, in-house optical lithography can be used to obtain 3-4 μm resolution when using good commercial masks. High resolution glass masks can be ordered through the UCB microlab. Another more economical option for masks is

CAD/Art Services Inc.
87509 Oberman Lane, Bandon, Or 97411
TEL: 541-347-5315 FAX 541-347-6810
e-mail: cas@outputcity.com

They can achieve 12.5 μm resolution and print 5"x7" masks for $35.50 (2010). They also have a 24 hour turn-around time. A third, extremely cheap option for lower resolution lithography is to print them using a commercial printer. The Konica printer in Birge B219 is excellent at printing masks; set the contrast as high as possible and the resolution as high as possible and print black and white only. A 600 dpi printer can achieve 125 μ resolution (see Fig. F.1.) Programs such as Adode Photoshop, Illustrator, or GIMP can be used to make mask designs.

We can also fabricate our own high resolution masks using electron beam lithography (see Appendix G). Metallize a glass or quartz substrate and perform lithography then etch with appropriate metal etchant (see Ref. [149].) The masks used for the work in Chapter 7 were made using e-beam lithography.

Once the mask is fabricated, we use the following I-line photolithography recipe:

1. Spin Resist (Rohm & Haas MEGAPOSIT SPR 955-CM 0.9 Photoresist)at 2000 rpm for 1 minute.

2. Bake @ 100 C for 90 seconds.

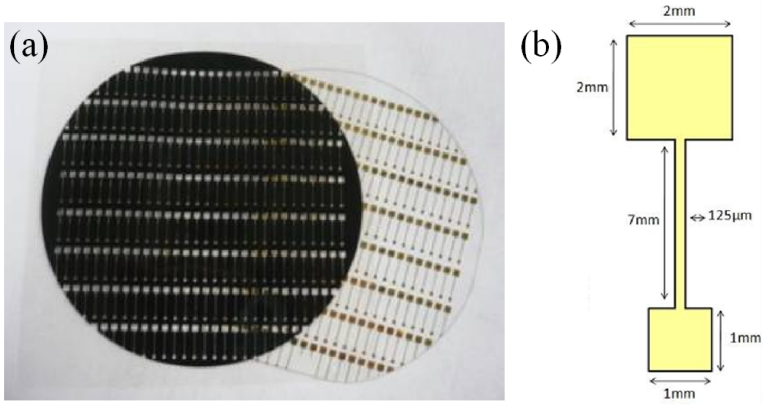

Figure F.1: Mask printed on with commercial 600 dpi printer. (a) Mask and final product on Borofloat wafer. (b) dimensions of individual repeated element of mask. Smallest resolved feature is 125 μm.

3. Warm up UV Ozone lamp for 2.5 minutes, then place masked substrate on stage and expose with UV for 2.5 minutes. Using a glass slide or a blank glass or quartz mask substrate is recommended so that the mask is in good contact with the substrate.

4. Post exposure bake @ 110 C for 90 seconds.

5. Develop with Fuji Films OPD4262 (Tetramethylammonium hydroxide) for 1 minute and rinse in DI.

6. Evaporate/Sputter metals or materials.

7. Lift-off in Acetone and rinse in IPA.

Printed Circuit Boards (PCBs)

PCB methods were fabricated in house for traditional uses (see Figure F.3) and to fabricate TEM blades (see Figure F.2) for the Nanofactory Holder. The process uses single mask photo lithography. If one is to design a PCB with for electronic circuits with commercial components (resistors, capacitors, ICs, etc.) then design is done most easily with commercial PCB CAD software. A good free solution is *EagleCAD*; it has a large library of components that can be inserted into designs as well as integrated with on-line catalogs (Newark), so that one can design and purchase components simultaneously.

We use double-sided, copper-clad G-10/FR4 (McMaster-Carr # 8521K44) because of its good high-vacuum compatibility. The PCB board must be very clean (Aceton, IpA, Water) before coating with resist. The PCB board is then coated in a double-layer of resist, and exposed as described above. The backside can be coated

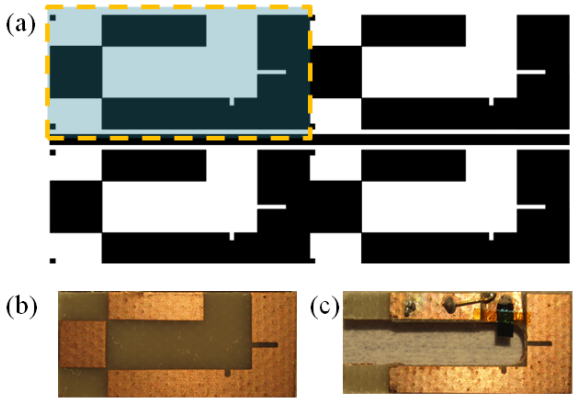

Figure F.2: PCB TEM Blade. (a) Mask (b) Blank (c) Machined blank

with scotch tape or resist to protect from etchant. Immerse the exposed PCB in a sodium persulfate (MG-Chemicals Product # 4101-1KG) solution, and lightly stirred (@ 100 rpm) for 1 hour. When designing PCBs for high-frequency electronics, one can use *TXline*, a transmission line calculator (Microstrip, Stripline, Coplanar waveguide, Grounded coplanar WG, Slotline) to aid in proper design. *Sonnet* is an excellent electrodynamics simulator for RF circuits and is also very helpful for modeling purposes.

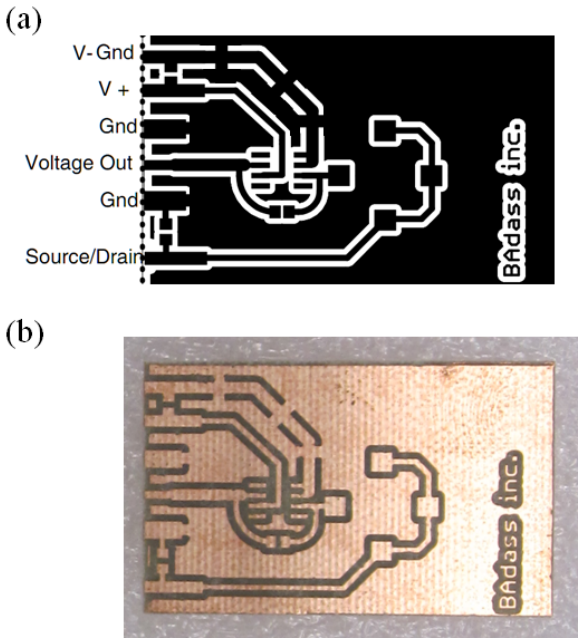

Figure F.3: PCB Amplifier Design (a) Mask (b) Blank

Appendix G

NPGS Guide

This appendix details the process of fabricating devices with nanoscaled features using electron beam lithography. In particular, here we show how to successfully use the commercial system NPGS (Nanometer Pattern Generation System) to generate nanoscaled features.

There are eight general steps for successfully accomplishing nanolithography:

1. Prepare a sample on substrate with alignment markers
2. Obtain SEM mappings or Optical mappings of sample on substrate including alignment markers.
3. Create a new or use an existing NPGS project.
4. Use mappings to generate DesingCAD file and define your pattern.
5. Prepare Run file. The run file will give directions to the SEM to write the pattern that you defined in your DesignCAD file.
6. Spin on resist
7. Preparing SEM for e-beam writing and writing (executing NPGS runfile.)
8. Developing, deposition, and lift-off.

G.1 Prepare a sample on substrate with alignment markers

The examples that I'll give in this outline will involve using predefined electrodes and alignment markers (as used with membrane devices, for example), and using bare substrates coated in PMMA with scratches as the alignment markers (as used in preparing graphene devices, for example)

G.2 Obtain SEM mappings or Optical mappings of sample on substrate including alignment markers

Once your sample is prepared, you must prepare mappings of your sample. The mappings will be used to define the components of your device (e.g. contacts, side gates, etc.) in Design CAD so it is important that the sample be well aligned to orthogonal axes. For example, when mapping a membrane device one can use "Align Feature" in "Stage" menu of Microscope Control to align the x-axis of the image with the lower edge of electrodes (it will also be important later when writing patterns that one repeats this x-y alignment.) Here is an example:

When preparing graphene samples, use the x-y stage control to scratch x and y axis into the PMMA

G.3 Create a new NPGS project

You can copy and paste NPGS runfile and DesignCAD templates from "c:\NPGS \Projects \NPGS Runfile and DesignCAD Templates"

G.4 Use mappings to generate DesingCAD file

Open your new project in NPGS and display Run files and DesingCAD files by using the "Display File Type" pull down menu in the upper RHS of NPGS (see Figure G.1). Open your DesignCAD file by highlighting it and then selecting "DesignCAD LT" in NPGS. If you are using a mapping of your sample then you should import the image and resize it appropriately. Import mapping image by going to "FileImage:Load Image File." Determine the pixel/micron ratio for you image and resize the image by opening the image details; you can do this by selecting the image and pressing "ctrl + i."

Now you can draw your device pattern (see Figure G.2; an easy way to do this is to use NPGS's Polyfill command "NPGS-Polyfill" or by pressing PF on LHS toolbar. The default layer assignment for the shapes generated with Polyfill is layer 1; to change layers or the properties of a layer press "CTRL + i." You can set different objects to different layers so that these layers can have varying writing parameters (i.e. spot size, area dose, center-to-center spacing, line spacing, etc.) The "Point Select Mode" mouse (see Figure G.2) comes in handy when you want to modify existing shapes by dragging points to new locations or adding points. Here are a few common DesignCAD commands:

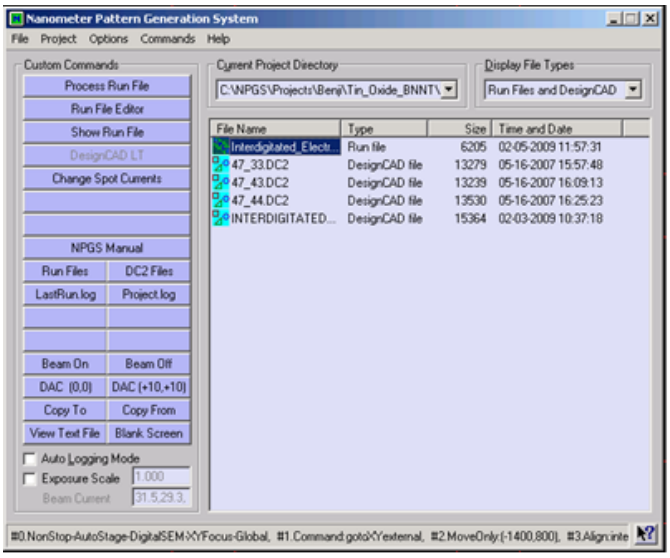

Figure G.1: NPGS Main Window

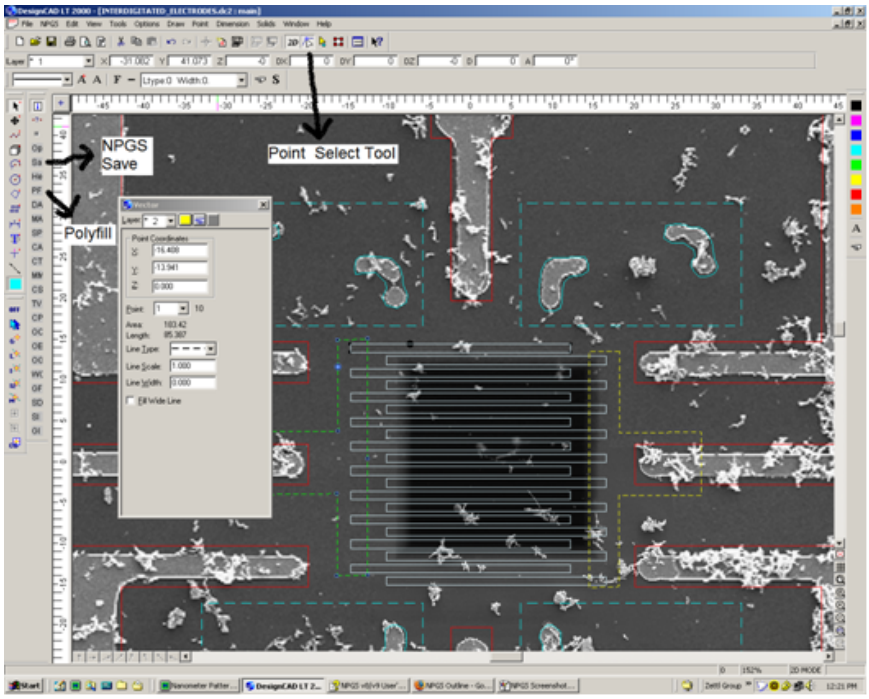

Figure G.2: DesignCAD. T-shaped pattern has been selected and CTRL + i shows the object information. The little black dots outlined in blue on the perimeter of the object can be selecting individually and moved using the "Point Select Tool" found in the upper tool bar.

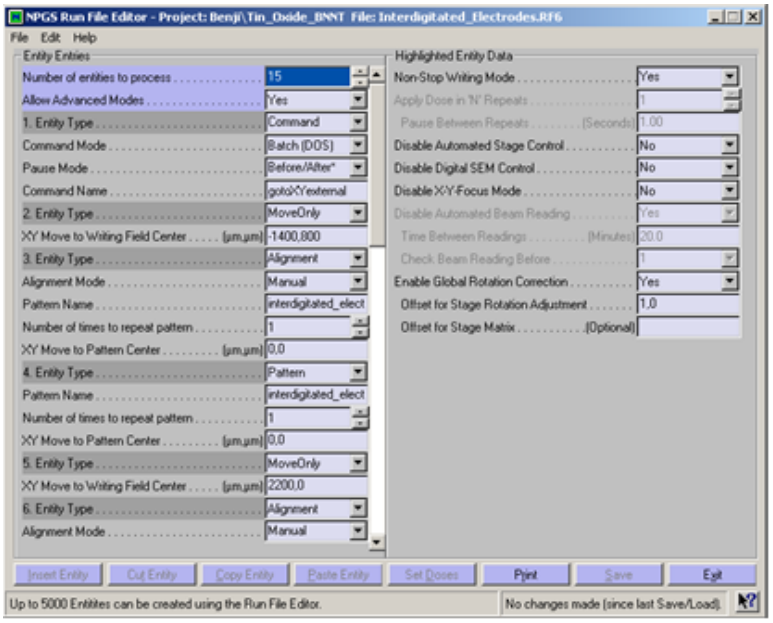

Figure G.3: NPGS Run File Editor

- Save with Sa on side or "NPGS-Save"!! Don't use File-Save (Not for NPGS Patterns)
- Ctrl I = Layer Information.
- "NPGS-Polyfill" or PF on LHS toolbar to draw objects.
- Ctrl + g turns on Grid.
- The @ (Shift + 2) sign is used for measurement.
- Rotate = R and rotate small amount
- Ctrl R redraws all pattern

When you are finished always center your pattern; do this by going to "NPGS-Most Useful DesignCAD Commands-Origin" and mouse-click to define your origin.

G.5 Prepare Run file

In NPGS, highlight your run file and click "Run file editor." You'll see the dialog box in Figure G.3: The left hand "Entity Entries" column lists the NPGS procedures in the order in which they will be executed. For instance, the second entity is a

"Move Only" procedure that commands the SEM's stage to move to (x, y) = (-1400 μm, 800 μm) relative to its starting position. The most common entities are the "Alignment," "Pattern," and "MoveOnly" entities. Whenever an entity is highlighted, more detailed information about the procedure is given in the right hand column. The first region of the "Entity Entries" column isn't a command, however, instead it lists the number of procedures or entities to be executed in the run file. Highlighting this first region brings up some general but important information about the run file that is displayed in the right had column (see Figure G.3.) The settings that are displayed in the screen shot are recommended. That is, run file should proceed from step to step without interruption (Non-stop writing mode: Yes), the SEM stage should be controlled remotely by NPGS (Disable Automated Stage Control: NO), the SEM (focussing, etc.) in general should be controlled remotely by NPGS (Disable Digital SEM Control: NO, Disable X-Y Focus Mode: NO), and the focusing should reference the user defined plane of the sample (Enable Global Rotation Correction: Yes.) We'll show how the user can define the plane of the sample later when we discuss Direct Stage Control.

First, let's describe the "Alignment" entity and give suggested parameters for PMMA A4 resist as deposited in step 6. Basically, an alignment entity will ask the SEM to scan a designated window (or four in the case of membrane devices) and collect an image and align features of the image with alignment markers defined in your DesignCAD file. Good alignment will lead to precise definition of your pattern, like contacts on a SWCNT. Every alignment entity has an alignment mode (usually manual, i.e. you do it, or autoalign1, i.e. the computer uses an edge finding algorithm to perform alignment) and performs alignment with respect to alignment markers defined in a specified DesignCAD file, i.e. Pattern Name. Click on the field of Pattern name to change the DesignCAD file. Now highlighting the first alignment entity we see the details in the right column (see Figure G.4.)

Layers 10-13 correspond to the 4 windows and alignment markers within the windows for a typical membrane device. Layers 1 and 2 get skipped since they define the pattern to be written. Since the beam is scanning all four windows for some time, the PMMA in these regions will get exposed so that one should keep features to be patterned out of and away from these windows. The alignment settings shown in figure G.4 work well for membrane devices, however one should check and adjust the beam current for spot 1 if necessary. We reproduce suggested alignment settings here:

```
Magnification = 2000X
Center-to-Center Spacing = 200 nm
Line Spacing = 200 nm
Spot Size = 1
Measured Beam Current   29 pA
Dwell = 5 counts
```

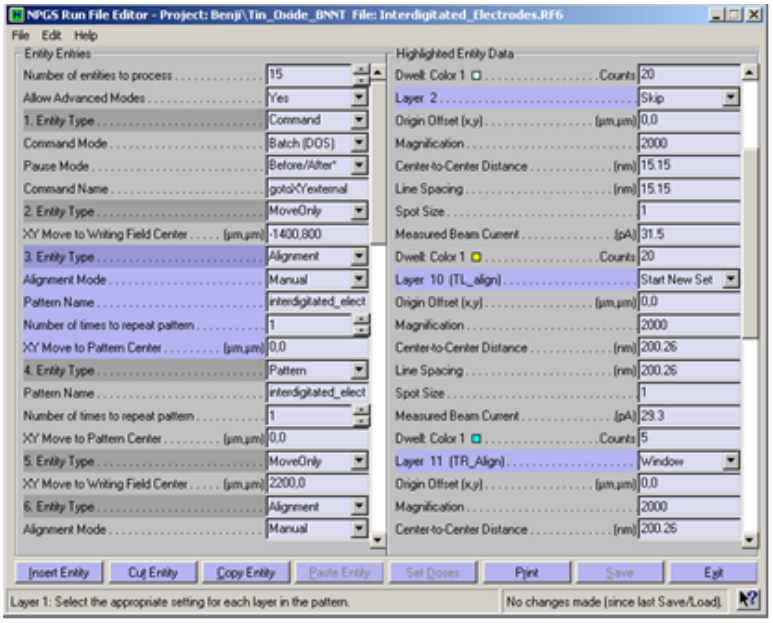

Figure G.4: NPGS run file editor highlighting an alignment entity.

Set the first alignment layer (layer 10 in figure G.4) to "Start New Set" and the remaining three layers to "Window" BEFORE changing settings, then changing the settings in one layer changes those in all other layers. Save your changes by clicking "Save" in the lower right hand corner of the dialog box.

Next we describe the Pattern entity. First choose your DesignCAD file in the Pattern field as above. The right hand Highlighted Entity Data column now displays the details of this particular Pattern entity (Figure G.5): Since we won't be using the alignment layers, we'll first make sure to skip these layers (for the example here, skip layers 10-13) and also set pattern layers to "Normal Writing" (for us here, we'll apply this to layers 1 and 2.) The "interdigitated_∗ electrodes" DesignCAD file has one layer (layer 1) that defines finer features (the actual interdigitated electrodes) and another layer (layer 2) that defines larger features (the electrode connecting all electrodes from the source or drain side of the device.) We'll be using spot size 1 for layer 1 and spot size 3 for layer 2.

Now we'll describe the parameters of layer 1. Origin offset is useful if you haven't aligned the beam correctly so that the image shifts when changing spot sizes. We will align the beam correctly for different spot sizes so origin offset will be (0, 0.) The magnification must be set so that the patterns that you wish to write fit in the field of view; when you are acquiring your SEM mappings take note of the magnification and us this value if all the features you wish to pattern are within the boundaries of the image. Normally, NPGS will not let you choose too large of a magnification. Here

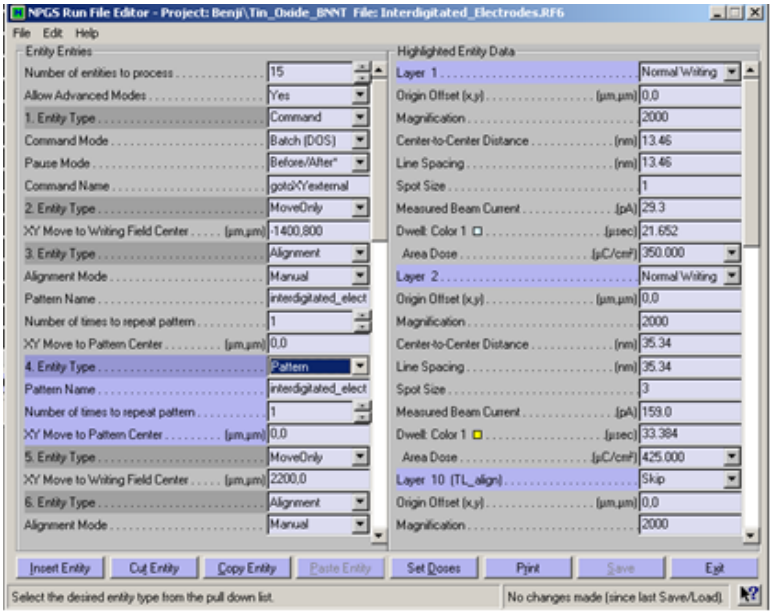

Figure G.5: NPGS run file editor highlighting a pattern entity.

we set the magnification to 2000. The SEM writes patterns by allowing its focused electron beam to rest or dwell in a spot for a fixed amount of time, exposing the PMMA resist. The Center-to-Center and Line spacing determines how far the beam will move the x and y directions when exposing spots of the resist. Normally, when patterning on a different substrate (other that Si, Si oxide, or Si nitride, for example) or when the SEM electron gun is changed one should perform dose tests in which center-to-center and line spacing varies as does the Area dose; these three parameters determine how well you expose the resist (too little, too much, or just right) as well as the minimum feature size. We set center-to-center and line spacing to about 14 nm. Spot Size should be set to 1 for this layer and the current should be set to that measured through the Faraday cup (more on this later), which at the time of this writing was between 28-29 pA. Finally, the area dose sets the number of electrons that will hit the a given area of surface and, with center-to-center and line spacing and the beam current, will determine the total time the electron beam sits in one spot exposing the resist. We set this value to 350 $\mu C/cm^2$ which automatically sets the dwell time. Here we reproduce suggested values for spot sizes 1 and 3 at 30 keV:

Spot 1:

```
Magnification = 2000X
Center-to-Center Spacing = 13-15 nm
Line Spacing = 13-15 nm
Spot Size = 1
```

Measured Beam Current 28-29 pA
Dwell = 22 μ sec
Area Dose = 325-350 $\mu C/cm^2$

Spot 3:
Magnification = 2000X
Center-to-Center Spacing = 35 nm
Line Spacing = 35 nm
Spot Size = 3
Measured Beam Current 158-160 pA
Dwell = 33 μ sec
Area Dose = 425 $\mu C/cm^2$

Spot 6:
Magnification = 150X
Center-to-Center Spacing = 200 nm
Line Spacing = 200 nm
Spot Size = 6
Measured Beam Current 7600-8000 pA
Dwell = 22 μ sec
Area Dose = 450 $\mu C/cm^2$

This completes the pattern part or the run file. If one were making multiple patterns on one substrate, the last pattern entity would be followed by a MoveOnly entity, another Alignment, and finally another Pattern entity. I usually end my run files with a MoveOnly and then a beam blank command. It is always a good thing, especially when new to NPGS, to check your run file for errors. To do this, go to "Commands: Process Run File: Error Check Mode." Hit the space bar a few times to get through the alignment part of the run file and just follow the on-screen directions to finish. If everything works OK, save your run file.

G.6 Spinning Resist

1. One drop PMMA A4
2. Spin on at 3000 rpm ramping up in 3 sec.
3. Spin for 60 sec.
4. Bake for 20-30 min. at 185 C.

5. Place 20 nm Gold Colloidal Particles on edges of chip (BB International) for focusing, or put small scratches in the PMMA.

G.7 Writing Patterns with the SEM

Load sample into SEM and prepare to turn on beam as usual (i.e. adjust stage height to 5mm from pole piece, set beam energy to 30 keV, and select spot size 3.) Additionally, one must:

1. Set the SEM electrostatic beam blanker (RHS of scope) to # 2 position.
2. Switch "black box" (to left of NPGS monitor) to NPGS.
3. Turn on beam blanker and set it to EXT.
4. Connect the BNC coaxial cable from Keithley to SEM, turn on the Keithley and select "ZCHK."
5. Set magnitude reference to "Display" in SEM control panel (Magnification : Reference : Display.)
6. In Microscope Control, make sure that scan rotations are set to zero and that tilt and rotation are set to 0.0 degrees (go to stage control and also check tilt on the SEM chamber door.)

Now turn on the beam and perform normal beam alignment @ 30 keV (not over your sample!!) for all spots being used (following the example given in this outline, we would check spots 1 and 3). If you do not get a beam, be sure that to press "Beam On" in NPGS. Make sure switching between spot sizes that the image doesn't shift too much. If the image does shift more than a micron (or whatever the limits of your pattern dictate) you can use "Control Area: Adjustments" to correct them if they are off. Have someone show you how to do this so that the beam condition isn't made worse. Here is the procedure: Choose "10 Gun Tilt and Shift", and press "+" to proceed. You can always cancel if things go wrong. Select 30.0 kV, then "+." Note position of image in spot 1 (probe current 1) then press "+" to desired spot size, say to spot 3 (probe current 3.) Use Gun Shift to move image to where it was when in spot 1. Press "+" until asked to save and save. Now go to the Faraday cup and repeat going to spot 3. Now adjust Gun Tilt to maximize the current reading on the Keithley. Save your adjustments. Now recheck that, for instance, spot 1 and spot 3 do not shift the image too much.

Once the spot sizes are correctly aligned and adjusted, measure and record beam currents for all spot sizes being used by zooming into the Faraday cup and checking the reading on the Keithley. Enter these new current values into your run files.

Align the stage to your sample using the procedure outlined in section 2, being careful not to expose the important parts of your sample. I usually do alignment using spot size 3 since the images look crisper. Now you must define the plane of your sample using NPGS's Direct Stage Control feature. NPGS needs to know the plane of your sample since your sample is not perfectly flat and as the beam moves around the focusing will drift. Then, NPGS will use the plane that you define during Direct Stage Control to adjust the focus at different points of your sample. In NPGS, go to "Commands:Direct Stage Control":

1. Press ESC to cancel all Global Rotation Corrections (unless working with large samplewriting over distances of a cm)
2. Hit any key, except ESC, to ignore Global Correction Data
3. Hit Space Bar to set rotation angle to zero.
4. Press Enter to acquire new X-Y Focus data.
5. Focus on some point on you sample and press SPACE.
6. Now move to new location far from first location and repeat step 5. Continue taking 4+ points.
7. When finished, press Enter. A, B coeff. ¡ 0.00001 is normally good. Press ENTER to keep data, then ESC to go back to NPGS.

Now go to a convenient, known position on your sample and change, if needed, your first MoveOnly entity to reflect your current position. Blank the beam in Microscope Control and in NPGS and click "Process Run File" to begin.

When NPGS prompts you about Global Rotation corrections, just follow steps 1-3 above and then hit the space bar to use the data you just took, followed by another space bar to begin processing the rest of your run file. If you are doing manual alignment, here are a few more details:

- "A" autocontrasts your image.
- "B" blanks the beam
- Alignment patterns can be moved to alignment markers by clicking and dragging them into place.
- When done, press Enter and "y" to recalculate the matrix.

When your run file execution is finished, turn beam blanker off, set electrostatic beam blanker back to # 4 position, replace grounding cap to BNC connector on SEM, turn off Keithley, and remove sample as usual.

G.8 Developing, Evaporating, and Lift-off

Developing is done with a 1:3 diluted solution of MIBK (4 Methyl-2 Pentenone) in IPA, followed by rinses in IPA and H_2O:

1. 1:3 MIBK:IPA for 90 seconds
2. IPA 15 seconds
3. H_20 15 seconds

Evaporate or sputter your metal (or whatever) onto your sample and lift off in Acetone or NMP overnight. One can also place sample in acetone or NMP and warm it up to 80° C or so.